FACULTY OF ENGINEERING
AND ARCHITECTURE

A speckle pattern image acquired from ultrasound imaging in mud.

Bart Brouwers - doctoral dissertation

Monitoring Fluid Dynamics of Mud

Bart Brouwers

Doctoral dissertation submitted to obtain the academic degree of
Doctor of Engineering Technology

Supervisors

Prof. Evert Lataire, PhD* - Prof. Jeroen van Beeck, PhD**

* Department of Civil Engineering
Faculty of Engineering and Architecture, Ghent University

** von Karman Institute for Fluid Dynamics

November 2024

2024

GHENT
UNIVERSITY

FACULTY OF ENGINEERING AND ARCHITECTURE

Monitoring Fluid Dynamics of Mud

Bart Brouwers

Doctoral dissertation submitted to obtain the academic degree of
Doctor of Engineering Technology

Supervisors

Prof. Evert Lataire, PhD* - Prof. Jeroen van Beeck, PhD**

* Department of Civil Engineering
Faculty of Engineering and Architecture, Ghent University

** von Karman Institute for Fluid Dynamics

November 2024

GHENT UNIVERSITY

ISBN 978-94-6355-917-1
NUR 950, 967
Wettelijk depot: D/2024/10.500/121

Members of the Examination Board

Chair

Prof. Hennie De Schepper, PhD, Ghent University

Other members entitled to vote

Prof. Ludwig Cardon, PhD, Ghent University
Prof. Mahya Roustaei, PhD, Ghent University
Peter Staelens, PhD, dotOcean
Prof. Erik Toorman, PhD, KU Leuven

Supervisors

Prof. Evert Lataire, PhD, Ghent University
Prof. Jeroen van Beeck, PhD, von Karman Institute for Fluid Dynamics

”The reward of the young scientist is the emotional thrill of being the first person in the history of the world to see something or to understand something.”

Cecilia Payne-Gaposchkin
(British-American Astronomer, 1900-1979)

Preface

Antwerp, 16/10/2024
Bart Brouwers

Why are you doing that? That is the question I got most often over the past five years when I told people I was working on a PhD. In the beginning, I answered that I wanted a new personal challenge. Now, at the end of the process, my answer is more comprehensive. Firstly, as someone who values innovation, there is no greater thrill than realising that you are the first person ever to try something and develop it further into something useful. During the experimental phase of this research, I got to experience this amazing feeling every day. What followed was a period during which I learnt and acquired new skills, such as programming, data and image processing, presenting and academic writing. All these, even the academic writing, I consider an asset for my further career and personal development. And finally, perhaps the biggest gain in completing this PhD trajectory is the boost in self-confidence every time another piece of the puzzle could be put in place.

Of course, it wasn't all sunshine and rainbows. But, surrounded and supported by the right people, the less pleasant moments do not prevail when looking back. The first

person I am grateful to for this is my wife An. When I first raised the idea of starting a PhD, you probably thought ”there he is again with another silly idea”. And right you were! What an idea to start something like a PhD at the age of 35 with two children and a third on the way, all in combination with a full-time job. Yet, you were never negative about it and despite the burden it imposed on our family and our relationship, I was always given the time and space I needed to pursue this PhD degree.

Secondly, my thanks goes to my two supervisors Evert and Jeroen. By sharing your experience and knowledge, you perfectly provided the support I needed for my entry into academia and the completion of this PhD project.

Furthermore, I would like to express my appreciation to my colleagues at Flanders Hydraulics:

I am grateful to previous management Frank Mostaert, Lieve van de Water and Stefan Geerts for believing in me and giving me the opportunity to start this PhD. My thanks also go to the current management, Karim Bellafkih, Patrik Peeters and Jurgen Latte, for providing the necessary time to pursue this endeavour.

To my close colleagues in E&O, thank you for covering for my partial absence and for your help when I needed it. Specific thanks go to Sam Das, Ben Wolput, Charlotte Cleen, Bart Van den Broeck, Ellen Bastiaensen and Lia De Bruyn for their contribution to the experiments. To Dieter Meire, who was both a substantive and spiritual companion during this journey. To Wim Van Hoydonck, for his help and patience while I struggled with Python and LaTeX. And finally to Steven Cerpentier, for his help in obtaining the literature I so often asked for.

Along the way, I also got help from researchers of other laboratories:

Thank you to the people at VKI for helping me understand the OpenPIV script.

My gratitude to

- the Cardiovascular Imaging and Dynamics division of the University Hospital Leuven
- department of materials, textiles and chemical engineering of Ghent University
- Institute of biomedical engineering and technology of Ghent University

to make your laboratory and equipment available for my experiments.

A final heartfelt thank you to the members of the jury. You are all very busy people, nonetheless you showed interest in my work and took the time to review and discuss it. There is no doubt that this provided a final boost to the quality of this dissertation.

Dutch summary

Slib komt wereldwijd voor op de bodems van oceanen, zeeën, rivieren, meren, enz.. Het is een donkere viskeuze vloeistof bestaande uit water, klei mineralen, organisch materiaal en silt deeltjes. In een energie arme omgeving zal gesuspendeerd slib bezinken en, indien dit lang genoeg aanhoudt (weken tot maanden), uiteindelijk consolideren. Anderzijds zullen bij verstoring eerder bezonken slibdeeltjes terug suspenderen in de bovenliggende watermassa. Niet geconsolideerd slib kan zo worden meegevoerd met stromingen in het water. Zeker in riviermondingen en hun omgeving kunnen sliblagen op deze manier over aanzienlijke afstanden verplaatst worden. Bijgevolg hebben veel havens, rivieren en navigatiekanalen te lijden onder dichtslibbing en zijn de autoriteiten genoodzaakt om regelmatig onderhoudswerken uit te voeren om de doorgang en veiligheid van het scheepvaartverkeer te garanderen.

Een goed begrip van het gedrag van slib is daarom vereist om de invloed van de aanwezigheid ervan volledig te begrijpen, baggerwerken te optimaliseren of de impact van nieuwe infrastructuurontwikkelingen in te schatten. Het mechanisch gedrag van slib is hierbij van groot belang en wordt bestudeerd in verschillende wetenschappelijke disciplines, zoals maritieme sedimentologie, waterbouwkunde en maritieme techniek. Hiervoor wordt gebruik gemaakt van

numerieke modellen en experimentele opstellingen, zowel in situ als in een gecontroleerde laboratorium omgeving.

Het gebruik van natuurlijk slib in fysische experimenten brengt echter een aantal uitdagingen met zich mee. Vooreerst is het bezinkgedrag en bijgevolg de mechanische eigenschappen van slib veranderlijk. Dit maakt het moeilijk om experimentele resultaten te reproduceren, wat ongunstig is voor de geloofwaardigheid van de experimenten en het vergelijken van verschillende experimenten compliceert. Hydraulische experimenten om de stromingsdynamica in slib te bestuderen brengen nog een bijkomende uitdaging met zich mee. Met de huidige gekende meettechnieken voor het meten van drukveranderingen of stromingssnelheden in slib kunnen immers enkel puntmetingen uitgevoerd worden. Dergelijke metingen dienen te gebeuren met behulp van sondes. Om ongewenste verstoring van de stromingen door sondes te beperken blijft het aantal sondes liefst beperkt. Dit is in tegenstrijd met de noodzaak om metingen over een groter gebied uit te voeren met een minimale ruimtelijke resolutie. Hier zijn immers meestal meerdere sondes voor nodig. Dit probleem kan op twee manieren worden aangepakt. Een eerste optie is om experimenten te herhalen waarbij de sondes bij elke experiment verplaatst worden. Dit is echter enkel mogelijk indien het gedrag van de vloeistof uniform is tijdens deze experimenten. Zoals eerder aangehaald kan dit niet gegarandeerd worden bij gebruik van slib. De andere optie is om een niet-intrusieve techniek toe te passen waarmee simultaan metingen op meerdere meetpunten uitgevoerd worden. Bij het meten van stromingssnelheden zijn dergelijke technieken gekend als ‘’whole-flow-field velocimetry techniques”. Een wijd toegepaste techniek is ‘’Particle Image Velocimetry” (PIV). Voor de toepassing van PIV is digitale visualisatie van de beweging van de vloeistof nodig. Op basis van kruiscorrelatie tussen opeenvolgende

beelden kunnen PIV algoritmes de richting en grootteorde van de gecapteerde stromingen kwantificeren met een zekere ruimtelijke resolutie. Er is echter nog geen techniek gekend waarmee visualisatie van stromingen in slib mogelijk is. Om de algemene kwaliteit van fysische experimenten gebruikmakend van natuurlijk slib te verbeteren, wordt met dit onderzoek beoogt om pragmatische methodes te bepalen waarmee enerzijds meer controle verkregen wordt over het gedrag van slib, en anderzijds waarmee de stromingsdynamica in slib gevisualiseerd kan worden met een voldoende kwaliteit voor verwerking met PIV algoritmes.

Er werd gestart met een uitgebreid (literatuur)onderzoek over diverse technische vakgebieden heen. Hierbij werd gezocht naar reeds bestaande technieken die potentieel tonen om de bovengenoemde tekortkomingen van fysische experimenten met slib te verhelpen. Op basis van theoretische inschattingen en eerder gepubliceerde ervaringen werden technieken beoordeeld en geselecteerd. Voor de visualisatietechnieken werd dit uitgebreid met een eerste snelle toepassingen ervan in slib. Op basis hiervan werd een definitieve selectie gemaakt. Enkel deze geselecteerde technieken werden gebruikt in de volgende fase van fysieke experimenten. Verschillende reeksen van experimenten werden bedacht en uitgevoerd om de toepassing van de technieken op slib verder te evalueren en te verfijnen. Deze experimenten werden uitgevoerd op het Waterbouwkundig Laboratorium en in externe laboratoria van de Universiteit Gent en het Universitair Ziekenhuis Leuven.

Het bezinkingsproces van slib wordt sterk beïnvloed door de spreiding en de grootte van de partikels en vlokken aanwezig in het slib. In dit onderzoek wordt aangetoond dat door slib te conditioneren met een combinatie van axiaal en radiaal mixen over beide eigensschappen meer controle kan worden verworven en bijgevolg dus ook over

het verloop van het bezinkingsproces. Op voorwaarde dat de samenstelling van het slib, de dichtheid en de intensiteit van het mixen hetzelfde zijn, kan hiermee afwijkend verloop van dergelijke experimenten dus geminimaliseerd worden. Bij de bezinkingsexperimenten die tijdens dit onderzoek werden uitgevoerd, werd het conditioneren uitgevoerd volgens een strikte procedure. Hierbij werd gebruik gemaakt van verschillende gangbare mengapparatuur met zowel axiale als radiale mengcapaciteit. Op deze manier werden maximale afwijkingen in bezinkingskrommen van 1 % tot 2 % verkregen. De minimaal vereiste intensiteit en duurtijd van het mixen hangt af van verschillende variabelen, zoals het volume en de samenstelling van het slib alsook de gebruikte mixapparatuur. Door middel van kortstondige bezinkingsexperimenten, zoals die tijdens dit onderzoek zijn uitgevoerd, kan dit worden bepaald ter voorbereiding van het eigenlijke experimenteel onderzoek. Alle bezinkingsexperimenten uitgevoerd tijdens dit onderzoek startten met eenzelfde dichtheid van het slib. Bovendien was deze lager dan de zogenaamde ”gel dichtheid” van het slib. Dit is een drempelwaarde van de dichtheid vanaf waar het verloop van het bezinkingsproces veranderd. Niettemin, aangezien het verloop van het bezinkingsproces onafhankelijk is van het gewichtspercentage van de verschillende componenten in het slib, wordt niet verwacht dat de dichtheid van invloed is op de manier waarop het slib best geconditioneerd wordt.

Echografie of ultrasone beeldvorming blijkt dan weer de meest effectieve visualisatietechniek voor toepassing van PIV op slib. De belangrijkste voordelen hiervan zijn dat er geen volledige doordringing van de sliblaag nodig is en dat er geen traceerbare partikels moeten worden toegevoegd. Echografische beelden van slib vertonen enkel een korrelig patroon van verschillende grijswaardentinten, gekend als ‘’spikkel” (speckle in het Engels). Dergelijke spikkelbeelden

geven een illusoire weergave van de positie van de slibdeeltjes die de ultrasone geluidsgolven verstrooien. De relatieve verplaatsing van een spikkelpatroon tussen opeenvolgende beelden is dan ook representatief voor de beweging van de slibdeeltjes en bijgevolg voor de stroming in het slib. Spikkel beelden zijn dan ook perfect bruikbaar voor verdere verwerking met standaard PIV algoritmen. Dit wordt verder Ultrasound Image Velocimetry (UIV) genoemd.

Voor toepassing van UIV op slib moeten verschillende afwegingen worden gemaakt. De hoogst registreerbare stromingssnelheid is evenredig met de beeldacquisitiesnelheid en de breedte van de beelden. Om het eerste te maximaliseren wordt de transducer gestuurd in zogenaamde ‘’plane wave mode”, waarbij alle piëzo-elektrische elementen van de transducer gelijktijdig worden geëxciteerd. Als gevolg hiervan is de breedte van de beelden beperkt tot de breedte van de transducer, wat dan weer de hoogst registreerbare stromingssnelheid opnieuw beperkt. Met een ultrasone transducer met een breedte van 13.9 mm, bestuurd met een scanner met een opnamesnelheid van ongeveer 350 Hz, was de maximale geregistreerde stroomsnelheid tijdens dit onderzoek ongeveer 1100 mm·s^{-1}. Dit kan gemakkelijk verhoogd worden tot ongeveer 2800 mm·s^{-1} door een meer gebruikelijke lineaire transducer met een breedte van 40 mm te gebruiken.

De nauwkeurigheid van de snelheidsvectoren neemt af met toenemende diepte. Tijdens de experimenten van dit onderzoek was het dieptebereik waarop snelheidsvectoren met acceptabele nauwkeurigheid werden verkregen beperkt tot slechts 70 mm. Het dieptebereik van UIV kan worden geoptimaliseerd door de demping van het ultrageluid te minimaliseren en de intensiteit ervan te maximaliseren. Een vermindering van de demping van het ultrageluid wordt bekomen door een verlaging van de ultrasoon frequentie.

Echter, de intensiteit van verstrooid ultrageluid is evenredig met de ultrasoon frequentie tot de vierde macht. Hierdoor is een lagere frequentie nadelig voor het dieptebereik van de spikkelbeelden en dus van UIV. De intensiteit van het terugkerend verstrooide ultrageluid moet immers voldoende zijn om de transducer terug te kunnen bereiken vóórdat ze volledig uitdoven. Aangezien de intensiteit van verstrooid ultrageluid eveneens evenredig is met de grootte van de partikels die het ultrageluid verstrooien, is de meest optimale ultrasoon frequentie afhankelijk van de dichtheid en samenstelling (oorsprong) van het slib. De laagste ultrasoon frequentie toegepast tijdens dit onderzoek is 1.75 MHz. Hiermee werd dan ook het grootste dieptebereik bereikt. Op basis van de korrelgrootteverdeling van het slib uit Zeebrugge wordt ingeschat dat het dieptebreik gemaximaliseerd kan worden met een ultrasoon frequentie van 0.6 MHz.

Ultrasone beeldvormingsapparatuur ontwikkeld voor medische doeleinden zijn het meest courant verkrijgbaar. In dit onderzoek werd dan ook standaard medische ultrasone beeldvormingsapparatuur gebruikt voor de toepassing van UIV. De eerder vernoemde beperkingen worden voornamelijk veroorzaakt door de begrenzing van de ultrasoon frequentie en de intensiteit van het uitgezonden ultrageluid. In het geval van medische apparatuur zijn beide beperkt voor respectievelijk diagnostische kwaliteitsdoeleinden en ter bescherming van de patiënt. Minder begrensde ultrasone beeldvormingsapparatuur, zoals hoge-resolutie sonars voor offshore onderzoek worden daarom voorgesteld ter verhoging van het dieptebereik van UIV in slib.

Met het conditioneren van slib door een combinatie van axiaal en radiaal mixen, en de mogelijkheid van ultrasoon geluid om stromingen in slib te visualiseren, werden pragmatische en haalbare manieren gevonden waarmee de kwaliteit

van experimenteel onderzoek met natuurlijk slib aanzienlijk kan worden verbeterd. Voor beide geldt dat de ideale procedure individueel voor elk onderzoek moet worden bepaald. Beide zijn immers afhankelijk van verschillende eigenschappen zoals, maar niet beperkt tot, de samenstelling en het volume van het slib alsook de gebruikte apparatuur. Het dieptebereik van UIV blijft een aandachtspunt. Voor toepassing in bezinkingsexperimenten of reologiemetingen is het dieptebereik dat tijdens dit onderzoek is bereikt voldoende. Dit kan niet meer gezegd worden in geval van grotere experimentele opstellingen met dikkere sliblagen. Op basis van de resultaten van dit onderzoek kunnen wel onderbouwde inschattingen van het dieptebereik met behulp van bepaalde apparatuur worden gemaakt. Dienovereenkomstig wordt een dieptebereik tot 900 mm haalbaar geacht met specifieke apparatuur. Door gebrek aan middelen en tijd is dit echter niet getest.

English summary

Mud is usually known as a mixture of sand and water. In marine environments, mud is referred to as the dark viscous fluid formed at the bottoms. It is a mixture of water, clay particles, organic matter and silt particles and is encountered all over the world. In a low-energy environment, suspended mud will settle and, if sustained long enough (weeks or even months), eventually consolidate. On the other hand, when disturbed, mud particles will resuspend in the overlying water mass. Unconsolidated fluid mud may even get entrained by currents in the overlying water layer. Especially in estuarine environments, mud layers can be moved over considerable distances in this way. Consequently, many ports, rivers and navigation channels suffer from siltation, forcing the authorities to regularly undertake maintenance works to safeguard and ensure passage of marine traffic.

A good understanding of the behaviour of such mud layers is therefore required to fully understand the influence of its presence, optimise dredging works or predict the impact of new infrastructure developments. The mechanical behaviour of mud is particularly of interest here and is studied by various engineering disciplines, such as marine sedimentology, hydraulic and marine engineering. Such research is done numerically and experimentally, both in situ and in a laboratory environment.

The application of mud in physical experiments does poses some challenges. Firstly, the settling behaviour and mechanical properties of mud vary, making it difficult to reproduce experimental results. This is an issue for the credibility of the experiments and makes it difficult to compare different experiments. Hydraulic experiments to study flow dynamics in mud present an additional challenge. Currently, only point measurement techniques to measure pressure changes or flow velocities are feasible in mud. Such measurements are intrusive using probes. To minimise the impact of the probes on the flow dynamics, the number of probes should be limited. This is contradictory if flow dynamics are studied over a large area. A large number of probes is then required to maintain a minimum spatial resolution. This issue can be dealt with in two ways. A first option is to conduct repetition experiments whilst rearranging the probes for each experiment. This is however only an option if the behaviour of the fluid is uniform during these experiments, which unfortunately cannot be guaranteed with mud, as mentioned earlier. The other option is to use whole-flow-field velocimetry techniques, like Particle Image Velocimetry (PIV). PIV requires input of images by which the motion in the fluid is captured. The PIV algorithm applies cross-correlation to these images, based on which the velocity and direction of flows in the fluid can be inferred. Currently, there is however no known technique capable of visualising motion in mud. To enhance the quality of physical experiments involving mud, this research aims to resolve these deficiencies by determining means to gain more control over the behaviour of mud and visualise the flow dynamics in it at an adequate quality for the application of cross-correlation like in PIV.

First, an extensive (literature) survey was conducted covering various fields of engineering. This involved searching for already existing techniques that show potential for resolving

the aforementioned deficiencies of physical experiments with mud. The shortlisted techniques were evaluated theoretically in combination with experiences from previously published work. The visualisation techniques were additionally tested with a rapid application on mud to (in)validate their potential. Based on this, a final selection of techniques was made for a next phase of physical experiments. Several series of experiments were devised and conducted to further refine the application of the selected techniques to mud. These experiments were conducted at Flanders Hydraulics and external laboratories of Ghent University and the University Hospital of Leuven.

The settling process of mud is greatly influenced by the dispersion and size of the particles and flocs present in the mud. It is shown that conditioning the mud in preparation of experiments by a combination of axial and radial mixing provides more control over these properties and consequently the course of the settling process. Provided that the composition of the mud, its density and the intensity of the mixing are the same, this will minimise the divergent course of experiments involving mud. For the settling experiments conducted during this research, conditioning was performed following a strict procedure. Various conventional mixing equipment with both axial and radial mixing capacity was used in this process. This way, maximum deviations of the settling curves of 1 % to 2 % were obtained. The minimum required mixing intensity and duration depends on several variables, such as the volume and composition of the mud and the type of mixing equipment used. Through short-term settling experiments, similar to those performed during this research, this can be determined in preparation for the actual intended experiments. The initial density of the mud was equal in all settling experiments of this research. Moreover, the density was below the so-called ”gel density” of the mud. This is a

density threshold from where the course of the settling process becomes different. Nevertheless, because the physics driving the settling process are independent of the weight percentage of the different components in the mud, neither are expected to affect the conditioning procedure required to maximise the reproducibility of experiments with mud.

Ultrasound imaging appears to be the most effective visualisation technique in mud to allow for the application of PIV. Its main assets are that it does not require full penetration of the mud layer and that it does not require the addition of tracing particles to the mud. Ultrasound imaging in mud produces images containing only grainy greyscale pattern, also known as ”speckle”. Such a speckle image is an illusive representation of the position of the particles in mud which scatter the ultrasound. Hence, the relative shift in the position of the speckle patterns between subsequent images is representative of the movement of mud particles and thus the flow in the mud. Standard PIV cross-correlation algorithms can be used to process these images. This is further referred to as Ultrasound Image Velocimetry (UIV).

When applying UIV on mud, several trade-offs need to be considered. The maximum recordable flow velocity is proportional to the image acquisition rate and the width of the images. To maximise the former, the transducer is operated in plane wave mode, where all piezoelectric elements of the transducer are excited simultaneously. Consequently, the width of the images is limited to the width of the transducer, which again limits the maximum recordable flow velocity. Using an ultrasound transducer with a width of 13.9 mm, operated at an acquisition rate of about 350 Hz, the maximum recorded flow rate during this research was about 1100 mm·s^{-1}. This can be easily increased to 2800 mm·s^{-1} by using a common linear transducer with a width of 40 mm.

The accuracy of velocity vectors decreases with increasing depth. For the experiments of this study, the depth range to which velocity vectors were obtained with acceptable accuracy was limited to only 70 mm. This depth range can be optimised by minimising attenuation and maximising the intensity of the emitted ultrasound. A reduction in attenuation can be achieved by lowering the frequency of the ultrasound. Since the intensity of scattered ultrasound is proportional to the ultrasound frequency by power four, a lower frequency is however detrimental for the depth range of speckle images and thus UIV. After all, the intensity of the backscattered ultrasound must be sufficient to enable them to return to the transducer before they are fully attenuated. Since the scattering intensity is also proportional to the size of the scatterers, the most optimal ultrasound frequency is dependent on the density and composition (origin) of the mud. The lowest ultrasound frequency applied during this research was 1.75 MHz. Consequently the greatest depth range was achieved with this. Based on the particle grain size distribution of Zeebrugge mud, it is estimated that the depth range can be maximised with an ultrasonic frequency of 0.6 MHz.

The most commonly available ultrasound imaging equipment are those developed for medical purposes. Likewise, standard medical ultrasound imaging equipment was used in this research for the application of UIV. The aforementioned limits are mainly prompted by the limitation of the ultrasound frequency and the intensity of the emitted ultrasound. In case of medical equipment both are limited for diagnostic quality purposes and patient safety, respectively. Therefore, to increase the depth range of UIV in mud, less constrained equipment such as high-resolution sonars for offshore survey is proposed.

With the preparation of mud by a combination of axial and radial mixing and the ability of ultrasound to visualise flows in mud, pragmatic and viable means have been identified by which the quality of experimental research using mud can be improved significantly. For both, the ideal procedure needs to be assessed on a case-by-case basis. After all, both are dependent on various properties such as, but not limited to, the composition and volume of the mud and the equipment used. The attainable depth range of UIV remains a concern. For its application in settling experiments or rheology measurements, the depth range achieved during this research is sufficient. In case of larger setups involving greater mud layers, it is not. The output of this study does allow for well-founded estimate of the depth range from a particular equipment. Accordingly, a depth range of up to 900 mm is considered feasible. Due to lack of resources and time, this was however not put to test.

List of Acronyms

A

ADAR	Airborne Data Acquisition and Registration
ALARA	As Low As Reasonably Achievable

B

B-mode	Brightness-mode

C

CDNB	Centraal Deel van de Nieuwe Buitenhaven
CFD	Computational Fluid Dynamics
CR	Contrast Ratio
CV	Coefficient of Variation

D

dB	deciBel

E

ECM	Electromagnetic Current Meter
EM	ElectroMagnetic

F

FBW	Fractional BandWidth
FT	Fourier Transformation
FH	Flanders Hydraulics
FWO	Fonds Wetenschappelijk Onderzoek

G *Blank*

H

HD-PULSE	High channel Density Programmable ULtrasound System based on consumer Electronics

I

ICP – OES	Inductive Coupled Plasma - Optical Emission Spectrometry

J *Blank*

K *Blank*

L

LDPE	Low-Density PolyEthylene

M

MRI	Magnetic Resonance Imaging

N

NaN	Not a Number
NDT	Non-Destructive Testing
NIST	National Institute of Standards and Technology
Np	Neper

O *Blank*

P

PB	Pitched Blade
PIANC	World Association for Waterborne Transport Infrastructure
PIV	Particle Image Velocimetry
PMMA	PolyMethylMethAcrylate

Q *Blank*

R

RPM	Revolutions Per Minute
SD	Standard Deviation
SNR	Signal to Noise Ratio
SPL	Sound Pressure Level
SONAR	Sound Navigation and Ranging

T

TGC	Time Gain Compensation

U

UDV	Utrasound Doppler Velocimeter
UIV	Ultrasound Image Velocimetry
US	UltraSound

V *Blank*

W *Blank*

X *Blank*

Y *Blank*

Z *Blank*

Symbol list

Note: For the readability of this thesis, SI units are not always used. All units used are listed below.

Latin symbols

a	[m]	radius of a particle or scatterer
A	[Bq]	activity of EM radiation source
A_m	[V]	amplitude of an ultrasound signal
c	[m·s^{-1}]	speed of sound of a medium
c_r	[-]	contrast ratio of (a section of) an image
C	[-]	greyscale intensity
d_{10}	[µm]	particle size corresponding to the cumulative distribution of 10 %
d_{20}	[µm]	particle size corresponding to the cumulative distribution of 20 %
d_{50}	[µm]	particle size corresponding to the cumulative distribution of 50 %
d_{80}	[µm]	particle size corresponding to the cumulative distribution of 80 %
d	[m]	distance or displacement (PIV)
D_{rate}	[Gy]	dose rate
e	[-]	Euler's number

E	[eV]	energy
f	[Hz]	ultrasound frequency
h	[m]	height of water-mud interface
I	[W·m^{-2}]	radiation intensity
i_w	[pixels]	image width
k	[m^{-1}]	wave number
l_0	[m]	integral length scale
l_λ	[m]	Taylor length scale
L_p	[dB]	Sound Pressure Level (SPL)
M	[-]	magnification factor
n	[bits]	bit depth
o_v	[pixels]	overlap of cross-correlation windows
P	[-]	propagation loss due to attenuation
r	[-]	reflection coefficient
r_{dyn}	[dB]	dynamic range
R^2	[-]	proportion of the variance
Re	[-]	Reynolds number
Re_0	[-]	turbulence Reynolds number
t	[seconds]	timestamp
t_w	[mm]	(wall) thickness
T	[-]	transmission ratio
U	[V]	voltage
v	[m·s^{-1}]	velocity
v_0	[m·s^{-1}]	integral velocity scale
w_s	[pixels]	cross-correlation window size
X	[-]	relative settlement
Z	[kg·m^{-2}·s^{-1}]	acoustic impedance

Greek and other symbols

α	[Np·m^{-1}]	ultrasound attenuation
Γ	[(R·m^2)·(hr·Ci)$^{-1}$]	gamma constant
λ	[m]	wavelength
μ	[m^{-1}]	attenuation coefficient of a medium
μ_{mass}	[cm^2·g^{-1}]	mass attenuation of a medium
ν	[m^2·s^{-1}]	kinematic viscosity of a fluid
ρ	[g·cm^{-3}] or [kg·m^{-3}]	density of a medium
ϕ	[rad]	scattering angle
ω	[%]	weight fraction
σ	[-]	standard deviation

Subscripts

0	initial value
Al	aluminium
belt	transmission belt
e	experiment
d	after a distance d
filter	electromagnetic radiation filter
i	index
in	incoming
j	index
max	maximum
mean	statistical average
min	minimum
mix	mixture of chemical compounds and elements
ms	mud-stainless steel interface
mud	mud
n	indication of a step in a sequence
p	photon
pixel	pixel
rec	received or recorded
ref	reference
rev	revolution
s	series
sc	scatterer or scattered
set	setting
ws	water-stainless steel interface

Lexicon

This thesis contains specific terminology from various engineering disciplines. Since this can sometimes cause confusion, this lexicon provides the explanation as intended in this thesis.

Displacement
The relative relocation of a pattern of speckles between sequentially acquired images.

Interrogation window
To determine the displacement of speckle patterns between successive images, the images are divided into interrogation windows. These usually are square shaped and overlap. During the cross-correlation process, windows with corresponding content (speckle pattern) are searched for in successive images. Each interrogation window eventually results in a velocity vector.

Gel density
The density of fluid mud from where the cohesive flocs in it start to become close enough for chemical and electrostatic forces to bind them. This results in the formation of a continuous structure yielding a true yield stress.

Marine impeller
An impeller with typically curved blades, resulting in a constant pitch distribution of the blades. Such design results in a uniform axial acceleration of the fluid and is therefore preferred for ship propellers, hence the name.

Pitched blade impeller
An impeller with straight blades pitched (inclined) relative to the shaft. As a result, they induce both axial and radial flows and are often used in the mixing industry.

Speckle pattern image
An image containing grainy texture resulting from the interference of numerous backscattered signals.

Table of Contents

Chapter 1

Introduction

1.1 Background and motivation

Muddy cohesive sediments are found worldwide in estuaries and coastal areas. Due to its dark colour, malodour and stickiness, its presence is usually perceived negatively. Apart from natural skin treatment sessions, adventurous activities such as mudflat hiking or mud-themed festivals, muddy shores are therefore generally less popular places to visit. Yet mud has played a crucial role in the development of civilisations throughout history. Indeed, at certain places river floods lead to large fertile mud deposits, ideal for agricultural development and the supply of building materials. Well-known examples are the flood plains along the Euphrates, Nile and Tigris rivers. In some areas, mud deposits are still used in this way.

To facilitate the ever-increasing industrialisation and globalisation of the world, continuous development of infrastructure along waterways is imperative. In regions were mud is present, this affects the concentration and movement of the mud in the surrounding area. In turn, this can have negative economic and environmental impacts, such as increased dredging activities or siltation of nearby wetlands. Assessing the viability of

Figure 1.1: *A picture of a mudflat in the Wadden Sea National Park. Because of its natural value, the park is recognized as a UNESCO World Heritage Site. This picture was copied from https://traveladdicts.net/wadden-sea-national-park, on 30/11/2023*

infrastructure development therefore requires knowledge and understanding of the behaviour and transport mechanisms of mud. This allows, for instance, (maintenance) dredging to be considered already during the design phase of such development projects. Similarly, in the case of existing infrastructure, such knowledge can enable the optimisation of maintenance dredging or even the definition of a set of conditions under which interaction between mud and passing vessels can be allowed. Regardless of its origin, mud generally contains fractions of organic matter and clay particles. These fractions account for the aforementioned appearance and behaviour of mud. The specific proportion of the different fractions present in mud from a particular location or area provides specific behavioural nuances. On a large scale, these small variances do make a significant difference.

Figure 1.2: *A picture of the Boryeong Mud Festival in South Korea (2019). This picture was copied from https://radseason.com/boryeong-mud-festival-koreas-international-summer-festival, on 29/03/2024*

One of the many research projects that have contributed to this is the FWO (Fonds Wetenschappelijk Onderzoek) funded project ”Development of a CFD tool and associated experimental validation techniques for fluid mud bottoms disturbed by moving objects” (grant nr. G0D5319N). During this project, various physical experiments involving fluid mud were undertaken, such as settling experiments, towing tank experiments (Sotelo et al., 2022, 2023) and rheology experiments (Doddugollu, 2021; Doddugollu and Toorman, 2023). Because of the typical characteristics of mud, its use in physical experiments is not as straightforward compared to using invariable fluids and sediments such as water and sand. As a result, compromises have to be made, meaning that not all the needs of the research can be met. This is what prompted the research described in this thesis. Although it

Figure 1.3: *1998 Airborne Data Acquisition and Registration (ADAR) image showing differential wave breaking due to shallow water mud deposits. The dark mud deposits are visible on the right half of the coastline captured in the image (Holland et al., 2009).*

would have been better to conduct this study prior to the FWO project experiments, both research projects proceeded more or less simultaneously.

1.1.1 Description of mud

In geotechnical and marine engineering, cohesive coastal and estuarine sediments are commonly referred to as mud. It is a saturated mixture of water, various clay minerals, organic matter and small amounts of sand and silt (Berlamont et al., 1993). This is not to be confused with the customary mixture of water and sand, also called mud. They differ not only in composition but also in behaviour. The flow behaviour of a water-sand mixture changes from Newtonian to granular with increasing sand concentration. Whereas from a concentration threshold onwards, cohesive mud develops a yield strength attributable to the presence of clay minerals (Fig. 1.4). Subjected to stresses smaller than the yield strength, mud will resist to fluidisation and return to its original state upon cessation of this submission. This is known as visco-elastic behaviour. When the yield strength is exceeded,

visco-plastic behaviour is observed, meaning that full recovery to its original state is no longer possible. Mud is therefore classified as a non-Newtonian fluid.

This yield strength is the result of inter-particle bonds formed by the clay minerals. If present, an organic fraction strengthens these clay bonds either by creating bridges between the particles or by charge neutralisation (Lagaly and Dékány, 2013). A higher organic fraction strengthens the bonds between clay particles more and vice versa. These inter-particle bonds are formed when the mud is in a low energy environment. This means that the parameters determining this yield strength change with time, which is called thixotropy (Toorman, 1997; Mewis and Wagner, 2009; Larson and Wei, 2019). The cohesive mud considered in this study originates from the Zeebrugge docks of the Port of Antwerp-Bruges, Belgium. It typically consists mainly of clay minerals and organic material, resulting in fine grain sizes ranging from 0.3 µm to 120 µm and a median grain size (d_{50}) of 7 µm.

1.1.2 Experimental research with mud

Various hydraulic engineering challenges, such as but not limited to dredging, coastal dynamics, geomorphology, erosion resistance, ship navigability, etc, are associated with mud. Therefore its behaviour has been and remains the subject of many research projects (Toorman, 1997). Various physical experiments are used to facilitate these studies.

Settling experiments in transparent columns are used to study sedimentation and consolidation behaviour of mud (Been and Sills, 1981; Lin, 1983; Elder, 1988; Bowden, 1988; Berlamont et al., 1993; Winterwerp et al., 1993; Merckelbach, 2000; Dankers, 2006; Fossati et al., 2015; van Rijn and Barth, 2019). Conceptually, these experiments are all similar. A

Figure 1.4: *Consolidated mud sampled in the Weser estuary. Picture copied from https://de.wikipedia.org/wiki/Fluid_Mud, on 28/09/2023*

preconditioned batch of mud is introduced into a transparent vertical tube and left undisturbed for a period of time to allow sedimentation and consolidation. To fully comprehend the physics during these sedimentation and consolidation processes, the change over time of various parameters such as mud density, pore pressure and the level of the water-mud interface is monitored (see Fig. 1.5). Typically the characteristics of mud in the consolidation phase are of interest, because it is in this phase that mud is mostly encountered in nature. Therefore settling and consolidation experiments are usually conducted over longer periods of time up to months. The objective of these studies is to develop mathematical models to estimate mud sedimentation

and consolidation rates. During these processes the settling rate alters with changing density (Toorman, 1996), adding to the complexity of such theoretical models.

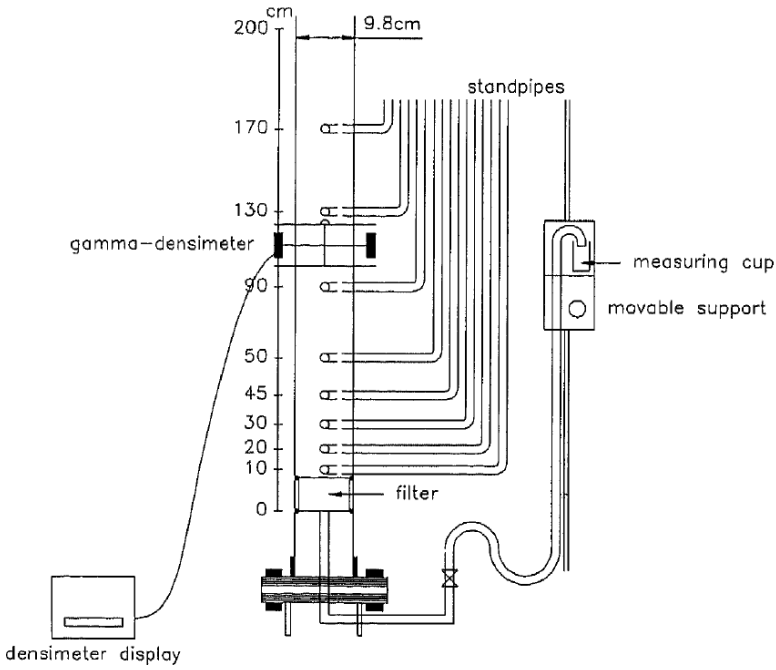

Figure 1.5: *Sketch of a settling column experimental setup. Copied from Berlamont et al. (1992). Pictures from recent settling experiments can be found further in this thesis (see Fig. 2.4 and Fig. 3.5)*

In turn, the flow behaviour of mud is determined by physical processes like sedimentation, consolidation and fluidisation. The presence of a cohesive fraction further complicates these processes, which is referred to as non-Newtonian and thixotropic behaviour. These processes are therefore strongly influenced by the rheological properties of the mud. Knowledge of these rheological properties is thus essential in the aforementioned fields of engineering. The rheological

properties of mud are studied using a vane-type rotational rheometer (Fig. 1.6) capable of performing both shear stress and shear rate controlled experiments (Toorman, 1994; Claeys et al., 2015; Doddugollu and Toorman, 2023).

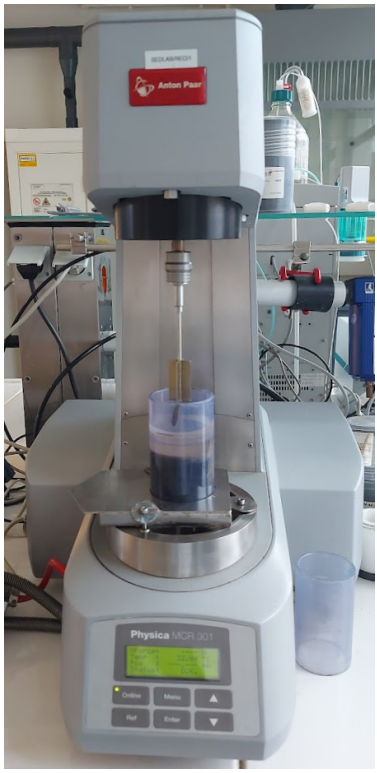

Figure 1.6: *Wide gap vane rheometer setup used at Flanders Hydraulics (FH). The rheometer is an Anton Paar Physica MCR 301. For illustrative reasons, the picture was taken with the vane spindle out of the mud. Before operation, the vane spindle is lowered into the cup containing the mud.*

A more specific study is the assessment of the ”nautical bottom” of a navigation channel of which the bottom is formed by fluid mud. In the nautical community, the term ”nautical

bottom" is used to define the maximum permissible draft of a ship in a navigation channel. In case the bottom of the channel is formed by sand or rock, the nautical bottom corresponds to the top level of it. When the bottom of this navigation channel is formed by a fluid bed of cohesive sediments (mud), there is no clear physical boundary to determine the nautical bottom of the channel (Vantorre, 1997). Nonetheless, in the case of a shallow navigation channel, such a bottom affects the manoeuvrability and controllability of passing ships, even if the bottom of the ship remains above it (Sellmeijer and Oortmerssen, 1984; Delefortrie et al., 2007; Delefortrie and Vantorre, 2009). This interaction between ship, mud and water is studied by nautical researchers with towing tank experiments (Delefortrie et al., 2007; Delefortrie and Vantorre, 2009). A conclusion was that due to the complexity further study should preferably be carried out through Computational Fluid Dynamics (CFD) models (Vanlede et al., 2014; Delefortrie and Vantorre, 2016). Because of the complex behaviour of mud, its modelling is the bottleneck in the development of such CFD models. Some existing models approximate the behaviour of mud by neglecting the non-Newtonian property (e.g. Kaidi et al. (2020)). Others simplify by solely including a viscosity model such as the Herschel-Bulkley model or the power law model (e.g. Gao et al. (2015); Lovato et al. (2022)). As proposed in Vanlede et al. (2014), using the rheological properties of mud yields the most accurate results. A dataset with such data is however not readily available. Furthermore the rheological properties of mud have various dependencies, such as composition and density. Therefore, Sotelo et al. (2022, 2023) conducted experiments to generate a dataset to validate such a comprehensive CFD model, including the rheological properties of Zeebrugge mud. The experiments involve towing a solid body through a flume filled with either mud alone or a layer of water on top of a mud layer, while pressure changes in the mud layer and the pressures and

forces exerted on the body are measured (see Fig. 1.7). Before and after each experiment, mud samples are taken to determine its rheological properties. This allows the measured pressures and forces to be correlated with the rheological properties of the mud. Finally, the measured pressures and forces are used to validate the pressures and forces derived from the flow dynamics theoretically determined with CFD at corresponding locations.

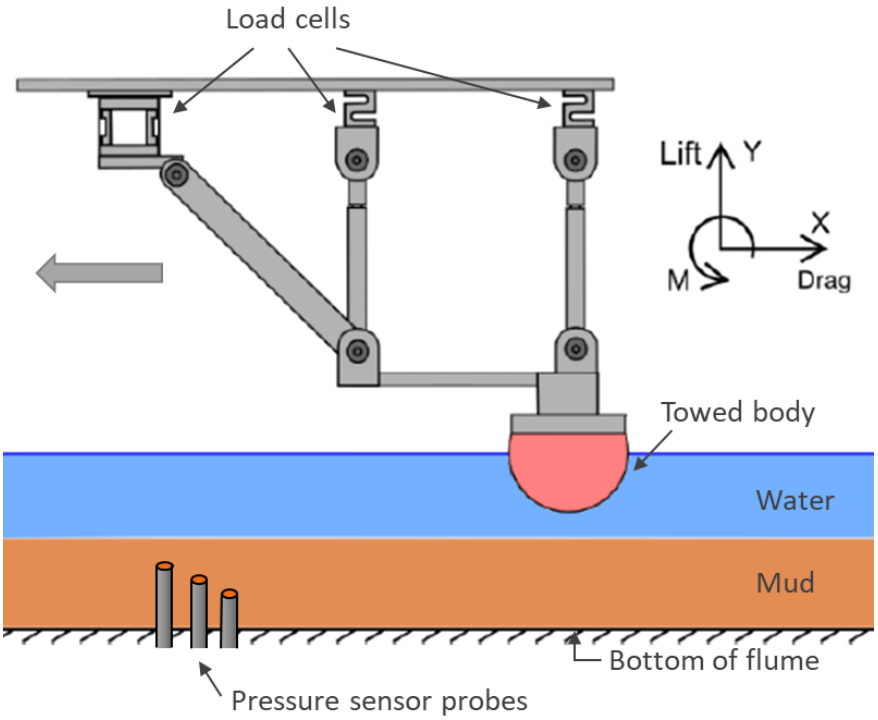

Figure 1.7: *Sketch of the setup of the towing experiments performed at FH by Sotelo et al. (2022). The width of the flume facilitating this setup is 560 mm and the combined thickness of the water and mud layers can reach 500 mm. Towing velocities up to 1.5 m· s^{-1} are feasible. Sketch copied from Sotelo et al. (2022) and modified.*

1.1.3 Deficiencies of present experimental research with mud

1.1.3.1 Divergent behaviour of fluid mud

Because of the complex behaviour of dense natural cohesive mud, the repeatability of physical experiments involving such mud is a challenge. Even in controlled laboratory conditions. Furthermore, the repeatability of settling experiments is not always discussed objectively. In some reports it is described qualitatively (Elder, 1988; Bowden, 1988; Winterwerp et al., 1993; Merckelbach, 2000; van Rijn and Barth, 2019). Other reports discuss the possible factors that may affect reproducibility (Been and Sills, 1981; Berlamont et al., 1993; Winterwerp et al., 1993). Been and Sills (1981) intentionally conducted repetition tests, but the results were not published. Some published settling curves in different reports do however allow for an objective evaluation of repeatability by estimating the maximum deviation between two similar tests. Doing so for various published results, the series of experiments of Been (1980) and Merckelbach (2000) showed settling curves with a maximum deviation below 3 % of the initial height. Lin (1983), Bowden (1988) and other series of Merckelbach (2000) show results between 3 % and 5 %. Deviations exceeding 5 % were found in Elder (1988), Dankers (2006) and Fossati et al. (2015). Furthermore, a recurring observation in these reports is that deviations fully develop in the early stages of sedimentation and are maintained in the subsequent course.

For experiments similar to the towing experiments of Lovato et al. (2022) and Sotelo et al. (2022, 2023) where small pressure differences and minor forces need to be monitored, such deviations in settling rates are unacceptable. After all, these experiments are carried out during the sedimentation phase in which these deviations in settling rate develop. Therefore they will result in additional variations of the measured forces and pressures. The primary effect is on

buoyancy. For example, Sotelo et al. (2022) conducted his experiments in an initially 500 mm thick mud layer. In this case, a 3 % deviation in settling means a variation of the mud-water interface level up to 15 mm. When towing a semi-submerged cylinder with a radius of 100 mm at a velocity of 0.5 m· s^{-1} like Sotelo et al. (2022), the difference in buoyancy due to such a variation in mud layer thickness already leads to an additional uncertainty of 3.5 % on the measured drag force and 8.1 % on the measured lift force. Secondly there is also the effect on the dynamics of the mud. After all, the settling rate of the cohesive fraction in the mud is one of the determining parameters for the mechanical behaviour of the mud (Berlamont et al., 1993; Teisson et al., 1993). The ultimate effect of this on the results of physical experiments is however less straightforward.

1.1.3.2 Monitoring of flow dynamics in fluid mud

Secondly, as elaborated in Section 1.1.2, the ability to measure flow velocities in dense ($>$ 1.10 g·cm^{-3}) natural cohesive mud would be beneficial for various physical experiments involving such mud. This would make it possible to validate the theoretical sedimentation and consolidation models and the numerically obtained velocity profiles in order to improve the processing of the results of rheometer experiments. Ultrasound Doppler Velocimeters (UDVs) are well known for monitoring erosion flows in the suspended top layers of a mud bed, which can measure flow velocities of up to 2 m·s^{-1}. This technique is however strongly limited in terms of mud density ($<$ 1.05 g·cm^{-3}), spatial and temporal resolution (Velasco and Huhta, 2009; Baas et al., 2016; Thorne et al., 2018).

Electromagnetic Current Meters (ECM) have been used to measure flow velocities in artificial mud in experimental research on wave-mud interaction (de Wit, 1995; Hsu et al., 2013; Soltanpour et al., 2018). These devices can measure flow velocities up to 2 m· s^{-1} as well, yet also in more dense

muds up to 1.25 g·cm^{-3} or even more. The technique is however intrusive and therefore less suitable for use in settling experiments and rheometer experiments. Furthermore the outcome is a point measurement. For experiments where the flow mechanics in the full mud layer need to be monitored, like those of Lovato et al. (2022) and Sotelo et al. (2022, 2023), this poses an issue. Using point measurement devices, the spatial resolution of the measurements is too limited. Whereas, due to the high labour intensity of experiments involving mud and the additional uncertainty caused by divergent mud behaviour, repetition experiments whilst relocating the measurement probes, are unwanted.

Preferably, this deficiency is remediated by applying a whole-flow-field velocimetry technique, like Particle Image Velocimetry (PIV) (Fig. 1.8), which is currently widely used in experimental fluid dynamics (Raffel et al., 2018). The working principle of PIV is illustrated in Fig. 1.9. PIV can be applied to fluids containing particles of which the displacement can be recorded over time. These particles can be inherently part of the fluid or added to it. In PIV, the motion of the particles is assumed to be governed by the flows in the fluid. Therefore, their motion can be used to derive the flow dynamics in the fluid.

The movements of the particles are captured in subsequent visual recordings. These images are subdivided into smaller areas which are further referred to as interrogation windows. For each interrogation window, the shift with which it best matches the corresponding window in the subsequent image is determined. This is done using a cross-correlation algorithm. This basically calculates the sum of the squared differences of the pixel values between the shifted interrogation window of the first image and that of the corresponding window in the second image. By doing this for various possible shifts, the shift that results in the lowest value of the sum of squared differences is considered

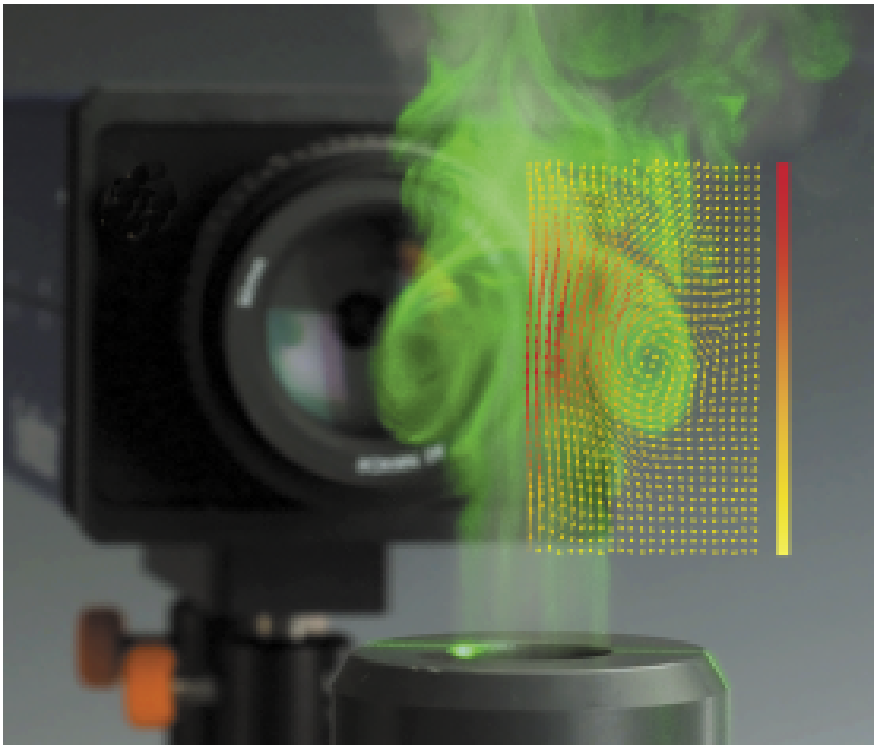

Figure 1.8: *Picture illustrating the capability of PIV to determine velocity vectors of a visualised airflow. Picture copied from https://analyticaltechnologies.com.sg/products/imaging-cameras-systems/particle-image-velocity/, on 28/12/2023.*

the most likely displacement of the particles depicted in the interrogation window. This procedure is illustrated in Fig. 1.10, where the peak in the diagram illustrates the best matching shift compared to the others.

With the intermediate time between the successive recordings known, the velocity of the moving particles and hence the flow can be deduced from this displacement. Since this method always results in a displacement value, this value

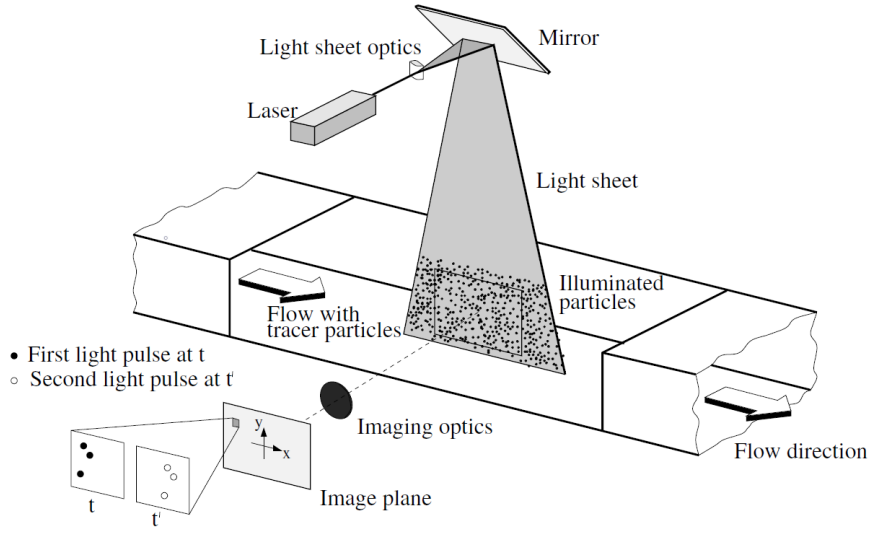

Figure 1.9: *Sketch of an experimental arrangement for PIV in a wind tunnel. In this case the transparency of the flowing medium (air) allows visualisation of the tracer particles by optical light. Figure copied from Raffel et al. (2018).*

is further evaluated with predefined filters. In this way, only the probably correct velocity vectors are preserved for further use. The output is a velocity vector for each interrogation window, resulting in a vector field of size corresponding to the size of the images. In most cases, a transparent fluid is studied, such as air and water. This enables visualisation of the particles through optical illumination to facilitate their recording as depicted in Fig. 1.8 and Fig. 1.9. Optical light, however, is greatly attenuated by mud, resulting in hardly any penetration ($<$ mm). This was experimentally observed by Dankers (2006), who wanted to track the settlement of particles in mud during sedimentation tests in transparent columns, but was unsuccessful because illumination could not penetrate the mud.

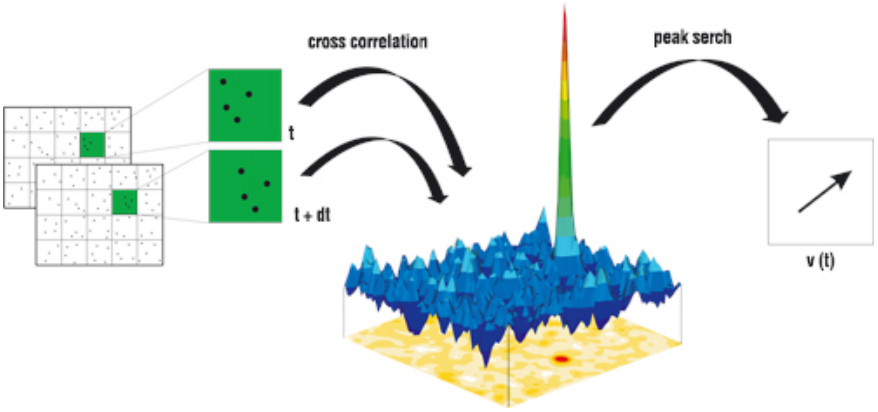

Figure 1.10: *Illustration of the cross-correlation principle. Picture copied from https://www.piv.de/piv/measurement_principle/page_1.php, on 10/09/2024.*

To bypass this issue, translucent fluids that allow the propagation of optical light and behave similarly as dense natural cohesive mud were explored. Pouv et al. (2012), showed that the rheological properties of mixtures of synthetic clay, laponite RD (Rockwood), and polymer, carboxymethylcellulose (Prolabo) are similar to those of cohesive natural mud. Physical experiments to simulate and study the erosion of cohesive sediments mimicked with this artificial mud were conducted by Pouv et al. (2014) and Zaynab et al. (2015). However, as mentioned by Pouv et al. (2014), the mixtures are made mainly of polymer molecules and therefore cannot fully represent real cohesive sediments in terms of the internal structures. Consequently, it can always be questioned whether the results are fully applicable for naturally cohesive muds. In fact, the execution of similar research using real non-transparent cohesive sediment to validate the use of the laponite mixtures was recommended.

In conclusion, the quality of results from current experimental research using dense natural cohesive sediments is question-

able. Firstly, because the behaviour of mud is difficult to reproduce, which adds to the uncertainty of the measurements. Secondly, because of the lack of non-intrusive techniques that can monitor flow mechanics in such sediments. The latter is currently tackled in various ways. Either by using point measurements and repeating the experiments, or by using artificial mud or by theoretical derivations based on other measurable parameters. However, because of the two aforementioned deficiencies, qualitative and accurate monitoring of flow mechanics can not be guaranteed when using these methods.

1.2 Outline of this research

Overall, the objective of this research is to make experimental research with dense natural cohesive sediments (fluid mud) a valuable asset to the various studies concerning such fluid mud. This is pursued by focusing on the two earlier identified shortcomings. Firstly, by enhancing the reproducibility of physical experiments with mud and, secondly, by finding a technique able to monitor the dynamics of flowing mud over an entire cross-section.

For each of these topics, the process followed during this study is briefly outlined in this section. A summary of the scope of each chapter is provided in Section 1.5.

1.2.1 Reproducibility of mud behaviour

As mentioned earlier in Section 1.1.3.1, divergent mud behaviour is caused by an irregular course of sedimentation, which develops in the early stages of sedimentation. It is also during this time frame that the towing experiments like those of Sotelo et al. (2022, 2023) are carried out after the mud is introduced into the flume. Consequently, ways to improve the reproducibility should be sought in the preparatory works of

these experiments, being the conditioning of the mud. The aim of this study is therefore to establish a clear mud conditioning procedure by which irregularities in the behaviour of similar muds can be minimised. This procedure should cover at least the technique to be used and the duration.

A literature review of previously published settling experiments showed that the sole uniformity in the way mud is conditioned in preparation for the experiments is that it is done by agitation. Conditioning by agitation was therefore the starting point for this part of this research. Based on the theoretical settling mechanisms at play in mud, the desired effects of the agitation to gain more control over the settling behaviour of the mud were defined. This was reflected in recommendations for different types of mixing equipment. The impact of these various conditioning techniques on the settling behaviour of mud was studied through settling experiments. The composition and density of the mud used during these experiments was uniform. The settling experiments differed only in the way the mud was conditioned, through the use of different types of mixing equipment and the duration of mixing. Repetition experiments were performed for each batch of mud. This was in turn repeated with different batches of the same mud.

Firstly, the obtained settling curve were analysed to confirm or not the targeted impact of each conditioning technique as well as the magnitude of their impact as a function of mixing time. Secondly, the uniformity of the settling curves from experiments where the mud was similarly conditioned was analysed. This was done both for experiments within one series, all extracted from one batch of mud, and for all similar experiments across the different series, extracted from different batches of mud. Thereby, the conditioning procedure that provides the most control over the settling behaviour is also expected to provide the highest degree of reproducibility in settling behaviour.

1.2.2 Monitoring flow dynamics in mud

To monitor the flow dynamics in experimental research involving flowing mud, the application of a non-intrusive, whole-flow-field velocimetry technique, like PIV, is preferred (see Section 1.1.3). The application of such a technique consists of two main steps. Firstly, the flow dynamics occurring in the fluid must be captured in sequential images. These images are then processed by a cross-correlation algorithm, identifying the displacements between two successive images. Ultimately, this results in fields of velocity vectors representing the flow velocities occurring over time in the recorded plane.

There is however no known technique capable of visualising flow dynamics in dense mud. The primary objective of this part of this research is therefore to find a technique that can. Because of similar restrictions and requirements, inspiration was mainly found in medical imaging techniques. Ultimately, ultrasonography was selected as the most promising technique, based on two major advantages. Firstly, because it does not require full transmission through the mud layer, which facilitates implementation in a laboratory set-up. Secondly, because there is no need to add tracer particles, which will affect the behaviour of the mud. The application of cross-correlation on ultrasound images to derive flow velocities is known as Ultrasound Image Velocimetry (UIV).

The quality of the acquired images must however be of sufficient quality to enable reliable cross-correlation results. Furthermore, the acquisition rate and depth range of the images must be sufficient to meet the requirements of the intended experimental research (see Section 1.1.3). To further optimise the application of UIV in mud, the acoustic properties of mud were first determined. This was followed by small scale experiments to assess the accuracy and identify the limitations and sensitivities of UIV when applied in dense natural mud.

1.3 Timeline of experimental research

The chronology of physical experiments conducted during this research is shown in Fig. 1.11.

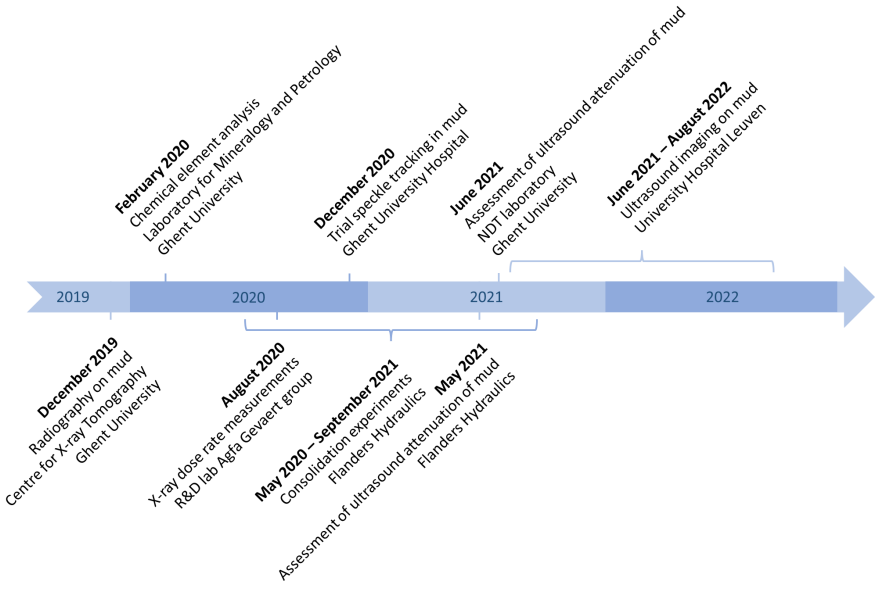

Figure 1.11: *Chronology of experiments.*

1.4 Novelty of this research

The pursuit of a whole-flow-field velocimetry technique to monitor flow dynamics in mud differentiates itself mainly from existing techniques by its application to real natural cohesive sediments of high density ($>$ 1.10 g·cm^{-3}). Indeed, the term ”mud” encompasses many similar fluids such as, but not limited to, sand-water mixtures or industrial clay suspensions. For most of these other muds, various techniques are known

and frequently used in experimental research or even in the industry. However, due to the limited size of the particles, most of these techniques do not work well in natural cohesive sediments, especially if at higher densities.

Concerning the part on the reproducibility of mud behaviour, the novelty of this research is less clear. After all, various published works on settling experiments already emphasise the importance of conditioning to preserve the quality of the experiments. This research differs in the degree of reproducibility that is strived for and how this can be achieved. Where previous research with settling experiments focussed more on the levels of the water-mud interface after long-term consolidation, deviations around 5 % were considered acceptable. This research takes this to the next level by focusing on the effects of the conditioning techniques used, especially during the early stages of sedimentation when these deviations develop.

Only Zeerugge mud was used in the experiments of this study. Nevertheless, the objective is to generalise the insights obtained so that they can be applied to other mud types of different composition. Therefore, this study makes it possible to support various studies on cohesive sediments with physical experiments but without simplifications, work arounds or compromises as has been done to date.

No artificial intelligence was used during the conduct of this research nor during the writing of this thesis.

1.5 Chapter by chapter

Chapter 1 is the introduction to this thesis.

The research on how to improve the reproducibility of mud behaviour is discussed in full in **Chapter 2**. Herein, a literature study is first discussed that identifies which part of the current procedures of experimental research should be changed to enhance the reproducibility of mud behaviour and how this should be done. This is followed by an elaboration of the experiments performed to confirm the conclusions of the literature study.

The continuation of this thesis further focuses exclusively on the search for a technique to monitor flow dynamics in mud. In **Chapter 3**, radiography and ultrasonography are evaluated as potential visualisation techniques to generate adequate images for the application of PIV.

Because ultrasonography emerges as the most promising visualisation technique, unknown ultrasound properties of mud need to be determined. Various experiments to assess the ultrasound attenuation capacity of mud and their results are therefore presented in **Chapter 4**.

Finally, **Chapter 5** covers conducted experiments applying Utrasound Image Velocimetry (UIV) to mud in order to determine the accuracy, depth range and limitations of the technique in mud.

The conclusions and recommendations on both the means to improve the reproducibility of mud behaviour as on the application of UIV to monitor mud dynamics are further consolidated in **Chapter 6**.

1.6 Publications

The content of this thesis is based on manuscripts written and published throughout this research. A list of these publications is provided hereunder:

- B. Brouwers, J. van Beeck, E. Lataire, (2022) Acoustic attenuation of cohesive sediments (mud) at high ultrasound frequencies. Paper presented at the International Conference on Underwater Acoustics (ICUA) 2022: Sediment Imaging and Mapping, Southampton, UK, 20-23 June 2022. doi: 10.1121/2.0001594
- B. Brouwers, J. van Beeck, D. Meire, and E. Lataire. Evaluation of known visualization techniques for the application on cohesive sediment layers in experimental fluid dynamics. Frontiers in Earth Science, 10, 2022. doi: 10.3389/feart.2022.878102.
- B. Brouwers, D. Meire, E. A. Toorman and E. Lataire (2023) Conditioning procedures to enhance the reproducibility of mud settling and consolidation experiments. Estuarine, Coastal and Shelf Science. doi: 10.1016/j.ecss.2023.108407
- B. Brouwers, J. van Beeck and E. Lataire. Application of Ultrasound Image Velocimetry (UIV) to cohesive sediment (fluid mud) flows. Discover Applied Science 6, 124 (2024). doi: 10.1007/s42452-024-05747-y
- B. Brouwers, J. van Beeck and E. Lataire. Optimisation of the depth range of UIV on cohesive sediment (fluid mud) flows. Discover Applied Science 6, 327 (2024). doi: 10.1007/s42452-024-06016-8

Bibliography

Baas J. H., Best J. L. and Peakall J. Comparing the transitional behaviour of kaolinite and bentonite suspension flows. *Earth Surface Processes and landforms*, 41:1911–1921, 2016.

Been K. *Stress strain behaviour of a cohesive soil deposited under water*. PhD thesis, Balliol College, University of Oxford, Parks Road, Oxford, UK, 1980.

Been K. and Sills G. C. Self-weight consolidation of soft soils: An experimental and theoretical study. *Géotechnique*, 31(4):519–535, 1981.

Berlamont J., Van den Bosch L. and Toorman E. Effective stresses and permeability in consolidating mud. *Coastal Engineering Proceedings*, 1(23):2962–2975, 1992. doi: 10.9753/icce.v23.%p.

Berlamont J., Ockenden M., Toorman E. and Winterwerp J. The characterisation of cohesive sediment properties. *Coastal Engineering*, 21(1–3):105–128, 1993.

Bowden R. K. *Compression behaviour and Shear strength characteristics of a natural silty clay sedimented in the laboratory*. PhD thesis, University of Oxford, Parks Road, Oxford, UK, 1988.

Claeys S., Staelens P., Vanlede J., Heredia M., Van Hoestenberghe T., Van Oyen T. and Toorman E. A. A rheological lab measurement protocol for cohesive sediment. In *INTERCOH2015: 13th International Conference on Cohesive Sediment Transport Processes*, pages 21–22, Leuven, Belgium, 7–11 September 2015.

Dankers P. *On the hindered settling of suspensions of mud and mud-sand mixtures*. PhD thesis, Delft University of Technology, Delft, The Netherlands, 2006.

de Wit P. *Liquefaction of cohesive sediments caused by waves*. PhD thesis, Delft University of Technology, Delft, The Netherlands, 1995.

Delefortrie G. and Vantorre M. Prediction of the forces acting on container carriers in muddy navigation areas using a fluidization parameter. *Journal of Marine Science and Technology*, 14:51–68, 2009. doi: 10.1007/s00773-009-0041-x.

Delefortrie G. and Vantorre M. Ship manoeuvring behaviour in muddy navigation areas : state of the art. In *Bundesanstalt für Wasserbau*, pages 26–36, 2016. doi: 10.18451/978-3-939230-38-0_4.

Delefortrie G., Vantorre M., Verzhbitskaya E. and Seynaeve K. Evaluation of safety of navigation in muddy areas through real-time maneuvering simulation. *Journal of Waterway Port Coastal and Ocean Engineering - ASCE*, 133(2):125–135, 2007. doi: 10.1061/(ASCE)0733-950X(2007)133:2(125).

Doddugollu S. P. A numerical study of the flow of fluid mud in a cylinder and vane rheometer. In *INTERCOH2021: 16th International Conference on Cohesive Sediment Transport Processes*, page pp. 17, Delft, The Netherlands, 13-17 September 2021.

Doddugollu S. P. and Toorman E. The determination of the true equilibrium flow curve for fluid mud in a wide-gap Couette rheometer. *Journal of Non-Newtonian Fluid Mechanics*, 321, 2023. doi: 10.1016/j.jnnfm.2023.105122.

Elder D. M. *Stress strain and strength behavior of very soft soil sediment*. PhD thesis, Wolfson college, University of Oxford, Parks Road, Oxford, UK, 1988.

Fossati M., Mosquera R., Pedocchi F. and Piedra-Cueva I. Self-weight consolidation tests of the río de la plata sediments. In *INTERCOH2015: 13th International Conference on Cohesive Sediment Transport Processes*, pages 165–166, Leuven, Belgium, 7–11 September 2015.

Gao Z., Yang H. and Xie M. Computation of flow around wigley hull in shallow water with muddy seabed. *Journal of Coastal Research*, 73:490–495, 2015. doi: 10.2112/SI73-086.1.

Holland K. T., Vinzon S. B. and Calliari L. J. A field study of coastal dynamics on a muddy coast offshore of cassino beach, brazil. *Continental Shelf Research*, 29(3):503–514, 2009. doi: 10.1016/j.csr.2008.09.023.

Hsu W. Y., Hwung H. H., Hsu T. J., Torres-Freyermuth A. and Yang R. Y. An experimental and numerical investigation on wave-mud interactions. *Journal of Geophysical Research: Oceans*, 118(3): 1126–1141, 2013. doi: 10.1002/jgrc.20103.

Kaidi S., Lefrançois E. and Smaoui H. Numerical modelling of the muddy layer effect on ship's resistance and squat. *Ocean Engineering*, 199, 2020. doi: 10.1016/j.oceaneng.2020.106939.

Lagaly G. and Dékány I. Chapter 8: Colloid clay science. In *Handbook of Clay Science*, pages 243–345. Elsevier, 2013. doi: 10.1016/B978-0-08-098258-8.00010-9.

Larson R. G. and Wei Y. A review of thixotropy and its rheological modeling. *Journal of Rheology*, 63:477–501, 05 2019. doi: 10.1122/1.5055031.

Lin T. *Sedimentation and self weight consolidation of dredge spoil*. PhD thesis, Iowa State University, Ames, Iowa, USA, 1983.

Lovato S., Kirichek A., Toxopeus S., Settels J. and Keetels G. Validation of the resistance of a plate moving through mud: Cfd modelling and towing tank experiments. *Ocean Engineering*, 258, 2022. doi: 10.1016/j.oceaneng.2022.111632.

Merckelbach L. *Consolidation and strength evolution of soft mud layers*. PhD thesis, Delft University of Technology, Delft, The Netherlands, 2000.

Mewis J. and Wagner N. J. Thixotropy. *Advances in Colloid and Interface Science*, 147-148:214–227, 2009. doi: 10.1016/j.cis.2008.09.005.

Pouv K., Besq A. and Guillou S. Rheometric study for elaborating transparent model cohesive sediments for local investigations of

erosion behaviour. *Revue paralia*, 5:1.1–1.14, 02 2012. doi: 10.5150/revue-paralia.2012.001.

Pouv K., Besq A., Guillou S. and Toorman E. A. On the cohesive sediment erosion: A first experimental study of the local processes of transparent model materials. *Advances in Water Resources*, 72:71–83, 2014. doi: 10.1016/j.advwatres.2014.05.012.

Raffel M., Willert C., Scarano F., Kähler C., Wereley S. and Kompenhans J. *Particle Image Velocimetry: A Practical Guide (third edition)*. Springer Cham, New York, USA, 2018. doi: 10.1007/978-3-319-68852-7.

Sellmeijer R. and Oortmerssen G. The effect of mud on tanker manoeuvres. *International Journal of Maritime Engineering*, 126: 105–124, 1984.

Soltanpour M., Shamsnia S. H., Shibayama T. and Nakamura R. A study on mud particle velocities and mass transport in wave-current-mud interaction. *Applied Ocean Research*, 78:267–280, 2018. doi: 10.1016/j.apor.2018.06.019.

Sotelo M., Boucetta D., Doddugollu P., Toorman E., Brouwers B., Delefortrie G. and Van Hoydonck W. Experimental study of a cylinder towed through natural mud. In *Proceedings of the 6th MASHCON International Conference on Ship Manoeuvring in Shallow and Confined Water*, pages 222–231, Glasgow, UK, 22–26 May 2022.

Sotelo M., Boucetta D., Van Hoydonck W., Doddugollu P., Vantorre M., Toorman E. and Delefortrie G. Hydrodynamic forces acting on a cylinder towed in muddy environments. *Journal of Waterway, Port, Coastal, and Ocean Engineering*, 149(6), 11 2023. doi: 10.1061/JWPED5.WWENG-1992.

Teisson C., Ockenden M., Le Hir P., Kranenburg C. and Hamm L. Cohesive sediment transport processes. *Coastal Engineering*, 21 (1):129–162, 1993. doi: 10.1016/0378-3839(93)90048-D.

Thorne P. D., Hurther D., Cooke R. D., Caceres I., Barraud P. A. and Sánchez-Arcilla A. Developments in acoustics for studying wave-driven boundary layer flow and sediment dynamics over rippled sand-beds. *Continental Shelf Research*, 166:119–137, 2018. doi: 10.1016/j.csr.2018.07.008.

Toorman E. A. An analytical solution for the velocity and shear rate distribution of non-ideal Bingham fluids in concentric cylinder viscometers. *Rheologica Acta*, 33:193–202, 1994. doi: 10.1007/BF00437304.

Toorman E. A. Sedimentation and self-weight consolidation: General unifying theory. *Géotechnique*, 46(1):103–113, 1996. doi: 10.1680/geot.1996.46.1.103.

Toorman E. A. Modelling the thixotropic behaviour of dense cohesive sediment suspensions. *Rheologica Acta*, 36:56–65, 1997. doi: 10.1007/BF00366724.

van Rijn L. and Barth R. Settling and consolidation of soft mud–sand layers. *Journal of Waterway, Port, Coastal, and Ocean Engineering*, 145(1), 2019. doi: 10.1061/(ASCE)WW.1943-5460.0000483.

Vanlede J., Toorman E., Liste-Muñoz M., Rocabado I., Heredia M., Delefortrie G. and Vantorre M. Towards cfd as a tool to study ship-mud interactions. In *Oceanology International*, page Poster, 2014.

Vantorre M. Approach channels - a guide for design. In *PTC 11-30: Final report of joint working group PIANC-IAPH II, in cooperation with IMPA and I ALA. Supplement to PIANC Bulletin no. 95*, page 108, 1997.

Velasco D. W. and Huhta C. A. *Experimental verification of Acoustic Doppler Velocimeter (ADV) performance in fine-grained,*. SonTek/YSI, Inc., San Diego, CA, USA, 2009.

Winterwerp J., Kuijper C., de Wit P., Huysentruyt H., Berlamont J., Toorman E., Ockenden M. and Kranenburg C. On

the methodology and accuracy of measuring physico-chemical properties to characteize cohesive sediments. In *Report of the MAST-1 G6-M Cohesive Sediment Project Group to the Commission of the European Communities, Directorate General XII.*, pages 1–60, 1993.

Zaynab T., Jarny S. and Texier A. Rheology and local study of a transparent model cohesive sediment. In *INTERCOH2015: 13th International Conference on Cohesive Sediment Transport Processes*, pages 107–109, Leuven, Belgium, 7–11 September 2015.

Chapter 2

Reproducing mud behaviour in a laboratory setting

The objective of this chapter is to present a clear procedure for mud conditioning in preperation of physical experiments. The focus here is exclusively on the reproducibility of physical experiments performed in a controlled laboratory environment. In natural environments, there are too many uncontrollable factors that affect the mud. These factors will therefore negate any treatment of in situ mud. Examples include weather conditions, tides and shipping traffic. Conditioning of the mud intends to ensure reproducibility of the behaviour of the mud during the experiments. The envisaged procedure aims to further enhance this reproducibility. This is essential for qualitative execution of hydraulic mud experiments. In addition, other experiments involving mud will also benefit. When used consistently, it will allow comparison of the behaviour of cohesive sediments of different origin and composition. This was already mentioned as a major shortcoming in the EC MAST-I research program report (Winterwerp et al., 1993).

2.1 Current conditioning techniques used

Some literature on mud settling experiments emphasise the importance of procedural conditioning of the mud in preparation of settling and consolidation experiments (e.g. Peirce and Williams (1966); Been (1980); Been and Sills (1981); Winterwerp et al. (1993)). Others merely describe the conditioning procedure applied (e.g. Michaels and Bolger (1962); Bowden (1988); Berlamont et al. (1992); Merckelbach (2000); van Rijn and Barth (2019)). There is however no uniformity in these procedures. In general, the objective is to homogenise the mud by agitation. The means by which this is done and for how long varies greatly, from minutes of stirring by hand with a wooden stick to hours of circulating pumping. Fully homogenised mud indeed seems a logical condition for the quality of settling experiments. Nevertheless, the repeatability in settling behaviour during these experiments is insufficient in view of hydraulic experiments (see Section 1.1.3.1). This could be explained by an inconsistent degree of homogenisation, or because homogenisation alone is insufficient and an additional function should be given to the conditioning.

2.2 Sedimentation mechanics

As indicated in Section 1.1.3.1, the deviations between settling curves of repetitive experiments develop during the first phases of sedimentation. The conditioning of the mud should therefore mainly affect these phases. To make a targeted choice in potential useful conditioning techniques, a basic understanding of the sedimentation mechanics is required.

Consider mud with an initial density below gel density, i.e. the density from which cohesive flocs begin to come close enough to each other for chemical and electrostatic forces to form a continuous structure yielding a true yield stress (Been, 1980;

Berlamont et al., 1993; Huysentruyt, 1995), left at rest in a reservoir. This gel density varies with the composition of the mud. For example, the gel density of Zeebrugge mud is about 1.10 g· cm^{-3}. In such a low energy environment, coarse and heavy particles (e.g. sand) will settle instantly, while aggregation with the formation of large flocs dominates the initial phase of flocculation for the cohesive particles. When these formed flocs are large enough that gravitation starts to prevail, these flocs too will settle down (Toorman, 1992b; Yu et al., 2022). The unhindered settling rate of the single particles and flocs are different due to difference in mass and shape, leading to segregation between the two. Moreover, the upward flow of displaced water caused by the settling particles will decrease the settling velocity of neighbouring particles and flocs. Due to their shape, flocs are more sensitive to this, facilitating further segregation. This decrease in settling velocity is a first reason for the occurrence of hindered settling (Toorman, 1996). Along with increasing density due to sedimentation, the probability of particle interactions, i.e. collisions, increases. These interactions add to the decrease of the settling flux, starting the hindered settling phase (Toorman, 1996). According to Toorman and Berlamont (1993), except for very watery mud (density lower than 1.03 g· cm^{-3}), the settling curve of mud, during these first two phases, develops in accordance with sedimentation theories like Kynch (1952). Fig. 2.1 shows a typical settling curve based on Kynch's theory. During the sedimentation process, Kynch distinguishes three phases of sedimentation. During the first phase, "constant rate settling", the water-mud interface moves downward linearly with time. In this thesis, the "constant rate settling" phase is further referred to as the "settling phase". The second phase, "hindered settling", starts when the settling rate starts to slow down due to increasing interaction between the particles as a result of increasing density. As stated earlier, the settling rate is a function of density. This is indicated by the slope of the characteristic lines depicted in Fig. 2.1. The

parallelism of these lines during the settling phase indicates a consistent density during this phase. While the changing slope throughout the remainder of the settling curve indicates the changing density.

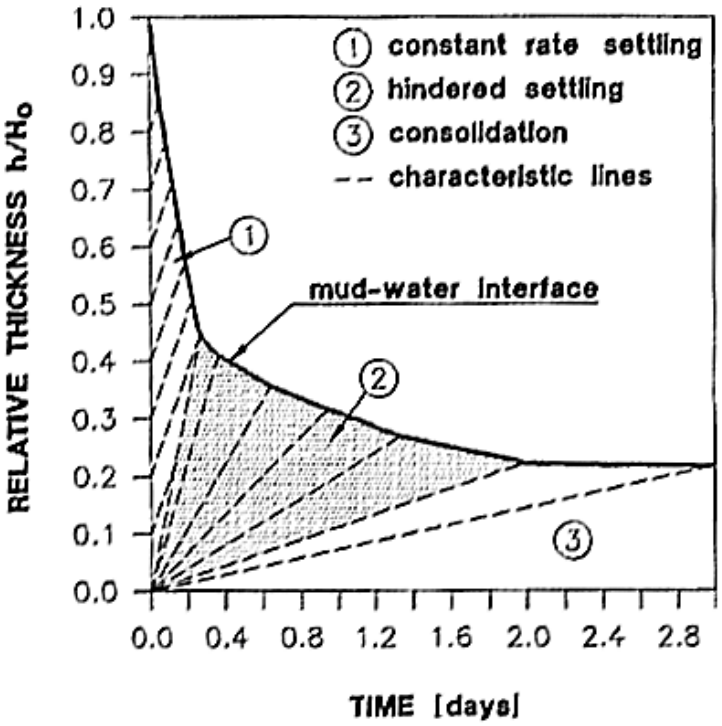

Figure 2.1: *Ideal settling curve based on Kynch's sedimentation theory, indicating the three phases of sedimentation and characteristic lines. The slope of the characteristic lines represent the density of the mud. The unchanging density during the first phase is illustrated by the parallel characteristic lines. The second phase is initiated by an increase in density, illustrated by the change in slope of the characteristic lines. This figure is copied from Toorman (1992a).*

With time, a density is reached that causes a second abrupt drop in settling rate, indicating the beginning of the

third and final phase, the ”consolidation” phase. From the consolidation phase onwards, the settling curve of mud deviates from Kynch's sedimentation theory (Toorman, 1999). The consolidation phase of mud begins when the density discontinuity between the suspension and the consolidating bed fades (Toorman, 1999). Furthermore, the consolidation phase of mud consists of two intermediate stages. First, the settling rate is determined by the permeability of the mud, since compression is mainly caused by the expulsion of pore water. Further settlement is caused by the deformation of the flocs (Toorman, 1999; Camenen and Pham van Bang, 2011). During the consolidation phase, the density will exceed the gel density after which the structure formed strongly impedes further settling. During the consolidation phase the settling rate continuously decreases and eventually tends to zero. According to Toorman (1992a), from the first part of the consolidation phase, the settling curve follows a power law function. A more detailed elaboration on the sedimentation mechanics of mud can be found in Toorman (1996), Toorman (1999) and Camenen and Pham van Bang (2011).

2.3 Experimental facilities

To come up with the optimal conditioning procedure, various conditioning techniques and durations are applied in preparation for multiple sedimentation and consolidation experiments. To allow for a large number of experiments in a limited period of time, only the settling of the water-mud interface is recorded. Plotting the level of this interface with time yields a settling curve. The resulting settling curves are used to evaluate repeatability. Because the focus is on the influence of the applied conditioning techniques, all mud samples are prepared to an equal density below gel density. Starting below gel density, settling starts almost instantly (minutes) forming a distinct interface between ”clear” water and mud. A possible difference in settling curve can

therefore be observed more rapidly, allowing the duration of the experiments to be limited to one week. This is different from hydraulic experiments using mud like for nautical research. Here a mud density higher than the gel density is usually used. Despite the different settling mechanics for densities above the gel density, there is however no reason to believe that the effects of conditioning will be different.

2.3.1 Selection of conditioning techniques

Following the elaboration on sedimentation mechanics in Section 2.2, it is clear that the distribution of different particles will influence the settling behaviour. Michaels and Bolger (1962) already demonstrated the influence of floc size on the settling rate in the settling phase. Adequate mixing to influence the settling rate should therefore affect both the size of the flocs and their dispersion in the mud volume. Uncontrolled influencing is however insufficient to reproduce settling rates. To achieve this, reference states are required, which in turn should be reproducible.

2.3.1.1 Homogenisation by axial mixing

Homogenisation of a fluid is typically done by agitation or mixing. Proper homogenisation requires a good dispersion of the mixing energy over the entire volume. According to Harnby et al. (1992b), an axial flow is recommended for this. In limited reservoirs axial flows can be created with so-called ”marine impellers”, depicted in Fig. 2.2 (A). Due to the design with constant pitch ratios, marine impellers cause an axial velocity increase. The flow is deflected by the walls of the reservoir creating circular flows over the entire volume (see Fig. 2.3 (A)). Determining a reproducible reference state for the degree of homogeneity is difficult because homogeneity is hard to monitor during conditioning. Therefore, perfect homogeneity should be aimed for. Assuming that the degree

of homogeneity improves with the duration of axial mixing, the minimum duration must be determined to achieve this goal. In preparation for the settling and consolidation experiments of this study, mixing times of 15 minutes, 30 minutes and 45 minutes are therefore applied.

2.3.1.2 Floc breakup by radial mixing

Floc breakup occurs when shear stress exerted on the floc exceeds the floc shear strength. Such shear stress can be induced on the flocs through flow and inter-particle collisions (Mehta, 2014). In nature, turbulent flows can already induce sufficient shear stress for floc breakup (Manning, 2004), indicating the low shear strength of flocs. This makes it unrealistic to assume floc breakup can be controlled during mixing. Hence, the only reproducible reference state that can be achieved by mixing is that in which all flocs are broken. According to Harnby et al. (1992b), shear is created by radial flows (see Fig. 2.3 (B)), which in turn are induced by mixing with so-called ”paddle impellers”, depicted in Fig. 2.2 (C). Given the low shear strength of flocs, it can be assumed that the duration of radial mixing can be limited. Nonetheless also 15 minutes, 30 minutes and 45 minutes of radial mixing are applied in preparation of the experiments.

2.3.1.3 Hybrid mixing

By applying only the two extremes of mixing (axial and radial), the level of impact of each can be demonstrated. However, both are probably required as stated earlier. A combination of the two is therefore also applied. This was tested in two ways. The easiest way is to use a ”pitched blade impeller”, depicted in Fig. 2.2 (B). The inclination of the blades determines the dominant flow type. The blade inclination of the pitched blade impeller used in this research is $\frac{\pi}{4}$ rad. It is however unknown if the distribution of energy at this angle is correct

to achieve both intended reference states. Therefore, a second combination method is used in which both extremes are applied in succession. First the mud is conditioned with radial mixing, followed by axial mixing. Because the impact of the duration for radial mixing is assumed to be limited, this was only done for 15 minutes, while axial mixing was performed for 30 minutes, 45 minutes and 60 minutes. For practical reasons, the pitched blade impeller is used in this combination for the radial mixing, rather than the paddle impeller. After all, due to the low shear strength of cohesive flocs it is assumed that the shear intensity produced by a pitched blade impeller is already sufficient to break all cohesive flocs.

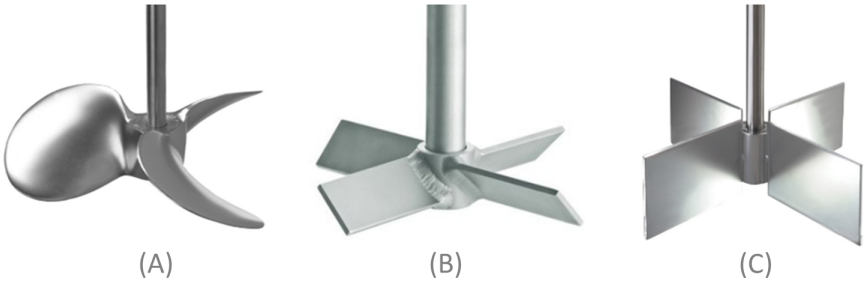

Figure 2.2: *Mixing impellers ordered from low shear (left) to high shear (right). (A) Marine impeller; (B) Pitched blade impeller; (C) Paddle impeller.*

The names used for the different impellers in this thesis are copied from the mixing industry. For readers with other backgrounds, these names may cause some confusion. For instance, the term ”pitched” in the name pitched blade impeller refers only to the inclination of the blades to the shaft. The pitch distribution over the blade of impeller (A) in Fig. 2.2 is constant (hence the different angle the blade makes at the root and tip to the shaft), resulting in a uniform axial acceleration of the fluid. A constant pitch ratio is preferred for ship propellers, hence the name marine impeller. Impeller (B) has a constant angle over the entire blade to the shaft, resulting in a non-constant pitch distribution over the blade. This will induce

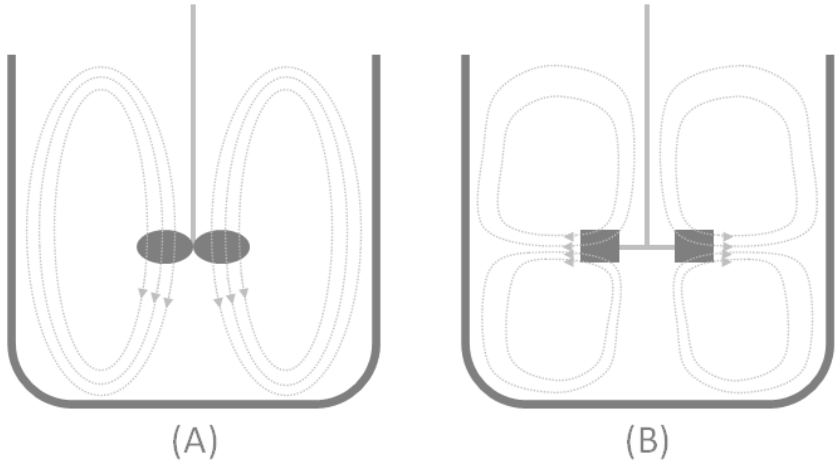

Figure 2.3: *(A) Axial flow for homogenisation; (B) Radial flow for shearing.*

different accelerations in the fluid depending of the point of interaction to the impeller. In theory, the pitch ratio of impeller (C) is infinite, hence it has no displacement capacity in the direction of the shaft.

2.3.2 Setup and instrumentation

2.3.2.1 Consolidation columns

Transparent plastic tubes of 2 m in length, an outer diameter of 63 mm and a wall thickness of 3.2 mm were used as settling columns. Nine of them were mounted together in a fixed upright position. Backlighting is used to accentuate the water-mud interface. For this purpose, four double fluorescent tubes of 1.2 m are mounted behind the columns. In between a plastic light diffuser panel is installed for optimal spreading of the light. A recorded image illustrating the results of this setup is depicted in Fig. 2.4.

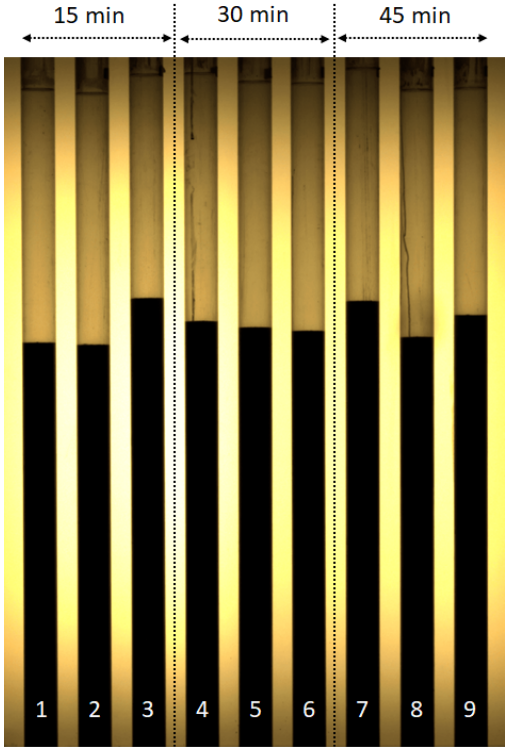

Figure 2.4: *A picture of the nine consolidation columns during consolidation tests. Each series of experiments consisted of three columns with mud conditioned for 15 minutes (columns 1, 2 and 3), 30 minutes (columns 4, 5, and 6) and 45 minutes (columns 7, 8, and 9). With backlighting the water-mud interface is accentuated.*

2.3.2.2 Automated interface level recording

An IDS uEye USB camera, type UI-3200SE-C-HQ is used to simultaneously record the water-mud interface levels of all nine columns. The camera was equipped with a color sensor having a resolution of 4104 by 3006 pixels. It was mounted at a distance of 6.5 m from the columns. With a fixed focal lens of 35 mm this results in a field of view of approximately

2258 by 3468 pixels. The resolution was approximately 0.63 mm per pixel. Image acquisition was managed with an in-house software application. To manage the amount of data, the acquisition frequency was variable throughout the experiment. The time intervals for these experiments varied from 15 minutes at the start of the experiment (high settling rates - see Fig. 2.1) to 2 hours at the end (low settling rates - see Fig. 2.1).

2.3.2.3 Image processing

The image processing software is programmed in LabVIEW, which has an extensive image processing library. For this application, the ”straight edge detection” algorithm is used to detect the water-mud interface. This algorithm searches for a transition from bright to dark (or vice versa) along search lines within a defined region of interest. This outputs a list of points (edges) through which the algorithm fits a line. This line is considered to be the water-mud interface. With the backlighting, the contrast between the dark opaque mud and the bright transparent water is high enough to ensure robust edge detection.

2.3.2.4 Floc size distribution

For each experiment, an attempt was made to analyse the size of the flocs after conditioning. A sample was taken while the mud was pumped into the columns. These samples were analysed using a Malvern Mastersizer 2000 (Mal, 2007). This device is used to perform particle size distributions based on laser diffraction in the Mie scattering regime. Although laser diffraction is a well-known technique to analyse floc sizes (e.g. Krishnappan (2006); Hill et al. (2011)), the results of the analyses during this study did not indicate any significant differences in particle size distribution between the different samples. There are, however, important differences in setup

compared to Krishnappan (2006) and Hill et al. (2011). In these studies, the laser diffraction setup was placed in the experimental setup or on-site, i.e. where the flocculation or floc break up occurred. This is not possible with the Malvern Mastersizer 2000, hence the sampling. From the samples, a small subsample is suspended in a beaker with water kept in motion with a rotating impeller to prevent settling of the particles. This highly diluted mud sample is circulated in the apparatus where laser diffraction is applied in a section of transparent tubes. Due to the fragility of the flocs, each of these intermediate steps is likely to lead to further break up of any flocs present. Thus, despite the initial differences in the presence of flocs, the particles present in each sample become similar prior to the laser diffraction analysis, which explains the similar results. The output of these analyses should therefore be considered as a particle size distribution when hardly any flocs are present in the mud. Fig. 2.5 shows a plot representing the volume distributions of particle sizes present in different samples. This plot shows two sets of curves, one where the sample is analysed as is, and one where the sample is exposed to high-intensity ultrasound before analysis. Ultrasonic treatment is a function of the Malvern Mastersizer 2000 to facilitate the dispersion of particles in a sample. Alternatively, it can also be used to break up flocs (Mal, 2007). When the results after ultrasonic treatment are considered as results with no flocs present, the slight difference between the two sets of curves feeds the previous presumption that additional flocs are broken during processing by the Malvern Mastersizer 2000, resulting in similar amounts and sizes of flocs. Therefore, to compare the differences between the mud after conditioning with the different mixing techniques, the results of these particle size analyses are not used.

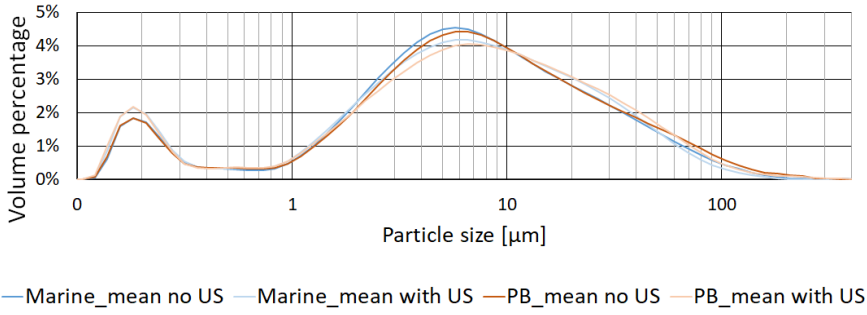

Figure 2.5: *Differential mean particle size distribution curves after mixing with the marine impeller and the pitched blade impeller, both without and with ultrasonic treatment. As elaborated in Section 2.3.2.4 these curves should be considered as particle size distribution curves when hardly any flocs are present in the mud.*

2.4 Experimental methodology

2.4.1 Conditioning procedure

The mud used originates from the central part of the outer harbor of Zeebrugge (known as CDNB) of the Port of Antwerp-Bruges, Belgium. Being North-Sea mud, the gel density is known to be about 1.10 g· cm^{-3} (Meshkati Shahmirzadi et al., 2015). A batch was collected from maintenance dredging and transported to the FH laboratory. The mud was transported, stored and conditioned in barrels of approximately 65 liters, made of HDPE. During transport and storage, the barrels were sealed airtight, while the HDPE prevented any light penetration, minimising any activity of the organic fraction. Two barrels of mud were prepared and alternately used per experimental series. During the project, the barrels were stored and processed indoors at a more or less constant temperature of 15°C to 20°C. A day before the start of the experiments the mud was prepared to the intended density of 1.08 g· cm^{-3}. For the first experiments, the mud was diluted. This was done with seawater obtained from the same

location as the mud to preserve the salinity of the mud. With each experiment, some of the consolidated mud was lost as it stuck to the wall of the columns. In preparation of subsequent experiments, the mud thus had to be thickened. This was done using mud from the delivered batch of mud from which the two different batches were prepared earlier.

Diluting and thickening were performed using the same conditioning setup as for the experiments themselves, illustrated in Fig. 2.6. The setup consists of a stationary mixer to allow for long mixing durations and a closed pump circuit, including a continuous density measuring device (Anton Paar DPRN 427). During conditioning, the rotational speed of the mixers was set as high as possible to maximise mixing intensity (Harnby et al., 1992b). However, the speed was limited to avoid spillage due to excessive turbulence. The impellers used were already available, so their dimensions were not optimised for the size of the reservoir in which mixing was performed. After all, according to Harnby et al. (1992a), the optimum impeller diameter is 25 % to 66 % of the inner diameter of the reservoir, which is about 350 mm. With diameters of 240 mm, 300 mm and 130 mm for the marine impeller, pitched blade impeller and paddle impeller, respectively, especially the pitched blade impeller falls outside this recommendation. All impellers were placed at a height from the bottom of about 10 % to 20 % of the height of the barrels, while the barrels were completely filled except for a practical margin of about 50 mm. While mixing, vortexing should be avoided, as this causes air entrapment. The presence of air in mud is unwanted, as air bubbles will rise when the mud is at rest, affecting the sedimentation and consolidation process. To prevent gross vortexing during mixing, two baffles are installed (Harnby et al., 1992a). Ideally there should be four, one per quadrant. However, due to practical limitations, the baffles were fixed to the frame of the mixer, allowing only two. After the mud was prepared to the desired density, it was left to rest until the start of the actual

experiment the next day (about 21 hours later). This way, the initial state of the mud at the beginning of each experiment, starting with conditioning, can be considered similar for all experiments. Upon conditioning, the mud is pumped around in a closed circuit to verify the density using a continuous density measurement device (Anton Paar DPRN 427). A peristaltic pump is used to prevent changes in the composition of the mud due to pumping (e.g. breakup of flocs). Meanwhile, the escape of any entrapped air is facilitated by low-intensity mixing. After a few minutes, the discharge hose from the pump is brought to almost the bottom of the column through the open top. During filling, the discharge hose is retracted while it remains just below the mud surface. On average the columns were filled to 1605 mm (varying from 1521 mm to 1695 mm), which is equivalent to about 4 litres per column.

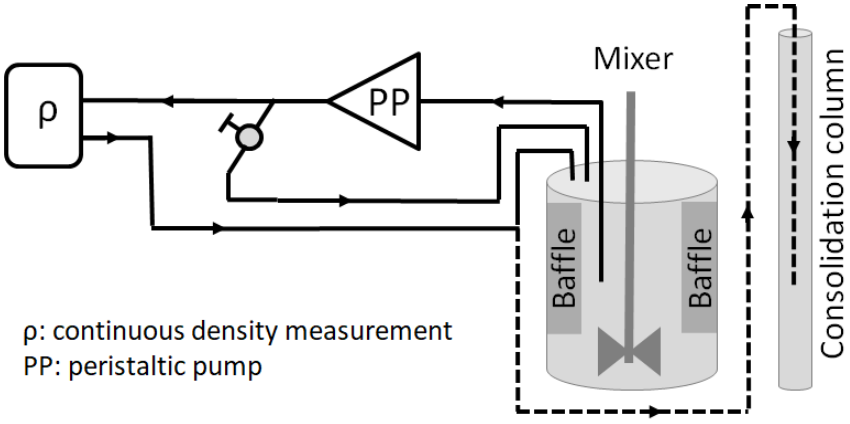

Figure 2.6: *Schematic overview of the mud conditioning setup as used during the experiments. The barrel and mixer were fixed to allow for long mixing durations. Two baffles were installed opposite to each other and fixed to the frame of the mixer. The density is checked using a continuous density measurement device (Anton Paar DPRN 427) in a closed pump circuit (solid lines). Once the mud was considered to be ready the closed circuit was broken and the discharge hose replaced to the columns (dashed lines).*

2.4.2 Experimental programme

One series of experiments consists of nine settling and consolidation experiments, as shown in Fig. 2.4. The mud from each experiment within a series comes from the same batch of mud, conditioned with one of the four mixing techniques discussed in Section 2.3.1. Three replicated experiments are set up per mixing duration, yielding the nine experiments per series. Each of these series was repeated three times, resulting in a total of twenty-seven settling and consolidation experiments per mixing technique. This programme is summarised in Table 2.1.

Halfway through the experiment of the series with the pitched blade impeller mud started to stick to the inner walls of the columns. Suspectedly this was caused by calcareous deposits on the inner walls of the settling columns during the experiments. Because of this, it was impossible to detect the water-mud interface as elaborated in Section 2.3.2.3. The tubes were cleaned with calcium solvent and the series of the pitched blade impeller was repeated. The valid recordings of the first attempt are however also taken into account when processing the results.

As mentioned in Section 2.4.1, the targeted initial density was 1.08 g$\cdot$ cm^{-3}. In practice, an interval of 1.079 g$\cdot$ cm^{-3} to 1.081 g$\cdot$ cm^{-3} was allowed. The densities of the second series with the combination of pitched blade and marine impeller exceeded the upper limit. Therefore, an additional fourth series was carried out.

Table 2.1: *Summary of the test programme for each mixing technique. Each series of tests per mixing technique was repeated three times, unless stated otherwise in Section 2.4.2. The indicated settling column numbers refer to the columns depicted in FIG 2.4.*

Mixing impeller	Mixing time duration [min]	Settling columns
Marine	15	1, 2 and 3
	30	4, 5 and 6
	45	7, 8 and 9
Pitched blade	15	1, 2 and 3
	30	4, 5 and 6
	45	7, 8 and 9
Paddle	15	1, 2 and 3
	30	4, 5 and 6
	45	7, 8 and 9
Pitched blade + Marine	15 + 30	1, 2 and 3
	15 + 45	4, 5 and 6
	15 + 60	7, 8 and 9

2.5 Experimental results and discussion

2.5.1 Averaged settling curves

With the recorded water-mud interface levels, the settlement of the water-mud interface is calculated at each timestamp of a recording as the difference between the level recorded at the corresponding time and the starting level of the experiment. With these values of settlement a settling curve can be plotted for each experiment. Because the starting levels of the experiments are not exactly the same, both the settling scale and the time scale have to be scaled to allow comparison

between the different experiments. The settling scale is converted into a relative scale by expressing it as the ratio of the recorded interface level (h) relative to the initial levels (h_0) of the experiments, i.e. around 1605 mm (see Section 2.4.1). The time scale of the settling curve of each experiment is scaled by a scale factor equal to the ratio between the starting level of the experiment (h_0) and the starting level of a fixed reference experiment ($h_{0,ref}$). The starting level of a random experiment was chosen as the reference level, in this case 1650 mm. Hence, with the aforementioned variation in starting levels (see Section 2.4.1), this scale factor varies between 92 % and 103 %. Average settling curves are calculated per mixing technique and duration across the different series of experiments. Plots of these averaged settling curves are shown in Fig. 2.7. These plots already show that when the mud is mixed using the combination of the pitched blade and marine impeller, the mixing time has a minor effect and even can be neglected.

Based on the typical shape of a settling curve (see Section 2.2) the start and end of the hindered settling phase is determined for each of the averaged settling curves. This procedure is illustrated in Fig. 2.8. The settling curve during the settling phase is linear. Hence, a linear trendline fitting the settling curve during this phase can be determined. The start of the hindered settling phase corresponds to the end of the linear settling phase. This moment can thus be determined as the point where the settling curve starts to deviate from the linear trendline. This is indicated by the orange dot in Fig. 2.8. In turn, the end of the hindered settling phase corresponds to the start of the consolidation phase, which, in the case of a well-homogenised suspension of cohesive sediments, occurs when the bulk density approximates the gel density. Since a continuous structure is formed from this moment, the point on the settling curve indicating this transition can be accurately determined from the effective stress, which is the difference between the total stress and the

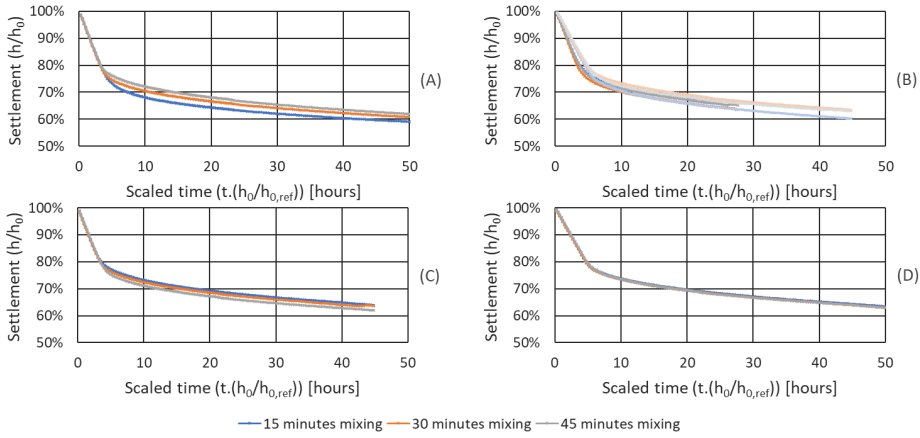

Figure 2.7: *Across the different test series averaged settling curves, sorted per mixing impeller (Fig. 2.2): (A) Marine impeller, (B) Pitched blade impeller, (C) Paddle impeller, (D) Combination of pitched blade and marine impellers. To account for the different starting levels of the experiments, the settlement is expressed relatively and the time scale is scaled as discussed in Section 2.5.1. Two experimental series have been conducted with the pitched blade impeller (B) (see Section 2.4.2). The results of the first series are plotted similar as in the other charts, while the results of the second series are plotted in the corresponding faded colour. The blue, orange and grey colours represent the shortest, middle and longest mixing durations (see Table 2.1), respectively. Each curve is averaged over at least nine experiments in accordance to Section 2.4.2 and Table. 2.1.*

pore water pressure (Toorman, 1996). Both parameters are however unknown and require additional measurements which were not conducted during the sedimentation experiments of this study. For this study, the determination of this moment is therefore approximated by a similar method as for the determination of the beginning of the hindered settling phase. The end of the hindered settling phase is determined as the moment when the difference between the settling curve and a power trendline (Toorman and Leurer, 2000) fitting the settling

curve during the consolidation phase becomes minimal. This moment is indicated by the green circle in Fig. 2.8. The resulting timestamps and corresponding settlement values at the beginning and the end of the hindered settling phases are presented in Fig. 2.9 and Table 2.2.

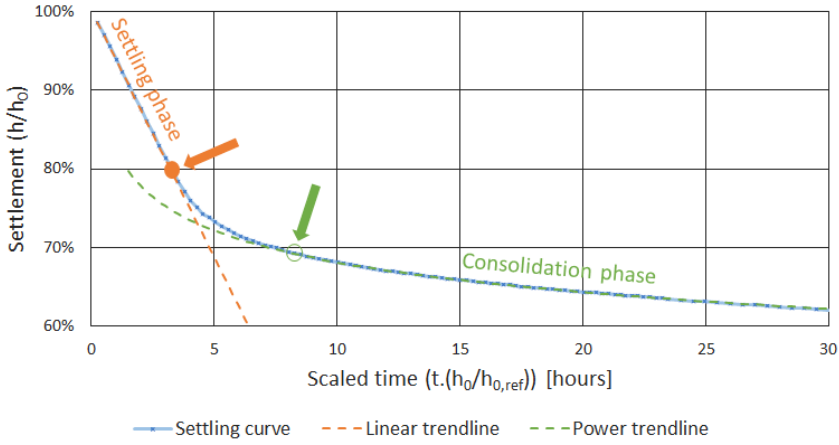

Figure 2.8: *Illustration of the procedure to calculate the start and end of the hindered settling phase of a settling curve as described in Section 2.5.1). The settling curve is plotted in blue. A linear trendline (dotted orange line) and a power law trendline (dotted green line) are determined fitting the settling phase and the consolidation phase, respectively. The beginning of the hindered settling phase is determined as the moment where the divergence between the settling curve and the linear trendline increases. The end of the hindered settling phase is determined as the moment where the divergence between the settling curve and the power law trendline becomes minimal.*

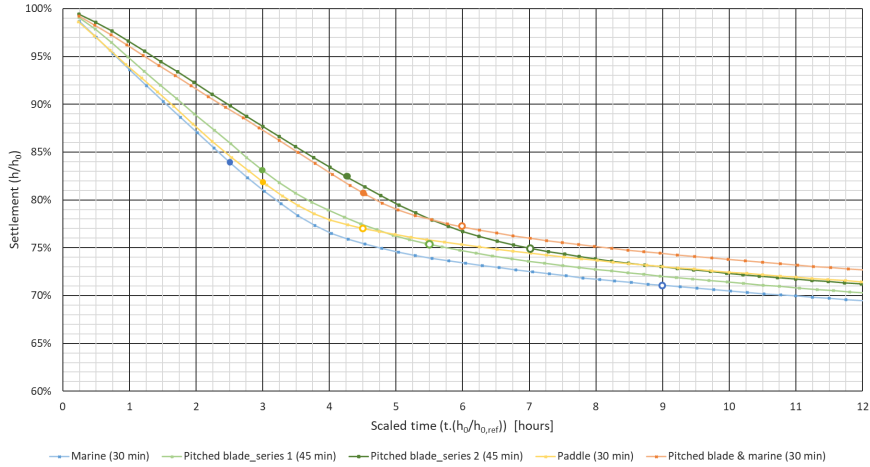

Figure 2.9: *Close-up on the settling phase and hindered settling phase of the different average settling curves for each conditioning technique. For the legibility of the figure and because the mixing time has only a minor effect (see Fig. 2.7), solely the intermediate curve is plotted for each conditioning technique. The start times of the hindered settling phase are indicated by the filled markers and the end times by the unfilled markers, in correspondence with Table 2.2.*

2.5.2 Influence of mixing technique and time duration

The results presented in Fig. 2.9 and Table 2.2 allow to evaluate the influence of the applied mixing techniques and mixing durations on the settling curves. Because the effect of the conditioning procedures may be different for each sedimentation phase, the observations for each sedimentation phase are discussed separately.

2.5.2.1 Settling phase

The results presented in Fig. 2.9 and Table 2.2 show that the settling rate during the settling phase is lowest after

Table 2.2: *Resulting duration and progress of settlement during the settling phase and the hindered settling phase of the various average settling curves presented in Fig. 2.7. The method to determine these results are described in Section 2.5.1 and illustrated by Fig. 2.8. The results are represented by the markers in Fig. 2.9. For the settling phase the constant settling rate is provided with an accuracy of 0.63 mm·s^{-1}. For readability, pitched blade is abbreviated as PB.*

Mixing impeller(s)	Settling phase			Hindered settling phase	
	Duration [hours]	Settlement [%]	Settling rate [mm· $hour^{-1}$]	Duration [hours]	Settlement [%]
Marine (15 min)	3.25	20.23	104	4.75	10.34
Marine (30 min)	2.50	16.20	108	6.50	12.75
Marine (45 min)	2.75	17.21	104	7.75	10.99
PB_series 1 (15 min)	2.25	12.76	92	3.50	11.65
PB_series 1 (30 min)	2.75	16.45	96	2.75	9.45
PB_series 1 (45 min)	3.00	17.01	91	2.50	7.56
PB_series 2 (15 min)	3.50	15.73	68	3.75	11.20
PB_series 2 (30 min)	3.75	16.31	70	3.50	8.33
PB_series 2 (45 min)	4.25	17.71	68	2.75	7.37
Paddle (15 min)	2.50	15.04	95	2.00	7.07
Paddle (30 min)	3.00	18.43	96	1.50	4.56
Paddle (45 min)	3.25	19.52	94	1.50	4.78
PB & marine (30 min)	4.50	19.30	68	1.50	3.55
PB & marine (45 min)	4.25	18.39	69	1.75	4.79
PB & marine (60 min)	4.50	18.96	67	2.75	5.42

conditioning by sequential mixing with the pitched blade and marine impellers. The highest settling rate is recorded during the experiments after mixing with only the marine impeller. A difference in settling rate is caused by a difference in the settling gradient or the duration of the settling phase, or both.

The duration of the settling phase during the experiments after conditioning with the paddle impeller show an increase with increasing mixing time. Since the paddle impeller induces mainly radial flows, which in turn induce shear stresses, this prolongation of the settling phase can be attributed to the extent of floc disintegration. After all, when cohesive flocs are broken into smaller flocs or even particles, these smaller flocs or particles must first merge back into larger flocs, corresponding the new low energetic condition in the column, before they will settle (see Section 2.2). Hence, settling is delayed and the settling phase prolonged. Increasing duration with increasing radial mixing time implies that the extent of floc breakup increases with radial mixing time. Since large cohesive flocs are considered to be weaker than small flocs (Serra and Casamitjana, 1998; Maggi, 2005), it can be assumed that further break up of flocs requires an increasingly higher shear stress as the size of the flocs decrease. As long as the shear stress induced by mixing exceeds the shear strength of the flocs, floc break up continues. Similar durations and increase in duration with increasing mixing time are observed after conditioning with only the pitched blade impeller, confirming the floc break up capacity of the pitched blade impeller. Although not the envisaged objective of axial mixing, the similar duration of the settling phase after conditioning with only the marine impeller implies that floc break up also occurs during axial mixing. After all, shear stresses are inevitable during high turbulent mixing, regardless of the type of dominant induced flow. When maximising mixing intensity, it is therefore reasonable to assume that the turbulence during mixing is much higher

than the turbulence level from where floc breakup occurs (van Leussen, 1994; Dyer and Manning, 1999). Moreover, further additional shear is induced when the flows collide with the baffles (see Section 2.4.1). An increasing duration of the settling phase with increasing axial mixing time cannot be observed. Consistent with the aforementioned relationship between the shear capacity of the mixing technique and the size of the remaining flocs after mixing, it can be concluded that for axial mixing, the induced shear stresses are limited and the maximum floc disintegration is obtained already after short-term mixing. Further breaking of the flocs by extending the mixing time is thus not feasible. Nonetheless, the small difference in duration of the settling phase compared to the other experiments shows that the difference in size of the residual flocs can be considered small.

Following the above, it is surprising that the durations of the settling phase of the experiments after sequential mixing with the pitched blade and marine impellers stand out. Since the floc breaking capacity of the marine impeller is considered to be lower than that of the pitched blade impeller, this excessive duration cannot be attributed to the size of the remaining flocs and can thus solely be ascribed to the subsequent axial mixing. The effect of axial mixing on the settling behaviour during the settling phase is more visible in the settling gradients (Table 2.2, column 3). On average, the settling gradients of the experiments after conditioning where the marine impeller was used, whether in combination with another propeller or not, were larger than in the other experiments. As discussed in Section 2.3.1, mixing with the marine impeller is expected to induce axial flows enhancing the homogeneity of the mud. Perfectly homogeneous mud implies equal dispersion of cohesive flocs and coarse particles throughout the entire mud volume, resulting in a uniform density profile across the mud column. On the other hand, when a perfectly homogeneous mud is not achieved, the concentration of dense coarse particles will be higher at the

bottom and lower in the upper layers and vice versa for the light cohesive particles. This results in a sloping density profile across the mud column. Consequently, the settled particles and flocs in the initial upper layers are denser as homogeneity increases, leading to higher effective stresses as they settle and consequently greater compaction and hence settling.

In case of similar floc size, and thus similar floc settling velocity, a greater settling gradient results in an extended settling phase. In the case of a combination of axial and radial mixing, the extension of the settling phase caused by both mixing techniques add up, resulting in the excessive durations of the settling phases of these experiments. This also explains the unexpected similar, or even longer, durations of the settling phase after mixing with only the pitched blade impeller compared to those after mixing with only the paddle impeller. After all, the floc breaking capacity of the pitched blade impeller is considered to be less. Since the pitched blade impeller also generates axial flows which enhance homogeneity, the duration of the settling phase is also extended twofold. That the elongation is less pronounced compared to the experiments after sequential mixing with the pitched blade impeller and the marine impeller can be attributed to either the shorter mixing times or lower homogenising capacity of the pitched blade impeller compared to the marine impeller.

2.5.2.2 Hindered settling phase

Overall, the longest durations and settling gradients of the hindered settling phase are recorded during the experiments following axial mixing using only the marine impeller. Added to the values of the settling phase, this leads to the most elapsed time and greatest settling at the beginning of the consolidation phase. Hence, it can be concluded that an increase in homogeneity postpones consolidation. The consolidation

phase is initiated when a higher density threshold is reached. This density is earlier attained when the local concentration of heavy particles is higher. As mentioned in Section 2.5.2.1, an increase in homogeneity leads to an increase in density in the upper layers and a decrease in density in the lower layers. An enhanced homogeneity therefore creates a setback in density development in the lower layers and consequently delays the initiation of the consolidation phase. The observation that the duration and, to a lesser extent, the settling gradient increase with increasing axial mixing time emphasises this conclusion and implies that the maximum homogenising capacity is not yet achieved.

This increase in duration and settling gradient with increasing axial mixing time can also be observed after sequential mixing with the pitched blade and marine impellers. In contrast, however, the values of both are the lowest of all experiments. This is remarkable since for these experiments, the settling gradients during the settling phase, are among the largest (see Section 2.5.2.1). Despite the settling gradients during the settling phase of the experiments after axial mixing with only the marine impeller being similarly high, this similarity is no more during the hindered settling phase. This reversal must therefore be caused by the higher floc breaking capacity of the preceding mixing with the pitched blade impeller. This is confirmed by the decreasing settling gradient with increasing radial mixing time during both the experiments after mixing with the pitched blade impeller and those after mixing with the paddle impeller. The duration of and the settling gradient during the hindered settling phase after mixing with the paddle impeller, however, are lower than after mixing with the pitched blade impeller. This confirms the presumed lower floc breaking capacity of the pitched blade impeller compared to the paddle impeller, as concluded in Section 2.5.2.1. The decrease in settling gradient is thus proportional to the extent of floc breakup during conditioning. After all, floc breakup leads to delayed settling of cohesive flocs during the settling

phase, as discussed in Section 2.5.2.1. While, other non-cohesive and more dense particles will settle almost instantly and faster. This difference in settling behaviour leads to segregation between the two (van Ledden, 2003; Winterwerp and Van Kesteren, 2004). In turn this will lead to less dense cohesive flocs (Toorman and Berlamont, 1993; Torfs et al., 1996) and therefore lower effective stresses when settled. Consequently, the settled layer of cohesive flocs will be less compact, resulting in a lower settling gradient. This is comparable to the difference in compaction when dumping dredged mud in water or on land. When dumped in water, the high-density mud will mix with water, resuspend and dilute, causing segregation. When dumped on land the density is maintained and the sand remains trapped in the cohesive flocs. Therefore, the cohesive flocs are denser which is beneficial for compaction and the settling rate (Toorman and Berlamont, 1993).

2.5.3 Repeatability

As mentioned in Section 2.3.1, repeatability of settling curves involves the ability to reproduce reference states by conditioning the mud. Section 2.5.2 concludes that such a reference state for floc size is most efficiently achieved by radial mixing. Axial mixing in mud, in turn, approximates the reference state of absolute homogeneity with increasing mixing durations. Since the settling behaviour of mud is determined by both the size of the flocs and their dispersion in the mud volume, reference states for both floc size and homogeneity must be achieved through mud conditioning. As discussed in Section 2.5.2, this is most effectively achieved by sequentially applying radial and axial mixing.

To objectify the level of repeatability between experiments, the standard deviation of the settling curves of those experiments is calculated along their time scale, i.e. for each timestamp

the standard deviation of the corresponding settling values is calculated. Low values of standard deviation indicate good repeatability and vice versa. For each combination of applied mixing impeller and duration, the repeatability is assessed per series and across the different series. Each series consists of three of the same experiments (see Section 2.4.2). Thus, to assess repeatability for each series, standard deviations of those three experiments are calculated (Eq. 2.1). To assess the repeatability across the different series, all experiments of the applicable combination of applied mixing impeller and duration are considered (Eq. 2.2). Including intermediate conditioning and use of mud from different batches, the latter best simulates the execution of hydraulic experiments for nautical research. Hence, it is the main goal of this research to improve the repeatability across the different series. In addition, repeatability is differentiated for each sedimentation phase by determining the mean standard deviation over the corresponding time frame of the sedimentation phase as determined in Section 2.5.1 and Fig. 2.8. The mean standard deviations per series are presented in Fig. 2.10. Those for the analysis across the different series are presented in Fig. 2.11.

$$\overline{\sigma}_{t,\text{per series}} = \frac{1}{3}\sum_{\text{s=1}}^{3}\sqrt{\sum_{\text{e=1}}^{3}\frac{(X_{\text{s,e},t} - \overline{X}_{\text{s},t})^2}{3}} \tag{2.1}$$

$$\sigma_{t,\text{across series}} = \sqrt{\sum_{\text{s=1}}^{3}\sum_{\text{e=1}}^{3}\frac{(X_{\text{s,e},t} - \overline{X}_{\text{s},t})^2}{9}} \tag{2.2}$$

Where $\overline{\sigma}_{t,\text{per series}}$ is the mean of the standard deviations at timestamp t of three repetition experiments within a series, $\sigma_{t,\text{across series}}$ is the standard deviation at timestamp t across the different series of experiments, X is the relative settlement of the water-mud interface (Section 2.5.1) and the indices e and s refer to the different experiments and series, respectively.

2.5.3.1 Repeatability of experiments per series

The results depicted in Fig. 2.10 show that the maximum standard deviations of most series are below or around 1 %. Two series using the marine impeller show higher values, but still below 2 %. Compared to the repeatability of previous studies (see Section 1.1.3.1), this is already a significant improvement, which can be attributed to the strict procedural conditioning following a fixed duration of mixing and constant mixing intensity. Indeed, this was not always the case in the previous studies, as elaborated in Section 2.1.

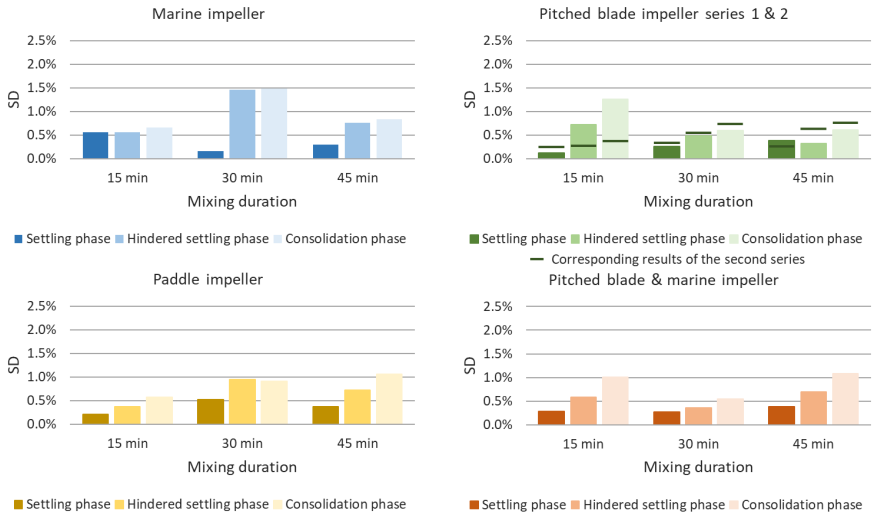

Figure 2.10: *Standard deviations (SD) of the settling curves averaged per series of three repetition experiments (see Section 2.4.2 and Table 2.1), sorted per mixing technique. The chart of the pitched blade impeller shows the results of both series performed with the pitched blade impeller (see Section 2.4.2). The results of the first series are presented with the bar charts. The results of the second series with the dark green lines aligned with the corresponding bar chart. For each mixing technique, a breakdown of the applied mixing duration and phases of settlement is provided.*

It is also noticeable that the repeatability is slightly better for the experiments following radial mixing. Within a single series of experiments, mud is used from one and the same conditioned batch. Thus, the degree of homogeneity of the mud is the same for all experiments and therefore becomes irrelevant when comparing the settling behaviour of the experiments within the same series. Consequently, only a difference in particle size can cause any deviating course of the settling processes. Because a higher floc breaking capacity provides more control over the residual floc sizes, the behaviour of radially mixed mud is more uniform within a single series of experiments. Nonetheless, the difference with the repeatability of the experiments after axial mixing with only the marine impeller is not significant. This confirms the slightly lower floc breaking capacity of axial mixing.

2.5.3.2 Repeatability of experiments across series

Fig. 2.11 shows the standard deviations of the mean settling curves, averaged across the multiple series of three experiments. This simulates the conduct of a series of hydraulic experiments using mud, such as for nautical research like Sotelo et al. (2022). With an overall standard deviation of about 1 % to 2 %, the combination of axial and radial mixing yields the highest repeatability throughout the full course of the experiments. There is no significant difference between the simultaneous combination using only the pitched blade impeller and the combination using sequentially the pitched blade impeller and the marine impeller. Again, this is a significant improvement over previous studies (see Section 1.1.3.1).

The repeatability of the experiments after radial mixing with the paddle impeller achieves the same high level as the experiments after the combination of axial and radial mixing, only during the settling phase. This shows that the course

of the settling phase is mainly governed by the residual size of the flocs after conditioning. Although slightly divergent, the various mixing techniques used all do have a significant capacity to break up flocs (see Section 2.5.2). So for all experiments, floc size variation was always more or less under control, resulting in high repeatability of all experiments during the settling phase. Since axial mixing with the marine impeller is considered to have the lowest floc breaking capacity, a longer mixing time is required to achieve comparable high repeatability.

Starting from the hindered settling phase, the further course of sedimentation and consolidation is governed more by the initial degree of homogeneity of the mud. This is reflected in the lower repeatability of the experiments after radial mixing with the paddle impeller, which has no significant homogenising ability (see Section 2.5.2). As a result, in the case of mud of similar composition, the behaviour during the hindered settling phase is similar for each experiment when a mixing technique with homogenising capacity is applied during conditioning.

The levels of repeatability during the consolidation phase are very similar to those during the hindered settling phase. Therefore, it can be concluded that neither initial floc size distribution nor initial homogeneity further influence the sedimentation process once the hindered sedimentation phase is passed. This confirms the statement that a difference in settling curve develops mainly during the settling and hindered settling phases (see Section 1.1.3.1).

2.6 Conclusions and recommendations

The importance of procedural conditioning of mud is reported in various published studies. Yet a uniform procedure was never suggested. The results of this study not only confirm the importance of procedural conditioning, but also show that

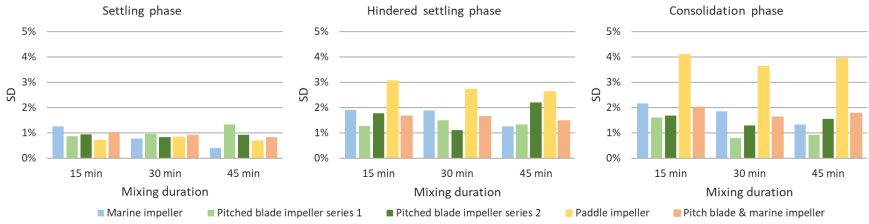

Figure 2.11: *Standard deviations (SD) of the settling curves averaged across the different series of three repetition experiments (see Section 2.4.2 and Table 2.1), sorted by phase of settlement. For each phase of settlement, a breakdown of the applied mixing duration and mixing technique is provided.*

the applied mixing technique during conditioning affects the settling behaviour of the mud. Therefore, to allow comparison between different studies and improve the reproducibility of mud behaviour, a conditioning procedure containing a combination of both axial and radial is proposed for any experiment involving the behaviour of mud. Whether the combination of both mixing techniques is done simultaneously with one and the same impeller or sequentially through multiple impellers makes little difference in repeatability. For practical reasons, the use of one and the same impeller, like a pitched blade impeller, is preferred. A condition, however, is that both the floc breaking capacity and the homogenising capacity of the impeller are sufficient.

Radial and axial mixing enable the creation of reproducible reference states for particle size and homogeneity, respectively. This way, the initial state of the mud at the start of an experiment can be reproduced, thereby optimising the repeatability of the course of the sedimentation process of mud of similar composition. Since particle size and homogeneity are difficult to measure or monitor during mixing, it was suggested (see Section 2.3.1) that such reference states can only be obtained by pursuing the extremes of these characteristics. For par-

ticle size, this means breaking up all cohesive flocs, leaving only unbound cohesive and non-cohesive particles. For homogeneity, this is somewhat less clear-cut and can only be aimed at the highest possible degree of homogeneity. The results of the experiments conducted during this study show that a minimum capacity for both is indeed required to have a positive effect on repeatability. However, if the maximum capacity of a mixing technique is insufficient to achieve the pursued extreme, the ultimate level achieved can also act as a reproducible reference state as long as the same equipment is used following the same procedure.

Overall, the combination of axial and radial mixing yields the best results for repeatability of mud settling behaviour. Depending on the conduct of the experiments or the sedimentation phase of interest, other procedures may also be adequate. For example, in the case of a one-off series of experiments with the same batch of mud, radial mixing alone can also be considered as an adequate mixing technique to achieve optimal repeatability. For multiple series of experiments with different batches of mud of similar composition, either only axial or only radial mixing may be an option, if only the settling phase is of interest. Because of the limited time between mud conditioning and the conduct of experiments, the latter may be the case, for example, during laboratory experiments for nautical research as performed by Lovato et al. (2022) and Sotelo et al. (2022).

Furthermore, it is recommended to determine the minimum required duration of conditioning as a function of the conditioning set-up, mud composition and mud volume, because all these factors are likely to be influential. If such a preliminary assessment is not possible, it is advisable to maximise the duration of conditioning.

As a reminder, it should be noted that this study is limited to experiments with mud with an initial density below the gel

density. Since the settling behaviour of mud with a density above the gel density is different, similar experiments with such mud are of interest to verify the conclusions of this study. However, the most ideal conditioning procedure is not expected to depend on the ratio of initial mud density to gel density.

Bibliography

Been K. *Stress strain behaviour of a cohesive soil deposited under water*. PhD thesis, Balliol College, University of Oxford, Parks Road, Oxford, UK, 1980.

Been K. and Sills G. C. Self-weight consolidation of soft soils: An experimental and theoretical study. *Géotechnique*, 31(4):519–535, 1981.

Berlamont J., Van den Bosch L. and Toorman E. Effective stresses and permeability in consolidating mud. *Coastal Engineering Proceedings*, 1(23):2962–2975, 1992. doi: 10.9753/icce.v23.%p.

Berlamont J., Ockenden M., Toorman E. and Winterwerp J. The characterisation of cohesive sediment properties. *Coastal Engineering*, 21(1–3):105–128, 1993.

Bowden R. K. *Compression behaviour and Shear strength characteristics of a natural silty clay sedimented in the laboratory*. PhD thesis, University of Oxford, Parks Road, Oxford, UK, 1988.

Camenen B. and Pham van Bang D. Modelling the settling of suspended sediments for concentrations close to the gelling concentration. *Continental Shelf Research*, 31(10):106–111, 2011. doi: 10.1016/j.csr.2010.07.003.

Dyer K. and Manning A. Observation of the size, settling velocity and effective density of flocs, and their fractal dimensions. *Journal of sea research*, 41:87–95, 1–2 1999. doi: 10.1016/S1385-1101(98)00036-7.

Harnby N., Edwards M. F. and Nienow A. W. Chapter 7 - a review of mixing equipment. In *Mixing in the process industries*, pages 118–136, 1992a.

Harnby N., Edwards M. F. and Nienow A. W. Chapter 8 - mixing of liquids in stirred tanks. In *Mixing in the process industries*, pages 137–158, 1992b.

Hill P. S., Boss E., Newgard J. P., Law B. A. and G. M. T. Observations of the sensitivity of beam attenuation to particle size in a coastal bottom boundary layer. *Journal of Geophysical Research*, 116(C2):1–14, 2011. doi: 10.1029/2010JC006539.

Huysentruyt H. Consolidation of mud - settling column test. In *Final report of the MASTG8M Coastal Hydrodynamics programme*, pages 1–61. Hydraulics Laboratory, KU Leuven, 1995.

Krishnappan B. G. Cohesive sediment transport studies using a rotating circular flume. In *The 7th Int. Conf. on Hydroscience and Engineering (ICHE), Sep 10–13, Philadelphia, USA*, number 9, 2006.

Kynch G. A theory of sedimentation. *Transactions of the Faraday society*, 48:166–176, 1952.

Lovato S., Kirichek A., Toxopeus S., Settels J. and Keetels G. Validation of the resistance of a plate moving through mud: Cfd modelling and towing tank experiments. *Ocean Engineering*, 258, 2022. doi: 10.1016/j.oceaneng.2022.111632.

Maggi F. *Flocculation dynamics of cohesive sediment*. PhD thesis, Delft University of Technology, Delft, The Netherlands, 2005.

Mastersizer 2000 User Manual - MANO384 issue 1.0. Malvern Instruments Ltd, 2007.

Manning A. J. The observed effects of turbulence on estuarine flocculation. *Journal of Coastal Research*, SI 41:90–104, 12 2004.

Mehta A. J. Chapter 4: Flocculation and floc properties. In *An introduction to hydraulics of fine sediment transport*, pages 144–231, 2014.

Merckelbach L. *Consolidation and strength evolution of soft mud layers*. PhD thesis, Delft University of Technology, Delft, The Netherlands, 2000.

Meshkati Shahmirzadi M. E., Staelens P., Claeys S., Cattrysse H., Van Hoestenberghe T., Van Oyen T., Vanlede J., Verwaest T. and Mostaert F. Experimental investigation on consolidation behaviour of mud: Subreport 1- methodology study. In *Versie 5.0. WL Rapporten, 12_082*, pages 1–26. Waterbouwkundig Laboratorium, Antwerp, Belgium, 2015.

Michaels A. S. and Bolger J. C. Settling rates and sediment volumes of flocculated kaolin suspensions. *Industrial & Engineering Chemistry Fundamentals*, 1(1):24–33, 1962. doi: 10.1021/i160001a004.

Peirce T. J. and Williams D. J. Experiments on certain aspects of sedimentation of estuarine muds. *Proceedings of the Institution of Civil Engineers*, 34(3):391–402, 1966. doi: 10.1680/iicep.1966.8930.

Serra T. and Casamitjana X. Structure of the aggregates during the process of aggregation and breakup under a shear flow. *Journal of colloid and interface science*, 206(2):505–511, 1998. doi: 10.1006/jcis.1998.5714.

Sotelo M., Boucetta D., Doddugollu P., Toorman E., Brouwers B., Delefortrie G. and Van Hoydonck W. Experimental study of a cylinder towed through natural mud. In *Proceedings of the 6th MASHCON International Conference on Ship Manoeuvring in Shallow and Confined Water*, pages 222–231, Glasgow, UK, 22–26 May 2022.

Toorman E. Sedimentation and self-weight consolidation: constitutive equations and numerical modelling. *Géotechnique*, 49(6):709–726, 1999. doi: 10.1680/geot.1999.49.6.709.

Toorman E. and Leurer K. An improved data-processing method for consolidation column experiments. In *Report HYD/ET/00/COSINUS8, Hydraulics Laboratory, K.U.Leuven*, page 14, 2000.

Toorman E. A. *Chapter 6: Numerical model for settling and consolidation, in Modelling of fluid mud flow and consolidation*. PhD thesis, KU Leuven, de Croylaan 2, 3001 Leuven, Belgium, 1992a.

Toorman E. A. Het mechanisch gedrag van slib in estuaria (the mechanical behaviour of estuarine mud). *Water: Tijdschrift over Waterproblematiek*, 27(66):159–167, 1992b.

Toorman E. A. Sedimentation and self-weight consolidation: General unifying theory. *Géotechnique*, 46(1):103–113, 1996. doi: 10.1680/geot.1996.46.1.103.

Toorman E. A. and Berlamont E. Settling and consolidation of mixtures of cohesive and non-cohesive sediments. In *Proceedings of the First International Conference on Hydro-Science and - Engineering*, pages 606–613, 1993.

Torfs H., Mitchener H., Huysentruyt H. and Toorman E. Settling and consolidation of mud/sand mixtures. *Coastal Engineering*, 29(1–2):27–45, 1996. doi: 10.1016/S0378-3839(96)00013-0.

van Ledden M. *Sand-mud segregation in estuaries and tidal basins*. PhD thesis, Delft University of Technology, Delft, The Netherlands, 2003.

van Leussen W. *Estuarine macroflocs and their role in fine-grained sediment transport*. PhD thesis, Utrecht University, Utrecht, The Netherlands, 1994.

van Rijn L. and Barth R. Settling and consolidation of soft mud–sand layers. *Journal of Waterway, Port, Coastal, and Ocean Engineering*, 145(1), 2019. doi: 10.1061/(ASCE)WW.1943-5460.0000483.

Winterwerp J., Kuijper C., de Wit P., Huysentruyt H., Berlamont J., Toorman E., Ockenden M. and Kranenburg C. On the methodology and accuracy of measuring physico-chemical properties to characteize cohesive sediments. In *Report of*

the MAST-1 G6-M Cohesive Sediment Project Group to the Commission of the European Communities, Directorate General XII., pages 1–60, 1993.

Winterwerp J. C. and Van Kesteren W. G. M. Introduction to the physics of cohesive sediment dynamics in the marine environment. In van Loon T., editor, *Developments in Sedimentology Series no. 56*, page 466. Elsevier, Amsterdam, The Netherlands, 2004.

Yu M., Yu X., Balachandar S. and Manning A. J. Floc size distributions of cohesive sediment in homogeneous isotropic turbulence. *Frontiers in Earth Science*, 10, 2022. doi: 10.3389/feart.2022.815652.

Chapter 3

Non-intrusive diagnostics of mud flow

This chapter first identifies techniques that show the most potential to visualise flow dynamics in mud layers. Considering the specific requirements of whole-flow-field velocimetry techniques and the intended application in physical experiments (see Section 1.1.2), their potential is further evaluated through theoretical assessments and complementary small-scale experiments. Also in this part of the study, the primary focus is on the application for laboratory purposes. If the eventually selected technique also proves to be applicable on site, this will logically be an added value.

3.1 Potential visualisation techniques

Given the opacity of human tissue and the preferred avoidance of probing, medical diagnostic techniques have have been developed to overcome similar issues as for experimental research using fluid mud (Section 1.1.3). Therefore, visualisation techniques used in medicine, such as radiography, magnetic resonance imaging (MRI), ultrasonography and nuclear imaging, all have the potential to be used in mud. Considering

cost and applicability in a typical experimental hydraulic setup, radiography and ultrasonography offer the most potential. The main difference between both techniques concerns the propagation path of the applied energy through the mud layer (see Fig. 3.1 (A) and Fig. 3.1 (B)), which is further elaborated in the following subsection.

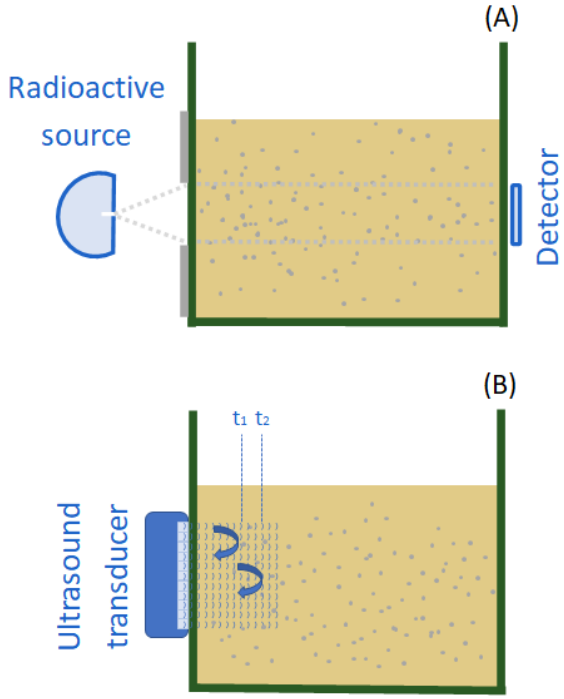

Figure 3.1: *(A) Sketch of radiography setup. Radioactive source and detector are positioned opposite to each other with the mud layer between the two. Hence full penetration of the mud layer is required; (B) Sketch of ultrasonography setup. The ultrasound transducer is positioned on one side of the mud layer and acts as both a transmitter and a receiver. As illustrated by the arrows at different timestamps (t_1 and t_2) along its path, the emitted radiation is reflected or scattered (partially) back to the transducer.*

3.1.1 Implementation in experimental setups

Visualisation with radiography is based on a difference in absorption of the radiation. When particles in the fluid absorb more radiation compared to the surrounding fluid, they will appear as shadows on the image. As a consequence, full propagation of the radiation through the mud layer is required. Visualisation using ultrasonography is based on the difference in acoustic impedance of particles compared to that of the fluid. When encountering a change in acoustic impedance the transmitted ultrasound waves will be reflected by the insonified particles. These reflection signals are recorded by the transducer and displayed as a function of pixel brightness on the images. The stronger the echo signal the brighter the reflecting particle will appear on the image. Hence, full penetration of the mud layer is not required, which allows for limitation of the propagation path of the waves and consequently loss of intensity. An initial more detailed evaluation of these two possible techniques involves determining the attenuation of the transmitted energy by mud. The physics of attenuation for both can be expressed with the Beer-Lambert law (Eq. 3.1, Beer (1854)). It shows that a medium attenuates the incoming radiation as a function of the attenuation coefficient and the distance over which the radiation propagates through the medium. The loss of radiation intensity due to attenuation is expressed by the transmission ratio (T), which is the ratio of the intensity of outgoing radiation (I_d) to that of the incomming radiation (I_{in}). The determination of the transmission ratio allows to assess whether or not the radiation intensity emitted by available radiation sources are sufficient. Therefore, the attenuation coefficient of the mud and the required minimum intensity of the outgoing radiation must be determined.

$$T = \frac{I_d}{I_{\text{in}}} = e^{(-\mu.d)} \tag{3.1}$$

Where T is the transmission ratio [-], I_{in} is the incoming radiation intensity [W·m^{-2}], I_d is the radiation intensity after propagation over a distance d through the medium [W·m^{-2}], μ is the attenuation coefficient of the radiated medium [m^{-1}] and d the distance over which the radiation propagates through the medium [m].

The attenuation coefficient is however different for each type of radiation. In case of electromagnetic waves, the attenuation coefficients of media are more or less stable and can therefore be retrieved from extensive databases as a function of the energy level (photon energy, E_p). Attenuation coefficients for ultrasound are less clear-cut. As mentioned by Ginzel and Turnbull (2016), the values of attenuation coefficients can already vary due to variations in material processing. Consequently, values of ultrasound attenuation coefficients of materials in the literature are sparse and if they are available, they should be used with caution.

3.1.2 Minimal required resolution

An additional requirement for the ultimately envisaged velocimetry technique is the resolution of the output. Typically, a whole-flow-field velocimetry technique generates a field of vectors covering the monitored cross-section. The spacing between these vectors must be sufficiently small (i.e. the resolution must be sufficiently high) to be of use for validation of a CFD model. For example, the purpose of the nautical CFD models referred to in this research (Vanlede et al., 2014; Delefortrie and Vantorre, 2016; Sotelo et al., 2022, 2023) is to study the interaction between a passing ship, the water layer and the underlying mud layer (see Section 1.1.2). To this end, the output of the envisaged velocimetry technique should be

able to visualise relevant vortex patterns (eddies). The minimal size of such an eddy depends on the subject of interest. For nautical research, like Sotelo et al. (2022, 2023), these are the forces acting between the towed body, the water and the mud layer. Therefore, it is reasonable to assume that the smallest eddy sizes to be visualised can be limited to the eddies within the energy-containing range. This is specified as the range of length scales between the integral length scale and the Taylor microscale (Hjertager, 2014). Since the Taylor microscale is the smaller of the two, the intended resolution of the output should be able to visualise eddies of this scale. The relation between the two scales is provided by Eq. 3.2 (Tennekes and Lumley, 1972).

$$\frac{l_\lambda}{l_0} = \sqrt{15} \cdot Re_0^{-\frac{1}{2}} \tag{3.2}$$

with,

$$Re_0 = \frac{v_0 \cdot l_0}{\nu} \tag{3.3}$$

Where, l_λ is the Taylor length scale [m], l_0 is the integral length scale [m], Re_0 is the turbulence Reynolds number corresponding the integral length scale [-], v_0 is the integral velocity scale [m·s^{-1}] and ν the kinematic viscosity of the fluid [m^2·s^{-1}].

According to Pope (2000), the integral length scale for a turbulent flow can be estimated to be about 10 % of the width of the flow. For the reference setup of Sotelo et al. (2022), the width of the flow is equal to the length of the cylinder, i.e. 0.55 m. Similarly, 10 % of the mean velocity is considered a good estimate for the integral velocity scale (v_0) (Pope, 2000). Based on the flow mechanics around a cylinder (Anderson, 1991), the mean flow velocity can be considered equal to the towing velocity of the cylinder. Sotelo et al. (2022) also conducted rheological measurements on samples

of Zeebrugge mud obtained from his test setup. This provided an average dynamic viscosity of 0.01228 Pa·s and an average density of 1.1588 g· cm^{-3}, yielding an average kinematic viscosity of about 10.6 ·10^{-6} m^2·s^{-1} (i.e. ten times that of water). A rule of thumb for an initial estimate of kinematic viscosity was provided earlier by Berlamont et al. (1993). Here, the kinematic viscosity is of the order of 0.003 Pa·s for a concentration of 100 g·l^{-1} and roughly doubles for every additional 100 g·l^{-1}. For a density of 1.16 g· cm^{-3}, this leads to a kinematic viscosity of 0.0079 Pa·s. Thus, in this case, the rule of thumb of Berlamont et al. (1993) leads to an underestimate, which emphasises the recommendation to conduct measurements for each type of mud, if possible.

The classification of mud as a non-Newtonian fluid means that its viscosity depends on the applied shear rate and therefore varies when flowing. Eq. 3.3, however, applies to Newtonian fluids. The use of this equation is thus a simplification of reality, similar to the development of the initial CFD models to simulate the behaviour of mud (see Section 1.1.2). In this case, this simplification seems less profound because the non-Newtonian effects only occur when gelling and consolidation effects are to be considered (Winterwerp, 1999).

This is not the case for flowing mud as the initial shear strength of consolidated mud is then already overcome. The Worrall-Tuliani rheological model (Worral and Tuliani, 1964) was proposed by Toorman (1994) to represent laminar flows of cohesive sediment suspensions. This model implies that as from mud flow, a constant differential viscosity (referred to as the Bingham viscosity) starts to apply, which remains applicable even at higher shear rates. This viscosity corresponds to the kinematic viscosity determined by Sotelo et al. (2022), which can thus be considered for the aforementioned simplification.

Basically, an eddy can be defined as a region of rotating flow. Thus, by selecting the minimum number of vectors deemed necessary to characterise an eddy, the maximum flow velocity (integral velocity scale), can be expressed as a function of vector spacing. For example, assuming a four-by-four vector grid to characterise a Taylor-scale eddy, Fig. 3.2 shows this relationship for multiple flow widths (integral length scales) for mud with a kinematic viscosity of $10.6{\cdot}10^{-6}$ $m^2{\cdot}s^{-1}$, like the Zeebrugge mud used by Sotelo et al. (2022). For the setup of Sotelo et al. (2022) with a flow width of 0.55 m, Fig. 3.2 shows that with a vector spacing of 2 mm, Taylor-scale eddies can be observed if the mean flow velocity, hence the towing velocity, is limited to approximately 1.25 $m{\cdot}s^{-1}$.

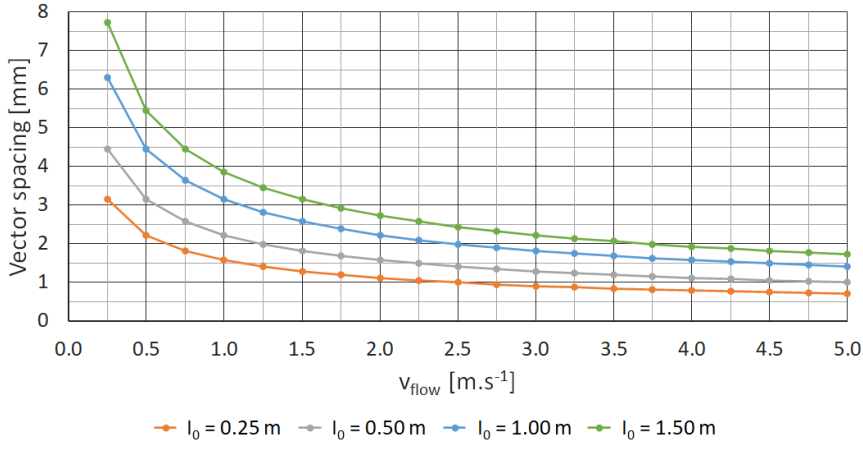

Figure 3.2: *Multiple plots for different flow widths (integral length scale) illustrating the relation between the required resolution (vector spacing) and the maximum mud flow velocity (v_{flow}), to enable monitoring of Taylor-scale eddies acting in the induced mud flow. The curves are determined using Eq. 3.2 and Eq.3.3. A four-by-four vector grid is considered adequate to characterise an eddy.*

The envisaged visualisation technique should thus eventually result in images that can be used to produce vector fields

of such resolution. This in turn means that the density of traceable parts on the images must be sufficiently high to allow for this. This requirement should be considered when assessing the suitability of a visualisation technique.

3.2 Radiography

Because radiography requires radiation to propagate throughout the mud layer (Fig. 3.1 (A)), further assessment of radiography will mainly focus on the amount of radiation able to do so. First the total loss in radiation energy caused by the setup and the mud layer will be estimated allowing the assessment of various radiation sources differing in emitted energy levels and amount of radiation.

When a point source is used, which is common for radiography, one should take into account that the size of particles will be magnified on the image depending on the distances between the source, particle and detector (Fig. 3.3). Magnification however needs to be limited to preserve the quality of the images and to avoid particles getting overshadowed by particles in front. The magnification limit is determined by the distance between source and particle (d_1) and the distance between particle and detector (d_2). While the latter is fixed as the thickness of the mud layer, the chosen magnification limit will determine the distance d_1.

As the magnification factor M [-] is inversely proportional to the distance between the radiation source and the mud particle d_1 [m] (Fig. 3.3), limitation of the magnification factor will lead to an increase of d_1. While on the other hand d_1 should be kept to a minimum to limit energy loss, as the irradiance degrades by the distance squared (Eq. 3.4).

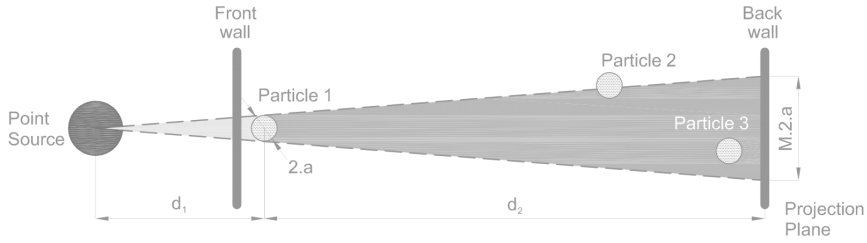

Figure 3.3: *Principle sketch of the magnification of a projection by using a point source. The sketch shows the projection of a particle of size 2· a, with a being the radius of the particle, present at the irradiated side of the flume (Particle 1), onto the projection plane of the detector at the opposite side of the flume. The size of the projection increases towards the projection plane. Ultimately, the projection is a factor M larger than the original particle size. This magnification factor M is determined by the distance between the point source and the particle (d_1), and the distance between the particle and the projection plane (d_2). Because of the magnification of the projection of Particle 1, background particles such as particles 2 and 3 are overshadowed, making them no longer or only partially visible on the projection.*

$$D_{\text{rate}} \propto \frac{A}{d^2} \tag{3.4}$$

Where D_{rate} is the dose rate [Gy], d the distance from the radiation source [m] and A is the activity of the radiation source [Bq].

For this evaluation the mud layer thickness is set to 0.55 m, corresponding to the flume used by Sotelo et al. (2022), present at FH. Based on a distance between the source and the irradiated object of 1 m, which is common in radiography, the magnification factor for the particles at the front is limited to 1.56, which is considered acceptable.

To create adequate images for diagnostic use, a minimal dose rate absorbed by the detector is required. Although

probably on the conservative side, the minimal dose rate for medical diagnostic imaging is used for this evaluation. Medical applications are always subject to the ALARA principle, which is an acronym for "As Low As Reasonably Achievable". Hence it is an indication of the minimum dose rate required to create images of sufficient quality for diagnostic use. Recommendations on minimal dose rates for multiple medical applications are presented in IEC62220-1-3 (2008). Although the application on mud is not directly bound by a maximum dose rate, estimations show that these minimum dose rates are already hard to achieve for the intended ranges of flow speed and mud layer thickness. Therefore the highest dose rate recommended for medical applications of 2 µGy per frame is used for the continuation of this assessment.

Knowing the required dose rate at the detector and the loss in intensity due to attenuation by the mud, the required initial intensity emitted by the source can be calculated. The loss in intensity is caused by the attenuation capacity of mud, which comprises both absorption and scattering of the incoming radiation. At higher energy levels, such as for X- and gamma radiation, intensity loss due to scattering becomes more significant and therefore cannot be neglected. If the attenuation coefficient of the radiated medium is known, the loss in intensity due to propagation through it can be calculated using the Beer-Lambert law, presented earlier as Eq. 3.1.

3.2.1 Attenuation of electromagnetic waves by mud

The attenuation coefficient of common materials or mixtures can be found in the literature. This is usually published by the mass attenuation, which is defined as:

$$\mu_{mass} = \frac{\mu}{\rho} \tag{3.5}$$

Where μ_{mass} is the mass attenuation of the radiated medium [$cm^2 \cdot g^{-1}$], μ is the attenuation coefficient of the radiated

medium [cm^{-1}] and ρ is the density of the radiated medium [$g{\cdot}cm^{-3}$]. Using the mass attenuation allows to express the attenuation as a function of density, which is convenient for media with changing density in time, like mud.

For this research the mass attenuation coefficients of the freely accessible database of the National Institute of Standards and Technology (NIST) are used (Berger et al., 2010). The NIST database contains a collection of published values of mass attenuation of chemical elements, compounds and common mixtures as a function of the energy level of the radiation, expressed in [MeV]. Unfortunately, the composition of mud varies according to its origin (port, river, area, etc.) and thus cannot be generalised. Therefore, the attenuation coefficient of each mud with different composition should be calculated. This can be done according to the method described in Ripan et al. (2016), using the values of mass attenuation of each compound (oxide) present in the mud in accordance with their weight fractions.

By means of a chemical element analysis using the Inductive Coupled Plasma – Optical Emission Spectrometry technique (ICP—OES, Wang (2004)), the different compounds present in Zeebrugge mud were first determined together with their weight fractions for three mud densities: 1.035 $g{\cdot}cm^{-3}$, 1.100 $g{\cdot}cm^{-3}$ and 1.200 $g{\cdot}cm^{-3}$ (Table 3.1).

The mass attenuation values of these compounds can be found in the NIST database. With these values, the mass attenuation of the mud mixture can be calculated using the so-called ”mixture rule”, presented in Burcu and Salih (2014) and shown as Eq. 3.6. Curves of the resulting values for mass attenuation coefficients are plotted as a function of photon energy for the three mentioned mud densities in Fig. 3.4.

$$\left(\frac{\mu}{\rho}\right)_{\text{mix}} = \sum_{i=1}^{N} \omega_i . \left(\frac{\mu}{\rho}\right)_i \tag{3.6}$$

Where μ is the attenuation coefficient [cm^{-1}], ρ is the density [$g{\cdot}cm^{-3}$], ω is the weight fraction [$\%$] and i is the reference to the elements in the mixture.

Table 3.1: *Weight fractions [$\%$] of the compounds present in Zeebrugge mud arranged by mud density.*

Weight fraction [$\%$]			
Compound	Density [$g{\cdot}cm^{-3}$]		
	1.035	1.100	1.200
Al_2O_3	4.01	7.84	8.25
CaO	7.43	13.37	13.99
Fe_2O_3	1.96	3.64	3.90
K_2O	1.22	1.45	1.44
MgO	3.58	2.27	2.08
MnO	0.05	0.08	0.08
Na_2O	17.32	5.54	3.82
P_2O_5	0.13	0.23	0.23
SiO_2	17.03	36.02	37.99
TiO_2	0.24	0.47	0.50
H_2O	49.3	29.68	27.08

All three curves plotted in Fig. 3.4 practically overlap. This shows that the attenuation of mud is hardly affected by its density, which is consistent with observations during settling experiments conducted at FH, presented in Meshkati Shahmirzadi et al. (2015) and Pirola Igoa et al. (2020). The setup of these experiments is depicted as Fig. 3.5. To accentuate the water-mud interface bright light panels were installed behind the settling columns. The picture was taken while the set-

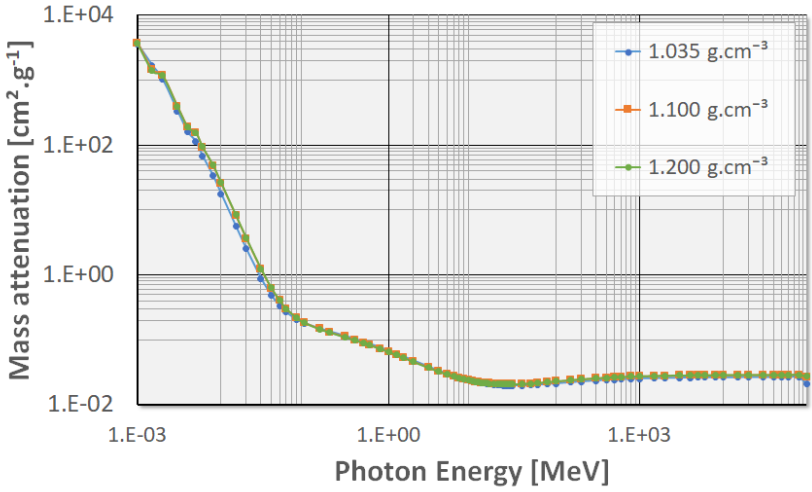

Figure 3.4: *Mass attenuation coefficient as a function of E_p for multiple mud densities. Calculations are made using (Eq. 3.6), based on the weight fractions presented in Table 3.1 and mass attenuation coefficients found in the NIST database (Berger et al., 2010) for each of the compounds present in mud.*

tling experiments were ongoing, which means that the density of the mud columns are no longer uniform, but increase with depth. The picture shows that despite such density profiles, no corresponding transition from light to dark can be seen with the depth of the mud column. Furthermore, the water-mud interfaces are always unambiguously clear. These observations indicate the uniform opacity of mud regardless of mud density. Calculating the transmission coefficients as a function of radiation energy level, using the Beer-Lambert law (Eq. 3.1), confirms the opacity of mud for optical light (Fig. 3.6). From the results it can be seen that even for mud layers of 1 mm thickness, a transmission ratio of minimal significance will be obtained with at least E_p levels of 10 keV. This corresponds with low energetic X-rays which are still far more energetic compared to optical light (2 eV to 3 eV). Further focus is therefore

on the use of high energy electromagnetic waves such as X-rays and gamma rays.

Figure 3.5: *Setup of mud settling experiments performed at FH. Bright light panels illuminate the columns from behind, accentuating the water-mud interface. (1) Initial mud level; (2) settled water-mud interface; (3) mud column.*

3.2.1.1 Gamma rays

The electromagnetic spectrum shows that gamma rays have a higher energy level and therefore have a greater penetration

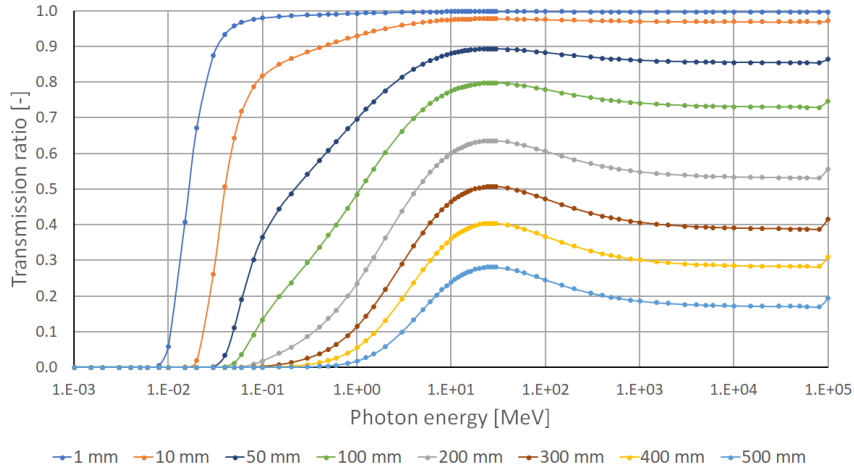

Figure 3.6: *Transmission ratios calculated using Eq. 3.1 and attenuation coefficients presented in Fig. 3.4 (mud density 1.10 g·cm^{-3}) and mud layer thickness ranging from 1 mm to 560 mm in a setup as depicted in Fig. 3.1 (A).*

capacity compared to X-rays. Hence it is reasonable to assume that with the use of gamma rays greater radiation doses are absorbed by the detector after full transmission through the mud layer.

Gamma rays are produced by radioactive nuclei, also referred to as radioisotopes. After a radioactive nucleus undergoes alpha or beta radiation, the nucleus is left in an ”excited” state. The nucleus then loses the excess energy by emitting gamma photons. As a consequence the radiation emitted by a gamma source is typically mono-energetic. A broad variety of gamma ray sources are available on the market for different usage ranging from medical use to use in industrial processes. Common isotopes for industrial use are ^{60}Co and ^{137}Cs. Specifications of sources available on the market with these isotopes can be found in Table 3.2.

Table 3.2: *Overview of the properties of high activity gamma ray sources available on the market (VEGA Americas, 2017).*

Isotope	Photon Energy [keV]	Gamma constant (Γ) [(R·m^2)·(hr·Ci)$^{-1}$]	Activity [GBq]
^{60}Co	1250	1.2987	3.7
^{137}Cs	662	0.3224	185

Knowing the properties of the gamma source together with the attenuation coefficient of mud (corresponding to the E_p of the isotope) and the chosen magnification limit, the expected dose rate at the detector can be calculated as stipulated in Cember and Johnson (2008) or using the freeware Rad Pro Calculator McGinnis (2020). With this dose rate, the time required to obtain the minimum required dose at the detector (see Section 3.2) can be determined per frame. Subsequently, this can be used to assess the maximum recordable flow rate, as a function of the thickness of the mud layer. By defining a particle displacement limit between two consecutive frames, the maximum flow velocity can be deduced for varying mud layer thickness. For a ^{137}Cs – 185 GBq source such results are presented in Fig. 3.7. A flowchart summarising the complete calculation procedure is presented as Fig. 3.8.

The results shown in Fig. 3.7 lead to the conclusion that with flow velocities up to 2 m·s^{-1}, the required dose rates at the detector can only be achieved for very thin mud layers of 1 mm to 2 mm, which are mostly irrelevant for fluid dynamics applications. Despite the higher energy level, hence penetration capacity, the results with the ^{60}Co radiation source (Table 3.2) are even worse due to the lower activity of the source. This illustrates the importance of the activity of the source over the emitted E_p level, making the use of X-rays more appropriate since activity rates of X-ray sources are much larger compared to the those of gamma ray sources.

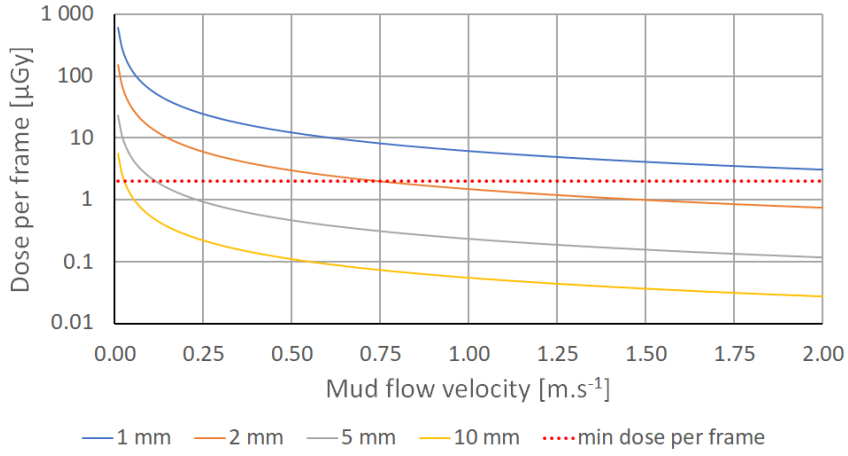

Figure 3.7: *Radiation dose, originating from a ^{137}Cs - 185 GBq source, received by the detector, in a setup as presented in Fig. 3.1 (A), during the time span allowed for per image frame. The time span is expressed as mud flow velocity, where a maximum mud particle displacement of 5 mm is allowed for between two consecutive frames. Increasing mud flow velocity decreases the radiation time span for each image frame, hence the dose received per image frame. Curves for different mud layer thicknesses varying from 1 mm to 10 mm are presented. The dotted red line indicates the minimum dose required per image frame for diagnostic image quality.*

3.2.1.2 X-rays

X-rays can be produced using an electric device like an X-ray tube. When electrical current is applied to it, X-rays are generated. While radiation from radioisotopes is mono-energetic, X-ray generators generate a spectrum of E_p. Because the attenuation coefficient of a medium depends on the energy level of the incoming radiation, the calculation of the transmission ratio of the radiation produced by an X-ray generator needs to be integrated over the fully generated energy spectrum. This makes the calculation of dose rates complex and requires the use of specially developed software.

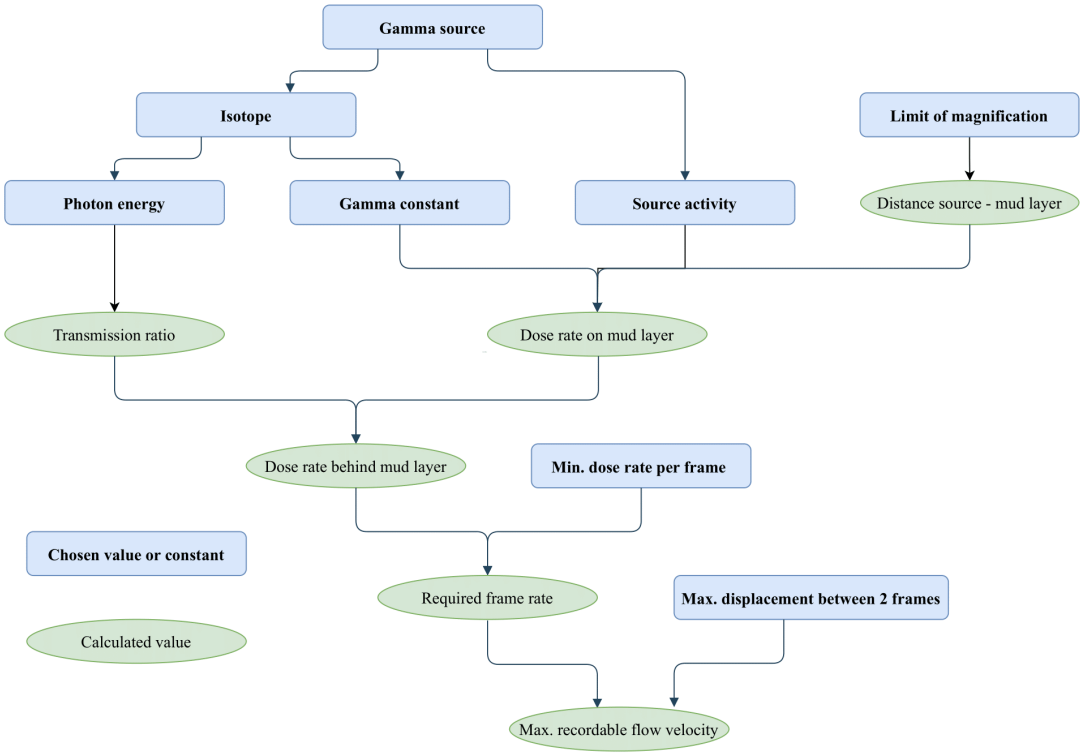

Figure 3.8: *Flowchart for calculating the maximum flow velocity while allowing sufficient radiation dose per frame using a gamma ray source.*

For this research, the ”SpekCalc” software is used which is developed as a tool for medical research and educational applications (Poludniowski and Evans, 2007; Poludniowski, 2007; Poludniowski et al., 2009).

Based on the voltage range of the X-ray source, the source angle and the distance between the X-ray source and the radiated object or patient, SpekCalc calculates the generated X-ray spectrum of the source and the dose rate received by the radiated object or patient. In medical practices a filter is placed between the source and the patient. A well chosen filter (thickness and material) filters out the part of the generated E_p spectrum which is not of interest or use. This prevents useless low-energy radiation from reaching the patient (ALARA principle). Therefore, a filter can also be taken into account in the SpekCalc software. The list of materials which can be chosen as filters is limited to a number of commonly used materials for X-ray filters, such as Be, Al, Cu, Sn, W, Ta, H_20, Ti and C. A combination of different filter materials is possible and the filter thickness is unrestricted.

The setup when applied in a hydraulic test facility with a source, mud layer and a detector (see Fig. 3.1 (A)) is similar to the setup of a medical application with a source, filter and the patient. The detector at the back of the flume acts as the patient while the mud layer acts as the filter. With SpekCalc the radiation reaching the patient, or in this case detector, can be calculated while taking into account the attenuation due to the filter, in this case the mud layer. If SpekCalc is therefore used to estimate the dose rate behind the mud layer, the filter should be replaced by the mud layer. SpekCalc’s ability to set an arbitrary filter thickness allows to simulate the filter capacity of the mud layer. For any standard filter material available in the SpekCalc software, a thickness can be found such that it has the same attenuation value as the mud layer over a part of the energy spectrum. When selecting aluminium as filter material, the ratio of attenuation of the aluminium filter over

the attenuation of mud with density 1.20 g·cm^{-3} is more or less constant over the entire energy spectrum of interest (see Table 3.3). It can therefore be concluded that, with regards to the attenuation of X-rays over a E_p spectrum of 10 to 400 keV, an aluminium filter with thickness of 26.69 cm is the equivalent of a 56 cm mud layer.

It must be noted that the convenience of a constant ratio over a wide energy spectrum as presented in Table 3.3 does not hold true for all filter materials. Other filter materials only show a more or less constant ratio over a limited part of the spectrum. Copper for instance shows a more or less constant ratio over a limited spectrum from 10 keV to 40 keV, while for Beryllium this is from 150 keV to 400 keV. In case no constant ratio can be found over the entire energy spectrum of interest, the spectrum needs to be split in parts. For each part of the spectrum a different equivalent filter material is then to be applied.

SpekCalc was originally developed for educational purposes, but meanwhile used in the medical community for first estimations of the expected dose rate. It is mostly referred to as "a commonly used analytical approximation" (Forth et al., 2017) and compared frequently in literature with other more advanced (Monte Carlo) code and/or measurements like in Poludniowski et al. (2009) and Forth et al. (2017). SpekCalc can therefore be considered as a reliable tool for first estimations of the dose rate. In Forth et al. (2017) an overestimation of 10 % and underestimation up to 20 % by SpekCalc compared to other simulations and validation measurements is mentioned.

Table 3.3: *Overview of the required thickness of an aluminium filter ($t_{w,\text{Al, filter}}$) for equivalent attenuation of X-rays as a 56 cm thick mud layer ($t_{w,\text{mud}}$) with density 1.20 g·cm^{-3}, as a function of E_p. The calculated mass attenuation values of mud, as presented in Fig. 3.4 were used to determine the attenuation values of the mud layer ($\mu_{\text{mud}} \cdot t_{w,\text{mud}}$). The mass attenuation values of aluminium were taken from the NIST database (Berger et al., 2010). By dividing the total attenuation values of the mud layer by the attenuation coefficient of aluminium (μ_{Al}), the thickness of the aluminium filter for equivalent attenuation as the mud layer is obtained.*

	mud (ρ = 1.20 g·cm^{-3}) $t_{w,\text{mud}}$ = 56 cm		Aluminum (ρ = 2.70 g·cm^{-3})		
E_p [keV]	$\mu_{mass,\text{mud}}$ [cm^2·g^{-1}]	$\mu_{\text{mud}} \cdot t_{w,\text{mud}}$ [-]	$\mu_{mass,\text{Al}}$ [cm^2·g^{-1}]	μ_{Al} [cm^{-1}]	$t_{w,\text{Al filter}}$ [cm]
10	26,61	1.787,89	26,21	70,77	25,26
15	8,42	565,60	7,96	21,48	26,33
20	3,73	250,86	3,44	9,29	26,99
30	1,25	84,03	1,13	3,05	27,59
40	0,63	42,41	0,57	1,53	27,63
50	0,41	27,28	0,37	0,99	27,44
60	0,30	20,41	0,28	0,75	27,21
80	0,22	14,60	0,20	0,54	26,80
100	0,18	12,22	0,17	0,46	26,56
150	0,15	9,80	0,14	0,37	26,35
200	0,13	8,68	0,12	0,33	26,29
300	0,11	7,39	0,10	0,28	26,26
400	0,10	6,58	0,09	0,25	26,26
				Average	26,69

Nonetheless, a validation of the outcome of SpekCalc with actual measurements was also performed in this study, if only to verify the software is properly used and the output correctly interpreted. The measurements were performed using an X-ray source allowing a voltage up to 250 kV, fitted with a

beryllium window of 3 mm and a copper filter of 2 mm. The electric current applied on the tube was always 2 mA and the dose rates were measured at a distance of 2 m. Table 3.4 shows a comparison of these dose rates with the dose rates calculated with SpekCalc, indicating an underestimation of the calculated dose rates of 18 % to 19 %, similar to the conclusion of Forth et al. (2017).

Table 3.4: *Comparison of measured dose rates with calculated dose rates using SpekCalc software. Results show an underestimation of the calculated dose rate of 18 % - 19 %, which corresponds with the conclusions mentioned in Forth et al. (2017)*

Voltage	Dose rate (measured) at 2 m distance		Dose Rate (Calculated) at 2 m distance		Ratio
[kV]	[R·min^{-1}]	[µGy·s^{-1}]	[µGy·mA^{-1}·s^{-1}]	[µGy·s^{-1}]	[-]
180	173	25,29	10,39	20,79	0,82
190	209	30,55	12,47	24,94	0,82
200	248	36,25	14,76	29,51	0,81
210	290	42,39	17,25	34,51	0,81
220	337	49,26	19,97	39,95	0,81
230	387	56,57	22,91	45,82	0,81
240	440	64,31	26,09	52,18	0,81
250	500	73,08	29,47	58,95	0,81

The evaluation of the use of gamma sources showed the importance of sufficiently high source activity. Consequently, the more powerful X-ray generators are probably required for the intended application in mud. Further focus in this research is therefore on devices used in the Non-Destructive Testing (NDT) industry. After all, unlike medical devices, these are not limited in power. Initially an X-ray generator with a high voltage range of 5 kV - 225 kV and a maximum current of 30 mA is considered. A schematic overview of the calculation procedure is presented as Fig. 3.9 and the results in Fig. 3.10.

These results show that with the X-ray generator in question, flow velocities of 2 $m{\cdot}s^{-1}$ can be recorded in mud layers with a thickness of almost 200 mm. This is suffucient for application in rheometer tests and settling experiments, however still insufficient for most hydraulic experiments like the aforementioned towing experiments (see Section 1.1.2). The most powerful ”freely” available X-ray sources in the NDT industry have a voltage capacity up to 450 kV and a maximum current of 30 mA. Because of its medical background, SpekCalc is however limited to a maximum voltage of 300 kV. By means of interpolation expected results for X-ray generators exceeding 300 kV can still be estimated. Doing so for 450 kV generators set at 30 mA, shows they are up to 33 times more powerful compared to a generator with a voltage capacity of 225 kV. Yet even with this, the maximum mud layer thickness is limited to only 300 mm.

3.2.2 Particle Image Velocimetry (PIV) on radiographic images

Although radiography is deemed to be insufficient for the required mud thickness and flow velocities for experiments as perfomed by Lovato et al. (2022); Sotelo et al. (2022), for other applications, like settling experiments or rheology measurements (see Section 1.1.2), radiography may still be an option. To evaluate its potential use, an X-ray scan of a mud sample was conducted. The result of this scan is shown as Fig. 3.11. The image shows that without the addition of contrast agents (e.g. the air bubbles which can be seen on the image as black dots), an X-ray scan of mud results in a homogeneous greyscale image, unsuited for the application of tracking algorithms. The black dots, originating from entrapped air bubbles, do can be used to be tracked. The air bubbles are the result of unwanted disturbance of the sample prior to the scan. However, due to their upward movement air bubbles influence the consolidation process, hence the behaviour of

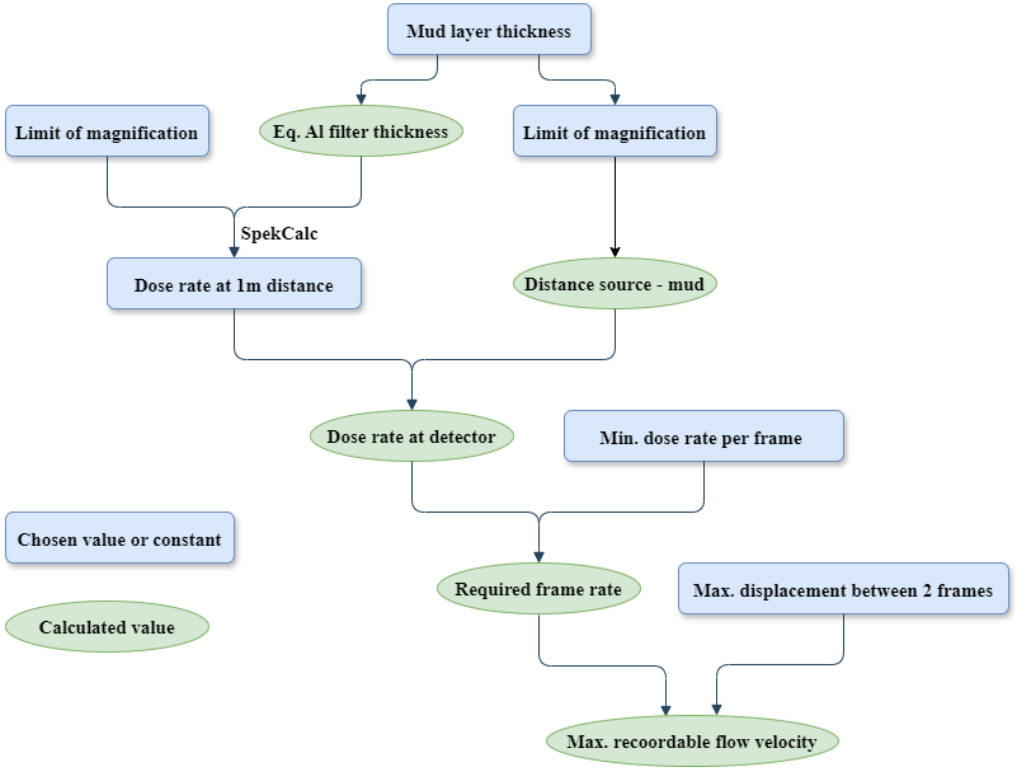

Figure 3.9: *Flowchart for calculation of the maximum flow velocity while allowing sufficient radiation dose per frame using an X-ray generator.*

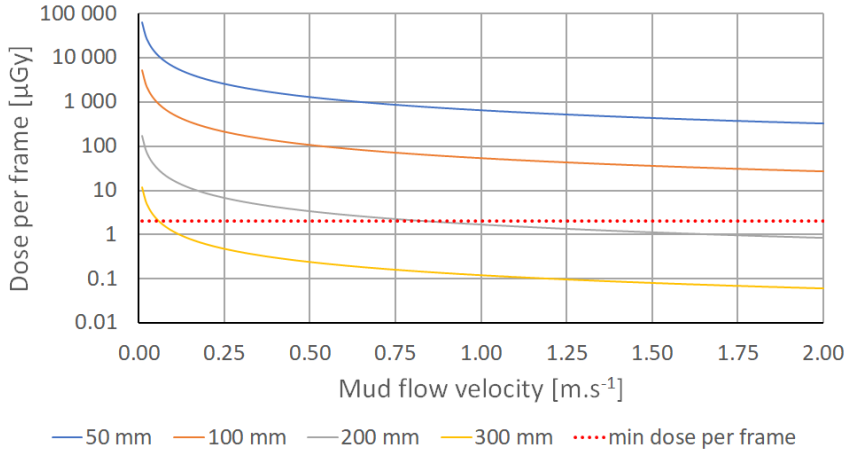

Figure 3.10: *Radiation dose, originating from an X-ray 225 kV - 30 mA generator at max power, received by the detector in a setup as shown in Fig. 3.1 (A)) during the time span allowed for per image frame. The time span is expressed as mud flow velocity, where a maximum mud particle displacement of 5 mm is allowed for between two consecutive frames. Increasing mud flow velocity decreases the radiation time span for each image frame, hence the dose received per image frame. Curves for different mud layer thicknesses varying from 50 mm to 300 mm are presented. The dotted red line indicates the minimum dose required per image frame for diagnostic image quality.*

mud. Therefore, when studying the dynamics in mud layer, the presence of air bubbles should be avoided. Thus, despite their suitability for tracking, the use of air bubbles cannot be considered in mud.

Seeding the mud with tracing particles like in a conventional experimental setup for PIV recording (Raffel et al., 2018) is also not preferred. Ideally the particles added to the fluid are neutrally buoyant, ensuring their movement is solely caused by the flows in the fluid. In case of mud the density changes over time, making it impossible to

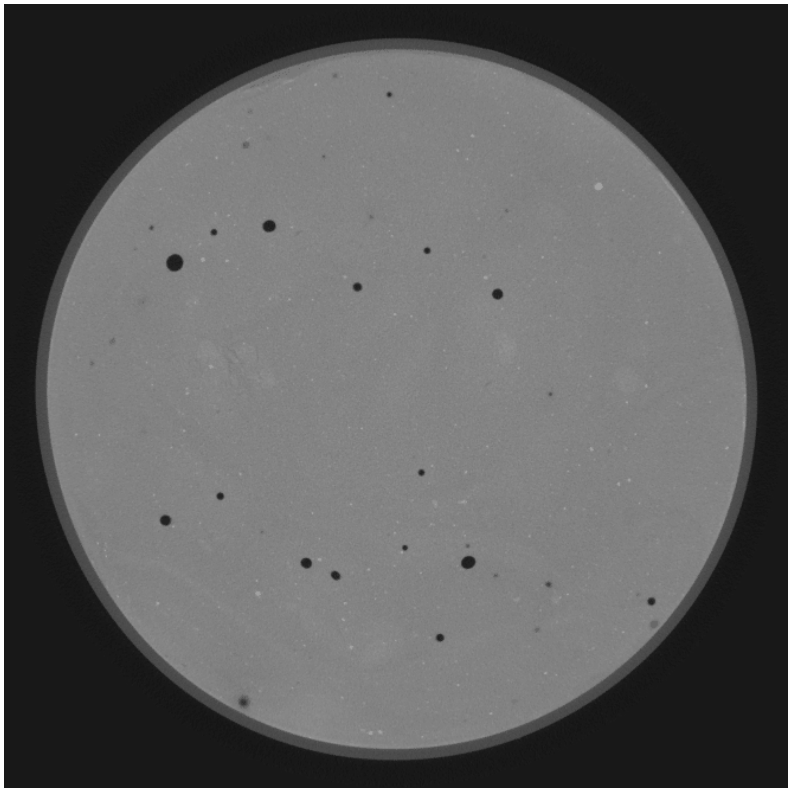

Figure 3.11: *X-ray scan of mud. Apart from the black spots, the greyscale image is homogeneous. The black spots originate from entrapped air bubbles after disturbance of the sample.*

guarantee this aspiration, and undermining the credibility of the measurements. Furthermore, Manning and Whitehouse (2009) has shown that a change in sand fraction present in mud, influences the flocculation and consolidation process of the mud. Because it is reasonable to assume that the presence of seeding particles will have a similar influence on the mud as sand particles, it can be questioned whether or not seeded mud is still representative. Especially also because the seeding concentration must be sufficient to

eventually meet the required vector field resolution (see Section 3.1.2). For applications where seeding with particles does not invalidate the study, PIV flow velocity measurements based on radiographic images can be considered as an option.

3.3 Ultrasonography

3.3.1 Fundamental physics of ultrasound

To assess the application of ultrasonography in mud, a brief outline of the basic physical principles of ultrasound is provided first. Sound consists of an alternating pattern of high and low pressure fields propagating through a medium. This is referred to as a sound (pressure) wave. In case of ultrasound, the frequency of the waves is above 20 kHz, i.e. above the audible range. While propagating through a medium, vibrations and mechanical stresses are induced. In case of a fluid, there is only an oscillatory movement of the fluid particles parallel to the direction of the sound wave (longitudinal waves), as illustrated in Fig. 3.12. In case of a solid, transverse shear waves also arise. Since mud possesses a yield strength (see Section 1.1.1), shear waves also develop in mud. In fact, Ma et al. (2022) links these shear waves to the geotechnical behaviour of mud. In medical diagnostic ultrasound, shear waves are not considered because of their low intensity (Swillens, 2010) and because this would require a change in setup using an additional transducer. For the same reasons, shear waves are also disregarded in this study.

While propagating through a medium, the intensity of the sound waves decreases. This is due to absorption and scattering of the sound waves by the particles of the medium, which is collectively referred to as attenuation. To assess to what depth images of sufficient quality can still be produced in mud, knowledge is needed about the rate at which sound waves are attenuated by mud.

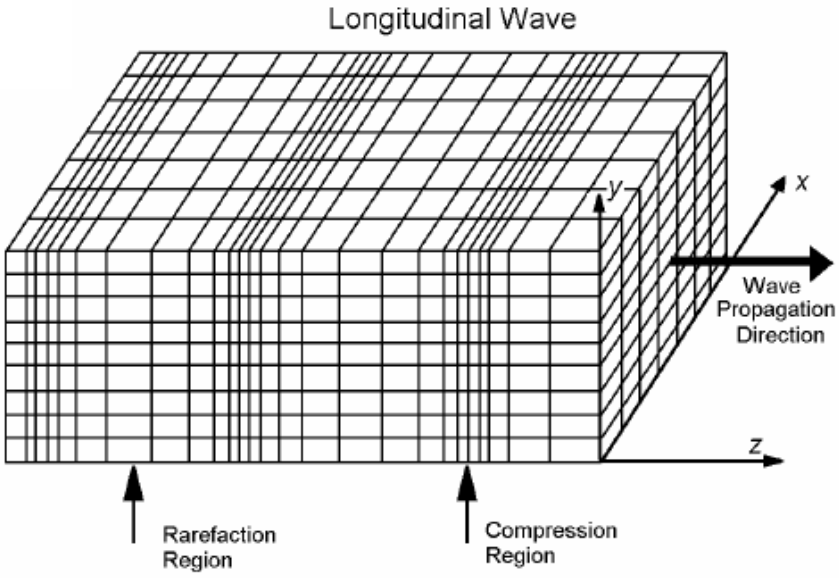

Figure 3.12: *A sketch illustrating the rarefaction and compression induced in a medium by sound waves. This figure is copied from Swillens (2010).*

A second important acoustic property of a medium is the speed at which sound propagates through it. This is determined by the density and the bulk modulus of the medium (Eq. 3.7). The latter is inversely proportional to the compressibility of the medium.

$$c_{\mathrm{i}} = \sqrt{\frac{K_{\mathrm{i}}}{\rho_{\mathrm{i}}}} \tag{3.7}$$

Where c is the speed of sound through a medium [m·s^{-1}], K the bulk modulus of the medium [Pa], ρ the density of the medium [kg·m^{-3}] and i the index referring to the medium.

The relevance of the speed of sound through a medium is twofold. Firstly, it is used to determine the distance of a reflector to the transducer. This is done based on the time

of flight of a signal. With knowledge of the propagating speed of the sound wave, this distance can be deduced from the time interval between transmission and receipt of the signal. Secondly, it is required to assess the acoustic impedance of a medium. This is the product of the speed of sound through, and the density of, the medium (Eq. 3.8). As mentioned in Section 3.1.1, the acoustic impedance dictates the magnitude of the reflected sound waves when a change in acoustic impedance is encountered. This is discussed further in Section 3.3.3 and applied for mud in Chapter 4.

$$Z_{\mathrm{i}} = c_{\mathrm{i}}.\rho_{\mathrm{i}} \tag{3.8}$$

Where Z is the acoustic impedance [kg·m^{-2}·s^{-1}], c is the speed of sound through the medium [m·s^{-1}], ρ is the density of the medium [kg·m^{-3}] and i the index referring to the medium.

Previous research on the acoustic properties of mud, like Pierce et al. (2015), however mention the lack of available and trustworthy data. Measurements to determine the acoustic properties of mud are therefore required to fully evaluate the potential of ultrasonography.

3.3.2 Ultrasound properties of mud

In the Port of Antwerp-Bruges (Belgium), a device called the Admodus USP pro (see Fig. 3.13), is used to measure the density of mud present in the docks (Claeys et al., 2012; Plancke et al., 2018). Through ultrasound reflection, it measures the acoustic impedance and speed of sound of the medium in which it is deployed. The density can be derived in accordance with

In addition, the Admodus USP pro also measures the attenuation of ultrasound by mud over a frequency spectrum of 1.0 MHz to 3.5 MHz. A more detailed desciption on how this is done can be found in Section 4.3.2. From the data

Figure 3.13: *Picture of the Admodus USP pro, copied from Schmidt (2016).*

of a survey campaign performed in February 2019 in the Zeebrugge docks of the Port of Antwerp-Bruges (Meire et al., 2021), these acoustic properties were retrieved as a function of mud density ranging from 1000 kg·m^{-3} to 1300 kg·m^{-3}. The speed of sound through mud shows small variation in this density range, from 1460 m·s^{-1} to 1485 m·s^{-1}. Consequently, so does the acoustic impedance, being the product of density and speed of sound (Eq. 3.8), ranging from 1500 kg·m^{-2}·s^{-1} to 1900 kg·m^{-2}·s^{-1}. The measured ultrasound attenuation values range over a wider spectrum as they are function of both mud density and ultrasound frequency, as shown in Fig. 3.14.

Despite the knowledge of these values of ultrasound attenuation and the speed of sound of mud, evaluation whether or not the use of ultrasound waves would allow for sufficient penetration and energy conservation to create images of adequate quality for the application of a velocimetry algorithm is still not possible. Like for all medical applications, an optimal compromise between penetration depth, field of view and the different types of resolution (axial, lateral and time) will need to be determined (Alexander and Swanevelder, 2011). Nonetheless, the fact that the speed of sound

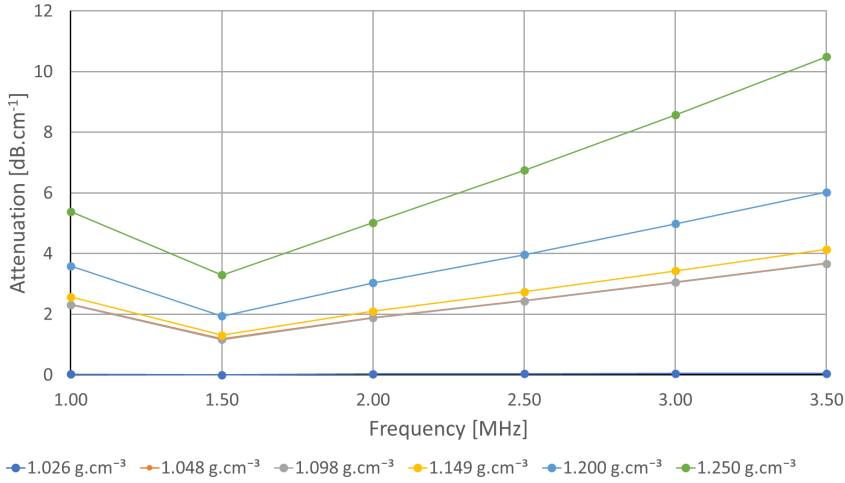

Figure 3.14: *Ultrasound attenuation values (α) of mud, as a function of ultrasound frequency and mud density. Values measured in the Zeebrugge docks, using the Admodus USP pro (Meire et al., 2021).*

and ultrasound attenuation of human tissue and organs as specified in Hendee and Ritenour (2002), are in the same order of magnitude as the aforementioned values for mud, gives confidence that such a compromise can be found within the limits of standard ultrasound medical equipment for depths similar to those for medical applications ranging from 50 mm to 150 mm.

3.3.3 Ultrasound brightness scan of mud

An ultrasound brightness scan, or B-mode scan, is the most familiar mode of ultrasound diagnostics for medical purposes. Probably the best known example is a fetal scan during a pregnancy (Fig. 3.15).

As mentioned in Section 3.1.1, ultrasound imaging is based on the reflection of previously emitted ultrasound. Transmitting

Figure 3.15: *Example of a fetal ultrasound brightness scan. The modelling foetus in the picture is my daughter, born on the 19th of September 2019.*

and receiving ultrasound is therefore usually done by one and the same transducer. The images are typically greyscale, where the brightness of a pixel is a measure for the amplitude of the reflected signal at the corresponding position in the insonified area. Therefore strong reflectors such as muscle tissue will appear bright, while fluids will appear dark. In order to see any distinction in an image created with a B-mode scan some variety in acoustic impedance, which causes reflection, is thus required. To evaluate whether or not mud complies with this requirement the results of the chemical element analysis (see Table 3.1) can be re-used, providing the different oxides present in mud. For some of these oxides, the acoustic impedance can be found in literature. While the strength of a reflected signal is determined by the reflection coefficient, the reflection coefficient in turn is related to the difference in acoustic impedance encountered during propagation (Eq. 3.9).

$$r_{ij} = \frac{Z_i - Z_j}{Z_i + Z_j} \tag{3.9}$$

Where r is the reflection coefficient [-], Z is the acoustic impedance [kg·m^{-2}·s^{-1}] and i and j are the indices referring to the encountered materials or media.

Acoustic properties found in literature should always be used carefully as such values are very variable contingent upon the origin of the medium (Ginzel and Turnbull, 2016). Nonetheless, they can be used as an indication to assess the probability of reflection. For example, the oxides Al_2O_3, SiO_2 and H_2O represent about 74 % of the weight percentage of Zeebrugge mud with a density 1.10 g·cm^{-3} (see Table 3.1). While their values of acoustic impedance found in literature vary widely, 37.9 kg·m^{-2}·s^{-1}, 13.2 kg·m^{-2}·s^{-1} and 1.5 kg·m^{-2}·s^{-1}, respectively (Capilla et al. (2012) and Sikorski (2019)). This indicates that significant reflections of ultrasound can be expected in Zeebrugge mud.

In wave physics there are different degrees of reflection depending on the ratio of the wavelength to the size of the reflecting object. This is expressed by the $k{\cdot}a$ ratio, where a is the radius of the scatterer [m] and k the wavenumber [m^{-1}], solely determined by the wavelength λ [m] (Eq. 3.10).

$$k = \frac{2{\cdot}\,\pi}{\lambda} \tag{3.10}$$

While specular reflections are created by reflection on large objects, objects equal or smaller in size than the wavelength of the incident sound wave, will scatter the sound wave omni-directionally. According to Szabo (2004), the scattering is diffusive if the ratio $k{\cdot}a$ is smaller than 0.35. From then on, the scattering becomes diffractive and tends further towards specular reflection with increasing $k{\cdot}a$ ratio.

When the concentration of isotropic scatterers is high, the amount of scattered signals is high, causing them to interfere with each other. Because in ultrasound imaging the transmission of ultrasound and the recording of returning signals are done by the same transducer, only the scattered signals returning to the transducer are of use. This scattering direction is referred to as backscattering. The recording of these superimposed backscattered signals results in the generation of so-called "speckle pattern images" (Poelma, 2016). In medical applications, this typically occurs when scanning muscle tissue.

Because of the similarities mentioned earlier, the frequency range for ultrasound imaging in mud is expected to be similar to that for medical imaging, ranging from 1 MHz to 10 MHz. With a speed of sound through mud of 1465 m·s^{-1} this results in wavelengths ranging from respectively 146 µm to 1465 µm. The particle size distribution of Zeebrugge mud shows a range of particle sizes between 0.3 µm and 120 µm (see Fig. 3.16).

When ultrasound imaging is applied to Zeebrugge mud, Fig. 3.17 shows the correlation between the size of the particles (potential scatterers) of the mud and the range of wavelengths of the ultrasound. The range of wavelengths corresponds to the aforementioned range of ultrasound frequencies for ultrasound imaging. Considering the threshold for diffusive scattering ($k{\cdot}a < 0.35$), diffuse scattering is likely to occur, ultimately resulting in speckle pattern images.

A small-scale test was performed at Ghent University Hospital, using a GE Vivid 7 ultrasound scanner equipped with a 10L linear array. For protection against the corrosive seawater present in mud, the array was inserted in a medical latex glove injected with acoustic gel to ensure good transmission of the ultrasound waves. This assembly was placed in a bucket of mud with a density of approximately 1.13 g·cm^{-3} (Fig. 3.18). A B-mode scan of the mud was conducted with the ultrasound

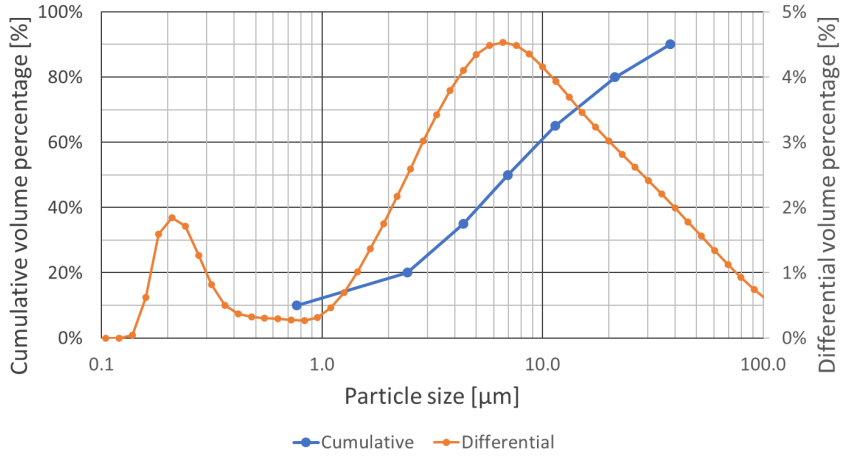

Figure 3.16: *Particle size distribution of Zeebrugge mud samples used during the experiments of this study. The distribution is plotted both cumulatively (blue) and differentially (orange). Analysis performed at FH using a Malvern Mastersizer 2000 (Mal, 2007)*

frequency set at 7 MHz. The resulting image, shown as Fig. 3.19, confirms the expectation of a speckle pattern image. As elaborated by Szabo (2004), a speckle pattern arises from the constructive and destructive interference of a great amount of scatterers, which appears as a light and dark mottled grainy pattern. For many years users of ultrasound systems assigned a diagnostic value to the appearance of speckle and assumed it was tissue microstructure. Despite its deceiving appearance as a tissue texture, speckle is however an illusion and an unwanted effect for medical imaging as it reduces both image contrast as the distinction of subtle gradations and boundaries in tissue structure. Yet speckle can also be of use, as it can be correlated to the position of scatterers and thus used to track their movement. Since speckle arises from the interference of backscattered signals, the appearance of speckle can be attributed to the position of the scatterers relative to each other. Moreover, in case of low $k{\cdot}a$ values (like < 0.35), the scatterers

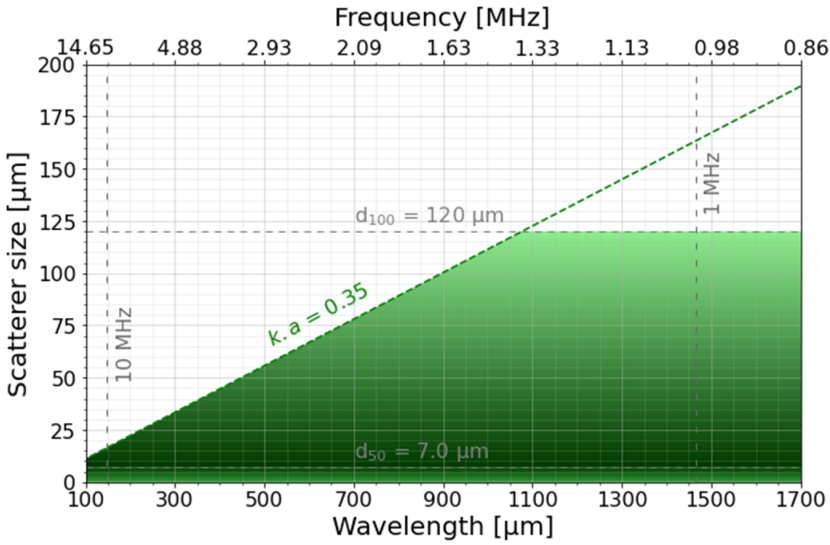

Figure 3.17: *Figure illustrating the correlation between wavelength, ultrasound frequency and size of the scatterers at which diffusive scattering occurs in Zeebrugge mud. The green dashed line indicates the threshold of $k{\cdot}a$ equal to 0.35, below which diffusive scattering occurs (Szabo, 2004). Based on the particle size distibution of Zeebrugge mud (Fig. 3.16), the green shading illustrates the density of potential scatterers and thus the probability of interference of the scattered signals, resulting in speckle pattern images.*

can be considered rigid spheres (Szabo, 2004), rendering their orientation irrelevant. Thus, as long as the relative position of the scatterers is maintained as they move with the flow in the fluid, the corresponding part of the speckle image will shift accordingly. In the case of a high density of scatterers, this is likely to be the case, as evidenced by multiple medical applications based on this principle, such as the monitoring of muscle tissue movement (cardiology) and the recording of blood flows. This technique is referred to as ”speckle tracking” (Garcia et al., 2018).

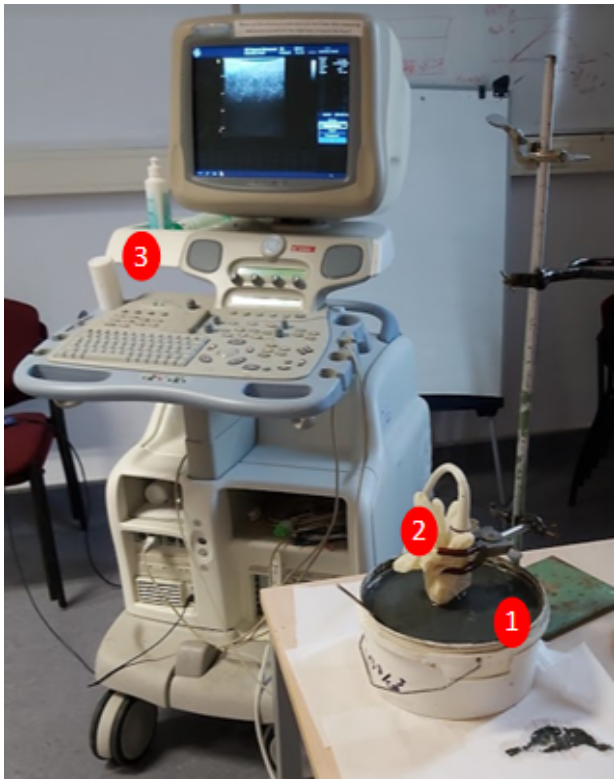

Figure 3.18: *Setup of performed B-mode scan on mud: (1) bucket of mud with density 1.13 g·cm^{-3}, (2) 10L linear ultrasound array protected in a latex glove, (3) GE Vivid 7 ultrasound scanner. Apart from the array being immersed partly in the mud, the setup is in line with Fig. 3.1 (B).*

3.3.4 Speckle tracking on ultrasonographic images

The aforementioned small-scale test using a standard medical ultrasound scanner on mud showed that the addition of seeding particles is uncalled for. Mud already contains a sufficient amount of small reflectors (scatterers) resulting in speckle pattern images suitable for the application of cross-

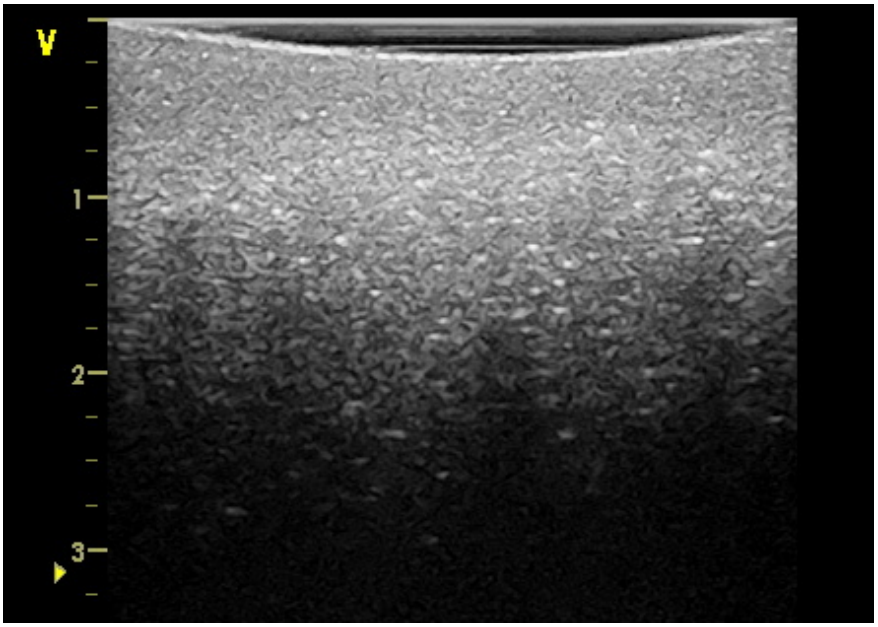

Figure 3.19: *B-mode scan of mud with a ultrasound frequency set at 7 MHz, resulting in a clear speckle pattern due to interference scattered signals. Depth scale expressed in cm.*

correlation algorithms, such as speckle tracking. Although yet to be confirmed, it can be expected that the structure of speckle images allows cross-correlation at sufficiently high resolution (see Section 3.1.2). The use of the technique for monitoring flows in something as small as human veins confirms this. To put its applicability in mud to the test, a flow was induced in the mud bucket by moving a kitchen spoon back and forth. The spoon was at sufficient depth ($>$ 30 mm) below the array to ensure it was out of reach of the ultrasound waves. With the use of the speckle tracking application the scanner was able to record the induced flows as depicted in the two screenshots of the scanner (see Fig. 3.20). These figures show the ensuing velocity vectors plotted in a color

scale in front of the B-mode speckle images. The blue and red colored vectors indicate similar flow velocities with opposite sign corresponding to the induced flows.

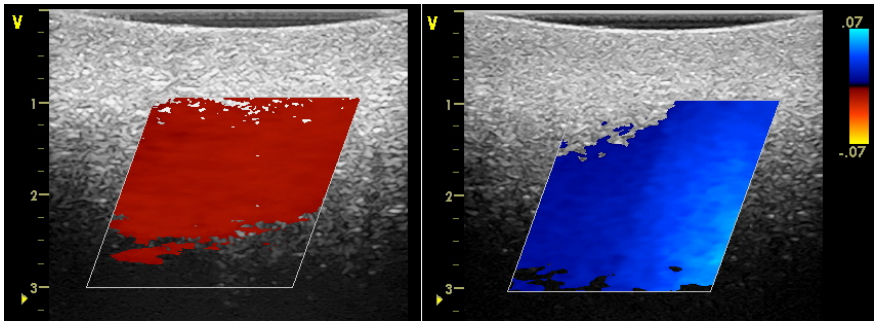

Figure 3.20: *Screenshots during recording of induced flows with speckle tracking application. Depth scale in cm. Velocity scale in* $m{\cdot}s^{-1}$.

Unlike for medical applications, visualisation of flows in mud does not require a clear distinction between different tissues or revealing tissue boundaries. Minimal requirements on lateral resolution are therefore not required, which allows to lower the ultrasound frequency (Alexander and Swanevelder, 2011) in order to decrease the attenuation (see Fig. 3.14) and hence increase the penetration depth. Lowering the frequency however lowers the wavenumber k (Eq. 3.10), while there will be a minimum value for the factor $k{\cdot}a$ as from where the scattering intensity becomes too low to be of any further use. Assuming the scatterers can be considered as rigid spheres, Szabo (2004) presents Eq. 3.11 for the Rayleigh scattering regime, showing the great influence of the ultrasound frequency (4^{th} power) and the scatterer radius (6^{th} power) on the scattering intensity. This shows the requirement to find a compromise between penetration depth and ultrasound frequency while considering the minimal scattering intensity as an additional restriction. Because of the origin of speckle, the speckle quality is also dependent on

the amount of scatterers present. As the latter is impossible to determine this new compromise will need to be determined experimentally.

$$\frac{I_{\text{sc}}}{I_{\text{in}}} = \frac{k^4.a^6}{9.{d_{\text{sc}}}^2}.\left[1 - \frac{3.cos\phi}{2}\right]^2 \tag{3.11}$$

Where I_{sc} is the scattering intensity [W·m^{-2}], I_{in} is the incoming intensity [W·m^{-2}], k is the wavenumber [m^{-1}], a is the scatterer radius [m], d_{sc} is the distance to the scatterer [m] and ϕ the scattering angle [rad].

The relation between the scattering angle ϕ and the scattering intensity I_{sc} also allows for alternative arrangements. Eq. 3.11 shows the bi-polar scattering pattern with maximal intensities at ϕ = 0 rad (forward scattering) and ϕ = π rad (backscattering). For medical applications this is of course an advantage as it allows the use and flexibility of only one transducer while preserving maximal efficiency. For a stationary setup, such flexibility has no added value, making rectilinear reflection no longer a requirement. In turn, this allows for the use of a seperate transmitter and receiver placed at an angle to each other, as illustrated in Fig. 3.21. Because in a single transducer setup (Fig. 3.1 (B)), the transducer has to continuously switch between transmitting and receiving, a setup with two transducers acting as either a transmitter or a receiver allows for a higher frame rate and hence a higher maximum recordable flow velocity. In addition, such an angled arrangement can optimise the propagation path, decreasing the required depth range or even allow for the recording of a flow field in 3D. According to Eq. 3.11, the intensity will decrease with a factor 6.25 when working in an angle ϕ = $\frac{\pi}{2}$ rad. Such a decrease in intensity can simply be compensated with an increase in frequency from 1 MHz to 1.58 MHz. However, an increase in frequency will also lead to higher attenuation (Fig. 3.14) and therefore a decraese in depth range. This discord shows that further customisation

of this technique requires knowledgde of the attenuation of ultrasound by mud.

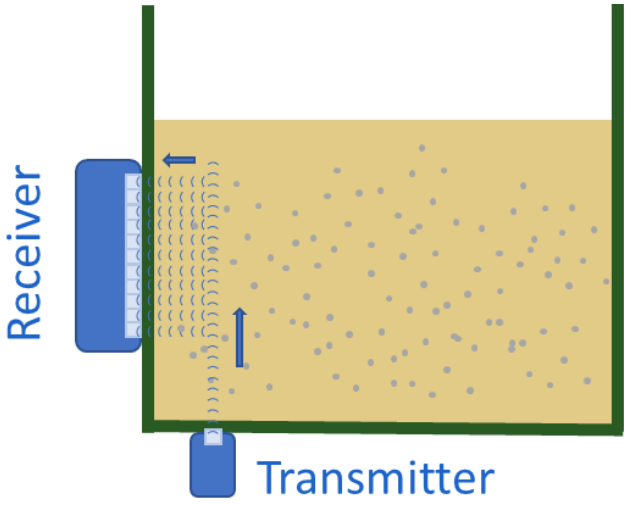

Figure 3.21: *Sketch of an alternative setup for ultrasonography using two transducers, one as transmitter and a second as receiver.*

3.4 Summary of the outcome of the evaluation of non-intrusive approaches for monitoring mud flow

Review of the potential of radiography on mud shows that the technique is not efficient enough to be used in typically larger hydraulic research facilities. Even with the use of the most powerful radiation sources available on the market, either the mud layer thickness or the flow velocity should be limited in such a way that they are no longer relevant ($<$ 300 mm or $<$ 2 m·s^{-1}, respectively). Furthermore, the requirement to seed the mud with tracing particles to enable the application

of PIV was demonstrated. Seeding with solid particles is however likely to influence the behaviour of mud, making the reliability of the results questionable. In addition, the total cost (direct and indirect) of using such a radiation source will be several hundred thousand euros. This probably exceeds most available budgets for research projects on mud behaviour. It can thus be concluded that radiography may work, but because of the discussed drawbacks, its use to monitor flows in fluid mud is rather unlikely.

More potential was found in the use of ultrasound imaging. Firstly, because a full transmission through the mud layer is not required here, limiting the required penetration depth. Secondly, ultrasound imaging of mud already provides images suitable for cross-correlation processing (like PIV), without the addition of tracer particles. With a small-scale test it was shown that a conventional ultrasound scan of mud results in a so-called ”speckle pattern” image. Although speckle patterns are an unwanted feature for medical diagnostics, they are also used to track tissue movement or blood flow, known as ”speckle tracking” (similar to PIV). With the same small-scale setup, speckle tracking was applied while inducing flows in the mud, demonstrating its ability to record and visualise the induced flows and determine flow velocities. Furthermore, the stationary deployment on hydraulic test facilities can provide the opportunity for alternative arrangements of the ultrasound equipment, potentially optimising its efficiency. Further customisation of ultrasonography applied on mud requires knowledge of the attenuation of ultrasound by mud. Such data is currently unavailable and therefore needs to be determined experimentally. For the relevant ultrasound frequencies and mud densities, this was also done during this study, which is described in the next chapter.

Bibliography

Alexander N. and Swanevelder J. Resolution in ultrasound imaging. *Continuing Education in Anaesthesia, Critical Care & Pain*, 11(5): 186–192, 2011.

Anderson J. D. Chapter 3: Inviscid, incompressible flow. In Beamesderfer L. and Castellano E., editors, *Fundamentals of Aerodynamics*, pages 153–245. McGraw-Hill, Inc., 1991.

Beer A. *Grundriss des photometrischen Calcüles*. Vieweg, 1854.

Berger M. J., Hubbell J. H., Seltzer S. M., Chang J., Coursey J. S., Sukumar R., Zucker D. S. and Olsen K. Xcom: Photon cross sections database, 2010. URL `https://dx.doi.org/10.18434/T48G6X`.

Berlamont J., Ockenden M., Toorman E. and Winterwerp J. The characterisation of cohesive sediment properties. *Coastal Engineering*, 21(1–3):105–128, 1993.

Burcu A. and Salih Z. E. The mass attenuation coefficients, electronic, atomic, and molecular cross sections, effective atomic numbers, and electron densities for compounds of some biomedically important elements at 59.5 kev. *Science and Technology of Nuclear Installations*, pages 1–8, 2014. doi: 10.1155/2014/901465.

Capilla J., Olivares J., Clement M., Sangrador J., Iborra E. and Devos A. High-acoustic-impedance tantalum oxide layers for insulating acoustic reflectors. *IEEE Transactions on Ultrasonics, Ferroelectrics and Frequency Control*, 59(3):366–372, 2012. doi: 10.1109/tuffc.2012.2205.

Cember H. and Johnson T. E. Chapter 8: Radiation safety guides. In *Introduction to health physics (fourth edition)*, pages 337–426. McGraw-Hill Medical, 2008.

Claeys S., Dierikx B., Paul S. and Reenen J. Fluid mud density determination in navigational channels. In *Proceedings of*

Hydro 12 - Taking Care of the Sea, pages 1–7, Rotterdam, The Netherlands, 13–15 november 2012. Hydrographic Society Benelux. doi: 10.3990/2.228.

Delefortrie G. and Vantorre M. Ship manoeuvring behaviour in muddy navigation areas : state of the art. In *Bundesanstalt für Wasserbau*, pages 26–36, 2016. doi: 10.18451/978-3-939230-38-0_4.

Forth L., Speller R. and Moss R. The importance of accurate X-ray energy spectra for modelling dose deposition with monte carlo techniques. In *IEEE Nuclear Science Symposium and Medical Imaging Conference (NSS/MIC)*, pages 1–2, Atlanta, GA, USA, 21–28 October 2017. doi: 10.1109/NSSMIC.2017.8533113.

Garcia D., Lantelme P. and Saloux E. Chapter 26: Introduction to speckle tracking in cardiac ultrasound imaging. In *Handbook of Speckle Filtering and Tracking in Cardiovascular Ultrasound Imaging and Video*, pages 571–598. Institution of Engineering and Technology, 2018. doi: 10.1049/PBHE013E_ch26.

Ginzel E. and Turnbull B. Determining approximate acoustic properties of materials. *e-Journal of Nondestructive testing (NDT)*, 21(12), 2016.

Hendee W. R. and Ritenour E. R. Chapter 19: Ultrasound waves. In *Medical Imaging Physics*, pages 303–316. Wiley–Liss, New York, USA, 2002. doi: 10.1002/0471221155.ch19.

Hjertager B. *Turbulence theory and modelling - Lecture notes*. University of Stavanger, N-4036 Stavanger, Norway, 2014.

IEC62220-1-3. Determination of the detective quantum efficiency - detectors used in dynamic imaging. In *Medical electrical equipment - Characteristics of digital X-ray imaging devices*, page 68. International Electrotechnical Commission, 2008.

Lovato S., Kirichek A., Toxopeus S., Settels J. and Keetels G. Validation of the resistance of a plate moving through mud: Cfd

modelling and towing tank experiments. *Ocean Engineering*, 258, 2022. doi: 10.1016/j.oceaneng.2022.111632.

Ma X., Kirichek A., Heller K. and Draganov D. Estimating p- and s-wave velocities in fluid mud using seismic interferometry. *Frontiers in Earth Science*, 10, 2022. doi: 10.3389/feart.2022.806721.

Mastersizer 2000 User Manual - MANO384 issue 1.0. Malvern Instruments Ltd, 2007.

Manning A. J. and Whitehouse R. J. S. Uop mini-annular flume – operation and hydrodynamic calibration. In *HR Wallingford Technical Report, TR 169*. HR Wallingford, Oxfordshire OX10 8BA, UK, 2009.

McGinnis R. Rad pro calculator, June 2020. URL `http://www.radprocalculator.com/`.

Meire D., Claeys S., De Maerschalck B. and Mostaert F. Evaluatie van meetinstrumenten voor de bepaling van slib karakteristieken: Deelrapport 3: Meetcampagne februari 2019 (" Evaluation of measurement equipment for determining mud characteristics: Sub-report 3: Measurement campaign february 2019"). In *WL Rapporten 18 059 3 Versie 5.0.* Waterbouwkundig Laboratorium, Antwerp, Belgium, 2021.

Meshkati Shahmirzadi M. E., Staelens P., Claeys S., Cattrysse H., Van Hoestenberghe T., Van Oyen T., Vanlede J., Verwaest T. and Mostaert F. Experimental investigation on consolidation behaviour of mud: Subreport 1- methodology study. In *Versie 5.0. WL Rapporten, 12_082*, pages 1–26. Waterbouwkundig Laboratorium, Antwerp, Belgium, 2015.

Pierce A. D., Siegmann W. L. and Brown E. Analytical discussion of past measurements of acoustic attenuation in mud sediments and of possible future experimental approaches. In *Proceedings of Meetings on Acoustics*, volume 25, Jacksonville, Florida, USA, 2–6 November 2015. doi: https://doi.org/10.1121/1.4934094.

Pirola Igoa E., Ibanez M., Claeys S., Meire D. and Mostaert F. Experimental investigation on the consolidation behaviour of mud: Port of hamburg. In *Versie 3.0. FHR Reports, 18_009_1*, page 59. Waterbouwkundig Laboratorium, Antwerp, Belgium, 2020.

Plancke Y., Meire D. and Mostaert F. Studie naar meettechnieken voor het onderzoeken van de opbouw van sliblagen in het Deurganckdok: Deelrapport 1 – Bundeling van de belangrijkste resultaten uit 3 masterproeven uitgevoerd op de Universiteit Antwerpen (”Study of measurement techniques for the investigation of the structure of mud layers in the Deurganckdok: Subreport 1 - Collection of the most important results of 3 master theses performed at University of Antwerp”). In *WL Rapporten 12 160 1 Versie 3.0.* Waterbouwkundig Laboratorium, Antwerp, Belgium, 2018.

Poelma C. Ultrasound imaging velocimetry: A review. *Experiments in Fluids*, 58(3), 2016. doi: 10.1007/s00348-016-2283-9.

Poludniowski G. Calculation of X-ray spectra emerging from an X-ray tube. Part II. X-ray production and filtration in X-ray targets. *Medical Physics*, 34(6):2175–2186, 2007. doi: 10.1118/1.2734726.

Poludniowski G. and Evans P. Calculation of X-ray spectra emerging from an X-ray tube. Part I. electron penetration characteristics in X-ray targets. *Medical Physics*, 34(6):2164–2174, 2007. doi: 10.1118/1.2734725.

Poludniowski G., Landry G., Deblois F., Evans P. and Verhaegen F. Spekcalc: a program to calculate photon spectra from tungsten anode X-ray tubes. *Physics in medicine and biology*, 54(19): N433–8, 2009. doi: 10.1088/0031-9155/54/19/N01.

Pope S. B. *Turbulent flows*. Cambridge University Press, Cambridge CB2 8RU, UK, 2000.

Raffel M., Willert C., Scarano F., Kähler C., Wereley S. and Kompenhans J. *Particle Image Velocimetry: A Practical Guide (third edition)*. Springer Cham, New York, USA, 2018. doi: 10.1007/978-3-319-68852-7.

Ripan B., Hossain S., Abdus S. M. and H. M. F. Calculation of gamma-ray attenuation parameters for locally developed shielding material: Polyboron. *Journal of Radiation Research and Applied Sciences*, 9(1):26–34, 2016. doi: 10.1016/j.jrras.2015.08.005.

Schmidt F. *Operating manual for Admodus USP pro, Operating Manual Version 1.4*. Synergetik GmbH, 2016.

Sikorski W. Development of acoustic emission sensor optimized for partial discharge monitoring in power transformers. *Sensors*, 19 (8):1865, 2019. doi: 10.3390/s19081865.

Sotelo M., Boucetta D., Doddugollu P., Toorman E., Brouwers B., Delefortrie G. and Van Hoydonck W. Experimental study of a cylinder towed through natural mud. In *Proceedings of the 6th MASHCON International Conference on Ship Manoeuvring in Shallow and Confined Water*, pages 222–231, Glasgow, UK, 22–26 May 2022.

Sotelo M., Boucetta D., Van Hoydonck W., Doddugollu P., Vantorre M., Toorman E. and Delefortrie G. Hydrodynamic forces acting on a cylinder towed in muddy environments. *Journal of Waterway, Port, Coastal, and Ocean Engineering*, 149(6), 11 2023. doi: 10.1061/JWPED5.WWENG-1992.

Swillens A. *A multiphysics model for improving the ultrasonic assessment of large arteries*. PhD thesis, Ghent University, Faculty of engineering and architecture, Jozef Plateaustraat 22, 9000 Gent, Belgium, 2010.

Szabo T. L. Chapter 8: Wave scattering and imaging. In *Diagnostic Ultrasound Imaging: Inside out*, pages 213–241. Elsevier Academic Press, Hoboken, NJ, USA, 2004.

Tennekes H. and Lumley J. L. Chapter 3: The dynamics of turbulence. In *A first course in turbulence*, pages 59–103. The Massachusetts Institute of Technology, Cambridge, MA 02139, USA, 1972.

Toorman E. A. An analytical solution for the velocity and shear rate distribution of non-ideal Bingham fluids in concentric cylinder viscometers. *Rheologica Acta*, 33:193–202, 1994. doi: 10.1007/BF00437304.

Vanlede J., Toorman E., Liste-Muñoz M., Rocabado I., Heredia M., Delefortrie G. and Vantorre M. Towards cfd as a tool to study ship-mud interactions. In *Oceanology International*, page Poster, 2014.

VEGA Americas I., July 2017. URL `https://www.vega.com/en-us/products`.

Wang T. Inductively coupled plasma optical emission spectrometry. In Cazes J., editor, *Ewing's Analytical Instrumentation Handbook, Third Edition*, pages 57–74. Marcel Dekker, New York, USA, 2004.

Winterwerp J. C. *On the dynamics of high-concentrated mud suspensions*. PhD thesis, Delft University of Technology, Delft, The Netherlands, 1999.

Worral W. E. and Tuliani S. Viscosity changes during the ageing of clay-water suspensions. *Transactions and journal of the British Ceramic Society*, 63:167–185, 1964.

Chapter 4

Assessment of ultrasound attenuation by mud

In the previous chapter, the use of ultrasound imaging is proposed as the most appropriate method to visualise flow dynamics in mud. Due to the attenuation of ultrasound radiation by mud, the depth to which flows can be visualised is however limited. During the small-scale experiments described in Section 3.3.3 even down to only a few centimeters. Although over a limited ultrasound frequency spectrum, the relationship between ultrasound frequency, mud density and ultrasound attenuation could be identified based on on-site measurements in the mud layers of the Zeebrugge docks. This revealed a proportional relationship between the attenuation, mud density and ultrasound frequency. Lowering the frequency during ultrasound imaging will thus reduce the attenuation and hence enable a greater depth range. On the other hand, Eq. 3.11 shows a decrease in intensity of the scattered radiation to the power of four when the ultrasound frequency is reduced. Since the scattered radiation must be sufficiently energetic to be able to return to the transducer, lowering the ultrasound frequency can thus also limit the depth range in this way. The magnitude of both effects

needs further investigation to determine which one prevails and what the ultimate impact of a decrease in ultrasound frequency will be. During this study, experiments were conducted to determine the relation between the rate at which the mud attenuates ultrasound, the density of the mud and the frequency of the ultrasound. These experiments and their results are presented in this chapter. They were performed in a laboratory environment to verify the aforementioned on-site measurements. Moreover, they cover a wider spectrum of ultrasound frequencies.

4.1 Methods to determine the ultrasound attenuation of mud

In general, ultrasound imaging is performed in the MHz frequency range. When the depth of the object to be visualised predominates the resolution at which the object is depicted, e.g. SONAR or fish spotting, frequencies of 0.7 MHz to 2.0 MHz will suffice (Dahl, 1999). In case the images are produced for diagnostic use, where high resolution is required, higher frequencies should be used at the expense of the depth range. For conventional medical imaging this can go up to 15 MHz (Szabo, 2004a). Other more specialised medical imaging applications use even higher ultrasound frequencies up to 60 MHz (Shung, 2009). Ultrasound imaging is also used for NDT purposes. Typically, ultrasound frequencies of up to 12 MHz are used for this. Even higher frequencies are sometimes applied using customised setups (Drinkwater and Wilcox, 2006).

When speckle images are the objective, there is no need to clearly visualise a boundary or interface. Speckle patterns are conceived by the interferences of multiple backscattered signals which add up or cancel each other out (Section 3.3.3). Hence, the requirement for resolution can be replaced by

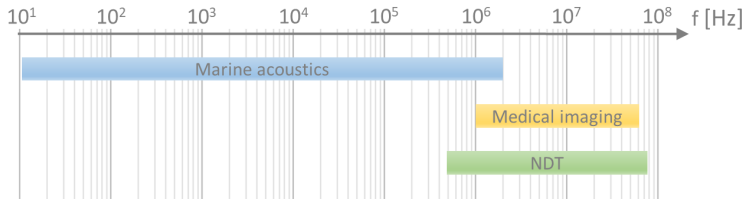

Figure 4.1: *An illustration of the different spectrums of ultrasound frequencies applied for various applications.*

the amount of scattering, which is determined by the ratio of wavelength of the ultrasound radiation to the size of the scatterers. As discussed in Section 3.3.3 the particle size distribution of Zeebrugge mud indicates an optimal ultrasound frequency range between 1 MHz and 10 MHz to generate speckle pattern images. The speckle pattern image shown in the same section, was produced with ultrasound with a frequency of 7 MHz, and showed to be of sufficient quality for cross-correlation processing. Therefore, the frequency range for which the ultrasound attenuation is assessed in this chapter is limited to 1 MHz to 7 MHz. According to (Pierce et al., 2015) and to the authors' knowledge, values for ultrasound attenuation of mud in this frequency range are not documented in existing literature, necessitating experiments.

The most straightforward method to assess the attenuation of a medium (solid or liquid) is with the so-called through-transmission technique (Chaffaï et al. (2000) and Ginzel and Turnbull (2016)). This technique requires two transducers placed opposite to each other with the medium of interest in between. One transducer transmits the ultrasound waves while the other receives (Fig. 4.2 (A)). In case the properties of a liquid are of interest, the two transducers are immersed in the liquid. The ultrasound attenuation can be deduced by comparing the amplitude received after propagation of the ultrasound wave through the liquid with a reference signal.

The latter is preferably obtained from calibration in water as water has low ultrasound attenuation values which in fact can be neglected (Hendee and Ritenour, 2002). The through-transmission demands the two transducers to have at least equal centre frequencies.

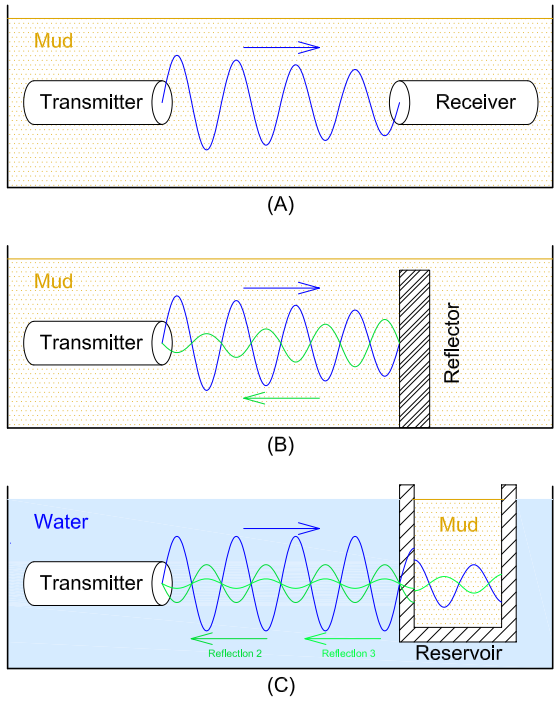

Figure 4.2: *Sketches of possible experimental setups to determine the attenuation of mud. Sketch (A) shows the setup for the through-transmission technique, sketch (B) the setup for the pulse-echo technique and sketch (C) the setup for the multiple-echo technique.*

A technique requiring only a single transducer is the pulse-echo technique (Selfridge (1985) and Wróbel and Pawlak (2007)). Here the transducer works as transmitter and receiver (Fig. 4.2 (B)). Again the transducer is immersed in the liquid of interest, but now an acoustic reflector is placed opposite to the transducer and perpendicular to the wave direction. The emitted ultrasound signal propagates through the liquid, reflects on the acoustic reflector propagates back to the transducer. Relative measurement of the amplitude of the reflection signal over multiple acquisitions with varying distance between transducer and reflector, allows to determine the ultrasound attenuation in the liquid (see Section 4.2.2.1).

Immersion of the ultrasound transducers for long periods or in media other than clear water can however cause contamination of the sensor surface, influencing the recordings and damaging the transducers (Püttmer et al., 1999). In case of mud this could be caused by the corrosive nature of the seawater present in mud. In such cases an alternative multiple-echo technique can be an option (Norisuye et al., 2011). In this method a secondary reservoir containing mud is immersed in water together with the transducer (Fig. 4.2 (C)). The attenuation is obtained from comparison between the reflection signals of the two reservoir-mud interfaces. This method suffers however from great energy losses. Before reaching the mud, a significant amount of energy is already lost by reflection on the water-reservoir interface and propagation through the reservoir material. Such losses can be compensated by amplifying the signals, however at the cost of accuracy.

Since a pair of transducers with equal centre frequency were not available for this research, the through-transmission technique (Fig. 4.2 (A)) could not be considered. While the relativity (see Section 4.2.2.1) of the pulse-echo measurement technique (Fig. 4.2 (B)) allows to simply protect the transducer from contamination by inserting it in a thin sheath-shaped rubber, the pulse-echo technique was preferred for these experiments. Additional experiments determining the ultrasound attenuation of mud were performed using various ultrasound devices. The results are compared with those of the measurements using the pulse-echo technique to evaluate the reliability of these alternative techniques for the purpose of similar future research. The used ultrasound devices were all developed for other applications like on-site marine measurements (Admodus USP pro and AQUAscat 1000R) and medical echography (DiPhAS beamformer platform and HD-PULSE). Nonetheless their output can be used to deduce the ultrasound attenuation of mud. All experiments were conducted in mud orginating from the Zeebrugge docks of the Port of Antwerp-Bruges (Belgium). Three subsamples of different density, around 1.116 g·cm^{-3}, 1.450 g·cm^{-3} and 1.175 g·cm^{-3}, were prepared by diluting the original mud with seawater sampled at the same location as the mud.

Besides for the application of UIV on mud, knowledge of the ultrasound attenuation of mud is also usefull to enable in situ measurements of the kinematic viscosity of natural mud. Knowledge of this rheological property is required to estimate the flow characteristics of mud, as described in Section 3.1.2. In turn this is of importance for the study of interactions between ships, water and mud and various other research topics (see Section 1.1.2). Today, the kinematic viscosity of mud can determined with a rheometer (Claeys et al., 2015; Doddugollu, 2021; Doddugollu and Toorman, 2023). For practical and quality reasons, this is preferably performed in a laboratory. Doing so for on-site mud therefore requires on-site sampling and transport towards the lab, which is a

laborious operation. Furthermore for continuous monitoring, this procedure should be repeated frequently as mud layer properties change over time (Toorman and Berlamont, 1991) and are continuously influenced by tidal currents, ship passing and dredging (Toorman and Berlamont, 2015). To asses the navigability of waterways, the ability to perform fast on-site measurements of the kinematic viscosity of mud would therefore be of great interest for port and waterway authorities. Because of the aforementioned impracticalities, this is currently mostly done based on density profiling of the on-site mud layers (Delefortrie et al., 2007). As mentioned in Section 3.3.2, in the docks of Zeebrugge this is done with ultrasound using the Admodus USP pro. In the (soil) drilling industry recent research has shown that ultrasound measurements in drilling mud exhibit a non-linear relationship between the attenuation of the ultrasound and the kinematic viscosity of the drilling mud (Jondahl et al. (2017) and Jondahl and Viumdal (2019)). Water-based drilling muds are most commonly based on clay suspensions, which are also frequently used to mimic the behaviour of natural mud in experimental research (a.o. Imai (1980); Gibbs (1985); de Wit (1995); Dankers (2006); Jacobs (2011); Hsu et al. (2013)). It can therefore be expected that a similar relation between ultrasound attenuation and kinematic viscosity also applies for natural muds. In fact, the required features to measure acoustic attenuation are therefore already integrated in the Admodus USP pro (see Section 4.3.2). The results presented in this chapter will help to assess this relationship.

This chapter describes the experiments and results to determine the ultrasound attenuation of mud at high ultrasound frequencies. First, a conventional method to determine the ultrasound attenuation of common fluids is used (see Section 4.2). Mud, however, cannot be considered a common fluid. After all, when left at rest, sedimentation occurs, changing the vertical density profile of the mud sample (Section 2.2). Because of the limited time frame of the experiments, these changes in

density can be considered minimal, though. Nonetheless, due to the influence of density on the attenuation (Section 3.3.3), a correction by alternative processing of the experimental output is suggested to cope with these changing properties. The corrected values are further used as reference to evaluate the reliability of alternative experiments using various ultrasound techniques. These alternative experiments are discussed in Section 4.3.

4.2 Reference experiment using an immersible single element transducer

4.2.1 Setup and measurements

The experimental setup used to assess the ultrasound attenuation of mud is based on the pulse-echo technique (Fig. 4.2 (B)). In practice the setup was however slightly different, as depicted in Fig. 4.3. To facilitate the changing distance between transducer and reflector a high precision XYZ gantry stage was used to hold the transducer upright with its transmission side facing down in the top layer of the mud. The mud sample was contained in a plastic bucket, positioned underneath the gantry stage. The used transducer is an immersible single element broadband (Fractional Bandwidth (FBW) 50 %) transducer type H5K from General Electric (GE , 2008). In mud with density 1.145 g·cm^{-3} the centre frequency produced by the transducer is around 2.75 MHz. Consequently, the FBW ranges from 2.06 MHz to 3.44 MHz. Due to the high attenuation values of mud the ultrasound waves were amplified (gain) using a pre-amp. A gain of 40 dB was applied for all mud samples. Stainless steel was chosen as the material for the acoustic reflector. With a speed of sound in stainless steel of 5800 m·s^{-1} (Ginzel and Turnbull, 2016) and a density of 7850 kg·m^{-3} the acoustic impedance of steel can be calculated using Eq. 3.8. The same can be

done for each mud sample with known density and a speed of sound of 1465 $m \cdot s^{-1}$ (see Section 3.3.2). With the impedance of both media the reflection coefficient of their interface can be determined using Eq. 3.9.

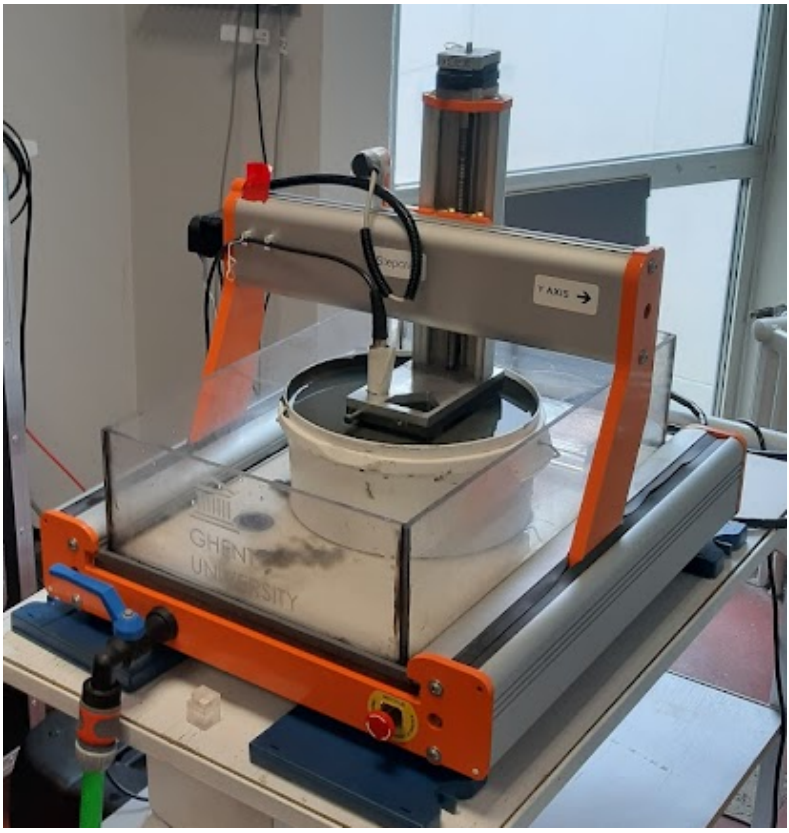

Figure 4.3: *Laboratory setup of the experiments using an immersible transducer. The transducer is held vertically with its transmission side in the mud, while protected by a sheath-shaped rubber. The gantry stage is used for vertical displacement of the transducer.*

The resulting reflection coefficient of the mud-reflector interface is around 0.93 meaning 93 % of the incoming

ultrasound radiation is reflected back towards the transducer. A plate of 100 mm by 100 mm and 10 mm thickness was placed at the bottom of the mud bucket. Using the XY positioning system of the gantry, the transducer was positioned more or less above the centre of the reflector. Adjustment of the distance between transducer and reflector was performed by moving the transducer towards the reflector. For each mud sample this was done in 140 steps, covering a total displacement of 1.315 cm (Fig. 4.4).

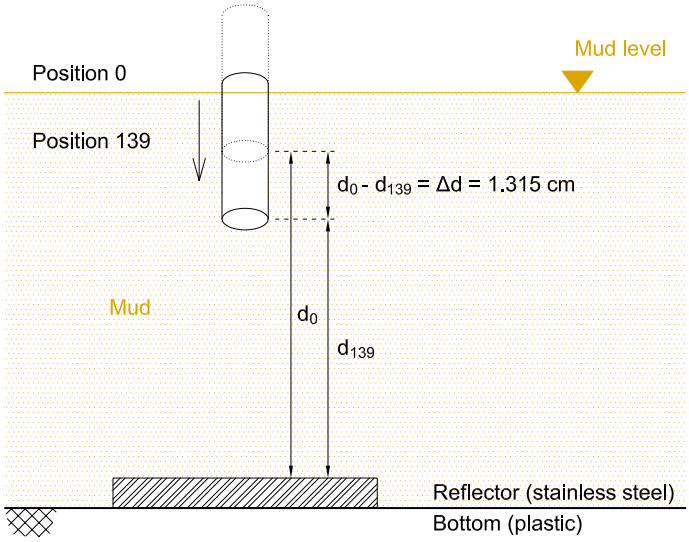

Figure 4.4: *Sketch of the experimental setup shown in Fig. 4.3, illustrating the effects of the transducers' displacement.*

At each step a scan was conducted, recording the amplitude of the reflected signal. The amplitude of the reflected signal can be expressed as:

$$A_{m,\text{rec}} = A_{m,0}.P_{\text{mud}}.r_{\text{ms}}.P_{\text{mud}} = A_{m,0}.r_{\text{ms}}.P_{\text{mud}}^2 \tag{4.1}$$

Where $A_{m,\text{rec}}$ is the amplitude of the received signal [V], $A_{m,0}$ is the initial amplitude of the emitted signal [V], r_{ms} is the

reflection coefficient of the mud-stainless steel interface [-] and P_{mud} the propagation loss due to attenuation by the mud [-].

In combination with Eq. 3.1, this can be rewritten as:

$$A_{m,\text{rec}} = A_{m,0}.r_{\text{ms}}.e^{(-2.\alpha_{\text{mud}}.d)} \tag{4.2}$$

Where α_{mud} is the frequency dependent ultrasound attenuation of the mud [Np·m^{-1}] and d the distance between the transducer and reflector corresponding to half the total propagation path of the ultrasound signals [m].

Fig. 4.4 and Eq. 4.1 show that loss in amplitude is caused first by attenuation when sound waves propagate through the mud towards the reflector (P_{mud}). Secondly, energy is lost at the mud-reflector interface. The reflection coefficient r_{ms} shows us that 93 % of the amplitude is reflected back. The remaining 7 % propagates further through the stainless steel and is no longer used. Finally, while propagating back towards the transducer, the reflected signal is attenuated again over the same path as the initial incoming ultrasound wave (P_{mud}). The propagation loss P_{mud} can be expressed with the Beer Lambert Law Eq. 3.1, where P_{mud} corresponds to the transmission ratio (T) after propagation over a distance d through the mud. It should be noted, however, that for the attenuation of ultrasound, the symbol α is more commonly used in the literature (Carlson et al., 2003; Szabo, 2004b; Zheng et al., 2007; Norisuye et al., 2011; Strohm and Kolios, 2011; Pierce et al., 2015). Therefore, for the remainder of this thesis, the symbol α will be used.

4.2.2 Processing of measurements

The recorded reflection signals are transformed into the frequency domain by Fourier Transformation (FT). This allows to select the reflection signal amplitudes and calculate the

ultrasound attenuation for each frequency step. For these experiments the frequency band was cut in steps of 12.5 kHz.

When at rest, the density profile of a mud sample changes over time due to sedimentation (Toorman and Berlamont, 1991). Therefore it can be questioned if a method to determine the ultrasound attenuation of a conventional fluid is suited for mud. Two different ways to cope with this challenge are described and compared in this section. Prior to the experiments, the mud was mixed to re-homogenise and thereby negate the unwanted effect of sedimentation (Berlamont et al., 1993). The first processing method assumes a homogeneous mud sample and is based on relative measurements, making knowledge of the value of some parameters unnecessary. The alternative approach assumes a non-uniform density profile of the mud sample and processes each scan separately. This method however requires knowledge of the values of parameters which are obsolete for the conventional method. Additional measurements are therefore required at the risk of deteriorating reliability of the final outcome due to error propagation.

4.2.2.1 Conventional method

The amplitude of the received signal at the first position of the transducer ($A_{m,\text{rec,0}}$), after propagation over two times the distance d_0 between transducer and reflector, is used as a reference. From the ratios with the amplitude of the signals received at other positions of the transducer ($A_{m,\text{rec,n}}$), after propagation over two times the distance d_n, the attenuation of mud can be deduced. Using Eq. 4.2 for each recording, this results in:

$$\frac{A_{m,\text{rec,n}}}{A_{m,\text{rec,0}}} = \frac{A_{m,\text{n}}.r_\text{ms}.e^{(-2.\alpha_\text{mud}.d_\text{n})}}{A_{m,0}.r_\text{ms}.e^{(-2.\alpha_\text{mud}.d_0)}} = e^{2.\alpha_\text{mud}.(d_0-d_\text{n})} \tag{4.3}$$

From which α_{mud} can be obtained:

$$\alpha_{\text{mud}} = \frac{1}{2.(d_0 - d_n)} . \ln \frac{A_{m,\text{rec,n}}}{A_{m,\text{rec,0}}} \tag{4.4}$$

Where α_{mud} is the frequency dependent ultrasound attenuation of the mud [Np·m^{-1}], d the distance between the transducer and reflector corresponding to half the total propagation path of the ultrasound signals [m], $A_{m,\text{rec}}$ is the amplitude of the received signal [V], index 0 refers to the initial position of the transducer and index n to the various positions of the transducer (139 positions).

In practice, the logarithm of the ratio of the reflection signal amplitudes recorded at each position of the transducer with the reference signal amplitude is plotted in function of the transducers' displacement ($d_n - d_0$). The slope of the linear trendline fitting these ratios is a measure of the attenuation. Mathematically this procedure corresponds to Eq. 4.4. Following this procedure for each frequency step allows to determine the ultrasound attenuation in function of frequency over the entire frequency band of the transducer. This was repeated for each mud sample with different density. The results are presented by the solid curves in Fig. 4.5. Excluding the outer frequencies, the presented relation between attenuation and frequency is fairly linear, which is common for most engineering materials (Ono, 2020).

4.2.2.2 Alternative method

Because the presented conventional method determines the attenuation only over a limited part of the mud sample ($d_n - d_0$) (see Fig. 4.4), it may not be the most suitable method for mud. In the case of homogeneous fluids, such a fraction is representative of the total volume. This, however, may not hold true for mud. Afterall, due to settling when at rest (see Section 2.2), mud cannot be considered a homogeneous

fluid. This unwanted effect can be minimised by mixing the mud in preparation for the experiments. However, as soon as the mud is at rest, settling begins, and by definition the mud becomes inhomogeneous (Toorman and Berlamont, 1991). It is therefore recommended to conduct the ultrasound scanning immediately after the conditioning of the mud. Practically this is not always possible, casting doubt on whether a limited top layer is representative of the full mud sample.

To verify this possible inaccuracy, an alternative method to process the recorded reflection signals was performed. A major advantage of the conventional method is its relative approach, eliminating the need for knowledge of the originally emitted amplitude $A_{m,0}$ and reflection coefficient r_{ms} (see Eq. 4.3). If these parameters are known though, the attenuation by the mud can be deduced directly for each recording, using Eq. 4.2. In this way, the entire propagation path of the ultrasound through the mud is taken into account.

An estimate of r_{ms}, based on previously published values, is provided in Section 4.2.1. This can be refined using the timestamps of the recordings. Based on these, the time of flight of the reflected signals can be deduced for each recording. Together with the known length of the propagation path through the mud ($2.d_{\text{n}}$), the actual speed of sound through the mud can be determined. This allows refining the acoustic impedance of mud and, in turn, the reflection coefficient of the mud-stainless steel interface r_{ms}.

To acquire the values of $A_{m,0}$ for each ultrasound frequency, additional experiments were performed. These experiments were similar to those described in the previous section, but using water instead of mud. The acoustic impedance and attenuation of water are well known (Strohm and Kolios, 2011). The latter is close to zero (0.0022 dB·cm^{-1}·MHz^{-1}), hence the propagation loss caused by water can be neglected ($<$ 1 %

for a propagation distance of 20 cm). With the acoustic impedance of water, the reflection coefficient of the water-stainless steel interface (r_{ws}) can be determined in the same way as described in Section 4.2.1. This is approximately 0.94. Using Eq. 4.1, the values of $A_{m,0}$ for the experiments with water can now be deduced from the recordings. These are equal to those for the experiments in mud.

With these values of $A_{m,0}$ and r_{ms}, the attenuation α_{mud} can be determined using Eq. 4.2. This was done for each scan and for each frequency (at a resolution of 12.5 kHz), resulting in 140 values for attenuation per frequency. The average of these is considered the final attenuation value for that frequency. These results are shown in Fig. 4.5 by the dashed curves. Again with the exception of the outer frequencies, these curves show a more linear relationship between attenuation and frequency compared to the solid curves resulting from the conventional processing method.

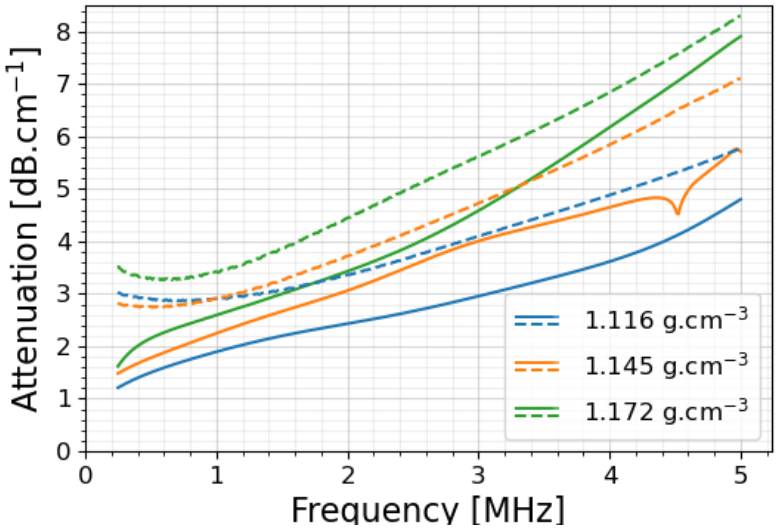

Figure 4.5: *Resulting values of ultrasound attenuation as a function of ultrasound frequency (resolution of 12.5 kHz) for each mud sample with different density. The solid curves show the results using the conventional method for fluids, considering mud as a homogeneous fluid (Section 4.2.2.1). The dashed curves show the results using an alternative method where mud is considered a non-homogeneous fluid (Section 4.2.2.2).*

The solid orange curve in Fig. 4.5 shows a strange kink around 4.5 MHz. This is due to anomalies in the recordings at positions 134 and 137 of the transducer. Due to COVID restrictions at the time the experiments were conducted, the experiments could not be repeated to correct this. The absence of similar deviations in the orange dashed curve indicates that the conventional processing method is more sensitive to these anomalous recordings than the alternative method. Since 4.5 MHz falls outside the transducer's FBW (see Section 4.2.1), this deviation is further ignored.

4.2.2.3 Comparison of both methods

In case of perfectly homogeneous mud, the results of both methods should match. This is however not the case as shown in the plots depicted in Fig. 4.5. While the precision of the conventional method can be questioned due to the inhomogeneous mud, the alternative method suffers from error propagation due to usage of multiple measured values. A reliability analysis was therefore performed for both methods. For the conventional method R^2 values were calculated, indicating how well the trendline fits the recorded relative amplitudes (Fig. 4.6 (A)). Reliability of the alternative method is evaluated with the standard deviation values of the averaged results (Fig. 4.6 (B)). Both show similar trends with rapidly increasing inaccuracy at the outer ends of the transducer's frequency range.

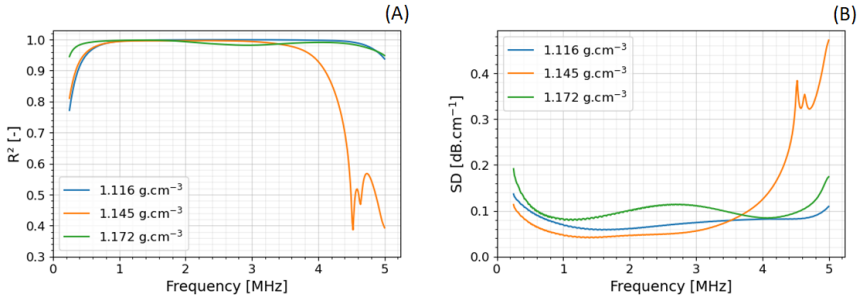

Figure 4.6: *(A) R^2 values plotted in function of frequency representing the proportion of variation of the assessed values for ultrasound attenuation using the conventional processing method. (B) Values of standard deviation plotted in function of frequency representing the reliability of the assessed values for ultrasound attenuation using the alternative processing method.*

The orange curves in both Fig. 4.6 (A) and Fig. 4.6 (B) deviate from the others at the higher frequencies. These deviations are caused by the anomalous recordings as mentioned in

Section 4.2.2.2. They indicate that both processing methods were applied to the same dataset and thus confirm that the conventional processing method is more sensitive to anomalies in the recordings than the alternative method as suggested in Section 4.2.2.2.

4.2.3 Ultrasound attenuation values of mud

To conclude, the average of the two methods is considered to be the best assessment for the ultrasound attenuation in function of ultrasound frequency (Fig. 4.7). The highest reliability applies to frequencies within the FBW of the transducer (see Section 4.2.1). In addition to the relation between ultrasound attenuation and frequency, the results show a linear relation between attenuation and density as well. An empirical equation Eq. 4.5 can therefore be determined expressing the relation between the three properties.

$$\alpha_{\text{mud}} = (7.035f + 8.831).(\rho_{\text{mud}} - 1) \tag{4.5}$$

where α_{mud} is the ultrasound attenuation [dB·cm^{-1}], 7.035 an empirically determined constant multiplier [cm^2·dB·g^{-1}·MHz^{-1}], f the ultrasound frequency [MHz], 8.831 an empirically determined constant coefficient [cm^2·dB·g^{-1}] and ρ_{mud} the mud density [g·cm^{-3}].

This equation is based only on the results within the FBW of the transducer and provides a good agreement with the averaged curves as depicted in Fig. 4.7.

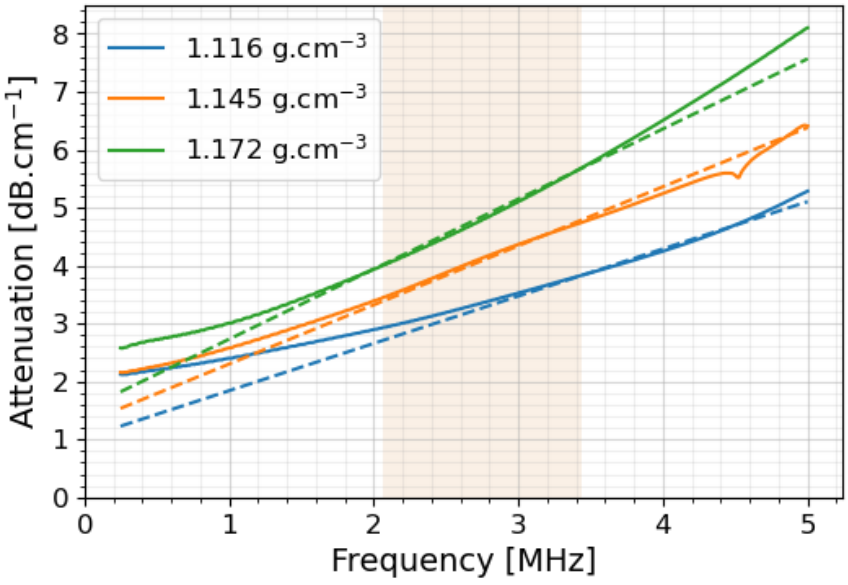

Figure 4.7: *Calculated values of ultrasound attenuation using Eq. 4.5 (dashed curves) compared to the measured values of ultrasound attenuation (solid curves). The FBW of the transducer (see Section 4.2.1) is indicated by the coloured shade.*

4.3 Alternative experiments using various ultrasound equipment

Single element immersible transducers and associated equipment are not always directly available. Nonetheless, a quick assessment of the ultrasound attenuation of a medium can be of great value for a first feasibility study of an experimental setup or new technique. Due to the extensive scope of ultrasound, it is likely that some other type of ultrasound equipment is more readily available. Although the application of such equipment might be very different, it can still be of use to assess the ultrasound attenuation. This was put to the test by performing additional experiments using various ultrasound

equipment designed for a variety of applications and consequently using different ultrasonic principles. Unless mentioned otherwise all these experiments were conducted in the same mud samples as the reference experiments of Section 4.2. Finally, the results are benchmarked against the results of these reference experiments.

4.3.1 Backscattering based techniques

Insonification of mud within the sound frequency band of 1 MHz to 7 MHz results in diffusive scattering of the ultrasound waves (see Section 3.3.3). Similar to the pulse-echo technique (Fig. 4.2 (B)) a single transducer can therefore transmit and record the backscattered signals. Based on these recordings the ultrasound attenuation can be deduced by the fading of the backscattered intensity with increasing penetration depth. The recording of backscattered signals requires highly sensitive transducers. Ultrasound transducers can be designed in different ways to create specific characteristics such as sensitivity. Customisable features are the piezoelectric element and backing, which both can vary in size and thickness (Oly, 2019). High ultrasound frequencies require thin piezoelectric elements, while width and focus depth of the ultrasound beam are proportional to the element size (Alexander and Swanevelder, 2011). The damping capacity of the backing determines the pulse length, which in turn defines the bandwidth of the transducer. High damping results in short pulse lengths and consequently in wide bandwidths. Low damping produces longer pulse lengths and narrow bandwidths. Narrow bandwidth transducers are considered to be more sensitive compared to broadband transducers which in turn result in a higher axial resolution due to the shorter pulse length (Silverman et al., 1995).

4.3.1.1 AQUAscat 1000R

The AQUAscat 1000R (Fig. 4.8) is a device developed by the Aquatec Group Ltd, for on-site monitoring of sediment concentration, turbidity and particle size (Caine, 2014).

Figure 4.8: *Picture of the AQUAscat 1000R, with permission copied from https://www.aquatecgroup.com/aquascat/aquascat-1000r.*

It uses multiple ultrasound transducers which act as transmitter and receiver. The device used for this research is equipped with 4 transducers of 0.5 MHz, 1 MHz, 2 MHz and 4 MHz. Because of its intended application, the transducers are narrowband transducers (Caine and Smerdon, 2007), making them highly sensitive at the cost of poor axial resolution as elaborated in Section 4.3.1. To determine the ultrasound attenuation of mud, all transducers were submerged in the different mud samples. Because the attenuation will be derived

from the recordings of signals backscattered by the scaterrers present in the mud, there should only be sufficient mud in front of the transducers. In the experimental setup used, this is about 110 mm to 120 mm. The output of the recordings are so-called ”counts”, which are proportional to the level of the backscattered signals, normalised on a 16-bit scale. The recordings by each transducer in the mud sample with density 1.116 g·cm^{-3} are presented in Fig. 4.9. They are referred to as Sound Pressure Levels (SPLs), which correspond to the normalised counts expressed on a logarithmic decibel (dB) scale.

The plots of Fig. 4.9 show a clear fading of the backscattered intensity with increasing depth. The slope of the linear trendlines fitting the measurements, are a measure for the attenuation of the ultrasound by mud. Apart from the 4 MHz transducer, all recordings show a peak at approximately 0.115 m. This is due to the reflection on the plastic side of the recipient containing the mud sample. The curve of the recordings with the 4 MHz transducer show that the ultrasound is completely attenuated at a depth of approximately 80 mm. In total 150 scans were conducted with each transducer in each mud sample, resulting in 150 values for ultrasound attenuation per frequency. Final results are obtained by averaging these series of 150 values. The resulting values for ultrasound attenuation per mud density are presented in Fig. 4.10.

4.3.1.2 Medical ultrasound scanners

Probably the most commonly known application of high frequency ultrasound is that of medical imaging. Two medical ultrasound scanners were used to create ultrasound images of mud. The scanners are specifically developed for research purposes, enabling them to cover a broad frequency range. One scanner is the DiPhAS beamformer platform (Risser et al., 2016), the other the High channel Density Programmable Ultrasound System based on consumer

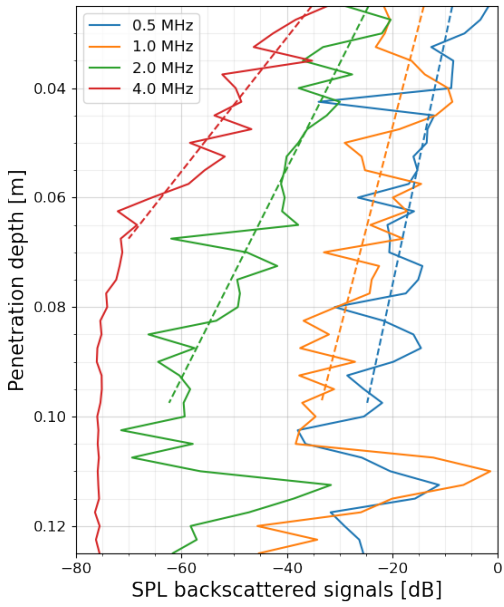

Figure 4.9: *Plots of the recordings by each transducer of the AQUAscat 1000R, while deployed in mud with density 1.116 g·cm^{-3}. The Sound Pressure Levels (SPL) of the received backscattered signals are plotted in function of penetration depth. The linear dashed lines are trendlines fitting the decreasing part of the SPL curve with corresponding colour.*

Electronics (HD-PULSE (Ortega et al., 2015)). A flexible linear array, a phased array and a conventional linear array with corresponding centre frequencies of 2.5 MHz, 3.5 MHz and 7.5 MHz were used to cover a total frequency band from 1.75 MHz to 6.67 MHz, in steps of approximately 0.5 MHz. In B-mode, the magnitude of the received signals is converted into pixel brightness. High amplitudes result in bright pixels and vice versa. Due to the large amount of scatterers present

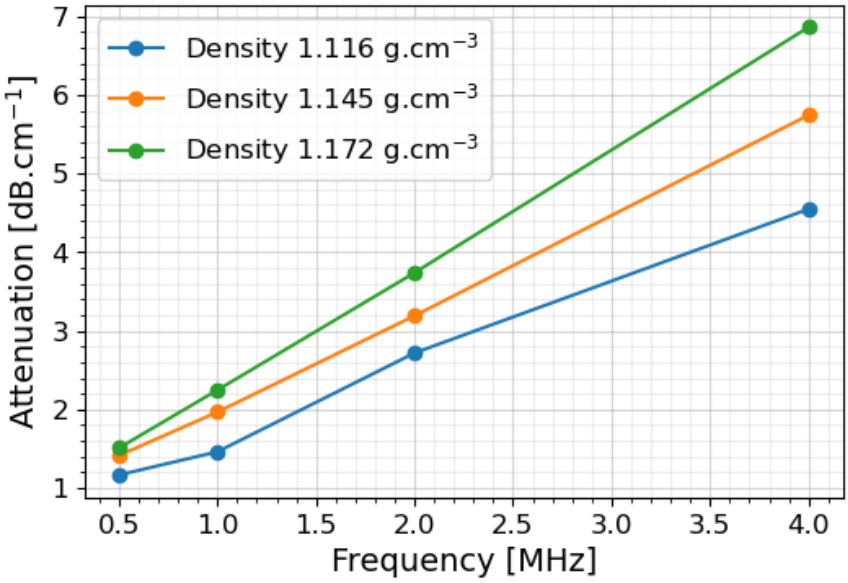

Figure 4.10: *Values of attenuation deduced from the measurements with the AQUAscat 1000R. The values of attenuation correspond to half the slope of the trendlines fitting the recordings (see Fig. 4.9).*

in mud many backscattered waves are created, causing them to interfere with each other by adding up or cancelling each other out. In the end this interference results in pictures with a mix of bright and dark pixels, so-called ”speckle pattern” images (see Section 3.3.3), as presented in Fig. 4.11 (A).

Since the brightness of the pixels in the image is proportional to the SPL of the corresponding received signals, SPL profiles of each pixel column can be derived from the image and plotted in function of penetration depth, as shown in Fig. 4.11 (B). Note that the scale of SPL is inverted compared to that in Fig. 4.9. This inversion is performed during the processing of the recordings into images to obtain the aforementioned proportional correlation between

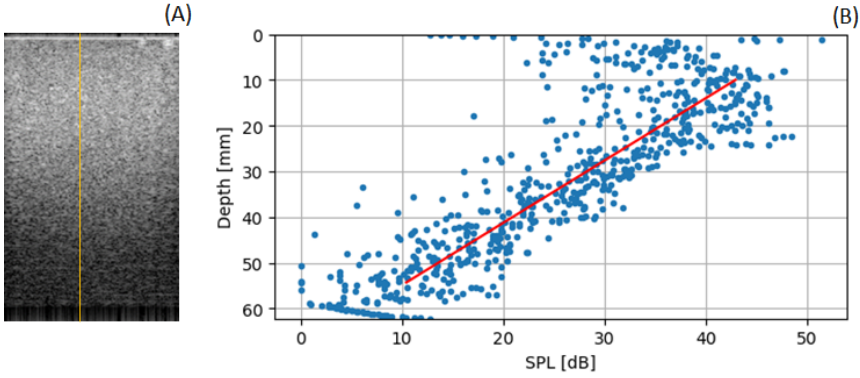

Figure 4.11: *(A) B-mode image of mud, typically showing only speckle pattern. A decreasing trend of pixel brightness with increasing depth can be observed. (B) Plots of the SPL values of the received signals, corresponding to the pixel brightness along the vertical profile indicated with the yellow line in Fig. 4.11 (A). Each marker represents a pixel along the vertical profile. The red trendline illustrates the decreasing trend of SPL values with depth. The slope of the trendline is proportional to the attenuation.*

pixel brightness and magnitude of the recorded signals. Furthermore, the absolute values of SPL of Fig. 4.9 and Fig. 4.11 (B) cannot be compared because of the dynamic range applied during creation of the B-mode images. This dynamic range is defined as the difference between the maximum and minimum values of the signals to be displayed (Lee et al., 2006). To optimise image quality, the dynamic range is different for each image, which then ultimately also applies to the SPL scale reference. The decay of the SPL with increasing penetration depth can be expressed with a linear trendline fitting the SPL plots (indicated with the red line in Fig. 4.11 (B)). The slope of the trendline is a measure of the ultrasound attenuation of mud, similar as with the AQUAscat 1000R (Section 4.3.1.1). This procedure results in a value for ultrasound attenuation for each pixel column. The

picture presented as Fig. 4.11 (A) was generated using the linear array and has a width of 383 pixels. One such picture thus provides 383 values for ultrasound attenuation. For the experiments using the flexible linear array or the phased array, these are 521 or 139 values, respectively. In addition, 20 to 100 images were recorded for each combination of ultrasound frequency and mud sample. For each of these combinations, the average of these obtained values for attenuation is further considered. They are presented in Fig. 4.12.

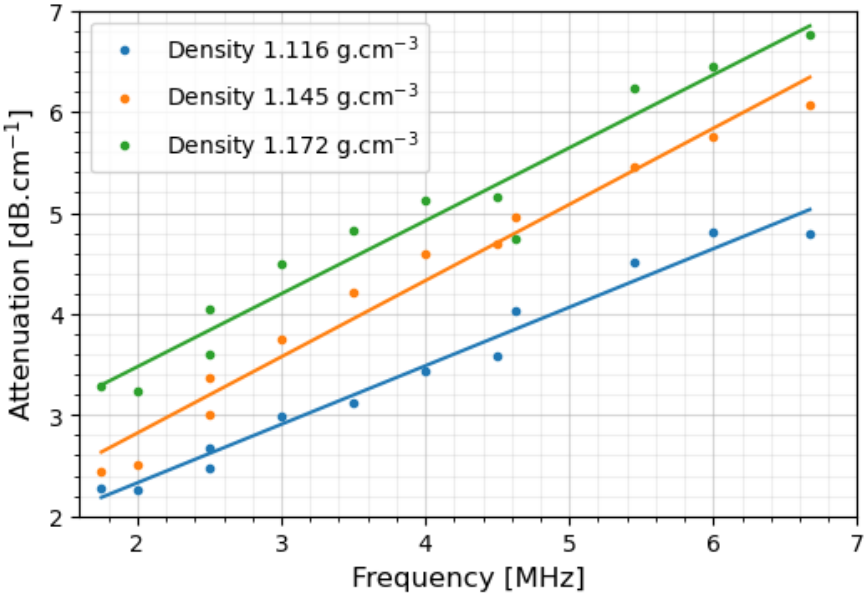

Figure 4.12: *Values of ultrasound attenuation of mud derived from the decay in pixel brightness of ultrasound images generated using medical ultrasound scanners. Different series of values, each for the corresponidng mud density, are shown.*

4.3.2 Through-transmission

As elaborated in Section 4.1, the through-transmission technique is a straight forward technique to assess the attenuation of a liquid. It uses two transducers positioned opposite to each other while submerged in the liquid (Fig. 4.2 (A)). One transducer emits an ultrasound signal which the other transducer receives after propagating through the liquid. Based on Eq. 4.1, the amplitude of the received signals for the through-transmission technique can be expressed as:

$$A_{m,\text{rec}} = A_{m,0}.P_{\text{mud}} \tag{4.6}$$

Where $A_{m,\text{rec}}$ is the amplitude of the received signal [V], $A_{m,0}$ is the amplitude of the initially emitted signal [V] and P_{mud} the propagation loss due to attenuation by the liquid, in this case mud [-].

The value of $A_{m,0}$ is firstly determined by performing the same measurement with the transducers submerged in water. With negligible attenuation by water (Hendee and Ritenour, 2002), $A_{m,\text{rec}}$ can be considered equal to the amplitude of the originally emitted signal $A_{m,0}$. With this amplitude known, the propagation loss in mud can be determined based on the amplitude of the received signal after propagation through mud $A_{m,\text{rec}}$ (Eq. 4.6). In turn this allows to determine the ultrasound attenuation α_{mud} using Eq. 3.1.

As mentioned earlier in Section 3.3.2, the Admodus USP pro is an in situ measuring probe, developed by Synergetik GmbH (Schmidt, 2016). It is used in ports and waterways to determine the density profile of the mud layers at the bottom of navigation channels (Claeys et al. (2012) and Plancke et al. (2018)). Measurements are recorded during gravitational sinking in the water and underlying mud layers. Temperature, speed of sound, acoustic impedance and ultrasound attenuation are measured, creating a depth profile for each of these properties. For density

profiling the measured attenuation values are not used. Nonetheless, because of the presumed relation between ultrasound attenuation and the kinematic viscosity of mud (Section 4.1), measurement of attenuation is already provided. The attenuation is measured using the through-transmission technique. The two transducers used have a centre frequency of 2.25 MHz and a FBW of 50 %. Expressed in MHz this corresponds to a FBW of 1.69 MHz to 2.81 MHz. The output of the attenuation is however given over a wider frequency band of 1.0 MHz to 3.5 MHz in steps of 0.5 MHz. A survey campaign of the mud layers in the Zeebrugge docks of the Port of Antwerp-Bruges (Belgium) was performed in February 2019 (Meire et al., 2021). The average values of attenuation measured during this campaign were previously presented in Fig. 3.14. Within the FBW of the transducers, this also shows a linear correlation between the attenuation and the ultrasound frequency. Outside the FBW the relation is no longer linear, especially at lower frequencies. Based on the outcome of the previously discussed experiments, this non-linear relation is considered to be incorrect, and the recorded attenuation values for 1 MHz are disregarded.

4.3.3 Verification of attenuation values derived from backscattering records and the through-transmission technique

Plots of the values of ultrasound attenuation of Zeebrugge mud with a density of 1.145 g·cm^{-3}, obtained from the reference experiment (Section 4.2) and those obtained from the alternative experiments (Section 4.3) are shown together in Fig. 4.13.

The results with the other mud samples show similar trends and correlations between the different curves as those in Fig. 4.13. The results of the experiments using the AQUAscat 1000R match best with the reference values. However, due

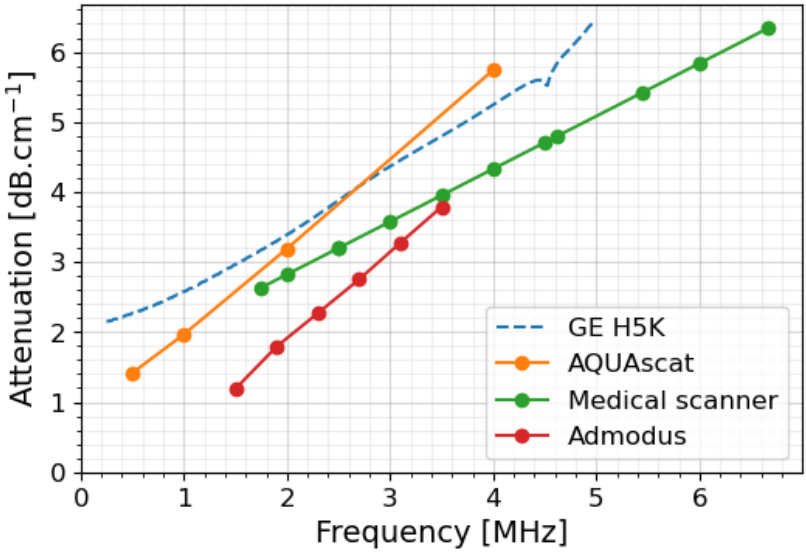

Figure 4.13: *Plots of all values of ultrasound attenuation obtained from the reference experiment (Section 4.2) and the alternative experiments (Section 4.3). The values apply to Zeebrugge mud with density 1.145 g·cm^{-3}.*

to the narrow bandwidth of the transducers, its measurement resolution is low. The results of the Admodus USP pro show an underestimation of the ultrasound attenuation. Unlike the other experiments, these measurements were performed on-site, in unconditioned mud. Since the mud is of the same origin, these anomalous results may be attributed to this. Further study of the relation between the kinematic vicosity of mud and the ultrasound attenuation as suggested in Section 4.1 might provide more insights on this. The outcome of the B-mode experiments show both an underestimation as a different rate of increase in ultrasound attenuation with increasing frequency. This mismatch for the B-mode experiments is probably caused by the design of the transducers. The other devices all have single transducers with large piezoelectric

elements. Medical ultrasound scanners however use arrays which consist of multiple small transducers activated together or in a controlled sequence. While they provide high axial resolution they are less sensitive (Silverman et al., 1995). Hence, they are less suitable for recording small differences in low signal amplitudes as in the case of backscattered signals.

4.4 Summary of experiences on the different methods used to determine the ultrasound attenuation by mud

By means of various lab experiments the ultrasound attenuation of mud has been determined in function of ultrasound frequency and for different mud densities. Because of the settling behaviour of mud, it was necessary to deviate from the conventional method to determine the attenuation of a fluid. Reliable results were obtained within the FBW of the transducer used. To allow estimation of attenuation outside the range of frequencies and densities of the experiments conducted, an empirical formula representing the relation between the three parameters was defined, matching well with the output of the experiments. The generated data will be of use for further development of UIV in mud by assisting in finding the optimal operating ultrasound frequency maximising the depth range. In addition, the results may be useful in searching for the assumed relationship between ultrasound attenuation and kinematic viscosity (see Section 4.1). Ultimately, this may lead to a technique for on-site monitoring of this rheological mud property, which would be of great value for port and waterway authorities.

A known method to determine the ultrasound attenuation of fluids was applied in the lab experiments using immersible ultrasound transducers. By using two different methods of processing, it was however shown that, when at rest, mud

can't be considered as a homogeneous fluid. While the conventional method assumes a homogeneous fluid, this is not applicable for mud due to its changing properties with time. On the other hand, the applied alternative processing method suffers from higher error propagation due to the requirement of results from multiple measurements. The average of the two is therefore considered as the best assessment for now. For similar experiments in the future it is advised to conduct the ultrasound scans while preventing sedimentation of the conditioned mud. This can be achieved, for example, by continuous mixing while performing the ultrasound scans. For this option, the impact of flow velocity on the recordings should however be considered. On a general note, only results for frequencies within the FBW should be taken into account as reliability of the measurements deteriorate drastically outside this bandwidth. A second series of experiments showed that other ultrasound devices, developed for various applications, can be used for a first quick assessment of the ultrasound attenuation of a liquid. A good understanding of the original application of the device and the associated specifications of the transducers is however recommended to fully appreciate the outcome of such measurements.

Bibliography

Alexander N. and Swanevelder J. Resolution in ultrasound imaging. *Continuing Education in Anaesthesia, Critical Care & Pain*, 11(5): 186–192, 2011.

Berlamont J., Ockenden M., Toorman E. and Winterwerp J. The characterisation of cohesive sediment properties. *Coastal Engineering*, 21(1–3):105–128, 1993.

Caine S. *AQUAscat 1000 User Manual 910-0001 1.07*. Aquatec Group Ltd., Basingstoke RG24 8FW, UK, 2014.

Caine S. and Smerdon A. The factors that affect the performance of multiple frequency acoustic backscatter instruments: The evaluation of a commercial abs system. In *Proceedings of the 2nd International Conference & Exhibition on Underwater Acoustic Measurements: Technologies and Results*, pages 1055–1062, Heraklion, Greece, 25–29 June 2007.

Carlson J., van Deventer J., Scolan A. and Carlander C. Frequency and temperature dependence of acoustic properties of polymers used in pulse-echo systems. In *IEEE Symposium on Ultrasonics, 2003*, volume 1, pages 885–888, Honolulu, HI, USA, 05–08 October 2003 2003. IEEE. doi: 10.1109/ULTSYM.2003.1293541.

Chaffaï S., Padilla F., Berger G. and Laugier P. In vitro measurement of the frequency-dependent attenuation in cancellous bone between 0.2 and 2 mhz. *The Journal of the Acoustical Society of America*, 108(3):1281–1289, 2000. doi: 10.1121/1.1288934.

Claeys S., Dierikx B., Paul S. and Reenen J. Fluid mud density determination in navigational channels. In *Proceedings of Hydro 12 - Taking Care of the Sea*, pages 1–7, Rotterdam, The Netherlands, 13–15 november 2012. Hydrographic Society Benelux. doi: 10.3990/2.228.

Claeys S., Staelens P., Vanlede J., Heredia M., Van Hoestenberghe T., Van Oyen T. and Toorman E. A. A rheological lab measurement

protocol for cohesive sediment. In *INTERCOH2015: 13th International Conference on Cohesive Sediment Transport Processes*, pages 21–22, Leuven, Belgium, 7–11 September 2015.

Dahl P. H. High-frequency underwater sound. In *Wiley encyclopedia of electrical and electronics engineering*. Wiley-Interscience, Hoboken, NJ, USA, 1999. doi: 10.1002/047134608X.W7430.

Dankers P. *On the hindered settling of suspensions of mud and mud-sand mixtures*. PhD thesis, Delft University of Technology, Delft, The Netherlands, 2006.

de Wit P. *Liquefaction of cohesive sediments caused by waves*. PhD thesis, Delft University of Technology, Delft, The Netherlands, 1995.

Delefortrie G., Vantorre M., Verzhbitskaya E. and Seynaeve K. Evaluation of safety of navigation in muddy areas through real-time maneuvering simulation. *Journal of Waterway Port Coastal and Ocean Engineering - ASCE*, 133(2):125–135, 2007. doi: 10.1061/(ASCE)0733-950X(2007)133:2(125).

Doddugollu S. P. A numerical study of the flow of fluid mud in a cylinder and vane rheometer. In *INTERCOH2021: 16th International Conference on Cohesive Sediment Transport Processes*, page pp. 17, Delft, The Netherlands, 13-17 September 2021.

Doddugollu S. P. and Toorman E. The determination of the true equilibrium flow curve for fluid mud in a wide-gap Couette rheometer. *Journal of Non-Newtonian Fluid Mechanics*, 321, 2023. doi: 10.1016/j.jnnfm.2023.105122.

Drinkwater B. W. and Wilcox P. D. Ultrasonic arrays for non-destructive evaluation: A review. *NDT & E International*, 39:525–541, 2006. doi: 10.1016/j.ndteint.2006.03.006.

Ultrasonic Transducers For Flaw Detection and Sizing. GE Sensing and Inspection Technologies, 2008.

Gibbs R. J. Settling velocity, diameter, and density for flocs of illite, kaolinite, and montmorillonite. *Journal of Sedimentary Research*, 55(1):65–68, 1985. doi: 10.1306/212F860C-2B24-11D7-8648000102C1865D.

Ginzel E. and Turnbull B. Determining approximate acoustic properties of materials. *e-Journal of Nondestructive testing (NDT)*, 21(12), 2016.

Hendee W. R. and Ritenour E. R. Chapter 19: Ultrasound waves. In *Medical Imaging Physics*, pages 303–316. Wiley–Liss, New York, USA, 2002. doi: 10.1002/0471221155.ch19.

Hsu W. Y., Hwung H. H., Hsu T. J., Torres-Freyermuth A. and Yang R. Y. An experimental and numerical investigation on wave-mud interactions. *Journal of Geophysical Research: Oceans*, 118(3): 1126–1141, 2013. doi: 10.1002/jgrc.20103.

Imai G. Settling behavior of clays suspension. *Soils and foundations*, 20(2):61–77, 1980. doi: 10.3208/sandf1972.20.2_61.

Jacobs W. *Sand-mud erosion from a soil mechanical perspective*. PhD thesis, Delft University of Technology, Delft, The Netherlands, 2011.

Jondahl M. H. and Viumdal H. Developing ultrasonic soft sensors to measure rheological properties of non-newtonian drilling fluids. *Tm - Technisches Messen*, 86(12):744–757, 2019. doi: 10.1515/teme-2019-0039.

Jondahl M. H., Viumdal H., Mozie K. N. and Mylvaganam S. Rheological characterization of non-newtonian drilling fluids with non-invasive ultrasonic interrogation. In *IEEE International Ultrasonics Symposium (IUS)*, pages 1–4, Washington, D.C., USA, 6-9 September 2017. doi: 10.1109/IUS36762.2017.

Lee D., Kim Y. S. and Ra J. B. Automatic time gain compensation and dynamic range control in ultrasound imaging systems. In *Medical Imaging 2006: Ultrasonic Imaging and Signal Processing*. SPIE, 16 March 2006. doi: 10.1117/12.653000.

Meire D., Claeys S., De Maerschalck B. and Mostaert F. Evaluatie van meetinstrumenten voor de bepaling van slib karakteristieken: Deelrapport 3: Meetcampagne februari 2019 (" Evaluation of measurement equipment for determining mud characteristics: Sub-report 3: Measurement campaign february 2019"). In *WL Rapporten 18 059 3 Versie 5.0.* Waterbouwkundig Laboratorium, Antwerp, Belgium, 2021.

Norisuye T., Sasa S., Takeda K., Kohyama M. and Tran-Cong-Miyata Q. Simultaneous evaluation of ultrasound velocity, attenuation and density of polymer solutions observed by multi-echo ultrasound spectroscopy. *Ultrasonics*, 51(2):215–222, 2011. doi: 10.1016/j.ultras.2010.08.005.

Ultrasonic Transducers - Technical Notes. Olympus Scientific Solutions Americas Corporation, 2019.

Ono K. A comprehensive report on ultrasonic attenuation of engineering materials, including metals, ceramics, polymers, fiber-reinforced composites, wood and rocks. *Applied Sciences*, 10(7):2230, 2020. doi: 10.3390/app10072230.

Ortega A., Lines D., Pedrosa J., Chakraborty B., Komini V., Gassert H. and D'hooge J. Hd-pulse: High channel density programmable ultrasound system based on consumer electronics. In *Proceedings of the IEEE International Ultrasonics Symposium (IUS)*, pages 2121–2123, Taipei, Taiwan, 21–24 October 2015. doi: 10.1109/ULTSYM.2015.0516.

Pierce A. D., Siegmann W. L. and Brown E. Analytical discussion of past measurements of acoustic attenuation in mud sediments and of possible future experimental approaches. In *Proceedings of Meetings on Acoustics*, volume 25, Jacksonville, Florida, USA, 2–6 November 2015. doi: https://doi.org/10.1121/1.4934094.

Plancke Y., Meire D. and Mostaert F. Studie naar meettechnieken voor het onderzoeken van de opbouw van sliblagen in het Deurganckdok: Deelrapport 1 – Bundeling van de belangrijkste resultaten uit 3 masterproeven uitgevoerd op de Universiteit

Antwerpen ("Study of measurement techniques for the investigation of the structure of mud layers in the Deurganckdok: Subreport 1 - Collection of the most important results of 3 master theses performed at University of Antwerp"). In *WL Rapporten 12 160 1 Versie 3.0.* Waterbouwkundig Laboratorium, Antwerp, Belgium, 2018.

Püttmer A., Hoppe N., Henning B. and Hauptmann P. Ultrasonic density sensor-analysis of errors due to thin layers of deposits on the sensor surface. *Sensors and Actuators A: Physical*, 76(1–3): 122–126, 1999. doi: 10.1016/S0924-4247(98)00365-3.

Risser C., Welsch H. J., Fonfara H., Hewener H. and Tretbar S. High channel count ultrasound beamformer system with external multiplexer support for ultrafast 3d/4d ultrasound. In *Proceedings of the IEEE International Ultrasonics Symposium (IUS)*, pages 1–4, Tours, France, 18–21 September 2016. doi: 10.1109/ULTSYM.2016.7728714.

Schmidt F. *Operating manual for Admodus USP pro, Operating Manual Version 1.4*. Synergetik GmbH, 2016.

Selfridge A. R. Approximate material properties in isotropic materials. *IEEE Transactions on Sonics and Ultrasonics*, SU–32 (3):381–394, 1985. doi: 10.1109/T-SU.1985.31608.

Shung K. K. High frequency ultrasonic imaging. *Journal of Medical Ultrasound*, 17(1):25–30, 2009. doi: 10.1016/S0929-6441(09)60012-6.

Silverman R., Vinarsky E., Woods S., Lizzi F. and Coleman D. The effect of transducer bandwidth on ultrasonic image characteristics. *Retina*, 15(1):37–42, 1995. doi: 10.1097/00006982-199515010-00008.

Strohm E. M. and Kolios M. C. Sound velocity and attenuation measurements of perfluorocarbon liquids using photoacoustic methods. In *Proceedings of the 2011 IEEE International Ultrasonics Symposium*, pages 2368–2371, Orlando, FL, USA, 18–21 October 2011. doi: 10.1109/ULTSYM.2011.0588.

Szabo T. L. *Diagnostic Ultrasound Imaging: Inside out*. Elsevier Academic Press, Hoboken, NJ, USA, 2004a.

Szabo T. L. Chapter 4: Attenuation. In *Diagnostic Ultrasound Imaging: Inside out*, pages 71–95. Elsevier Academic Press, Hoboken, NJ, USA, 2004b.

Toorman E. and Berlamont J. A hindered settling model for the prediction of settling and consolidation of cohesive sediment. *Geo-Marine Letters*, 11:179–183, 1991. doi: 10.1007/BF02431009.

Toorman E. A. and Berlamont J. E. Fluid mud in waterways and harbours: an overview of fundamental and applied research at KU leuven. In *PIANC Yearbook 2015 - Edition 2015*, pages 211–218, 01 2015.

Wróbel G. and Pawlak S. A comparison study of the pulse- echo and through-transmission ultrasonics in glass/epoxy composites. *Journal of Achievements in Materials and Manufacturing Engineering*, 22(2):51–54, 6 2007.

Zheng R., Le L. H., Sacchi M. D., Ta D. and Lou E. Spectral ratio method to estimate broadband ultrasound attenuation of cortical bones in vitro using multiple reflections. *Physics in Medicine & Biology*, 52(19), 2007. doi: 10.1088/0031-9155/52/19/008.

Chapter 5

Time resolved Ultrasound Image Velocimetry (UIV) in mud

5.1 Introduction

The concept of Ultrasound Image Velocimetry (UIV) in mud first entails generating successive ultrasound images of flowing mud from a stationary reference. As with conventional PIV (see Section 1.1.3.2), these images are then processed with a cross-correlation algorithm to determine the displacement of speckle patterns between two consecutive images. Knowing the time span between the two images, the velocity can be deduced. The obtained velocities and directions are considered to correspond to the flows in the mud. The output consists of a field of velocity vectors. The size of the vector field corresponds to the size of the images, while the vectors indicate the magnitude of the velocity and direction of the flow at different positions in the plane visualised by the images. The application of UIV in fluid dynamics is relatively new and has developed over the past two decades for various applications. As an example, Crapper et al. (2000) was one

of the first to report the application for sediment transport. Yet only a low density suspension of kaolin (clay mineral) was used at very low flow rates ($<$ 60 mm·s^{-1}). Further development of UIV on sediment laden flows was performed by Chinaud et al. (2010) by identifying the limiting factors. The limited recordable flow rates in particular posed a problem for further use of UIV. This is mainly caused by the conventional operating principle of an ultrasonic array for diagnostic imaging. An ultrasonic array is a transducer that contains a number of individually connected piezoelectric elements (Szabo, 2004b). These elements convert electrical energy into mechanical energy, in this case sound waves, and vice versa. Depending on the purpose for which the array is designed, the width of these elements can vary from 0.2 mm to 1.5 mm. To optimise image resolution, the elements are excited one after the other. The time between two excitations allows sufficient time for the sound wave to propagate to the desired depth and back to the transducer after reflection. In this process each excitation generates a narrow segment of the final image. Merging all the segments forms the overall image. This is referred to as ”electronic sweeping” (Szabo, 2004c). The time required to obtain the total image is thus equal to the number of elements times the return time of the sound wave after reflection at the desired depth range (Fig. 5.1).

Because in diagnostic imaging the importance of image quality prevails, this incremental process, which results in a ”slow” acquisition rate, is not an issue. Since the application of UIV requires the ability to capture the displacement at the flow rate between two consecutive images, the acquisition rate in sweep mode may quickly prove insufficient, even for a limited depth range. This was addressed by Poelma and Fraser (2013) by introducing a novel steering sequence of the elements, referred to as ”interleaved imaging”, enabling to double the frame rate. This technique however requires access to the transducer imaging read-out protocol allowing it only to be used with research oriented equipment. Another

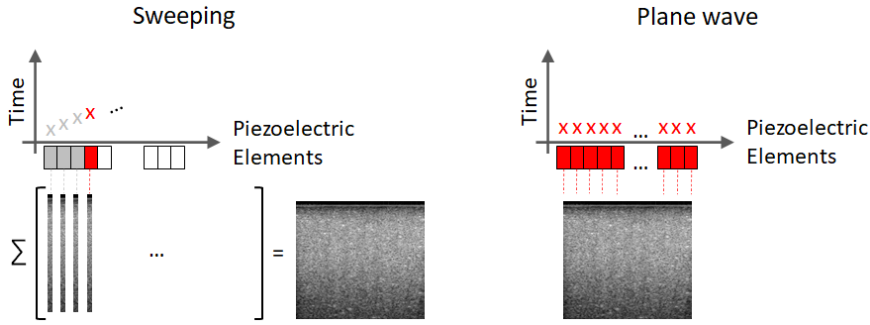

Figure 5.1: *Sketches outlining the difference between the operating principles of "sweeping" and "plane wave" using a linear ultrasonic array.*

operational mode that allows higher acquisition rates is used in plane wave imaging. Hardware limitations aside, plane wave imaging allows frame rates in the kilohertz range (Tanter and Fink, 2014). In plane wave mode, all piezoelectric elements are excited simultaneously. In this way, an image with a width equal to the width of the array is generated in the time frame of a single acquisition. Consequently, it is the number of elements times faster than sweeping (Fig. 5.1). This increase in acquisition rate does come at the expense of image quality. When generating speckle pattern images this is however trivial. Recently, plane wave imaging has been further developed for medical purposes, making it more available in medical devices (Jensen, 2017). Plane wave imaging was therefore used by Dash et al. (2022) to further develop UIV in particle-laden flows at higher flow rates up to almost 1.5 $\mathrm{m{\cdot}s^{-1}}$.

Meanwhile, the application of UIV to sediment-laden flows has found various applications. Gurung et al. (2016) used UIV to determine rheological properties of the fluid. Others used UIV to characterise the topography of a sediment bed (Zou et al., 2015) or infer sediment concentration from local scattering intensity (Zou et al., 2014). However, clay suspensions and drilling fluids were used in these studies and not natural muds.

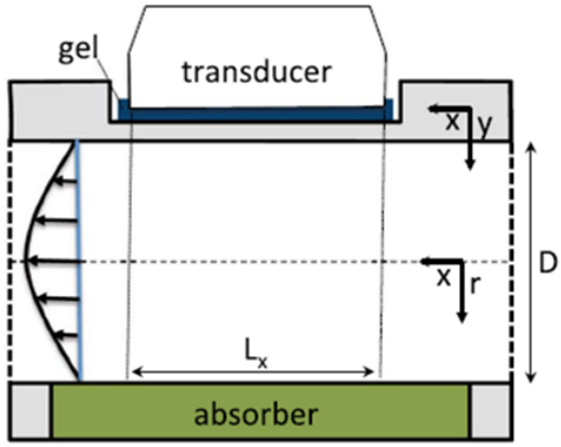

Figure 5.2: *Sketch of an experimental setup, previously used by Gurung and Poelma (2016) to study the capability of UIV on sediment-laden flows. The sketch shows a close-up of the interface between the ultrasound transducer and the pipe. This image is copied from Gurung and Poelma (2016). The encapsulation of the fluid by the pipe material causes unwanted loss of ultrasound radiation energy.*

In addition, most experiments were performed with a fluid flowing through a pipe (see Fig. 5.2), which restricts the depth and makes it impossible to determine the full depth range of UIV. Moreover, the intermediate pipe material between the ultrasound transducer and the mud causes unwanted loss of ultrasound energy. This loss is caused both by reflection at the two interfaces, transducer-pipe and pipe-fluid, and by attenuation while propagating through the pipe material. To fully utilise the potential of the ultrasound energy, it is therefore preferred to install the ultrasound transducer flush with the walls containing the mud, as illustrated in Fig. 5.3.

Because of the interaction between numerous backscattered signals, B-mode ultrasound imaging in mud results in speckle images (see Chapter 3). The variation in pixel brightness

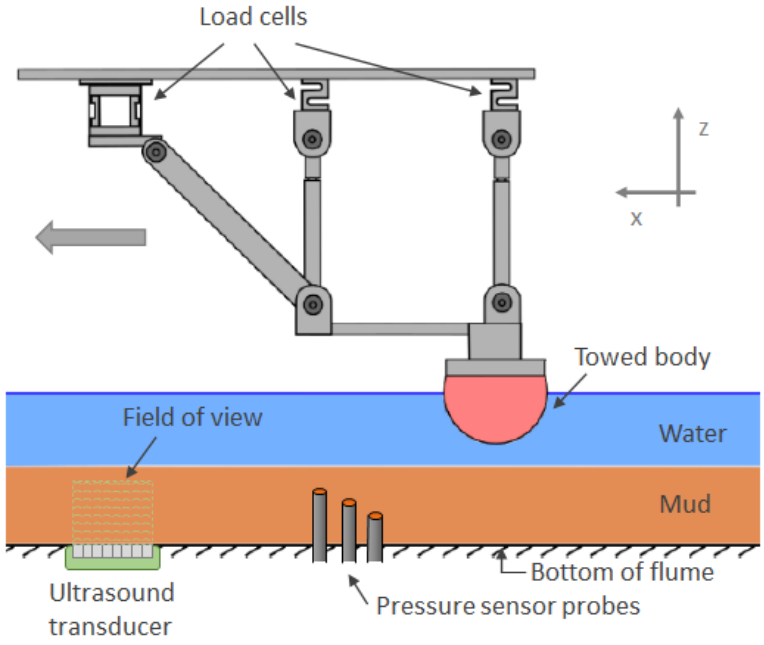

Figure 5.3: *A duplication of the sketch of the experimental setup of Sotelo et al. (2022, 2023), previously presented as Fig 1.6, but now with the addition of the ultrasound transducer (bottom left) to illustrate how UIV could be implemented in this setup.*

makes such images ideal for cross-correlation techniques like PIV. The appearance of the speckle patterns is determined by the position of the scatterers in the fluid. Assuming that the movement of the particles is determined by the flow in the fluid, such techniques can be used to record the flow dynamics in that fluid. The intensity of the backscattered signals is reflected in the brightness of the pixels on the generated image. High intensity results in bright pixel brightness and vice versa. In Chapter 4 it is shown that due to attenuation of the ultrasound by the mud, the intensities of the backscattered signals decrease with depth and hence also the brightness of the pixels of the images (see Fig. 4.11). This degradation

of speckle intensity with depth is likely to affect the depth range of the measurements. Consequently, there must be a minimum pixel brightness level for the PIV algorithm to work effectively. The experiments presented in Chapter 4 showed that the ultrasound attenuation of Zeebrugge mud is governed by the ultrasound frequency and the density of the mud. Moreover, ultrasound imaging uses a single and constant ultrasound frequency. This implies that in the case of mud with homogeneous density, the attenuation and hence the rate of degradation of pixel brightness is constant, as illustrated by the linear trendline in Fig. 4.11. The slope of the trendline reflects the attenuation. A decrease in attenuation (steeper slope of the trendline) is therefore expected to increase the depth range. Secondly, by increasing the intensity of the emitted ultrasound, the intensity of the reflected signals and in turn the overall pixel brightness on the image will increase proportionally. This way the trendline shifts to higher SPL values, hence enhancing the depth range. The effects of both adjustments are conceptually illustrated in Fig. 5.4. In addition, due to the degrading quality of the speckle image with depth, the accuracy of velocity measurements is expected to decrease with depth. Hence, indirectly, increasing the depth range will also enhance the accuracy of the velocity measurements at a given depth.

In this chapter the dependencies of UIV in mud are studied. Two series of experiments with UIV applied in Zeebrugge mud were conducted to facilitate this. As discussed in Chapter 1, the implementation of UIV in an experimental setup similar to the setup used by Sotelo et al. (2022, 2023) is ultimately envisaged. An example of how this can be achieved is depicted in Fig.5.3. The specifications of this setup are therefore used to set the goals for the application of UIV in mud. The first series of experiments focuses on the limits of recordable flow velocity and the accuracy of the velocity measurements. The towing velocities applied by Sotelo et al. (2022, 2023) range from 100 mm·s^{-1} to 500 mm·s^{-1}. Based

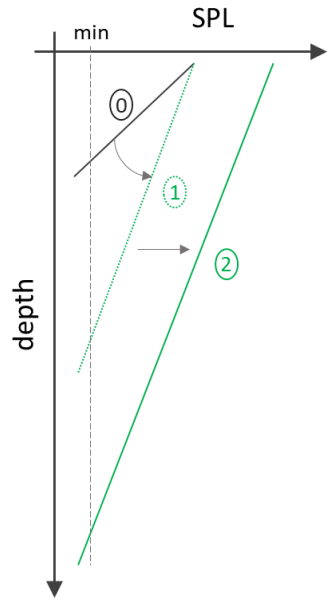

Figure 5.4: *Sketch illustrating how the proposed adjustments can improve the depth range of UIV. Lines ⓪, ① and ② indicate the degrading SPL with depth, like the trendline in Fig. 4.11. The minimum required SPL for application of UIV is marked with the dashed line. The intersections with the degration trendlines indicate the depth range of UIV. Trendline ⓪ illustrates the initial SPL degration with depth. Lowering the attenuation changes the slope of the trendline, illustrated by trendline ①. Increasing the initial SPL shifts the trendline to the right, illustrated by trendline ②.*

on the potential theory of flow around the cylinder (Anderson, 1991), maximum flow velocities double the towing velocity are to be expected. Multiple velocities ranging between 500 mm·s^{-1} and 1500 mm·s^{-1} were therefore applied during the experiments. The primary objective of the second series of experiments is to determine the limiting factor(s) of the depth range of UIV in fluid mud. For this, UIV was applied in flowing mud with variable ultrasound frequency and intensity, and mud

density. The thickness of the mud layer in the setup used by Sotelo et al. (2022, 2023) varies between 0.25 m and 0.5 m. A depth range of the UIV technique of minimum 0.25 m is thus envisaged. Based on the results of the experiments, it is examined whether the depth range is governed by attenuation and thus dependent on ultrasound frequency and mud density, as presumed. Subsequently, the influence of these variables on the depth range is evaluated to determine how they can be tweaked to enhance the depth range.

5.2 Ultrasound imaging

5.2.1 Ultrasound imaging equipment

Multiple ultrasound arrays were used to cover a wide spectrum of ultrasound frequencies. A lower range from 1.75 MHz to 2.5 MHz was covered using a flexible linear array, type XACT-10134 by Olympus. This array consists of 128 elements with a pitch (center-to-center distance between adjacent elements) of 0.41 mm and generates an ultrasound spectrum with a centre frequency of 2.5 MHz over a fractional bandwidth of 55 %. A mid-range from 2.5 MHz to 4.5 MHz was covered using a phased array transducer, type P2-5AC from Samsung. This array consists of 64 elements with a pitch of 0.22 mm and generates an ultrasound spectrum with a centre frequency of 3.5 MHz over a fractional bandwidth of 60 %. A final range from 4.62 MHz to 6.67 MHz was covered using a linear array transducer, type L7-Xtech from Vermon. This array consists of 128 elements with a pitch of 0.3 mm and generates an ultrasound spectrum with a centre frequency of 7.5 MHz over a fractional bandwidth of 60 %. The flexible linear and phased arrays were operated by the HD-Pulse system Ortega et al. (2015), while the linear array was controlled by the DiPhAS beamformer system (Risser et al., 2016).

Both the difference in operating system and array transducer design can affect the resulting images. Of the aforementioned available ultrasound equipment, the flexible linear array transducer and the DiPhAS control system are the biggest outliers in this regard. To maintain the flexibility of the array transducer, the damping material behind the piezoelectric elements is minimised. Damping is generally used to reduce the pulse length of the ultrasound signals, thereby improving the axial resolution of the images (Fig. 5.5, Alexander and Swanevelder (2011).

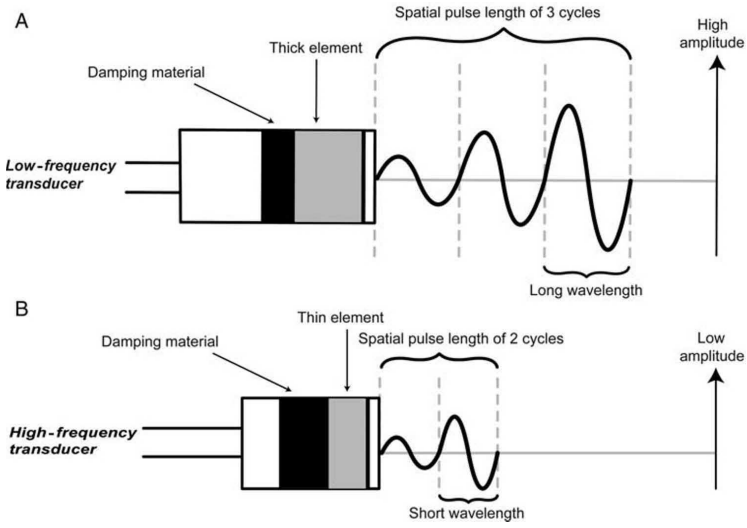

Figure 5.5: *A sketch illustrating the influence of the amount of damping material embedded in the transducer on the emitted ultrasound. This figure is copied from Alexander and Swanevelder (2011)*

More conventional array transducers like the phased and the linear arrays therefore have more damping material and hence greater damping capacity. Apart from axial resolution, damping capacity also affects other properties of transducers. Less damping, for instance, increases the intensity of the emitted ultrasound, enhances the sensitivity of the transducer

and reduces its bandwidth (Silverman et al., 1995). To allow for an unbiased evaluation of the physical interactions between the ultrasound and the mud, the choice was made to disable any gain (amplification) of the received signals. This was not successful when using the DiPhAS operating system for the linear array, where Time Gain Compensation (TGC) was applied during the acquisitions. TGC is a function in ultrasound imaging to compensate for the accumulating attenuation with depth by applying increasing gain with depth, resulting in better image quality. In ultrasound imaging, depth is derived from the time between transmission of the ultrasound and receipt of the reflection signals, based on the speed of sound through the medium. Depth and time are thus related when using ultrasound. How the TGC was applied during the acquisitions could not be retrieved from the system. Because of these major differences in equipment, the results of experiments using different equipment cannot be compared. Yet even when limiting comparison of the results to experiments conducted with the same equipment, the SPL scale can still vary because of the decreasing intensity of the emitted sound waves as the ultrasound frequency deviates from the centre frequency of the transducer. Therefore, in this study, only the results of experiments with the same equipment are compared and the comparison is based solely on a difference in trends.

5.2.2 Image data processing

As conventionally done in medical ultrasound imaging the recordings are converted in digital images by envelope detection (absolute value of Hilbert transform), log compression (20·log10(Data)) and normalisation to maintain a dynamic range of -60 dB to 0 dB. Furthermore, a spatial resolution of 10 pixels per mm was set for all images. No additional image processing was performed prior to analysis by the PIV algorithm.

5.3 Validity of UIV applied in mud

5.3.1 Experiments

5.3.1.1 Experimental setup

To validate a cross-correlation flow velocity measurement technique, the technique is usually applied to a flow with known or measured properties. In this way, the output of the technique can be verified. As discussed in Chapter 1, current existing CFD models developed to simulate the behaviour of mud are based on simplifications and do not take into account the full complexity of mud. Therefore, an induced mud flow, however controlled, cannot yet be used for validation. Moreover, because of the preferred open-channel arrangement (Fig. 5.3), flow measurement using an alternative measurement technique, such as an electromagnetic flowmeter (Dash et al., 2022), is no option either. Therefore, it was chosen to work the other way round, by moving the recording device, in this case the ultrasonic transducer, through stationary mud at known velocities. Using simple mechanics the motion of the transducer, and hence the relative velocity between the transducer and the mud, can be well controlled. In this way, the velocities at which the transducer is moved can be used to validate the output of the UIV. Therefore, the accuracy of the velocities imposed on the transducer were verified first. To enable transmission of ultrasound radiation in the mud, the emitting part of the ultrasonic transducer must be immersed in the mud. Moving the transducer while immersed will induce flows in the mud, biasing the flow measurements. Because of the viscosity of the mud (Sotelo et al., 2022), the depth to which flow is induced is expected to be limited.

To facilitate this, a small-scale setup as shown in Fig. 5.6 and Fig. 5.7 was prepared. The setup consists of a basin of about 100 mm wide, 100 mm high and 500 mm long, to contain the

mud. The mud used originates from the Zeebrugge docks of the Port of Antwerp-Bruges (Belgium). Prior to starting the experiments, it was prepared to a homogeneous density of 1.15 g·cm^{-3} by mixing it with seawater sampled at the same location. The experiments took about 30 minutes. Although settling starts immediately when the mud is left at rest, it is not yet significant in such a time frame (see Chapter 2). A uniform density is therefore considered throughout the experiments. Consequently, the ultrasound attenuation and ultimately the depth range of the UIV technique can be considered equal for all experiments. Similarly, the speed of sound through mud, which is hardly affected by the density of the mud anyway, can also be considered the same for all experiments and was set at 1465 mm·s^{-1} (see Chapter 3) to determine the vertical scale (Z-axis in Fig. 5.6 and Fig. 5.8). A rail was mounted above the basin to provide horizontal motion of a carriage. A stepper motor was installed next to the rail to drive the carriage, which was transmitted by a belt. The resolution of the stepper motor (movement per step) was fixed to allow accurate control of the velocity. A downward stand was attached to the carriage on which the ultrasonic transducer was clamped. The horizontality of the rail and verticality of the stand were set with the accuracy of a conventional spirit level. The tip of the transducer, from where the ultrasound radiation is transmitted and received, is inserted several millimetres into the mud. This is to avoid the presence of a layer of air between the transducer and the mud. Such a layer of air would cause high reflection and thus prevent the ultrasound energy from entering the mud. Because of the corrosive nature of the seawater present in the mud, the tip of the transducer was protected by a sheath-shaped rubber. The rubber was filled with water, again to avoid the presence of air and maximise the transfer of radiation from the transducer to the rubber material.

Prior to the experiments, the imposed velocities were verified by measuring the actual mean velocities and comparing them with the set target velocities. For this purpose, the carriage

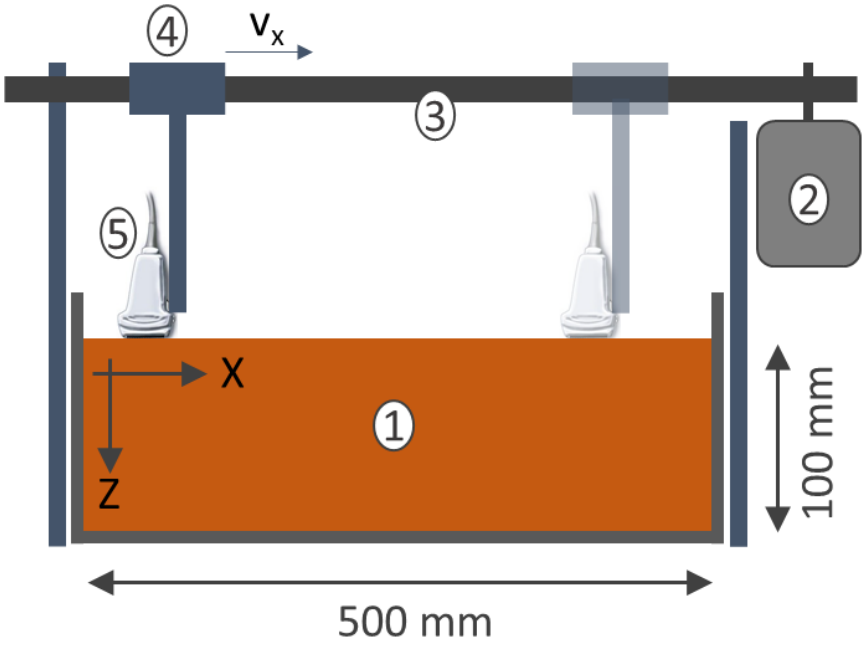

Figure 5.6: *Sketch of the experimental setup used during this study: (1) basin to contain the mud; (2) stepper motor providing the drive to move the carriage at a velocity v_x; (3) belt transmitting the drive from the stepper motor to the carriage; (4) carriage with vertically fixed stand; (5) ultrasound array transducer clamped to the stand.*

was disconnected from the belt to allow full revolutions of the belt. A small piece of reflective tape was applied to the belt. The length of the belt is known and specified by the supplier. Each test was performed at a different velocity. The stepper motor was programmed to run just over eleven times the belt length ($>$ 11 revolutions) per test. A tachometer, in a static position, was used to measure the time between the first and last pass of the reflective tape. This time corresponds to ten revolutions, excluding any accelerations, i.e. at uniform velocity. This allows the mean velocity to be determined by dividing ten times the length of the belt by it. The carriage

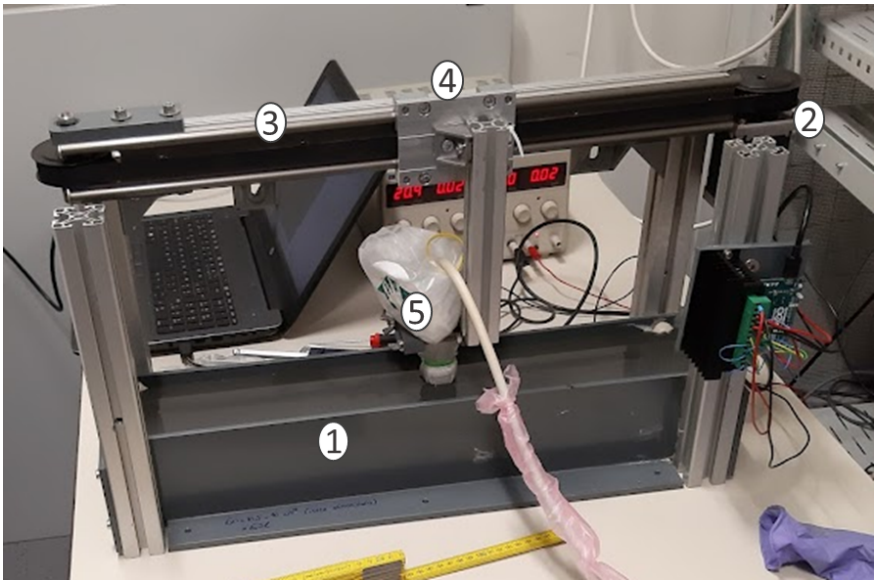

Figure 5.7: *A picture of the actual setup as sketched in Fig. 5.6. The labels identifying the main components correspond to those of Fig. 5.6.*

velocity is verified by assessing the ratio of the measured mean velocity to the set target velocity (Eq. 5.1). At a velocity of 500 mm·s^{-1}, a ratio of 99.72 % was achieved. For higher velocities, this ratio decreased by 0.15 % per velocity increment of 250 mm·s^{-1} .

$$\frac{v_{\text{mean}}}{v_{\text{set}}} = \frac{\frac{10 \cdot l_{\text{belt}}}{t_{10\ \text{rev}}}}{v_{\text{set}}} \tag{5.1}$$

Where v_{mean} is the assessed mean velocity of the belt and thus the carriage [mm·s^{-1}], v_{set} is the set target velocity [mm·s^{-1}], l_{belt} the length of the belt [mm] and $t_{10\ \text{rev}}$ is the time measured for ten revolutions of the belt [s].

For UIV validation experiments, only the phased array transducer was used at its centre frequency of 3.5 MHz.

During the experiments it was operated in plane wave mode (see Section 5.1), resulting in an average image acquisition rate of 354.2 $\pm$ 8.2 frames per second. This way, a set of 500 images was acquired for each experiment, representing a time frame of about 1.4 s. In preparation for processing with the PIV algorithm, each image other than the first and last is copied. This allows 499 pairs of consecutive images to be formed to facilitate cross-correlation processing. Each pair results in a vector field as output from the PIV algorithm.

5.3.1.2 Cross-correlation algorithm settings

The open access OpenPIV python script Liberzon et al. (2020) was used as the cros-correlation algorithm. It is conventionally used for optical PIV, but can be applied universally regardless of the origin or type of the images. As mentioned earlier in Section 5.1, the width of the images is constant and equal to the size of the array when ultrasound imaging is performed with the array transducer in plane wave mode. In case of the phased array used, this is limited to 13.9 mm or 139 pixels (spatial resolution of the images of 10 pixels/mm). Even for ultrasound imaging, such limited width of images is unusual. The use of a linear array with a typical width of about 40 mm is more common. Such a transducer was also used by Gurung and Poelma (2016); Dash et al. (2022). The use of a phased array in this study was dictated by the required frame rate, which was more limited for the scanner compatible with the available linear array. For the application of PIV, this limited width poses constraints on the choice of interrogation window sizes and overlap (see Section 1.1.3.2). Two main restrictions of the OpenPIV script must be taken into account when choosing the size of the interrogation windows and their overlap. Firstly, because the correlation is FT based, the maximum recordable displacement is limited to half the size of the interrogation windows. And secondly, the dimensions selected should accommodate for at least four

windows, i.e. three window overlaps, in both vertical and horizontal directions:

$$\frac{i_w - w_s}{w_s - o_v} \geq 3 \tag{5.2}$$

Where i_w is the width of the image [pixels], w_s is the size (height and width) of the cross-correlation windows [pixels] and o_v the overlap of the cross-correlation windows [pixels].

To avoid oversampling of the data (excessive resolution of the vector field output of the OpenPIV script), an overlap of 50 % of the window size is additionally recommended and commonly used (Roth and Katz, 2001). In case of images limited in width, this recommendation, in combination with the aforementioned limitations, strongly limits the maximum recordable displacement and hence velocity. In this case, with a maximum window size of 54 x 54 pixels and thus an overlap of 27 pixels, this is limited to 956 mm·s^{-1}. The recording of higher velocities is however envisaged. This requires larger interrogation windows and therefore greater window overlap to meet the requirement of at least three window overlaps (Eq. 5.2). This in turn will increase the resolution of the vector field, since the spacing between the vectors is equal to the difference between the size of the windows and their overlap. The latter leads to longer processing times, which is not always wanted. Given the nature of this study, which is merely to validate the UIV technique, larger overlaps were permitted, although at the cost of longer processing times. To maintain a practical processing time, the combination of a window size of 100 x 100 pixels and an overlap of 88 pixels is considered the limit, resulting in a theoretical maximum recordable velocity of 1771 mm·s^{-1}. Two iterations were allowed for each run of the OpenPIV script. The window size and overlap of the second iteration are half of those of the first iteration. The window size of the first iteration determines the maximum recordable displacement, while the window size and overlap of the second iteration will determine

the resolution of the vector field. Further settings are the threshold values for the vector validation filters. Four filters are applied based on the displacement, the signal-to-noise ratio (SNR - ratio of the maximum possible measure (power) of the signal to the power of distorting noise (peak-to-peak)), the global standard deviation and the median test. The filter based on the displacement was disabled by setting a threshold far too high. The other threshold values were determined after multiple processing with varying values to assess their impact. Thereby the UIV depth range showed to be optimal with the SNR threshold set at 1.25. Therefore, this value was retained for all further experiments. The influence of the set thresholds for global standard deviation and median test was found to be marginal. The thresholds for these two statistical filters were therefore set to arbitrary values, 5 and 3, respectively. Vectors that do not meet the set thresholds are masked and not considered further.

5.3.1.3 Experimental programme

All scans were performed with the ultrasound frequency set at 3.5 MHz. The carriage accelerated (at 6000 mm·s^{-2}) until the target velocity was reached. This velocity was maintained for a maximised period followed by deacceleration to a final stop. Target velocities range from 500 mm·s^{-1} to 1500 mm·s^{-1} in increments of 250 mm·s^{-1}. The useful length over which the carriage could move was limited to 480 mm. For each experiment, the combinations of minimum interrogation window size and overlap that allow at least the acquisition of the target velocity, were determined. The results are summarised in Table 5.1. Following the regulations mentioned in Section 5.3.1.2, experiment 1 will render the lowest vector resolution with a spacing of 1.2 mm. As elaborated in Section 3.1.2, this is more than sufficient for experiments like those of Sotelo et al. (2022, 2023).

Table 5.1: *Overview of the imposed velocities during the various experiments, along with the minimum required window size and overlap to allow their recording. As discussed in Section 5.3.1.2, the window size and overlap of the first iteration are limited to 100 pixels and 88 pixels, respectively. The window size and overlap of both the first and second iteration are mentioned (first/second iteration).*

Exp.	Target velocity [mm·s^{-1}]	Window size [pixels]	Overlap [pixels]
1	500	48/24	24/12
2	750	72/36	52/26
3	1000	88/44	72/36
4	1250	100/50	88/44
5	1500	100/50	88/44

5.3.2 Experimental results

The OpenPIV algorithm generates vector fields in both data format (txt file) and visual format (image file). An example of a visualised vector field is shown in Fig. 5.8. Each vector illustrates the velocity and direction of the flow at the corresponding location in the cross section. Considering the configuration of the experimental setup, the direction of the vectors should be consistent. For each row of vectors, representing a depth (see Section 5.3.1.2), the average velocity is calculated, resulting in an average vertical velocity profile. As an example, the vector row corresponding to a depth of 24 mm on Fig. 5.8 is marked in yellow. Doing so for all vector fields generates 499 average vertical velocity profiles per experiment. These profiles are used for further processing of the experimental results.

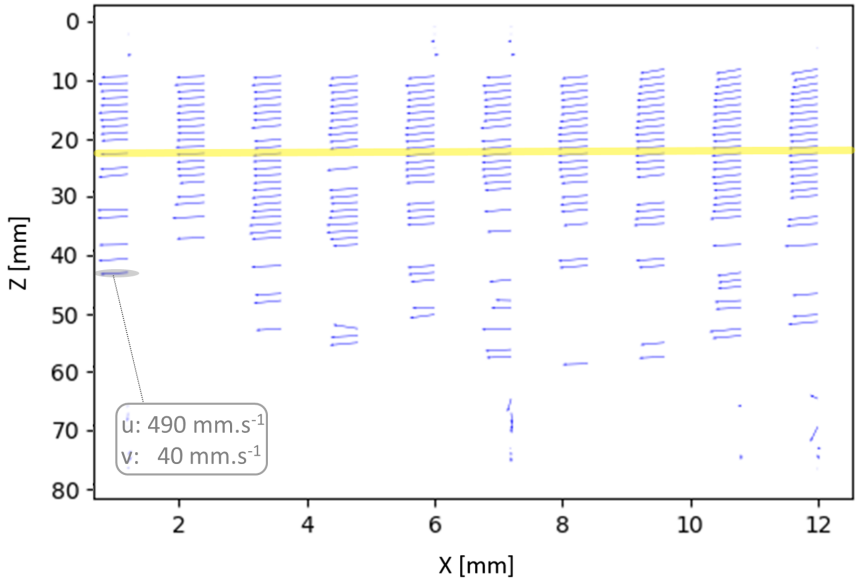

Figure 5.8: *Vector field number 204 of experiment 1, corresponding to the period of uniform velocity. To ratify this, the horizontal and vertical velocity components (u and v) of the marked vector on the left are specified. Apart from some artefacts, the direction of the vectors is uniform and virtually horizontal from right to left. The vector row marked in yellow corresponds to a depth of 24 mm.*

5.3.2.1 Average velocity profile over time

Based on the average vertical velocity profiles, the measured change in velocity can be plotted as a function of time for each depth corresponding to a vector row and for each experiment. To validate the measured velocities, a profile of the enforced velocity is plotted along, as shown for multiple experiments in Fig. 5.9 to Fig. 5.12.

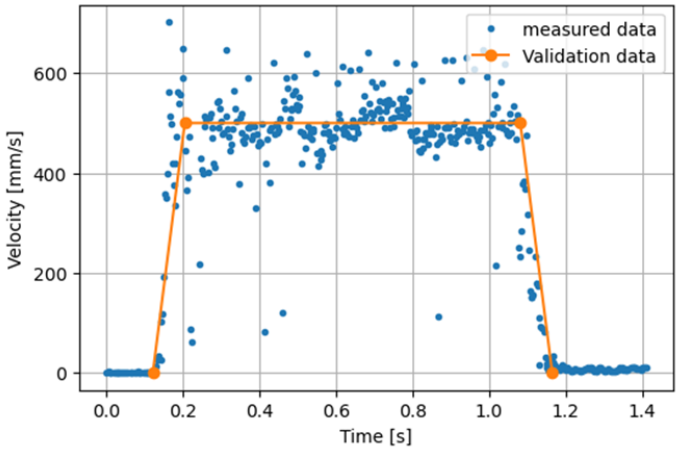

Figure 5.9: *Plots of the average velocities measured at a depth of 24 mm (blue markers) along with the imposed velocity of 500 mm·s^{-1} (orange curve). Both plotted as a function of time. The velocities were measured using UIV.*

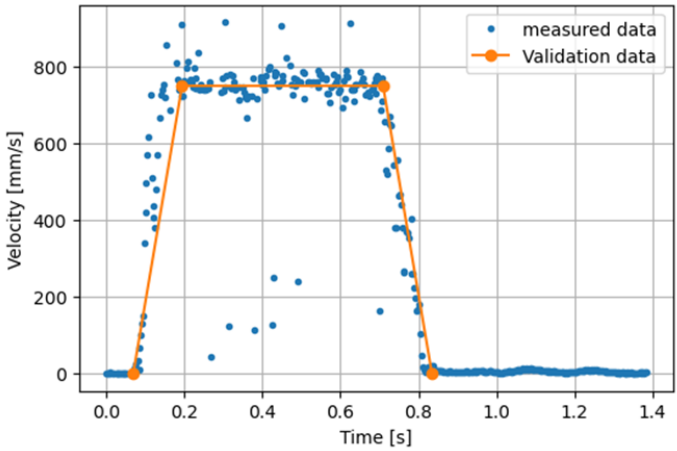

Figure 5.10: *Similar plot as Fig. 5.9 but for the experiments with an imposed velocity of 750 mm·s^{-1}.*

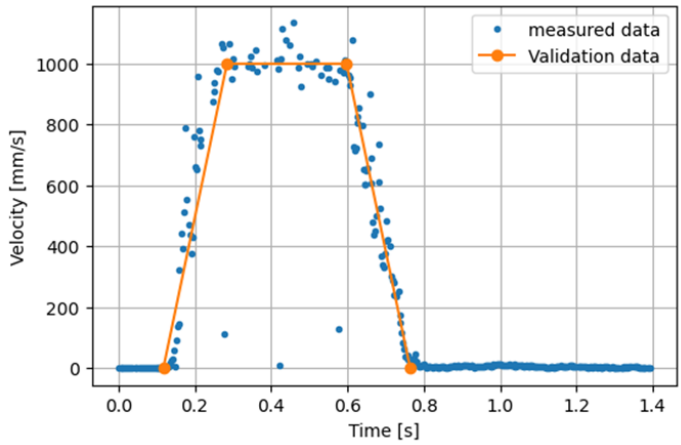

Figure 5.11: *Similar plot as Fig. 5.9 but for the experiments with an imposed velocity of 1000 mm·s^{-1}.*

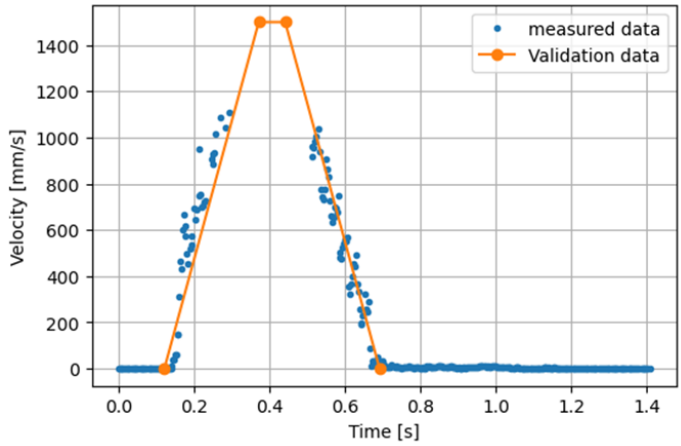

Figure 5.12: *Similar plot as Fig. 5.9 but for the experiments with an imposed velocity of 1500 mm·s^{-1}.*

5.3.2.2 Measurement accuracy as a function of depth

To allow further examination of the influence of depth on the accuracy of the velocity measurements, a selection of vector fields corresponding to the periods of uniform velocity during the experiments was made for each experiment. Using the average vertical velocities profiles of these selected vector fields (see Section 5.3.2.1), the average and standard deviation of the velocities over the period of uniform velocity are calculated for each vector row. Each row of vectors represents a depth, which is determined by the vertical distance between the vectors (see Section 5.3.1.2). By plotting these average measured velocities against the depth at which they were measured, as shown in Fig. 5.13 and Fig. 5.14, the influence of depth on the accuracy of the measured velocities can be assessed. Commonly used inaccuracy thresholds of 5 % and 10 % are plotted along to facilitate the determination of the depth range.

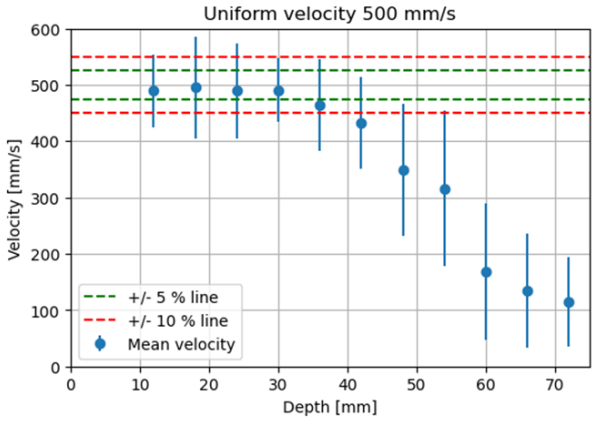

Figure 5.13: *Plots showing the average and standard deviation of the velocities measured during the period of uniform target velocity of 500 mm·s^{-1}, as a function of depth. Arbitrary boundaries of ± 5 % and ± 10 % inaccuracy are indicated by the green and red dashed lines.*

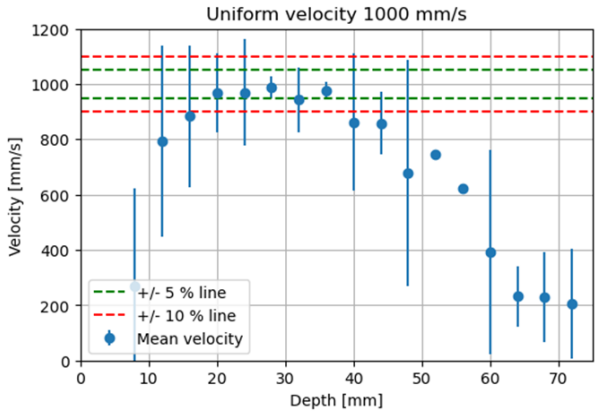

Figure 5.14: *Similar plot as Fig. 5.13 but for the experiments with a target velocity of 1000 mm·s^{-1}.*

5.3.2.3 Depth range as a function of window size

To assess the influence of the interrogation window size on the depth range, additional processing of the images was performed using multiple window sizes. Using all combinations of window size and overlap listed in columns 5 and 6 of Table 5.1, multiple graphs as shown in Fig. 5.13 and Fig. 5.14 were generated for each experiment. The depths from where the average velocities tend to deviate more than $\pm$ 5 % and $\pm$ 10 % under the influence of window size and for different velocities are presented in Fig. 5.15. Overlapping curves indicate such a rapid decline in average velocity, making it impossible to distinguish between the depths from which the deviation starts to exceed $\pm$ 5 % and $\pm$ 10 %. When no markers are shown in the curves at an applied window size, it means that there was no validated output in that case.

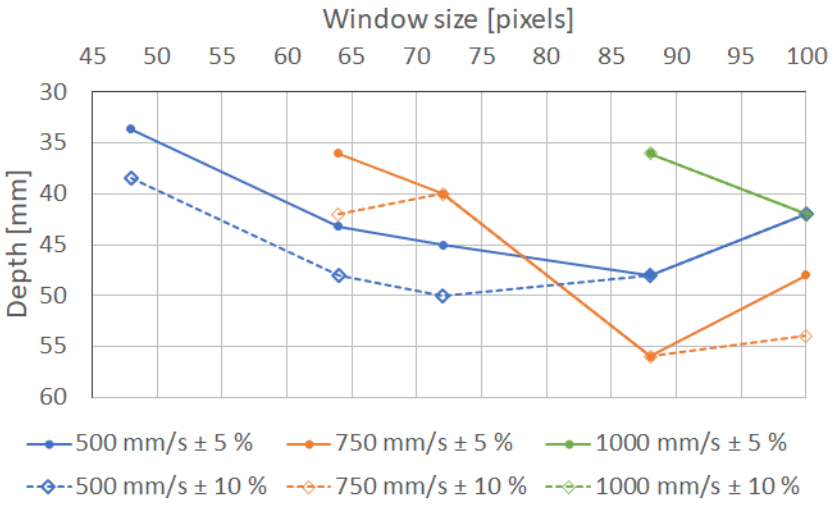

Figure 5.15: *Curves showing the depth at which the inaccuracy of the measured velocities remains below ± 5 % and ± 10 % and per velocity, as a function of the window size used during cross correlation processing. The reference values for uncertainty of ± 5 % and ± 10 % are chosen arbitrarily and visualised by a solid curve with circular markers and a dashed curve with diamond-shaped markers, respectively.*

5.3.3 Discussion on the outcomes of the UIV validation experiments

5.3.3.1 Uncertainty analysis

Prior to proceeding with the analysis of the results, a discussion of the limitations of the experimental setup is in order. For example, the setup used during these experiments was designed and built in-house. As mentioned in Section 5.3.1.1, the alignment of the carriage and the vertical stand, to which the transducer was attached, was performed with spirit level precision. Despite the horizontal motion of the transducer, all velocity vectors contain a vertical component (see Fig. 5.8). This indicates that despite efforts with the

spirit level, the transducer was not perfectly vertical to the mud surface. The magnitude of the vertical components is however small ($<$ 5 %) compared to their horizontal component. The error in velocity measurement due to this misalignment is therefore considered marginal. The magnitude of the vertical components is proportional to that of their horizontal component and no change in sign (direction) of the vertical component can be observed during the periods of acceleration and deceleration. Both indicate that there was no shifting of the transducer due to acceleration forces, meaning that the connection of the transducer to the stand was sufficiently rigid and no additional error in measurement occurred.

The output of the cross-correlation was kept as raw as possible to facilitate identification of the sensitivities of UIV when applied in mud. No filters or additional functions were thus used to embellish the output (see Section 5.3.1.2). As a consequence, the plots in Fig. 5.9 to Fig. 5.12 and in Appendix A show many outliers. When UIV is effectively applied to perform flow velocity measurements, the available filters and functions are likely to be used to improve output though. For the experiments of this study, for example, the "replace_outliers" function would be very useful. This function identifies outliers and replaces them with the average of their neighbouring vectors.

The speed of sound through mud varies slightly with changing density and compressibility (see Section 3.3.2). An assessment of the speed of sound is thus justified for any mud sample. This was however not done in preparation for these experiments, as the speed of sound does not affect the accuracy of the velocity measurements. In UIV, the speed of sound is used solely in the ultrasound imaging process to assign the recorded reflection signals to a depth in the mud. The use of an incorrect speed of sound thus only leads to a vertical offset of the speckle pattern and hence of the vectors. Due to the limited variation in speed of sound, this offset is

also limited. Considering the two extremes of 1460 m·s^{-1} and 1485 m·s^{-1} (see Section 3.3.2), this offset is at most 0.85 mm at a depth of 100 mm.

5.3.3.2 Validation of velocity measurements

The plots in Fig. 5.9 to Fig. 5.12 show a good match between the measured and the enforced velocities. Fig. 5.12 shows that the measurable velocity is limited, in this case to approximately 1100 mm·s^{-1}. Nonetheless, as elaborated in Section 5.3.1.2, the combination of window size (100 pixels) and overlap (88 pixels) used for this experiment (see Table 5.1) should allow the measurement of velocities up to 1771 mm·s^{-1}. This indicates that factors other than window size also can limit the maximum recordable displacement, hence velocity.

While searching for the minimum window size and overlap to allow recording of the target velocity (see Section 5.3.1.3), such limits in the recordable displacement ($d_{max,rec}$), and thus velocity, smaller than those imposed by the window size ($d_{max,set}$) were also encountered. An overview is provided in Table 5.2. Apart from the value associated with the window size of 72 pixels, the different values for the ratio $\frac{d_{max,rec}}{d_{max,set}}$ show an inverse proportional relation with the window sizes. The inconsistent value for the window size of 72 pixels is caused by outlier maximum velocities in the dataset. Such outliers are not present in the datasets of the other window sizes. When excluding these outliers, the maximum velocity in the dataset of window size of 72 pixels is 1075 mm·s^{-1}. The corresponding $\frac{d_{max,rec}}{d_{max,set}}$ ratio does fit well with the overall linearly decreasing trend.

So as the windows enlarge to enable measurement of larger displacements and hence velocities, the largest measured displacement deviates further from the theoretically maximum measurable displacement. In other words, with increasing

velocities, the largest measurable velocity is determined more by constraints other than the theoretical maximum displacement of half the window size. The decreasing number of markers with increasing velocity in the plots of Fig. 5.9 to Fig. 5.12 already indicate this. Each vector field (499 per experiment, see Section 5.2.2) should yield a marker in these plots. However, if there are no validated vectors at the selected depth in that vector field, no marker is plotted.

Table 5.2: *Overview of the largest recorded displacements, arranged by window size, and how they relate to the maximum recordable displacement equal to half the window size.* w_s *stands for window size,* $d_{\text{max,set}}$ *is the maximum recordable displacement following the settings during processing with the OpenPIV script [mm],* v_{max} *is the largest measured velocity across all experiments processed using the corresponding window size and* $d_{\text{max,rec}}$ *is an approximation of the largest recorded displacement determined by dividing the largest measured velocity by the average frame rate of 354.2 Hz (see Section 5.2.1).*

Settings		Recordings		$\frac{d_{\text{max,rec}}}{d_{\text{max}}}$
w_s [pixels]	$d_{\text{max,set}}$ [mm]	v_{max} [mm·s^{-1}]	$d_{\text{max,rec}}$ [mm]	[%]
48	2.40	793	2.24	93.3
64	3.20	991	2.80	87.5
72	3.60	1182	3.34	92.7
88	4.40	1132	3.20	72.6
100	5.00	1130	3.19	63.8

Based on the set thresholds of the vector validation filters and the observed impact of these filters (see Section 5.3.1.2), the SNR-based filter seems to be a plausible cause for the increasing number of unvalidated vectors. The number of validated vectors as a function of the measured horizontal velocity is therefore illustrated by the red curve shown in

Fig. 5.16. A clear decrease in the number of validated vectors with increasing velocity can be observed, confirming this hypothesis. Furthermore, peaks in the number of validated vectors can be observed around the target velocities of the experiments. These peaks become less pronounced at higher velocities. The markers, representing the SNR values of validated vectors relative to their horizontal velocity component, illustrate that this is merely caused by the durations of uniform velocity during the experiments. After all, high SNR values can be seen during the periods of acceleration and deceleration (i.e. at lower velocities) as well. Higher target velocities require longer periods of acceleration and deceleration, while the distance over which the transducer can move remains the same (see Section 5.3.1.1). Consequently, the period of uniform velocity is shorter, resulting in fewer recordings and vectors, which explains the decrease of these peaks in the number of validated vectors at the target velocities.

The identified relation between SNR and velocity is however indirect. In fact, the decrease in SNR is caused by the enlarged windows enabling the recording of larger velocities. This is illustrated by Fig. 5.17, showing two sets of SNR values resulting from processing the same recordings of an experiment, but with different window sizes. Both window sizes are sufficient to capture the displacements corresponding to the target velocity. Yet a clear distinction is observed in SNR's, with higher values after processing with smaller windows.

5.3.3.3 Accuracy of velocity measurements

The plots shown in Fig. 5.13 and Fig. 5.14 should be discussed in conjunction with the plots of average velocities at different depths in Appendix A. Fig. 5.13 of experiment 1, with a target velocity of 500 $mm{\cdot}s^{-1}$, shows that the deviation of the average measured velocities from the target velocity

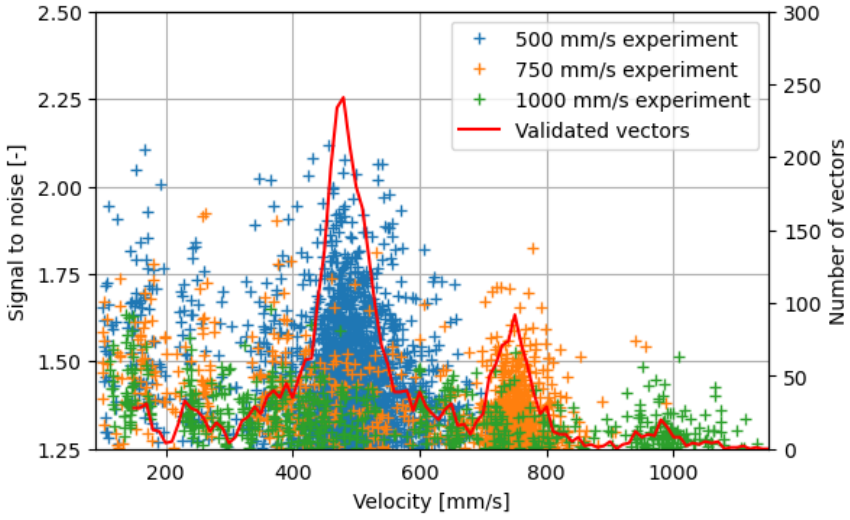

Figure 5.16: *Plot of the SNR of validated vectors relative to the horizontal velocity component of those same vectors. The SNR values are plotted as markers corresponding the the vertical axis on the left. Secondly, a red curve is plotted showing the total number of validated vectors as a function of velocity. This curve corresponds to the vertical axis on the right. All validated vectors at a depth of 24 mm of experiments 1, 2 and 3 are considered (Table 5.1).*

remain under $\pm$ 5 % and $\pm$ 10 % to depths of about 33 mm and 38 mm, respectively. When measuring at greater depths, the measured velocities are increasingly below the enforced velocity and the standard deviations increase. Both indicate a decrease in accuracy with increasing depth. These conclusions are confirmed by observations in the plots of experiment 1 in Appendix A. Firstly, an increase in the relative number of average measured velocities underestimating the imposed velocity can be observed with increasing depth. Secondly, the degree of underestimation increases with increasing depth. Finally, the number of markers, and thus validated vectors, decreases with depth. At greater depths,

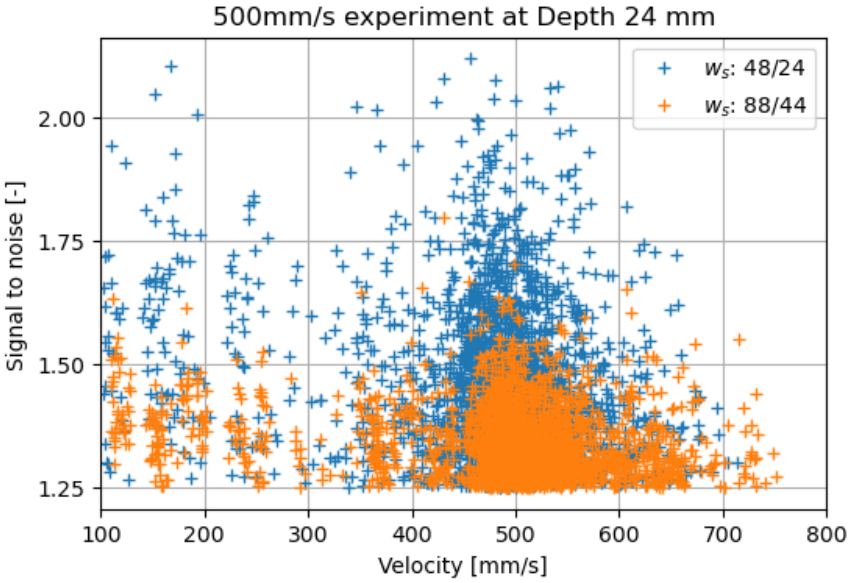

Figure 5.17: *Plots of the SNR of all velocity vectors at a depth of 24 mm, resulting from experiment 1 (see Table 5.1), relative to the corresponding horizontal velocity component of those vectors. The results of PIV processing with different window sizes (w_s) over two iterations are shown. The window sizes of both iterations are mentioned (first/second iteration) and expressed in pixels.*

such as 54 mm, the number of validated vectors is still sufficient for a correct statistical analysis. Their inaccuracy, however, is too much for them to be relevant.

At higher velocities, as in experiment 3 with a target velocity of 1000 mm·s^{-1} (Fig. 5.14), the graph first shows a decrease in deviation with increasing depth, until an optimal match with the target velocity is achieved from a depth of, in this case, 20 mm. This is maintained until a depth of about 36 mm. From then on, there is a trend of increasing deviation with increasing depth, similar to experiment 1. At the end of the depth range

where there is good agreement with the imposed velocity of 1000 mm·s^{-1} (between 28 mm and 36 mm), the smaller standard deviations of experiment 3 stand out compared to those of experiment 1. This is unlikely to indicate a lower variation in measurements, and can be explained by the plots of experiment 3 in Appendix A. These plots show the same trends as for experiment 1, but due to the higher velocity, the SNRs of the vectors are lower and the time span of uniform velocity is shorter. Hence, compared to experiment 1, the number of validated vectors (indicated by the number of markers) is already lower at the shallower depths. With a further decrease, the number of validated vectors from a depth of 36 mm, becomes so low that the standard deviation can no longer be considered representative. The aforementioned initial decrease in deviation during the first 20 mm is also unexpected. After all, the intensity of the pixels on the images is high at the beginning and decreases linearly with depth. Therefore it is unlikely that the inaccurate measurements at low depths are related to the pixel intensity. This observation is discussed further in Section 5.3.3.4, demonstrating that it is solely related to the setup of the experiments.

Fig. 5.15 shows that there is an optimal window size for each velocity, which optimises the depth to which velocities can be measured within the allowed limits of deviation. This optimal window size increases with increasing velocity. The perception of a decreasing depth range due to oversized windows is however somewhat contradictory. After all, an increase in window size typically increases the SNR and hence the validation of the resulting vector. This at least holds true in the case of a uniform particle density in the windows (Raffel et al., 2018). For ultrasound speckle pattern images, the particle density corresponds to the contrast ratio in the patterns, and thus to the pixel brightness which in turn degrades with depth (see Chapter 4). In other words, from a certain depth the contrast ratio becomes insufficient for cross-correlation processing. When approaching this depth limit,

the overall detectable displacements per window therefore decrease with increasing window size. Consequently, the SNR value of the vector resulting from those windows decreases, filtering out the vectors earlier and thus reducing the depth range. Furthermore, it can be observed that for velocities of 1000 mm·s^{-1}, the optimum window size will be larger than the maximum window size of 100 pixels for this image width (see Section 5.3.1.2). This indicates that with wider images, not only can higher velocities be measured in the horizontal direction (see also Section 5.3.1.2), but at greater depths as well.

5.3.3.4 Zone of influence of moving transducer

As discussed in Section 5.3.1.1, the motion of the immersed transducer will induce flows in the mud that will distort the velocity measurements. Due to the viscosity of mud, the depth to which such flows are induced is expected to be limited. Hence, the validity of the velocity measurements is subject to the depth at which the measurements are conducted. The depth threshold, from which undistorted measurements can be made can be determined from the variation in vertical velocity profiles. Whereas each row of vectors shows a horizontal velocity profile at a given depth (as depicted in Fig. 5.8), each column of vectors shows a vertical velocity profile at a given horizontal position in the image. For each experiment, a vertical profile of the standard deviation was calculated taking into account all vector columns of all vector fields. A plot of these profiles is shown in Fig. 5.18. The trend of all profiles is similar.

For all profiles, relevant data can only be found from a depth around 10 mm. This is preceded by a blind zone with no recordings and a zone of noise. The blind zone is visualised by the black strip at the top of the ultrasound image (see Figs. 3.19, 4.11 and 5.1). Its thickness corresponds to the

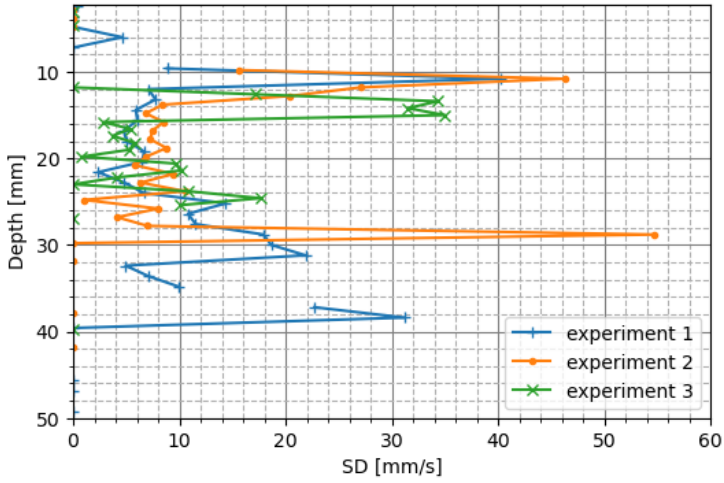

Figure 5.18: *Vertical profiles of standard deviation of the measured velocities during the periods of uniform velocities of experiments 1, 2 and 3 (Table 5.1).*

duration of transmission of ultrasound by the transducer. After all, no recordings can be made while transmitting. The noise is caused by the ultrasound scanner's electronics. This is more difficult to distinguish from the speckle because it is also visible as a grainy greyscale pattern on the image. Although it is similar for all images, there is some variation, which the cross-correlation algorithm may register as movement. Hence, some SD values can be seen in this zone. Because of their origin, these can be neglected. The relevant data start with high SD values indicating a large variation in measured velocities. The depth range covered by this part increases with increasing velocity. For target velocities of 500 mm·s^{-1} (experiment 1), 750 mm·s^{-1} (experiment 2) and 1000 mm·s^{-1} (experiment 3), it covers up to depths of about 12 mm, 14 mm and 16 mm, respectively. From these depths, the variation in measured velocities is small until the depths with higher inaccuracy are reached (Section 5.3.3.3), where variation increases again.

Because the depth to which the flow is induced by the moving transducer is likely to increase with increasing velocity, the parts with large standard deviation values (up to depths of 12 mm, 14 mm and 16 mm for experiments 1, 2 and 3, respectively) are considered to correspond to the zone of influence of the moving transducer. The transition to a lower variation in measured velocities as from these depths confirms this. After all, considering the configuration of the test setup, uniform velocity vectors are to be expected.

5.4 Depth range of UIV in mud

The maximum depth range obtained in the experiments of Section 5.3 is around 50 mm. As elaborated in Section 5.1, this limit in depth range is presumed to be determined by the attenuation rate of the ultrasound by the mud. Before investigating this further in this section, it should be verified whether the depth range is not earlier limited by the frame rate applied during these experiments. While operational, the function of the ultrasound transducer alternates between transmitting and receiving sound waves. The transmission of ultrasound occurs in short bursts of fixed duration. This is followed by a period of time during which the transducer acts as a receiver. Meanwhile, the ultrasound propagates back and forth in the mud. This cycle is repeated at a pace based on the set frame rate. Hence, a higher frame rate shortens the period of time during which incoming sound waves are recorded and therefore also limits the depth range. This is jointly determined by the speed of sound through the mud, which was assessed to be 1465 $m \cdot s^{-1}$ (see Chapter 3). Thus, for a depth range of 50 mm, the sound waves need about 0.069 ms to propagate back and forth to generate an image. The applied frame rate was about 350 frames per second, meaning the time window available to generate each image was 2.857 ms. So in this case, the frame rate was not the limiting factor for the obtained depth range.

5.4.1 Experiments

5.4.1.1 Experimental setup

This series of experiments was conducted with three batches of Zeebrugge mud, each with its own density of about 1.120 g·cm^{-3}, 1.150 g·cm^{-3} and 1.175 g·cm^{-3}, respectively. The mud originally provided was therefore diluted by mixing it with seawater sourced from the same location. This was done just before conducting the experiments to ensure a homogeneous density of the mud throughout the experiments. The duration of the experiments themselves was limited to a few minutes, such that the influence of sedimentation can be ignored. The different mud batches were prepared and retained in separate buckets to allow convenient and swift change of mud density during the experiments. The buckets have a diameter of 270 mm and were filled with mud for about 150 mm.

A sketch and a picture of the experimental setup is shown in Fig. 5.19 and Fig. 5.20, respectively. The ultrasound array transducers are clamped to an appendage extending over a bucket containing a mud sample. To enable effective transmission of the ultrasound in the mud, the arrays were positioned face down, with the part from where the ultrasound is emitted and received submerged in the mud by only a few millimetres. All arrays were inserted in a water-filled, sheathing rubber to protect them from the corrosive seawater in the mud. A magnetic stirrer was used to induce flow in the mud. The magnetic rod had a diamater of 25 mm and a length of 160 mm. Due to increasing viscosity with increasing density, the applied rotational velocity differed for each mud bucket. It was set to the level where a laminar flow was noticeable at the surface of the mud. With a maximum selectable rotational speed of 1400 RPM, this was only just achieved for the highest mud density. With this setup, the velocity of the induced flow is unknown. Therefore, the validity of the obtained velocity

measurements can only be evaluated qualitatively. This is no concern when these experiments only consider the depth range of UIV. Based on Halász et al. (2007), using a magnetic stirrer yields a vortex-like flow in the fluid. In turn, the insonified mud is found in a vertical plane perpendicular to the tangent of the rim of the bucket. The width of the plane is 52.1 mm, 13.9 mm and 38.1 mm for the flexible linear, phased and linear array, respectively. Both the flow pattern and the position of the insonified plane are indicated in Fig. 5.19. Consequently, a dominant horizontal flow is expected as output of the UIV.

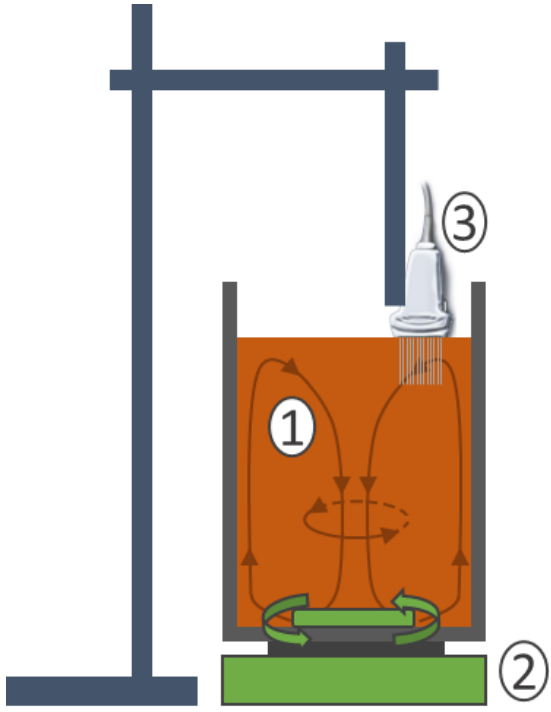

Figure 5.19: *Sketch of the experimental setup. (1) bucket containing the mud. The expected flow patterns are indicated in dark; (2) magnetic stirrer to induce vortex-shaped flow in the mud; (3) ultrasound transducer clamped on an appendage fixed to a laboratory stand.*

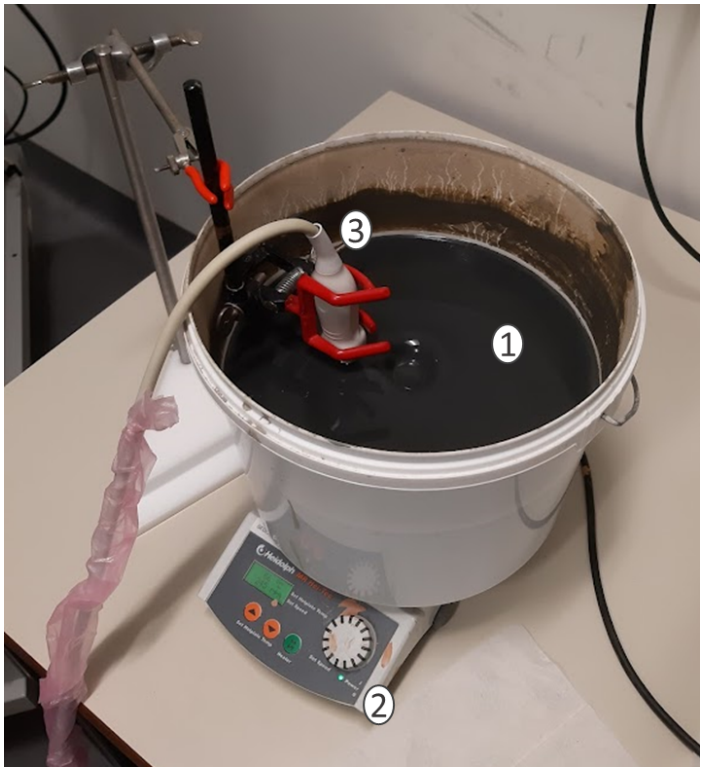

Figure 5.20: *A picture of the actual setup as sketched in Fig. 5.19. The labels identifying the main components correspond to those of Fig. 5.19.*

5.4.1.2 Cross-correlation algorithm settings

Similar to the previous experiments (see Section 5.3), the open access OpenPIV python script Liberzon et al. (2020) was used as the PIV algorithm to process the acquired ultrasound images. For these experiments, the four filters (see Section 5.3.1.2) were configured to be virtually disabled. This way, the evaluation of the influence of pixel brightness on depth range could not be biased.

Two iterations were performed during PIV processing. For each array, the optimal window size that maximises the depth range was sought, considering only square windows. For the flexible linear array, these were window sizes of 80/40 pixels (first iteration/second iteration), while for both the phased and linear arrays, these were sizes of 48/24 pixels. The overlap of the interrogation windows was set to a recommended value of 50 % (Roth and Katz, 2001).

5.4.1.3 Experimental programme

For each combination of array and mud density, ultrasound scans were performed at multiple ultrasound frequencies. The image recording time was limited to approximately 1 second to contain the amount of data. An overview of all applied combinations of ultrasound frequency and mud density is provided in Table 5.3. All experiments from Table 5.3 were performed with the transducer operating at a voltage of 60 V. One additional experiment was performed by repeating the experiment with the ultrasound frequency set at 3.5 MHz and a mud density of 1.151 g·cm^{-3} but with the transducer operating at a higher voltage of 150 V.

5.4.2 Limiting factor of depth range

An appropriate method to determine the depth range of each vector field is established first. This way, the influence of various parameters on the depth range can be evaluated objectively.

5.4.2.1 Results

By the design of the experimental setup, the resulting vectors are expected to be coherent, with an increasing velocity with depth and a dominant lateral direction. The results presented in Fig. 5.21 show that this holds true up to a certain depth,

Table 5.3: *Overview of all experiments performed with the ultrasound transducers operated at a constant voltage of 60 V. Three different ultrasound array transducers, a flexible linear array, a phased array and a linear array, were used to cover a wide spectrum of ultrasound frequencies. Although they are different in design, they were all operated similarly. The densities mentioned were measured after preparation of the mud samples. Given their similarity, the densities are grouped into generically named groups: low, medium and high density.*

Array	Frequency [MHz]	Density [g·cm^{-3}]		
		Low	Medium	High
Flexible linear	1.75 2.00 2.50	1.120	1.146	1.175
Phased	2.50 3.00 3.50 4.00 4.50	1.116	1.151	1.175
Linear	4.62 5.45 6.00 6.67	1.120	1.146	1.173

from where non-validated and unrealistic vectors alternate. A slight downward deflection at the outer sides of the vector field can also be observed. This however correlates well with the expected vortex-like flows as indicated in Fig. 5.19.

The depth of this transition is considered the depth range of the UIV and is determined based on the appearance of the non-validated vectors. Such vectors are indicated by ”NaN” (Not a

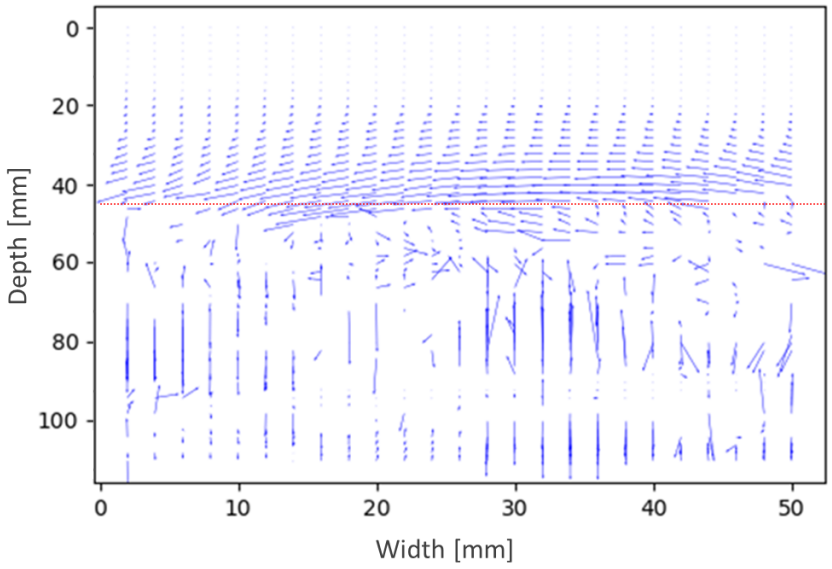

Figure 5.21: *A vector field resulting from the experiment with an ultrasound frequency of 2.5 MHz (flexible linear array) and a mud density of 1.146 $g{\cdot}cm^{-3}$. The red dotted line indicates the depth from which the tendency of coherent vectors stops. The increase in vector size (flow velocity) with depth, correlates with the experimental setup. Velocities up to 350 $mm{\cdot}s^{-1}$ were measured at the transition level from coherent to incoherent vectors.*

Number) in the data file for the corresponding vector. For each vector column (vertical profile) of each vector field, the depth from where successive NaN values are found is considered the depth of this transition. Hence, for each experiment, the average of all these transition depths is regarded as the depth range for the corresponding combination of ultrasound frequency and mud density. These averages along with their standard deviation are presented in Fig. 5.22.

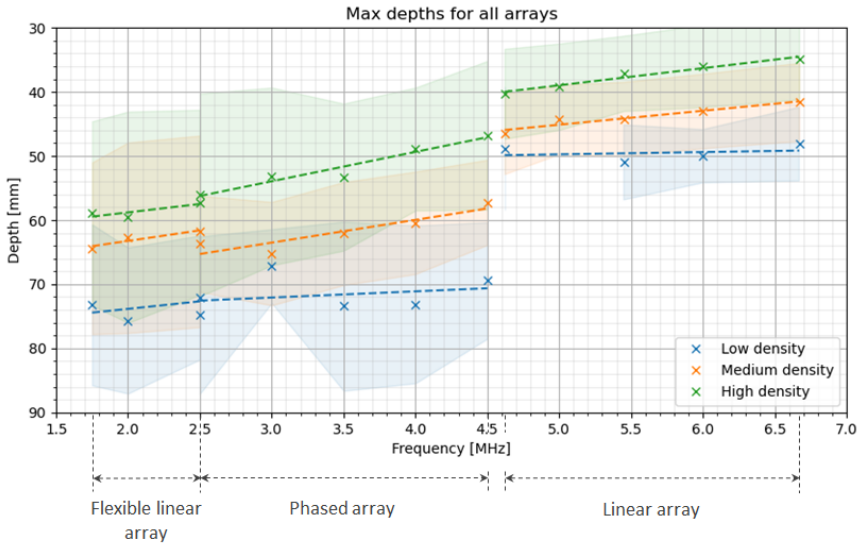

Figure 5.22: *Plots of the average depth range found for each experiment representing a combination of ultrasound frequency and mud density. A trendline based on the depth ranges obtained is plotted as dashed lines for each combination of mud density and array transducer used. Variation in depth ranges is indicated by the shades. The frequency ranges of the array transducers are mentioned in Section 5.4.1.1 and indicated on the horizontal axis.*

Knowing the depth ranges for each experiment, the corresponding pixel brightness values can be determined. To assess the presumed relation with attenuation, the pixel brightness values of the images are converted to SPLs, expressed on a logarithmic scale in decibels. The correlation between pixel brightness and SPL depends on the bit depth and dynamic range of the images (see Eq. 5.3). For all experiments in this study, these were fixed at 16 bits and 60 dB, respectively.

$$L_p = \frac{C_{\text{pixel}}}{2^n} \cdot r_{dyn} \tag{5.3}$$

Where L_p is the SPL of the returning sound wave upon receipt by the transducer [dB], C_{pixel} is the linear greyscale intensity value of a pixel, corresponding to its brightness [-], n is the bit depth of the images [bits] and r_{dyn} the dynamic range applied to produce the images [dB].

Subsequently, for each experiment, the average SPL of each pixel row across all images is calculated. The result is an average vertical SPL profile for each combination of mud density and ultrasound frequency. Together with its Coefficient of Variation (CV - i.e. ratio of the standard deviation to the average) such an average SPL profile is shown in Fig. 5.23. The average SPL corresponding to the assessed depth range can be determined as illustrated in Fig. 5.23 by the intersection between the average vertical SPL profile and the red dashed line indicating the average depth range. This SPL is further considered the minimum SPL required for the application UIV in that experiment. This was done for all experiments. The resulting minimum SPLs are summarised in Fig. 5.24.

In conventional PIV, cross-correlation is based on patterns formed by various visualised scatterers contrasting with the image background (Raffel et al., 2018). This is different when speckle pattern images are used. As elaborated in more detail in Section 3.3.3, speckle occurs when the density of scatterers is so high that the backscattered signals interfere (constructively and destructively), creating an illusory image based on the position of the scatterers without visualising them themselves (Wells and Halliwell, 1981; Thijssen and Oosterveld, 1986). As a result, images are completely filled with speckle patterns, leaving no ”blank” background to contrast with (see Fig. 3.19 and Fig. 4.11). Cross-correlation between speckle pattern images is thus based on patterns of contrast which are part of the speckle image. Along with the

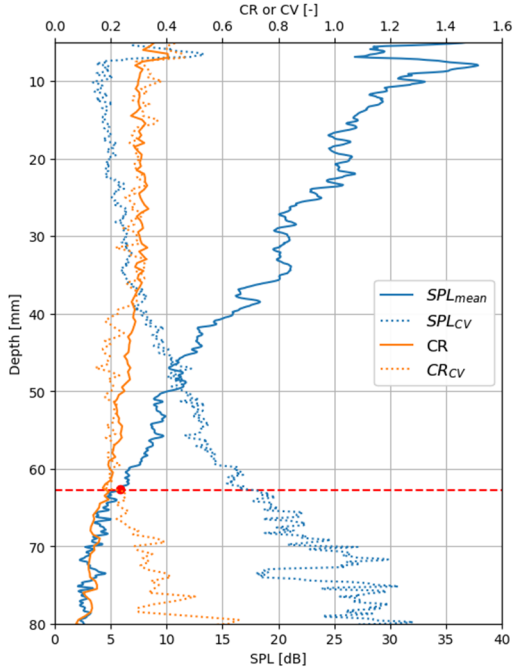

Figure 5.23: *Plots of the average vertical SPL profile and the corresponding coefficient of variation (CV) for the experiment with an ultrasound frequency of 2.0 MHz and a mud density of 1.146 g·cm^{-3}. The red dashed line indicates the average depth range determined for the experiment (Fig. 5.22). Profiles of the average Contrast Ratio (CR) and the corresponding coefficients of variation (CV) are plotted along. Similar plots for other experiments are annexed in Appendix B.*

fading pixel brightness with depth, the contrasts in the speckle patterns degrade with depth. To assess the detectability of such patterns with depth, a Contrast Ratio (CR) profile is determined. The CR of a section of the image is defined as the ratio of the difference between the maximum and minimum SPLs within that section to the dynamic range of the image (Eq. 5.4).

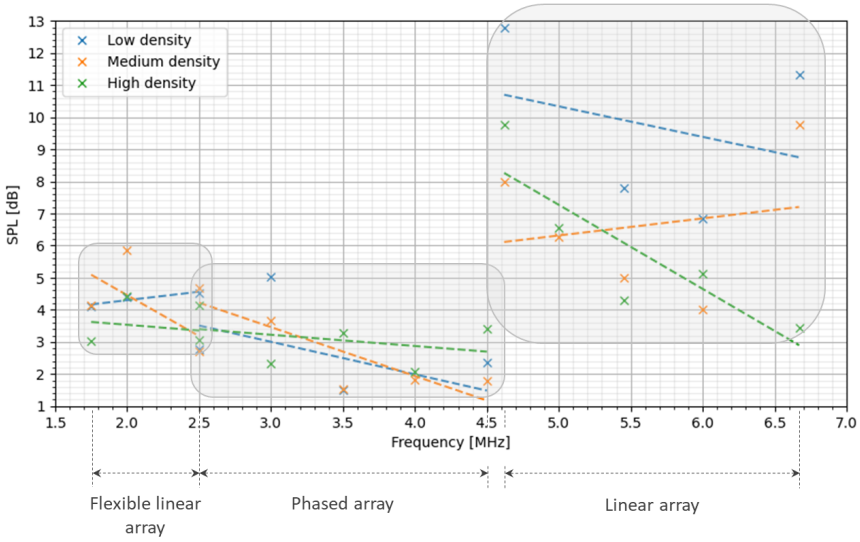

Figure 5.24: *Plots of the minimum SPLs attained for each experiment (see Table 5.3). The diagrams enclose the results for each array transducer. The dashed lines are trendlines for each combination of density and the array transducer used.*

$$c_r = \frac{L_{p,\text{max}} - L_{p,\text{min}}}{r_{dyn}} \tag{5.4}$$

Where c_r is the CR of a section of the image [-], $L_{p,\text{max}}$ is the highest SPL value within the same section of the image [dB], $L_{p,\text{min}}$ is the lowest SPL value within the same section of the image [dB] and r_{dyn} the dynamic range of the image [dB].

In this study, the sections for which the CRs are determined are 10 by 10 pixels in size. For each column of 10 pixels wide, a vertical CR profile is thus determined with a vertical resolution of 10 pixels. By doing so for each 10-pixel-wide column of an image and for all images of an experiment, an average vertical CR profile can be determined for each

experiment. For the corresponding experiment, such a CR profile together with its CV are shown along in Fig. 5.23.

5.4.2.2 Discussion

For each array transducer, the results plotted in Fig.5.22 reveal an increasing depth range with a decrease in both mud density and ultrasound frequency. These observations confirm the depth range of UIV is primarily dictated by the attenuation of the ultrasound by mud.

With the significantly lower depth ranges for the linear array experiments, the influence of the TGC (Section 5.2.1) is clearly visible. This is however somewhat counterintuitive. After all, for diagnostic imaging, gain is used to improve image quality. Greater depth ranges could therefore be expected. Since the TGC is applied to the recordings prior to normalisation (including a cutoff of values below -60 dB), a larger range of data is compressed in the dynamic range of 60 dB (see Section 5.2.2). Consequently, it narrows the distinction between signals, ultimately leading to a loss of contrast between surrounding pixels. This in turn complicates the preservation of speckle patterns and thus the cross-correlation between successive images. In a way, gain thus creates an additional filter that eliminates low-contrast speckle patterns, thereby reducing the depth range of UIV. The influence of TGC can also be observed in the significantly lower SD of the average depth ranges (Fig. 5.22). This means that due to gain the depths at which cross-correlation is no longer successful becomes less variable. An explanation must therefore be sought in the vertical CR_{CV} profiles as presented in Fig. 5.23 and Appendix B. These profiles show that for the experiments using the flexible linear array and the phased array the variation in CR is more or less constant with depth until just above the specified maximum depth, from where variation in CR increases. This is different for the experiments

using the linear array. These results show consistent or even slightly decreasing variation in CR with depth. This means that the depth from where the minimum CR values are encountered is more delineated, and hence also the identified depth ranges.

To facilitate the analysis of the minimum SPLs shown in Fig. 5.24, diagrams have been drawn enclosing the results for each array transducer. Generally a trend of decreasing minimum SPL with increasing frequency can be observed. Assuming that there is a fixed minimum CR defining the depth range, this observation implies that the differences in SPLs of surrounding pixels increase as the ultrasound frequency increases. After all, the CR is determined by the range of SPLs of nearby pixels. This is confirmed by the differences in SPL_{CV} profiles of the experiments, as shown in Appendix B. Within each series of plots of a combination of mud density and array transducer used, it can be seen that the rate at which SPL_{CV} increases with depth becomes faster with higher ultrasonic frequencies. Because of the random interference of backscattered sound waves, greater variance in recorded SPLs can be explained by higher intensities of the backscattered signals. This, however, contradicts with the greater attenuation of higher-frequency ultrasound. Therefore, this observation can only be explained by the number of particles that scatter the ultrasound, which increases when the frequency of the ultrasound is higher. Indeed, the number of scatterers depends on the ratio between the size of the scatterers and the wavelength of the sound waves (Szabo, 2004a). This is further elaborated in Section 5.4.3.1.

5.4.3 Optimisation of depth range

In previous Section it is shown that the depth range of UIV applied to natural cohesive mud is determined by the pixel brightness of the speckle pattern images. As discussed in Section 5.1, when ultrasound imaging is applied to a volume

of mud of homogeneous density, the pixel brightness of the images degrade with depth at a constant rate proportional to the attenuation of the applied ultrasound by the mud. Hence, the depth range can be optimised by reducing the attenuation or increasing the intensity of the initially emitted ultrasound.

5.4.3.1 Lowering attenuation

A conclusion of Chapter 4 is that the attenuation of ultrasound by mud is determined by the density of the mud and the applied ultrasound frequency. These dependencies are empirically expressed by Eq. 4.5. For experimental fluid dynamics involving natural cohesive fluid mud, variation in these two parameters is limited. In fact, the density of mud can vary from 1.050 g·cm^{-3} to 1.500 g·cm^{-3} or even more. However, in most research topics involving mud density, this is an imperative parameter. Therefore, it is considered unwanted to change the density solely to optimise the UIV depth range. For diagnostic imaging, high ultrasound frequencies are preferred to achieve optimal axial resolution to clearly distinguish boundaries or transitions. Because of their uniformity, this is less crucial for images containing only speckle. In order to reduce acoustic attenuation, it therefore seems obvious to use low ultrasound frequencies. This is however limited. In ultrasound imaging, speckle patterns arise from the interference of scattered sound waves. In turn, scattering occurs when tiny particles (scatterers), with an acoustic impedance different from that of its surrounding media, are insonified with ultrasound of which the wavelength is larger than the size of these particles (D'hooge, 2008). Different scattering regimes are distinguished based on the $k{\cdot}a$ ratio (see Section 3.3.3).

The ultrasound frequencies applied during the experiments of this study ranged between 1.75 MHz and 6.67 MHz (see Table 5.3). With a speed of sound of 1465 m·s^{-1} (see

Chapter 3), this corresponds to a range of wavelengths between 220 µm and 837 µm. Since the maximum particle radius is 60 µm (see Section 3.3.3), the wavelength of the ultrasound is always much larger than the particles. According to Szabo (2004a), this results in diffusive scattering, where the intensity of the scattered signals (I_{sc}) is proportional to the frequency to the fourth power (see Eq. 3.11). Since the returning sound waves are attenuated as they propagate through the mud, a minimum backscattering intensity (I_{sc}) is required for them to reach back to the transducer. Consequently, a lower limit for the ultrasound frequency can be expected beyond which the quality of the speckle images become insufficient. Due to attenuation, this is expected to occur first at greater depths, with the ultrasound frequency thus becoming the limiting factor for the depth range.

Eq. 3.11 was derived from the expression defined by Lord Rayleigh (Strutt, 1871) and Morse and Ingard (1968) for the scattering of pressure waves by spheres much smaller than the wavelength of the pressure waves. It therefore shows great resemblance to other derived expressions such as for scattering of electromagnetic waves in the Rayleigh scattering regime (e.g. by Seinfeld and Pandis (2006)). In fact, the parts expressing the influence of wavelength and particle size (factors k and a) are equal. While a bottom limit for significant scattering of electromagnetic waves is identified around $k{\cdot}a$ = 0.002, no such limit for ultrasound scattering was found in literature. Although the size of the actual scatterers cannot be assessed, an estimate of such a lower limit can be made based on the experiments conducted and a particle size distribution of the mud. After all, the lowest ultrasound frequency of 1.75 MHz still provided adequate images for the application of UIV and can thus be used as a reference.

Earlier in Chapter 3 the particle size distribution of Zeebrugge mud was presented, see Fig. 3.16. Since difference in density of mud samples of the same origin is solely attributable to the

water content, the particle size distribution is independent of the density. The cumulative distribution shows a d_{10} particle size (the size compared to which 10 percent of the particles are smaller) of 0.766 µm. This means that when insonified with an ultrasound frequency of 1.75 MHz, a $k{\cdot}a$ ratio of at least 0.003 applies for ninety percent of the particles. This lower limit of the $k{\cdot}a$ ratio is just above the aforementioned limit of negligible scattering intensity for electromagnetic waves. Because of the resemblances to electromagnetic scattering, it is provisionally presumed that this limit can be adopted for the scattering of ultrasound waves. Because the intensity of the sound waves eventually returning to the transducer is the result of the superposition of various backscattered signals, the number of scatterers present will also have an impact on this. In Chapter 3, the chemical compounds silicon dioxide (SiO_2) and aluminium oxide (Al_2O_3) were identified as probable ultrasound reflectors present in Zeebrugge mud. Silicon dioxide, or silica, is mostly found in nature as quartz in silt and sand (Iler, 1979; Assallay et al., 1998), which in turn are classified as particles with sizes ranging from 2 µm to 63 µm and 63 µm to 2000 µm, respectively (Blott and Pye, 2012). Aluminium oxide, in turn, is a so-called associated mineral commonly found in clays. Depending on the literature consulted, in geoengineering, clay minerals are considered smaller than 2 µm or 4 µm (Bergaya et al., 2006; Chassagne, 2019). Based on the particle size distribution of Zeebrugge mud, it can thus be concluded that scatterers may be found across the entire spectrum of particle sizes present in Zeebrugge mud. To set a limit somewhere, the smallest particle size further considered to cause adequate scattering when insonified with 1.75 MHz ultrasound is the d_{20} with a size of 2.439 µm. The corresponding $k{\cdot}a$ ratio is 0.009. This is illustrated by the green area in Fig. 5.25 which represents correlations of ultrasound frequency and particle size that result in $k{\cdot}a$ ratios larger than 0.009. Hence, its lower boundary is specified by a curve of constant $k{\cdot}a$ ratio equal

to 0.009. Similar curves of constant $k{\cdot}a$ ratio corresponding to particle sizes d_{50} and d_{80} are shown as well. Furthermore, particle sizes d_{20}, d_{50} and d_{80} of Zeebrugge mud are marked by vertical red dashed lines. The intersection of the d_{50} line with the $k{\cdot}a_{(d_{20})}$ curve indicates that with an ultrasound frequency of 0.6 MHz, half of the particles still qualify for adequate scattering intensity for UIV. With an ultrasound of 0.6 MHz, the $k{\cdot}a$ ratio for scatterers of size equal to the d_{20} particle size is 0.003. This is still above the considered lower limit of 0.002 as indicated earlier. In fact, as long as sufficient scatterers are present in the larger particle size ranges, even lower ultrasound frequencies down to 0.2 MHz may still suffice.

Based on Eq. 4.5, the attenuation of 0.6 MHz ultrasound by Zeebrugge mud with a density around 1.15 g·cm^{-3} is approximately 2 dB·cm^{-1}. While the depth range of 50 mm was achieved in Zeebrugge mud of similar density with an ultrasound frequency of 3.5 MHz and thus an attenuation of 5 dB·cm^{-1} (see Section 5.3). Hence, lowering the ultrasound frequency to 0.6 MHz would increase the depth range by a factor of 2.5 to 0.125 m.

It should be emphasised that only Zeebrugge mud is considered in this research. Muds of other origins have different particle size distributions. Hence, the optimal ultrasound frequency for applying UIV will be different for each mud. Eq. 3.11 shows that the intensity of the scattered ultrasound (I_{sc}) is proportional to the size of the scatterers (a) to the power six. In this way, the size of the particles affects the depth range of UIV twofold. On the one hand, larger particles in the mud will generate scattered ultrasound of higher intensity. The scattered ultrasound can thus propagate further, which eventually results in an increased depth range of the UIV. On the other hand, since the attenuation of ultrasound is largely determined by the extent of scattering, the rate at which ultrasound is attenuated by the mud will also increase with increasing particle sizes. This in turn again

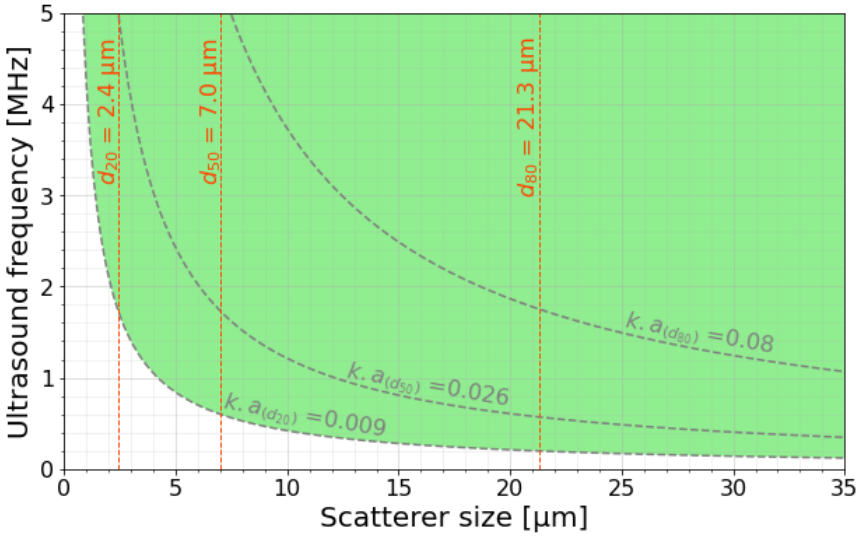

Figure 5.25: *Illustration of the applicable $k{\cdot}a$ ratios for insonation of scatterers as a function of scatterer size and ultrasound frequency. Where k is the wavenumber of the ultrasound and a is the radius of the scatterer. Three curves of constant $k{\cdot}a$ ratio are plotted in dashed grey lines. The $k{\cdot}a$ ratios of these curves apply to the insonation with 1.75 MHz ultrasound of scatterers with sizes equal to the d_{20}, d_{50} and d_{80} particle sizes of Zeebrugge mud. The green fill indicates the correlations of ultrasound frequency and scatterer size for which the $k{\cdot}a$ ratio exceeds the presumed minimum of 0.009. The vertical red dashed lines indicate the d_{20}, d_{50} and d_{80} particle sizes of Zeebrugge mud (see Fig. 3.16).*

limits the depth range of UIV. Whether one of these effects predominates the other or whether they compensate for each other is best assessed experimentally.

5.4.3.2 Increasing ultrasound intensity

In case of a mud sample of homogeneous density, the attenuation and hence the deterioration rate of pixel brightness

is constant with depth (see Fig. 4.11). This enables to shift the minimum pixel brightness to greater depths by increasing the intensity of the emitted ultrasound, proportionally increasing the SPLs of the returning sound waves. This was tested by redoing an experiment with a higher voltage applied to the transducer (see Section 5.4.1.3). All original experiments listed in Table 5.3 were conducted with a voltage of 60 V. The altered experiment was done with a voltage of 150 V. The increase in emitted SPL can be estimated using Eq. 5.5 (ter Haar, 2012). For the aforementioned increase in voltage this results in a theoretical increase of 7.96 dB.

$$\Delta L_p = 20 \cdot \log \frac{U_\mathrm{j}}{U_\mathrm{i}} \tag{5.5}$$

Where ΔL_p is the difference in emitted SPL between emissions where the transducer was operated with different voltages (U_i and U_j).

A random but corresponding SPL profile resulting from both experiments is shown in Fig. 5.26. These plots show a shift of the SPL profile towards higher values when a higher voltage is applied to the transducer. Averaged across all profiles of all images, an increase of 7.334 dB was determined, matching well with the estimated increase. With an attenuation of 2 dB·cm^{-1}, like when insonifying Zeebrugge mud of density around 1.15 g·cm^{-3} with 1.75 MHz ultrasound, this increase in SPL yields an additional depth range of 36.7 mm.

5.5 Alternative setup - intermediate material

For a setup as shown in Fig. 5.3, a submersible transducer is required. This requirement can limit the choice in standard commercially available ultrasound equipment. Moreover, the setup requires the creation of holes in the walls or bottom of

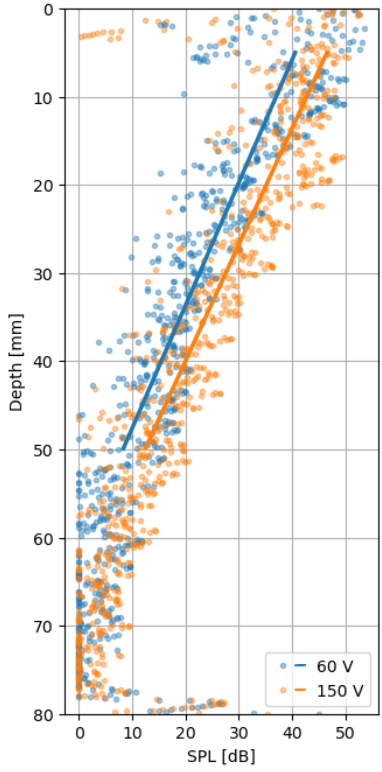

Figure 5.26: *Random but corresponding SPL profiles of the recorded returning sound waves after transmission with the transducer operating at 60 V (blue markers) and 150 V (orange markers).*

the flume, which might be unwanted. In such case a setup with a sheet material in between the transducer and the mud may be the only option.

Therefore, a second series of experiments to validate the velocity measurements was initially planned. For this, the experimental setup (Fig. 5.6) was modified by interchanging the rail and basin position, placing the bottom plate of the

basin between the transducer and the mud (see Fig. 5.27 and Fig. 5.28). To facilitate a straight line of travel of the transducer, a slot was milled on the outside of the bottom plate. This slot was filled with acoustic gel to allow optimal transmission of the ultrasound energy to the bottom plate. When stationary, this setup worked fine. However, upon movement the transmission gel was pushed aside, losing the acoustic contact between transducer and the bottom plate. Therefore, in the case of a setup with an intermediate material, a stationary transducer is recommended.

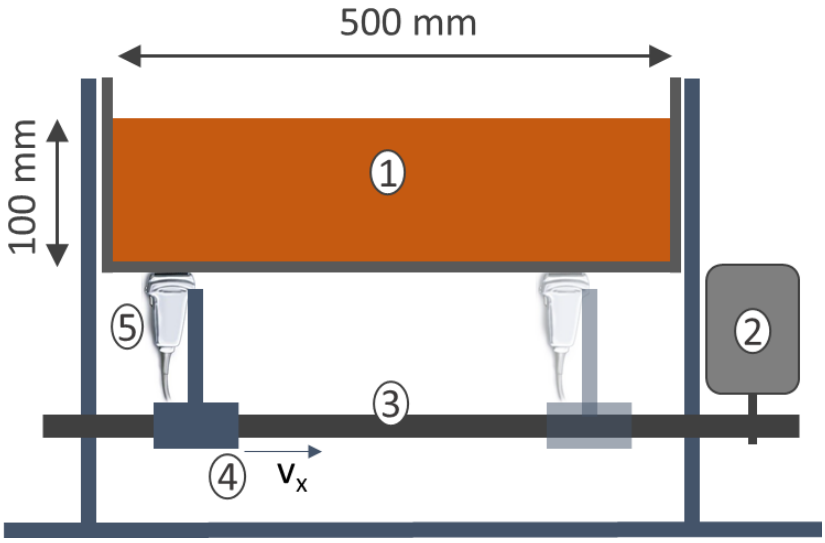

Figure 5.27: *Altered setup as an alternative to the setup used in Section 5.3, using a material in between the ultrasound transducer and the mud. (1) basin to contain the mud; (2) stepper motor providing the drive to move the carriage at a velocity v_x; (3) belt transmitting the drive from the stepper motor to the carriage; (4) carriage with vertically fixed stand; (5) ultrasound array transducer clamped to the stand.*

As mentioned in Section 5.1, a material placed in between the ultrasound transducer and the mud causes unwanted loss in

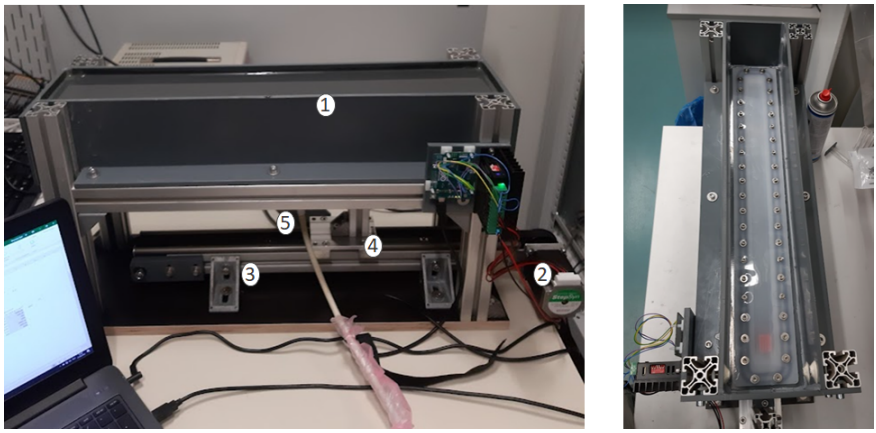

Figure 5.28: *On the left, a picture of the actual setup as sketched in Fig. 5.27. The labels identifying the main components correspond to those of Fig. 5.27. On the right, a top view of the setup showing the LDPE bottom of the (empty) basin.*

ultrasound energy. This can be minimised by a conscious choice in the type of material. As stated by Gurung and Poelma (2016), energy loss is mainly governed by reflection and not by attenuation (absorption and scattering) by the material. Loss due to reflection occurs when ultrasound radiation passes an interface of two media with different acoustic impedance. This can be estimated by calculating the reflection loss coefficient based on the impedances of both media (see Chapter 3).

Hence, the greater the mismatch in impedance, the greater the loss in radiation intensity due to reflection. The acoustic impedance of the intermediate material is therefore preferably similar to that of mud. With a speed of sound of 1465 $m \cdot s^{-1}$ and a density of 1150 $kg \cdot m^{-3}$, the acoustic impedance of the mud used in this study is equal to $1685 \cdot 10^3$ $kg \cdot m^{-2} \cdot s^{-1}$. Of all the materials commonly available as sheet materials, low-density polyethylene (LDPE), with an acoustic impedance

equal to $1997{\cdot}10^3$ kg·m^{-2}·s^{-1} (Ginzel and Turnbull, 2016), seems to provide the best match with mud. To illustrate, the loss due to reflection at an LDPE-mud interface, calculated using Eq. 3.9, is limited to 8.47 %. Because of its optical transparancy, Dash et al. (2022) used polymethylmethacrylate (PMMA) in his experimental setup. The acoustic impedance of PMMA is $3214{\cdot}10^3$ kg·m^{-2}·s^{-1} (Ginzel and Turnbull, 2016). With the same mud, the loss due to reflection would be 31.22 %.

To complete the comparison, attenuation by the material must also be considered. The loss due to attenuation can be calculated using the Beer Lambert Law (see Eq. 3.1). This law indicates that the loss in intensity due to attenuation can be decreased by reducing the thickness of the intermediate material. This was also considered by Gurung and Poelma (2016), as illustrated in Fig. 5.2, and by Dash et al. (2022). The attenuation rates of ultrasound with a frequency of 5 MHz by LDPE and PMMA are 1.32 dB·mm^{-1} and 0.57 dB·mm^{-1}, respectively (Ginzel and Turnbull, 2016).

Note the difference in unit in which attenuation is expressed compared to that in the Beer Lambert law (Eq. 3.1). The correlation between decibels (dB) and nepers (Np) is:

$$1 \text{ Np} = 20{\cdot}\, log(e) \text{ dB} \tag{5.6}$$

For a thickness of 1 mm, as in the setup of Dash et al. (2022), the loss due to attenuation is 14.10 % in case of LDPE and 6.35 % in case of PMMA. This shows that in terms of attenuation, the use of LDPE is less favourable compared to PMMA. Because of the limited thickness of the intermediate material, however, this cannot compensate for the aforementioned losses due to reflection. To illustrate, the total loss, adding the losses due to reflection and attenuation, is 22.57 % for LDPE and 37.57 % for PMMA.

5.6 Conclusions on the suitability of UIV for experimental mud flow diagnostics

The ability of UIV to accurately record flow properties in natural dense cohesive mud is demonstrated through various experiments. Using standard medical ultrasound imaging equipment, the resolution and velocity range obtained are adequate for experimental research using mud, such as Sotelo et al. (2022). At the same time, some restrictions were identified.

The maximum recordable flow velocity, for instance, showed to be limited by both the width of the images and the frame rate of the ultrasound scanner. To allow recording at high frame rates, the transducer is operated in plane wave mode. This limits the width of the images to the width of the ultrasound transducer. With a phased array transducer of 13.9 mm wide, operating at a frame rate of about 350 Hz, the highest recorded flow velocity was 1100 mm·s^{-1}. The limiting factor here is the width of the transducer. A wider transducer allows for wider interrogation windows, increasing the maximum recordable displacement between two frames. With a 40 mm wide linear transducer operating at the same frame rate of 350 Hz, the maximum recordable velocity would increase to 2800 mm·s^{-1}.

On the other hand, the results show that using enlarged windows reduces the SNR and hence the quality of the measurements. Higher frame rates can resolve this contradiction. While maintaining the smallest window size used in this study, i.e. 48 pixels, increasing the frame rate to 1167 Hz would allow to preserve the maximum recordable flow velocity of 2800 mm·s^{-1}. Using plane wave technology, such frame rates are attainable. As an example, the equipment used by Dash et al. (2022) can record images at a frame rate ranging from 400 Hz to 4000 Hz. Therefore, it can be concluded that with the appropriate equipment, the magnitude

of the flow velocity relevant to nautical research such as that of Lovato et al. (2022) and Sotelo et al. (2022), should not pose any further constraints.

A more severe restriction is the depth to which velocities can be adequately measured. This limitation was presumed to be caused by the attenuation of ultrasound by the mud, which in turn is linearly proportional to both the applied ultrasound frequency and the density of the mud. Multiple experiments applying UIV with varying ultrasound frequency in various mud samples of different density were therefore performed. The results confirm an increasing depth range with both decreasing ultrasound frequency and decreasing mud density and thus decreasing attenuation in general. A maximum depth range of 70 mm was obtained in mud with a density of 1.12 g·cm^{-3} with 2 MHz ultrasound.

Because of the loss of ultrasound energy, even lower depth ranges can be expected when an intermediate material is placed between the ultrasound transducer and the mud. To minimise the additional loss resulting from such an arrangement, a material whose acoustic impedance matches closely to that of the mud is recommended. LDPE is therefore suggested for sheet materials.

The results of the linear array experiments stand out for their shallow depth ranges and low variation in the assessed depth ranges. This can be attributed to the TGC applied by the operating system. The greater consistency in depth range does not outweigh the decrease in depth range. Therefore, gain can generally be considered unfavourable for the depth range of UIV. Together with the conclusion of Sivesgaard et al. (2009) that gain does not enhance the accuracy of cross-correlation between ultrasound images, it can be concluded that the application of gain should not be considered for future application of UIV.

The experimental results allowed an assessment of possible measures to increase the depth range without changing the ultrasound equipment. Because the density of mud is usually fixed in experimental research involving mud, lowering the density was not considered. The velocity validation experiments were conducted in mud with a density of 1.150 g·cm^{-3} and with 3.5 MHz ultrasound. The achieved depth range was 50 mm. In conjunction with the results of the particle size analysis of the mud (Fig. 3.16), doubling this depth range is considered feasible by lowering the ultrasound frequency to 0.6 MHz. If sufficient scatterers are present among the larger particles in the mud (above the d_{50}), even greater depth ranges are possible by further lowering the ultrasound frequency. Without knowing the size, occurrence and chemical composition of the particles in mud, a more precise assessment cannot be made. Unfortunately, this assessment could not be verified because such low ultrasound frequencies are far below the frequency range of the equipment available for this study and by extension ultrasound equipment for medical diagnostics. In conclusion, based on the experiments conducted during this research, UIV can be applied in Zeebrugge mud with ultrasound frequencies ranging from 1.75 MHz to 7 MHz. Taking into account the above assessment, it is likely that this can be extended to a range of 0.6 MHz to 7 MHz. An update of Fig. 4.1, including the application of UIV in mud, is therefore provided in Fig.5.29.

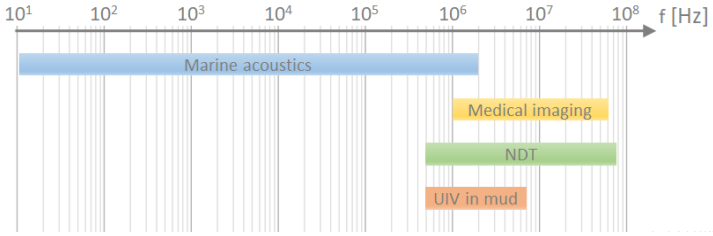

Figure 5.29: *Update of Fig. 4.1, including the frequency range for application of UIV in Zeebrugge mud in accordance with the findings of this study.*

Secondly, increasing the power of the emitted ultrasound proved to be an effective way to increase the depth range. By increasing the voltage applied to the ultrasound transducer from 60 V to 150 V, an average increase of 7.334 dB was observed. The increase in depth range resulting from this depends on the attenuation rate. In case of the aforementioned example of Zeebrugge mud with a density of 1.150 g·cm^{-3} and an ultrasound frequency of 0.6 MHz, an additional depth range of 36.7 mm can be achieved this way. Together with the lowering of the ultrasound frequency, a total depth range of 136.7 mm is thus considered feasible. This does not yet meet the targeted goal of 250 mm for application in experimental research as carried out by Sotelo et al. (2022, 2023). It does offer options for an alternative intrusive setup, where the transducer is placed at an offset to the bottom of the flume or even inside the the towed object, flush with its outer shell.

The ultrasound power emitted by medical ultrasound scanners is limited due to safety limits for patient protection (Quarato et al., 2023). This can be optimised using the pulse compression technique, thereby increasing the depth range while still respecting patient safety limits (Kaczkowski, 2016). A conventional compression of 100 cycles results in an increase in transmitted SPL of 20 dB. For the aforementioned example, this results in an additional depth range of 100 mm. Such a technique was not used in this study, as it requires more specialised equipment and experience. A second option for further depth range optimisation is the use of more powerful ultrasound imaging equipment, such as high resolution sonars used for offshore site surveying and archaeology. They emit ultrasound with an intensity of about 200 dB, potentially resulting in a depth range of up to 900 mm. The maximum recordable flow velocity with this may well be limited because the frame rate of such equipment is significantly lower compared to medical equipment. In turn, this can however be compensated for by the greater widths of the transducers.

Bibliography

Alexander N. and Swanevelder J. Resolution in ultrasound imaging. *Continuing Education in Anaesthesia, Critical Care & Pain*, 11(5): 186–192, 2011.

Anderson J. D. Chapter 3: Inviscid, incompressible flow. In Beamesderfer L. and Castellano E., editors, *Fundamentals of Aerodynamics*, pages 153–245. McGraw-Hill, Inc., 1991.

Assallay A., Rogers C., Smalley I. and Jefferson I. Silt: 2–62 µm, 9–4φ. *Earth-Science Reviews*, 45(1):61–88, 1998. doi: 10.1016/S0012-8252(98)00035-X.

Bergaya F., Theng B. K. G. and Lagaly G. *Handbook of clay science*. Elsevier, Oxford, UK, 2006.

Blott S. J. and Pye K. Particle size scales and classification of sediment types based on particle size distributions: Review and recommended procedures. *Sedimentology*, 59(7):2071–2096, 2012. doi: 10.1111/j.1365-3091.2012.01335.x.

Chassagne C. *Introduction to Colloid Science - Applications to sediment characterization*. TU Delft Open, Delft, the Netherlands, 2019. doi: 10.34641/mg.16.

Chinaud M., Delaunay T. and Tordjeman P. An experimental study of particle sedimentation using ultrasonic speckle velocimetry. *Measurement Science and Technology*, 21(5):1–7, 2010. doi: 10.1088/0957-0233/21/5/055402.

Crapper M., Bruce T. and Gouble C. Flow field visualization of sediment-laden flow using ultrasonic imaging. *Dynamics of Atmospheres and Oceans*, 31:233–245, 2000. doi: 10.1016/s0377-0265(99)00035-4.

Dash A., Hogendoorn W., Oldenziel G. and Poelma C. Ultrasound imaging velocimetry in particle-laden flows: Counteracting attenuation with correlation averaging. *Experiments in Fluids*, 63 (56), 2022. doi: 10.1007/s00348-022-03404-x.

D'hooge J. Chapter 2: Principles and different techniques for speckle tracking. In Marwick T., Yu C.-M. and Sun J. P., editors, *Myocardial Imaging: Tissue Doppler and Speckle Tracking*, pages 17–25. Wiley-Blackwell, 2008.

Ginzel E. and Turnbull B. Determining approximate acoustic properties of materials. *e-Journal of Nondestructive testing (NDT)*, 21(12), 2016.

Gurung A. and Poelma C. Measurement of turbulence statistics in single-phase and two-phase flows using ultrasound imaging velocimetry. *Experiments in fluids*, 57(171), 2016. doi: 10.1007/s00348-016-2266-x.

Gurung A., Haverkort J. W., Drost S., Norder B., Westerweel J. and Poelma C. Ultrasound image velocimetry for rheological measurements. *Measurement Science and Technology*, 27(9), 2016. doi: 10.1088/0957-0233/27/9/094008.

Halász G., Gyüre B., Jánosi I., Szabó G. and Tél T. Vortex flow generated by a magnetic stirrer. *American Journal of Physics*, 75, 03 2007. doi: 10.1119/1.2772287.

Iler R. K. *The Chemistry of Silica: Solubility, Polymerization, Colloid and Surface Properties and Biochemistry of Silica*. John Wiley and Sons, Hoboken, New Jersey, USA, 1979.

Jensen J. *Fast Plane Wave Imaging*. PhD thesis, Technical University of Denmark, Lyngby, Denmark, 2017.

Kaczkowski P. *Arbitrary Waveform Generation with the Verasonics Research Ultrasound Platform*, 2016.

Liberzon A., Lasagna D., Aubert M., Bachant P., Käufer T., Jakirkham, Bauer A., Vodenicharski B., Dallas C., Borg J., Tomerast and Ranleu. Openpiv/openpiv-python: Openpiv - python (v0.22.2) with a new extended search piv grid option. Open access, Zenodo, Jul 2020. URL https://doi.org/10.5281/zenodo3930343.

Lovato S., Kirichek A., Toxopeus S., Settels J. and Keetels G. Validation of the resistance of a plate moving through mud: Cfd modelling and towing tank experiments. *Ocean Engineering*, 258, 2022. doi: 10.1016/j.oceaneng.2022.111632.

Morse P. M. and Ingard K. U. *Theoretical acoustics*. Princeton University Press, Princeton, New Jersey, USA, 1968.

Ortega A., Lines D., Pedrosa J., Chakraborty B., Komini V., Gassert H. and D'hooge J. Hd-pulse: High channel density programmable ultrasound system based on consumer electronics. In *Proceedings of the IEEE International Ultrasonics Symposium (IUS)*, pages 2121–2123, Taipei, Taiwan, 21–24 October 2015. doi: 10.1109/ULTSYM.2015.0516.

Poelma C. and Fraser K. H. Enhancing the dynamic range of ultrasound imaging velocimetry using interleaved imaging. *Measurement Science and Technology*, 24(11), 2013. doi: 10.1088/0957-0233/24/11/115701.

Quarato C., Lacedonia D., Salvemini M., Tuccari G., Mastrodonato G., Villani R., Fiore L., Scioscia G., Mirijello A., Saponara A. and Sperandeo M. A review on biological effects of ultrasounds: Key messages for clinicians. *Diagnostics*, 13, 2023. doi: 10.3390/diagnostics13050855.

Raffel M., Willert C., Scarano F., Kähler C., Wereley S. and Kompenhans J. *Particle Image Velocimetry: A Practical Guide (third edition)*. Springer Cham, New York, USA, 2018. doi: 10.1007/978-3-319-68852-7.

Risser C., Welsch H. J., Fonfara H., Hewener H. and Tretbar S. High channel count ultrasound beamformer system with external multiplexer support for ultrafast 3d/4d ultrasound. In *Proceedings of the IEEE International Ultrasonics Symposium (IUS)*, pages 1–4, Tours, France, 18–21 September 2016. doi: 10.1109/ULTSYM.2016.7728714.

Roth G. and Katz J. Five techniques for increasing the speed and accuracy of piv interrogation. *Measurement Science and Technology*, 12:238, 2001. doi: 10.1088/0957-0233/12/3/302.

Seinfeld J. H. and Pandis S. N. Chapter 15 - interaction of aerosols with radiation. In *Atmospheric Chemistry and Physics – second edition*, pages 691–718. John Wiley & sons, inc., New Jersey, USA, 2006.

Silverman R., Vinarsky E., Woods S., Lizzi F. and Coleman D. The effect of transducer bandwidth on ultrasonic image characteristics. *Retina*, 15(1):37–42, 1995. doi: 10.1097/00006982-199515010-00008.

Sivesgaard K., Christensen S. D., Nygaard H., Hasenkam J. M. and Sloth E. Speckle tracking ultrasound is independent of insonation angle and gain: An in vitro investigation of agreement with sonomicrometry. *Journal of the American Society of Echocardiography*, 22(7):852–858, 2009. doi: 10.1016/j.echo.2009.04.028.

Sotelo M., Boucetta D., Doddugollu P., Toorman E., Brouwers B., Delefortrie G. and Van Hoydonck W. Experimental study of a cylinder towed through natural mud. In *Proceedings of the 6th MASHCON International Conference on Ship Manoeuvring in Shallow and Confined Water*, pages 222–231, Glasgow, UK, 22–26 May 2022.

Sotelo M., Boucetta D., Van Hoydonck W., Doddugollu P., Vantorre M., Toorman E. and Delefortrie G. Hydrodynamic forces acting on a cylinder towed in muddy environments. *Journal of Waterway, Port, Coastal, and Ocean Engineering*, 149(6), 11 2023. doi: 10.1061/JWPED5.WWENG-1992.

Strutt J. W. XXXVI. on the light from the sky, its polarization and colour. *The London, Edinburgh, and Dublin Philosophical Magazine and Journal of Science*, 41(273):274–279, 1871. doi: 10.1080/14786447108640479.

Szabo T. L. Chapter 8: Wave scattering and imaging. In *Diagnostic Ultrasound Imaging: Inside out*, pages 213–241. Elsevier Academic Press, Hoboken, NJ, USA, 2004a.

Szabo T. L. Chapter 5: Transducers. In *Diagnostic Ultrasound Imaging: Inside out*, pages 97–135. Elsevier Academic Press, Hoboken, NJ, USA, 2004b.

Szabo T. L. Chapter 10: Imaging systems and applications. In *Diagnostic Ultrasound Imaging: Inside out*, pages 297–335. Elsevier Academic Press, Hoboken, NJ, USA, 2004c.

Tanter M. and Fink M. Ultrafast imaging in biomedical ultrasound. *IEEE Transactions on Ultrasonics, Ferroelectrics, and Frequency Control*, 61:102–119, 2014. doi: 10.1109/tuffc.2014.2882.

ter Haar G. *The safe use of ultrasound in medical diagnosis - third edition*. The British Institute of Radiology, London, UK, 2012.

Thijssen J. and Oosterveld B. Speckle and texture in echography: Artifact or information? In *Proceedings of IEEE Ultrasonics Symposium, Williamsburg, VA, USA, 17-19 November*, pages 803 – 810, 1986. doi: 10.1109/ULTSYM.1986.198845.

Wells P. and Halliwell M. Speckle in ultrasonic imaging. *Ultrasonics*, 19(5):225–229, 1981. doi: 10.1016/0041-624X(81)90007-X.

Zou X.-j., Ma Z.-m., Zhao X.-h., Hu X.-y. and Tao W.-l. B-scan ultrasound imaging measurement of suspended sediment concentration and its vertical distribution. *Measurement Science and Technology*, 25(11), 2014. doi: 10.1088/0957-0233/25/11/115303.

Zou X.-j., Ma Z.-m., Hu W.-b., Wang J.-c., Song H., Hu X.-y. and Tao W.-l. B-mode ultrasound imaging measurement and 3d reconstruction of submerged topography in sediment-laden flow. *Measurement*, 72:20–31, 2015. doi: 10.1016/j.measurement.2015.04.026.

Chapter 6

Conclusions and recommendations to enhance the quality of experimental research with mud

Natural cohesive mud is found all over the world. Because of its complex nature, it poses various challenges in multiple fields of engineering. Experimental research is therefore necessary to determine its properties and better understand its behaviour. The overall objective of this research is to enhance the quality and potential of any experimental research involving dense natural mud. This is especially needed to enable hydraulic experiments investigating the effects of the behaviour of mud on its surroundings. To this end, two deficiencies were identified that currently impede this objective. Firstly, the lack of competence to make the behaviour of mud sufficiently consistent across different experiments. Secondly, the absence of available techniques to monitor flow dynamics over a sufficiently large area, in

natural cohesive dense mud. These two topics are discussed separately in the following subsections.

6.1 Reproducibility of settling behaviour of mud

6.1.1 Recommended preparation of mud for use in experiments

Earlier published experimental data show that the settling behaviour of natural cohesive mud can vary, even in case of repetitive experiments. This can be assessed from the settling curves, which illustrate the decline of the water-mud interface level over time. Deviations between settling curves of 3 % to 5 % are considered the better results in terms of repeatability. The majority however exceeds 5 %. Such deviations are unacceptable for hydraulic experiments. Moreover, the settling curves show that the divergent settling behaviour occurs in the early stages of sedimentation. During the subsequent consolidation phase, the developed deviations are maintained. Measures to improve repeatability were therefore sought in the preparatory phase of the experiments.

Mud contains both cohesive and non-cohesive particles. The cohesive particles can be present as primary particles or in the form of flocs. In a low energy environment, they tend to flocculate and form larger flocs. Based on the mechanics that occur during sedimentation, the size of particles and flocs as well as their dispersion in the mud volume, are identified as the factors determining the overall settling behaviour. The purpose of conditioning mud prior to experiments should therefore be to gain control over these properties. An issue is however that both properties are difficult to assess. This can be bypassed by striving to create reproducible reference states of the properties in question, making their assessment redundant.

When a volume of mud is left at rest, the heavy particles and flocs will settle instantly. The smaller cohesive particles and flocs will first aggregate to form larger flocs. Once these flocs are sufficiently heavy, they too will settle. This way, the size of the flocs and their dispersion in the mud volume at the start of sedimentation influences the overall settling behaviour of the mud. Given their low shear strength, the breaking of flocs is the most effective way to gain control over their size. Exposure of a fluid to shear can be achieved by radial mixing. A uniform dispersion of the various particles and flocs is obtained by homogenising the mud, which in turn can be done effectively with axial mixing. Due to practical limitations (spills, vortexing, power limits of mixers, etc.), achieving the extremes like perfect homogeneity and complete disintegration of all flocs into their primary cohesive particles is not realistic. For the reference states of both homogeneity and floc size to be reproducible, the maximum possible condition with the applied mixing intensity must be attained. In turn, the intensity is determined by the duration and the applied energy during the mixing. The energy and the area over which it is applied are fixed by the equipment and its settings, leaving only the duration as a variable. Since the shear strength of a floc is inversely proportional to the size of the floc, the magnitude of the shear will determine the extent to which the flocs will break up. Similarly, the intensity of axial mixing determines the highest achievable degree of homogeneity. With a resolution of fifteen minutes, no minimum required mixing time could be determined by the experiments of this research. Considering fifteen minutes as a pragmatic minimum duration, shorter mixing periods were not further explored.

Conditioning of the mud prior to an experiment, by a combination of axial and radial mixing, will thus provide control over the settling behaviour of the mud during the experiment. Combined with a fixed procedure on how and how long this should be applied, deviations in settling curves of experiments within the same series of experiments during this research

are limited to 1 %. When different series of experiments are considered, performed with a different mud volume (of the same origin and therefore composition) or at a different moment in time, the deviations are slightly larger, in the worst case up to 2 %. In both cases, there is a significant improvement in the reproducibility of the settling behaviour compared to previously published experimental results.

6.1.2 Establishing a mud conditioning procedure

How the axial mixing should be performed and for how long depends on the available mixing equipment, the volume and composition of the mud. If this is not yet known for a specific combination, small-scale sedimentation experiments are recommended upfront to determine this.

If multiple experiments are conducted with mud samples from the same batch of mud, these experiments are considered a series. In such case, the degree of homogeneity of all samples can be considered equal. Therefore, one could argue that conditioning by radial mixing alone should already be sufficient. Nonetheless, conditioning by a combination of axial and radial mixing is always recommended to ensure the possibility of comparing the results with those of other future experiments.

When comparing the results of experiments across different experimental series, the equipment, settings and duration of mixing should be the same. In the case of a collaborative research project between different laboratories or a replacement of equipment over time, this is not always practical or even feasible. In such cases, small short-term settling experiments should be carried out in advance to match the mixing intensities during conditioning.

This study only considers repeatability in settling behaviour. Yet density and pore pressure also determine the mechanical

behaviour of mud. Since density and pore pressure result from the progress of sedimentation, their repeatability is assumed to be similarly influenced by the mud conditioning procedure. This remains however to be verified by further experimental research.

Similarly, further research is required to assess the influence of density on the outcome of this study. Especially if the density at the beginning of the experiment is higher than the gel density of the mud. The gel density is the density threshold from which the distance between the cohesive flocs is sufficiently small for the attraction forces between the flocs to form a structure that leads to a yield strength. Consequently, the settling process proceeds differently depending on whether the initial density is above or below the gel density. During this study, only settling experiments were performed with an initial density lower than the gel density. Apart from the possibility that the required mixing intensity may be higher, no significant difference in conclusions is however expected.

6.2 Flow monitoring

6.2.1 Preferred visualisation technique for application of PIV to mud

Various techniques have been used in previous research to monitor flow dynamics in clay suspensions and natural cohesive muds. None of these techniques however fully cover the needs for hydraulic experiments involving mud, like those conducted by Sotelo et al. (2022, 2023). To truly serve such experimental research, a whole-flow-field velocimetry technique is required. Not surprisingly, Particle Image Velocimetry (PIV) is widely used in experimental fluid dynamics. The challenge for applying PIV in mud is to find a technique able to visualise the flow dynamics in the mud.

Furthermore, this technique may not restrict the range of recordable velocities, the resolution of velocity measurements and the depth range. For the experimental research by Sotelo et al. (2022, 2023) this comes down to flow velocities of up to 1000 mm·s^{-1}, a resolution of about 2 mm vector spacing and a depth range of up to 250 mm.

Radiography and ultrasonography both offer the ability to visualise flow dynamics in mud. Since radiography requires full penetration of the mud layer, a considerable amount of energy is already required to visualise flow dynamics in mud layers of limited thickness. Even with the most powerful X-ray source available on the market, the maximum mud layer thickness would still be limited to 300 mm. Although this would still be of interest for the envisaged research projects, the direct costs of purchasing the X-ray source and the indirect costs of safety measures are in the order of hundreds of thousands of euros, which is considered too expensive. For the ultimate application of PIV on radiographic images, radiography has some drawbacks as well. With regards to application in mud, this is primarily the need for seeding particles. Radiographic images of mud result in uniform greyscale images. Similar to the application of optical PIV in translucent fluids, particles must be added to create traceable contrasts in the images. This way, the movement of the particles can be monitored and correlated to the flow dynamics in the mud. Such particles are rigid and have a fixed density. Hence, their presence will affect the settling mechanics in the mud. Ultimately, this affects the behaviour of the mud, making it less representative and casting doubt on the relevance of the experiments.

Ultrasonic images of mud, on the other hand, are directly suitable for processing with PIV algorithms. Typically, ultrasound imaging of mud results in speckle pattern images, which can be described as grainy greyscale images. This arises from the physics between the mud particles and the ultrasound radiation. The ratio between the size of the

particles present in the mud and the wavelength of the ultrasound in the megahertz range causes the ultrasound to scatter in the mud. Because of the numerous particles scattering the ultrasound, the scattered signals interfere with each other by adding up or cancelling each other out. Ultrasound imaging in B-mode translates the strength of the returning signals into pixel brightness on the images. High-strength signals result in bright pixels and vice versa. As a result of the interfering backscattered signals, ultrasound images of mud do not show individual particles, but speckle patterns representing the relative positions of the scattering particles in the mud. Hence, the change in successive speckle images can be correlated to the movement of the mud particles and thus to the flow dynamics in the mud. This application of processing ultrasound images with PIV algorithms is referred to as Ultrasound Imaging Velocimetry (UIV).

The maximum flow velocity recordable with UIV is determined by the width of the ultrasound images and the image acquisition rate of the ultrasound imaging equipment. Conventional frame rates for medical ultrasound imaging are in the order of 50 frames per second. This suffices for monitoring low velocity ranges such as in settling and rheologic experiments. For higher velocity ranges as for the envisaged towing experiments, this is insufficient. Higher frame rates can be achieved when the ultrasound transducer is operated in plane-wave mode. This involves all piezoelectric elements forming the array transducer emitting simultaneously, forming a plane of ultrasound radiation. Hence, the frame rate can be maximised up to the limit imposed by the time of flight of the sound waves. Ultrasound imaging equipment developed for research purposes can yield frame rates of up to 4000 frames per second when used in plane wave mode.

A consequence of operating in plane wave mode is that the width of the acquired images is limited to the width of

the transducer. In turn, this limits the maximum detectable displacement between successive images and thus the maximum recordable flow velocity. Altogether, with a frame rate of 350 Hz and a conventional 40 mm wide array transducer, flow velocities of up to 2800 $mm{\cdot}s^{-1}$ can be recorded, which amply meets the aforementioned objective.

The resolution of the velocity measurements to be pursued is determined by the experimental setup of the research. When seeding with additional particles is required, the density at which these particles are added may limit the resolution of the PIV output. As evidenced by the creation of speckle images, the density of scattering particles in Zeebrugge mud is high. In theory, there is thus no restriction to the resolution of the PIV output. In practice, it comes down to a trade-off between resolution and processing time. Higher resolutions require longer processing times and vice versa. Therefore, a maximum resolution achievable with UIV cannot be defined. For the experiments of this research, no disproportional processing times were required to meet the targeted resolution.

The UIV depth range achieved during the experiments of this study is insufficient for the intended purpose. Using standard medical ultrasound imaging equipment, a maximum depth range of 70 mm was obtained. Two methods have been identified to enhance the depth range. Firstly, the depth range is restricted due to the attenuation of the ultrasound by the mud. In turn, the attenuation is linearly proportional to the ultrasound frequency and the mud density. During this research, this relationship was determined for Zeebrugge mud (see Eq. 4.5). In most research involving mud, the density of the mud is an integral part of the research topic and thus cannot simply be changed to meet the requirements of the measurement technique. The ultrasound frequency, on the other hand, can be lowered. The lowest ultrasound frequency applied during the UIV experiments of this study

was 1.75 MHz. This is a common lower limit when using medical ultrasound imaging equipment. After all, image resolution is proportional to the ultrasound frequency, resulting in a lower limit for diagnostic applications. In case of speckle images, there is no requirement for image resolution. Nonetheless, lowering the ultrasound frequency negatively affects the performance of UIV in two other ways. Firstly, the intensity of the backscattered signals is reduced with decreasing frequency to the power of four. As a result, the contrast between the brightest and darkest pixels will decrease, making the image overall more faint. Secondly, the number of particles of adequate size to scatter the lower frequency ultrasound with sufficient intensity may become too small, ultimately causing the speckle pattern image to fade as well. Similar to the fading of speckle patterns with depth, there will be a lower limit to the ultrasound frequency from which PIV processing of the resulting images is no longer feasible. A reasoned estimate based on the results of the experiments of this research indicates that for Zeebrugge mud the ultrasound frequency can be lowered to 0.6 MHz. Due to the lower attenuation rate, this should allow a depth range of 125 mm using the same equipment. Without knowing the size and chemical composition of the particles scattering the ultrasound, a more detailed assessment cannot be made.

Secondly, a greater depth range can be achieved by increasing the intensity of the initially emitted ultrasound. With medical ultrasound imaging equipment, this is restricted for patient safety. Whereas when applied in mud, there is no need for such restrictions. Hence, greater depth ranges should be feasible with other, more powerful equipment.

Since the depth range is primarily determined by the attenuation of the ultrasound, gain (amplification) can be considered as an option to enhance the depth range. After all, gain is used in diagnostic imaging to compensate for the loss in image quality due to attenuation. This does come

at the cost of a loss in contrast, which is detrimental to the detection of speckle patterns and hence the performance of UIV. Experiments of this research confirm that the application of gain has the opposite effect and limits the depth range even more.

6.2.2 Optimal utilisation of UIV on mud

Since the limited depth range remains an issue, even for laboratory purposes, a thoughtful choice in ultrasound equipment and the way it is deployed is required when considering the application of UIV.

Even with a potential depth range of 900 mm (see Section 5.6), this is too limited for in situ monitoring of flow dynamics in mud as envisaged for in laboratory setups. For potential applications other than in a laboratory setup, applications with similarly limited thickness of the mud layer can be considered. For instance, the ability to apply UIV to mud can be useful in the dredging and (soil) drilling industry. In both cases, a fluid mud, or a clay suspension, is pumped. This involves monitoring the pump flow rate, with which the average flow rate is also known. For a better understanding of the pumping process in order to optimise it, it would be useful to obtain a velocity profile over the cross-sectional area of the pump pipeline. This can be obtained by velocity measurements with a probe at different penetration depths across the cross-section of the pipeline. Since pipelines are not always easily accessible, this is not an obvious operation. With UIV, such a velocity profile can be obtained with a fixed arrangement of an ultrasound array, eliminating the issue of accessibility.

For on-site applications it should be considered that in situ ultrasound imaging is likely to be distorted by unwanted strong reflectors in the mud, such as entrapped gas bubbles or parts of scrap metal. When the ultrasound encounters such a

reflector, most of it is reflected, leaving only a small fraction that propagates further. This fraction is probably too limited to allow further imaging behind the reflector. In this way, the presence of such strong reflectors will result in unwanted black streaks on the speckle images. UIV is therefore further considered for laboratory applications only.

To maximise the depth range, the useful ultrasound energy must be maximised. For this reason, the ultrasonic transducer is preferably in direct contact with the mud. If this cannot be met, an intermediate material separating the two can be considered. In such case, material selection should be based on acoustic impedance. To minimise reflection losses, this should match that of the mud as closely as possible. In case of Zeebrugge mud, LDPE is identified as the best option for sheet materials. Moreover, the thickness of the intermediate material should be limited as much as possible to minimise energy loss through attenuation.

Subsequently, the depth range is proportional to the intensity of the emitted ultrasound, while there is no indication of a required limitation in intensity. The ultrasound imaging equipment should thus be as powerful as possible. When the attenuation rate is known, the required initial intensity for a given depth range can be specified. In turn, the attenuation rate can be determined using various ultrasound equipment and techniques, as done during this research for Zeebrugge mud (see Chapter 4).

The design of the ultrasound transducer can also impact the intensity of the emitted ultrasound. To optimise axial resolution for diagnostic use, the oscillation of the piezoelectric elements in the transducer is damped by placing an elastic material behind these elements. This comes at the cost of a lower intensity of the emitted ultrasound and hence results in a lower depth range. Whenever possible, transducers with low damping capacity are therefore preferred.

Considering the proportionality between the attenuation rate and the ultrasound frequency, the latter should be as low as possible to maximise the depth range. The creation of speckle pattern images, however, entails a lower limit to the ultrasound frequency. As mentioned in the previous section, this lower limit cannot be assessed in advance without knowledge of the size and chemical composition of the scatterers. The optimal frequency must thus be determined experimentally. To facilitate this, the use of a broadband transducer covering the frequency range of interest is advised to limit the number of transducers to be used. A wide bandwidth is produced by damping the piezoelectric elements in the transducer. As mentioned earlier damping comes at the expense of the intensity of the emitted ultrasound and thus the depth range. Once the optimal frequency is known, a matching narrowband transducer can therefore be considered to optimise the depth range again.

6.3 Application of gained insights for other muds

This study was applied only to mud from Zeebrugge (Port of Antwerp-Bruges, Belgium). Nonetheless, the findings of this study can be generalised to support research involving other mud types of different origins.

Like Zeebrugge mud, the type of mud to which this study applies contains a clay fraction, which causes the specific settling behaviour of the mud. Therefore, sedimentation mechanisms are similar for different mud compositions where the dispersion and size of particles and flocs ultimately determine the specific settling behaviour. Consequently, the recommendation to condition mud for experimental research by axial and radial mixing remains valid. The composition of the mud does affect the procedure by which axial and

radial mixing are applied. In the case of a larger fraction of cohesive particles, the optimal share of radial mixing will increase. Similarly, the share of axial mixing is proportional to the fraction of coarse particles. For each type of mud, it is thus recommended to determine the conditioning procedure that maximises the reproducibility of the settling behaviour. Short-term settling experiments as conducted during this study can serve this purpose. The conditioning procedure also affects the course of the settling behaviour as such. Hence, if the difference in settling behaviour of different mud types is investigated, a uniform conditioning procedure should be applied. To maximise reproducibility for all mud types, this procedure should combine the greatest minimum shares of axial and radial mixing for the considered mud types.

The composition of a mud determines the most optimal ultrasound frequency to maximise the accuracy and depth range of the UIV applied to it. Therefore, when UIV is first applied to a mud, it is best to identify this first. For this, the presence of potential scatterers in the mud must be verified. Similar to the present study, this can be assessed based on the particle size distribution and a chemical element analysis of the mud. Without the ability to assign a size to the particles that scatter the ultrasound, this will always remain an estimate resulting in a spectrum of frequencies. To the author's knowledge, there is no available technique capable in doing this. Therefore, further narrowing of this spectrum in search of the optimal ultrasound frequency should be done experimentally. The advantage of being able to estimate the optimal frequency as best as possible is that the best suited transducer can be selected. The narrower the frequency spectrum a transducer needs to cover, the less damping is required in it. This benefits the intensity of the emitted ultrasound and the sensitivity of the transducer. Both result in enhanced contrast ratios in the speckle images and thus ultimately in improved accuracy and increased depth range of the UIV.

Bibliography

Sotelo M., Boucetta D., Doddugollu P., Toorman E., Brouwers B., Delefortrie G. and Van Hoydonck W. Experimental study of a cylinder towed through natural mud. In *Proceedings of the 6th MASHCON International Conference on Ship Manoeuvring in Shallow and Confined Water*, pages 222–231, Glasgow, UK, 22–26 May 2022.

Sotelo M., Boucetta D., Van Hoydonck W., Doddugollu P., Vantorre M., Toorman E. and Delefortrie G. Hydrodynamic forces acting on a cylinder towed in muddy environments. *Journal of Waterway, Port, Coastal, and Ocean Engineering*, 149(6), 11 2023. doi: 10.1061/JWPED5.WWENG-1992.

Appendix A

Plots of average velocities per depth

A.1 Plots of average velocities per depth of experiment 1

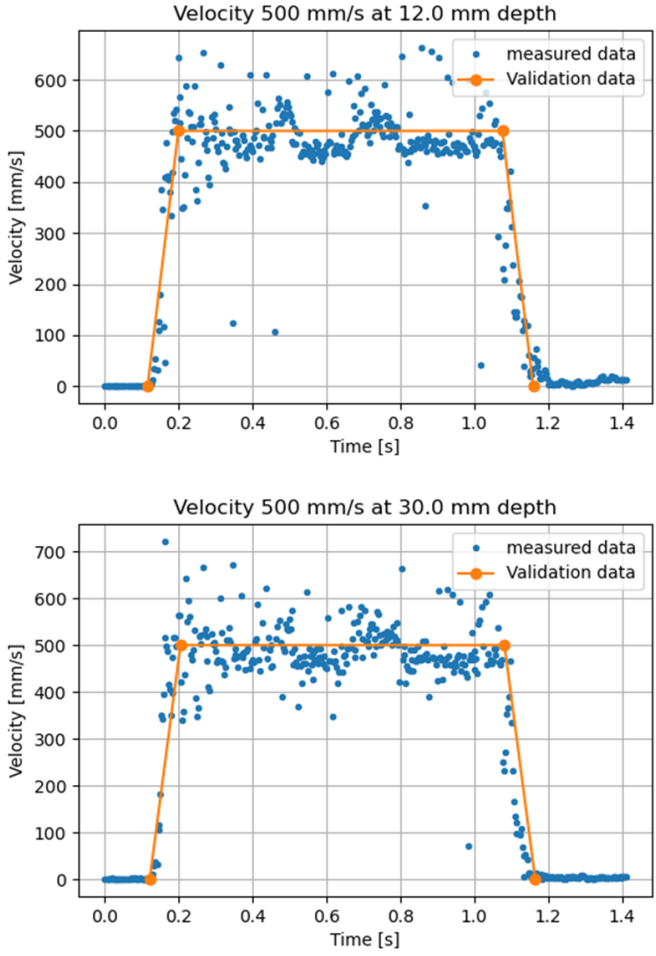

Figure A.1: *Series of plots of average measured velocities as a function of time for experiment 1 (see Table 5.1). Each plot corresponds to a depth as indicated in their titles.*

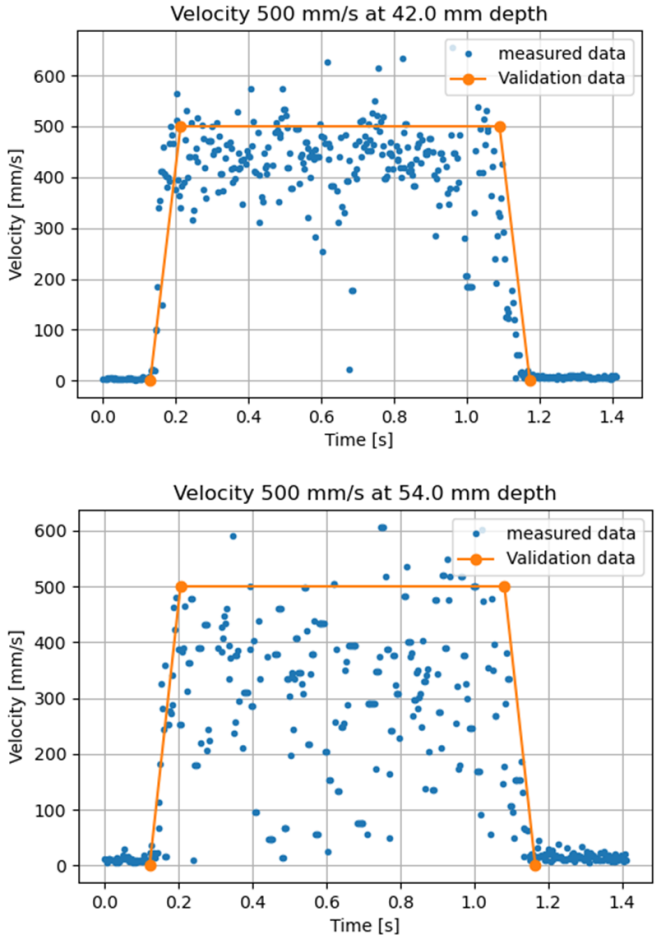

Figure A.2: *Series of plots of average measured velocities as a function of time for experiment 1 (see Table 5.1). Each plot corresponds to a depth as indicated in their titles.*

A.2 Plots of average velocities per depth of experiment 3

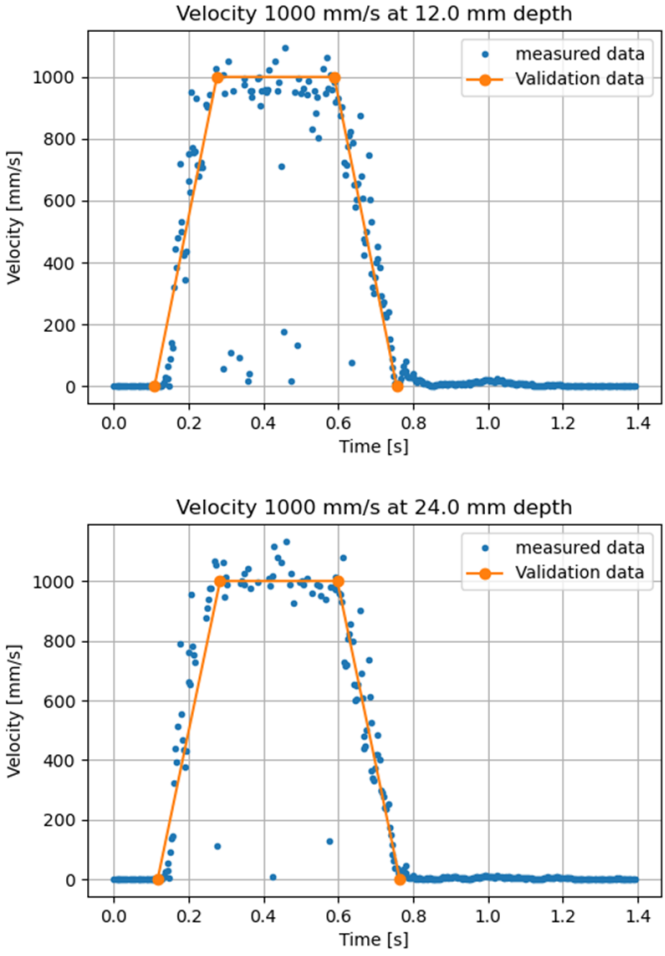

Figure A.3: *Series of plots of average measured velocities as a function of time for experiment 3 (see Table 5.1). Each plot corresponds to a depth as indicated in their titles.*

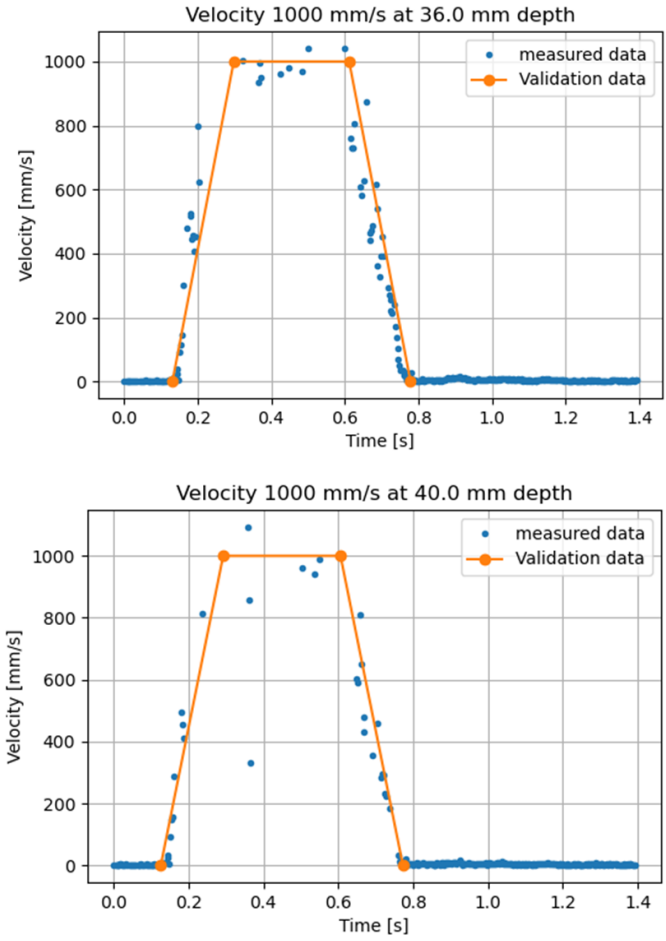

Figure A.4: *Series of plots of average measured velocities as a function of time for experiment 3 (see Table 5.1). Each plot corresponds to a depth as indicated in their titles.*

Appendix B

Supplementary plots of SPL and CR profiles

In addition to the information from the manuscript, plots of vertical SPL and CR profiles (solid curves) along with their corresponding coefficients of variation (dotted curves) from experiments conducted in the mid mud density are provided in this appendix.

B.1 Plots of SPL and CR profiles of experiments using the flexible linear array

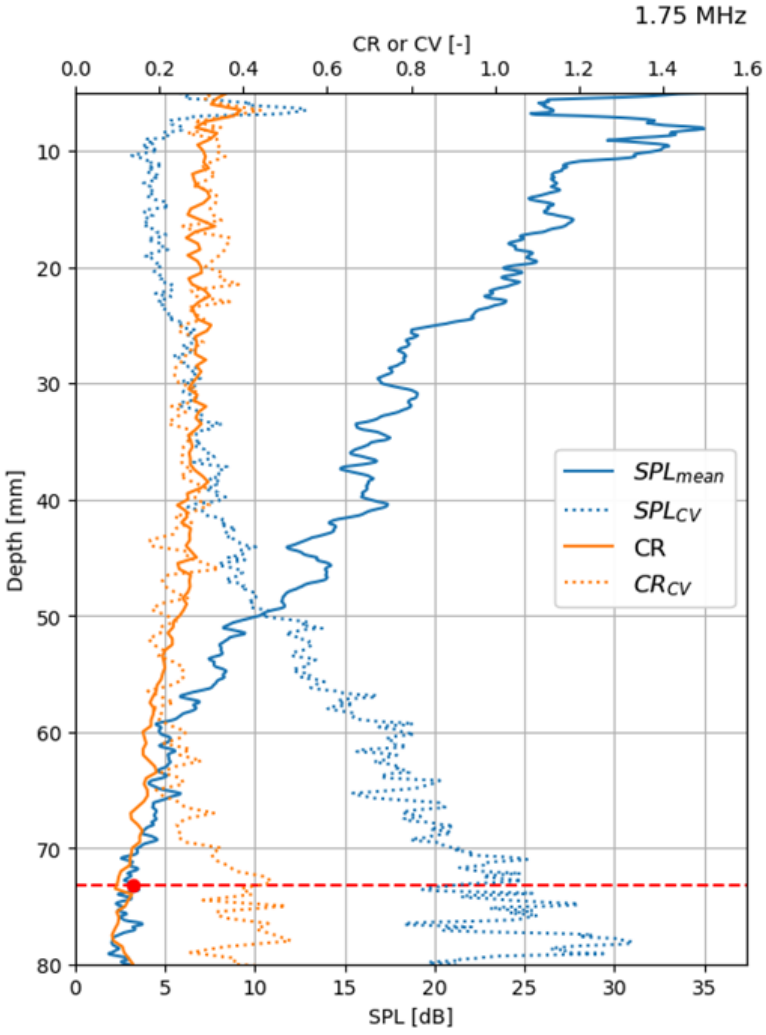

Figure B.1: *SPL and CR profiles resulting from experiments in mud with a density 1.146 g·cm^{-3} and an ultrasound frequency of 1.75 MHz, using the flexible linear array.*

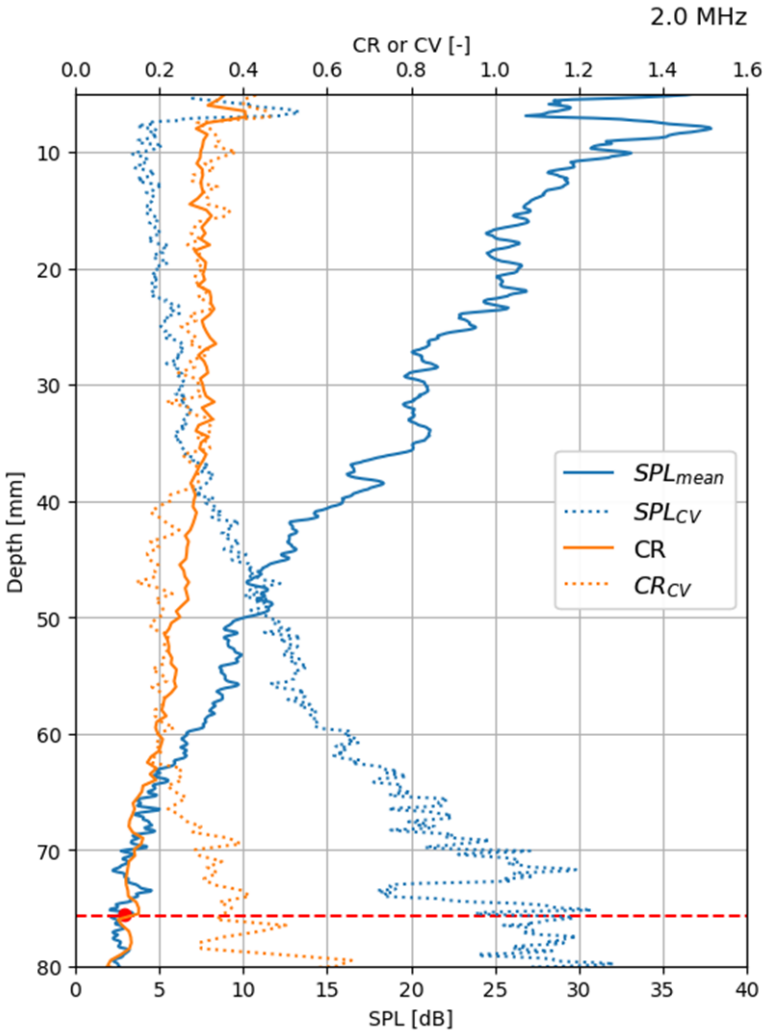

Figure B.2: *SPL and CR profiles resulting from experiments in mud with a density 1.146 $g{\cdot}cm^{-3}$ and an ultrasound frequency of 2.00 MHz, using the flexible linear array.*

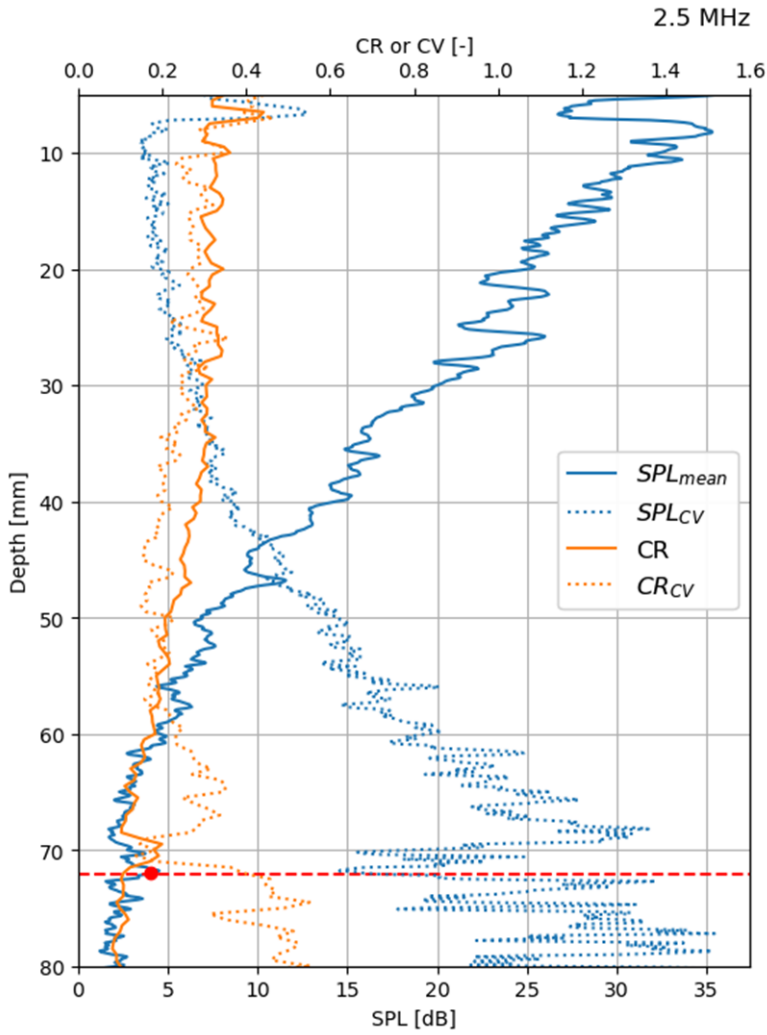

Figure B.3: *SPL and CR profiles resulting from experiments in mud with a density 1.146 g·cm^{-3} and an ultrasound frequency of 2.50 MHz, using the flexible linear array.*

B.2 Plots of SPL and CR profiles of experiments using the phased array

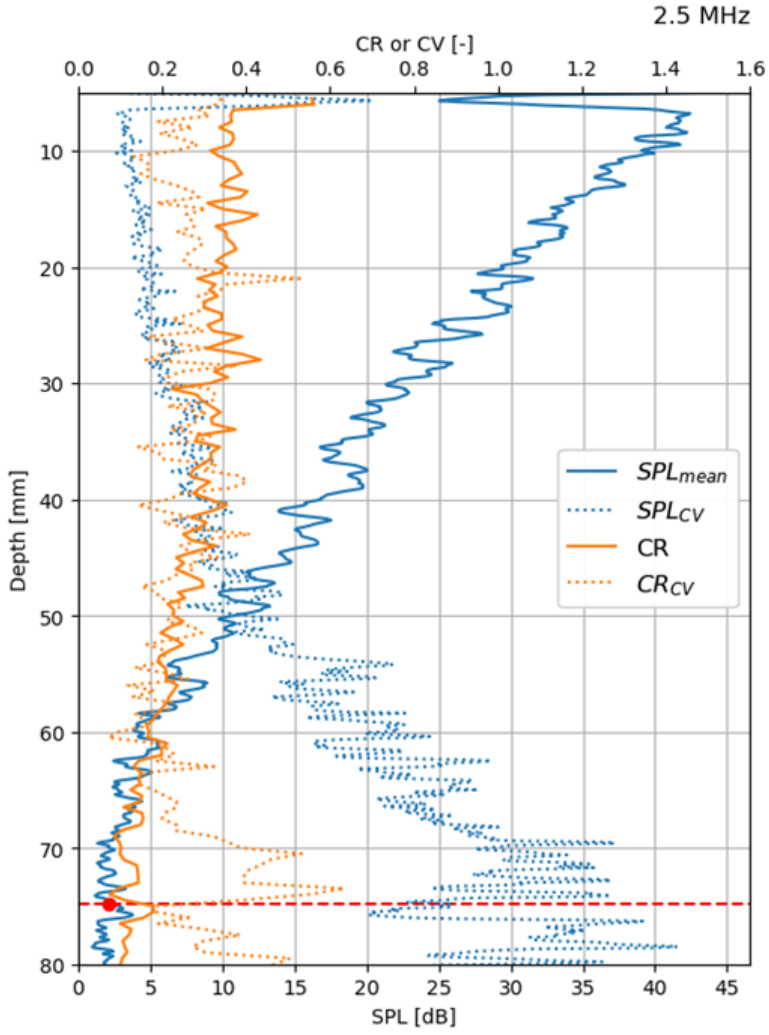

Figure B.4: *SPL and CR profiles resulting from experiments in mud with a density 1.151 $g{\cdot}cm^{-3}$ and an ultrasound frequency of 2.50 MHz, using the phased array.*

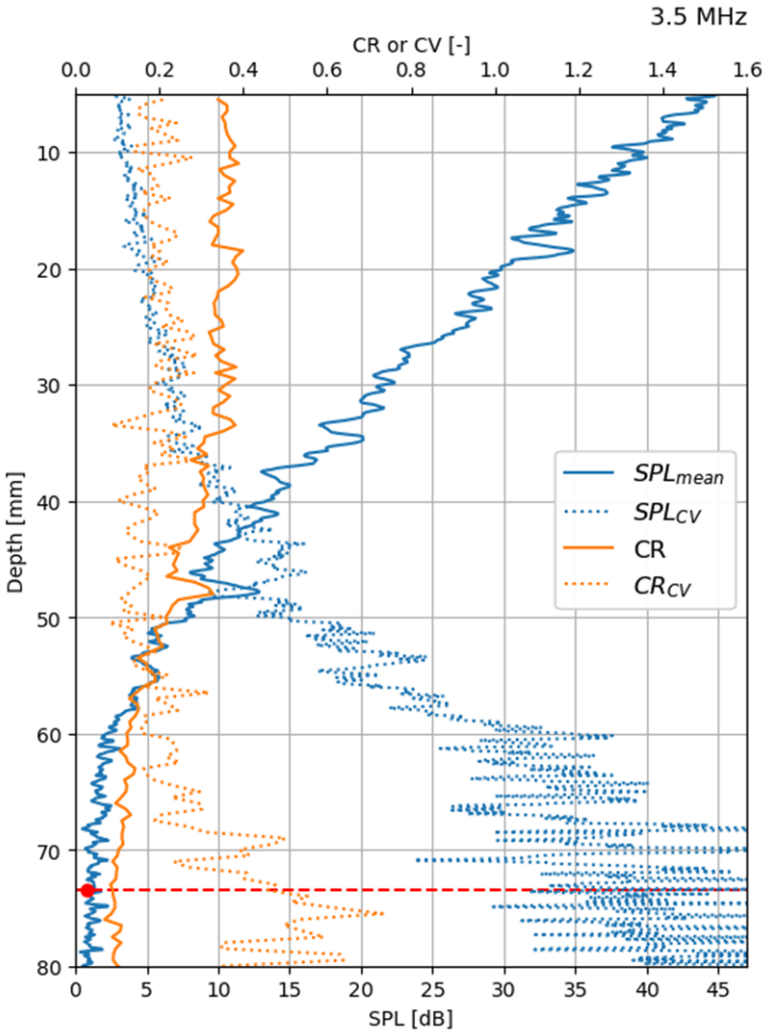

Figure B.5: *SPL and CR profiles resulting from experiments in mud with a density 1.151 $g{\cdot}cm^{-3}$ and an ultrasound frequency of 3.50 MHz, using the phased array.*

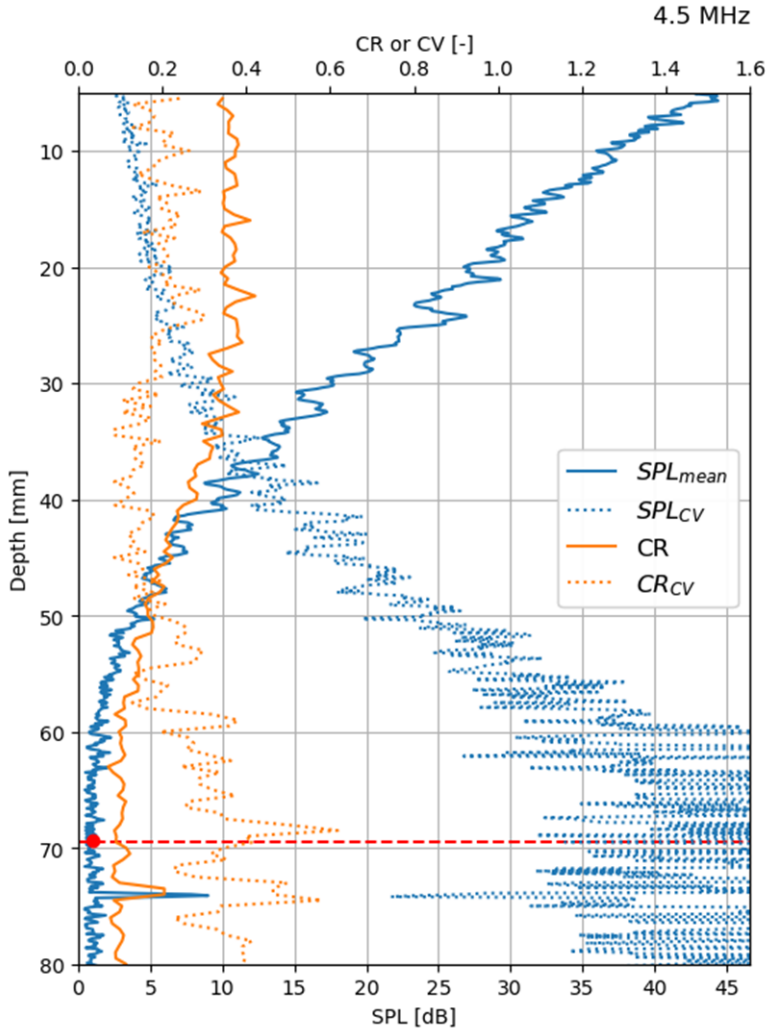

Figure B.6: *SPL and CR profiles resulting from experiments in mud with a density 1.151 g·cm^{-3} and an ultrasound frequency of 4.50 MHz, using the phased array.*

B.3 Plots of SPL and CR profiles of experiments using the linear array

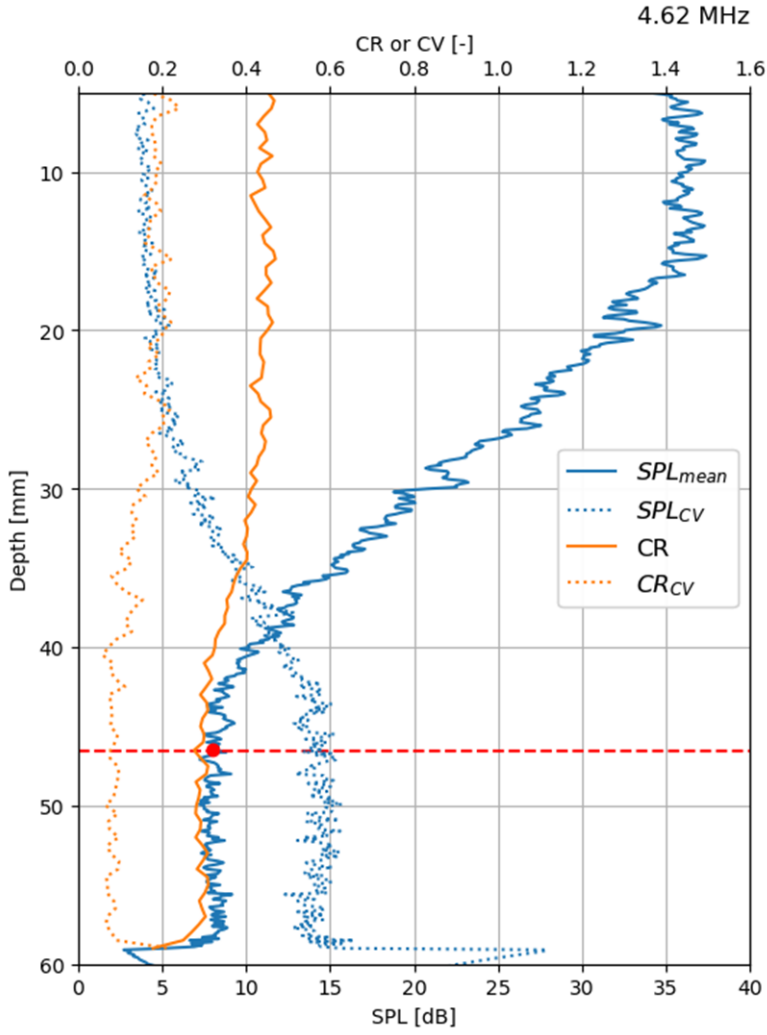

Figure B.7: *SPL and CR profiles resulting from experiments in mud with a density 1.146 g·cm^{-3} and an ultrasound frequency of 4.62 MHz, using the phased array.*

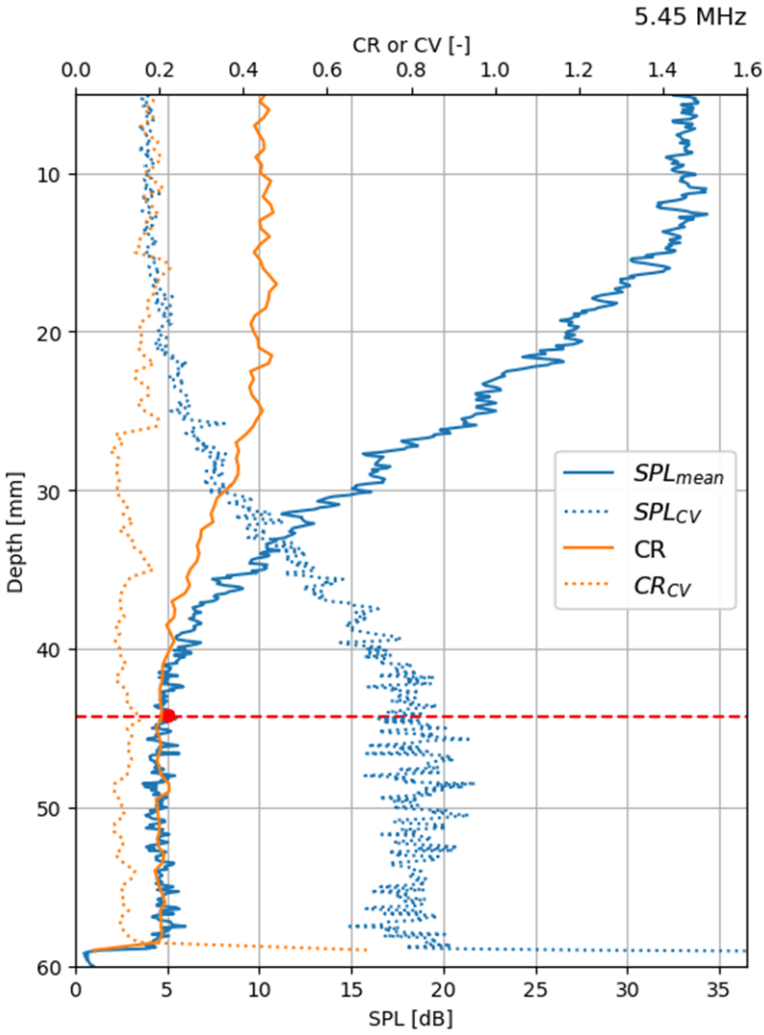

Figure B.8: *SPL and CR profiles resulting from experiments in mud with a density 1.146 $g{\cdot}cm^{-3}$ and an ultrasound frequency of 5.45 MHz, using the phased array.*

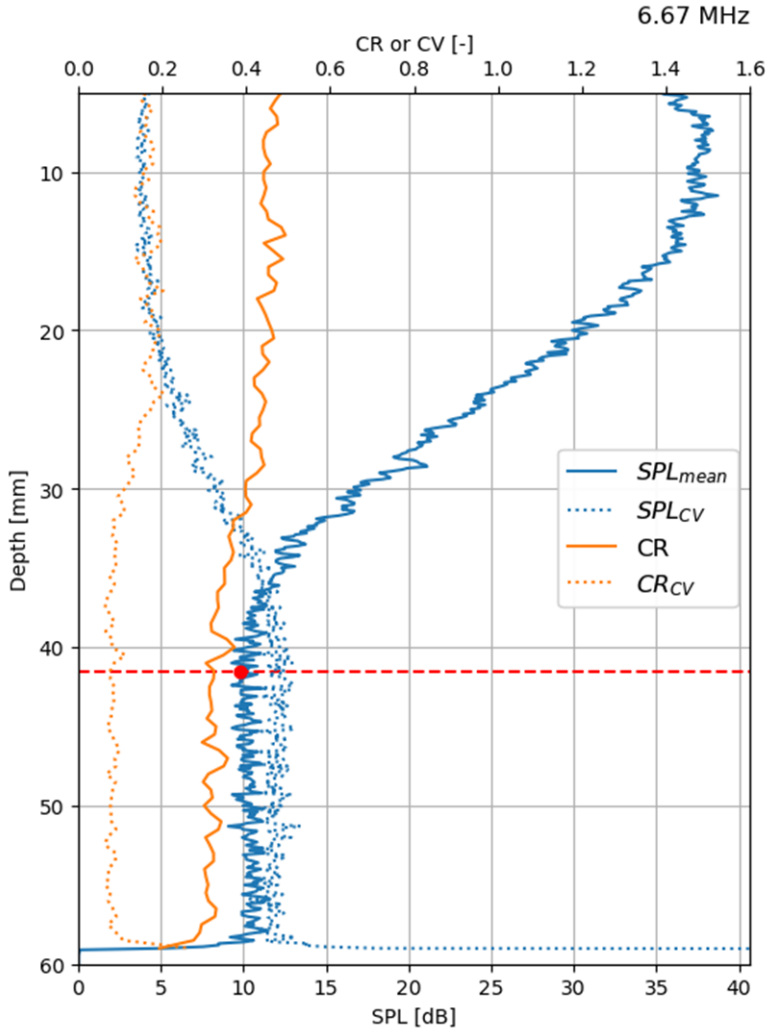

Figure B.9: *SPL and CR profiles resulting from experiments in mud with a density 1.146 $g{\cdot}cm^{-3}$ and an ultrasound frequency of 6.67 MHz, using the linear array.*

List of Figures

List of Tables